PHD

Fuel Pump Motor-Drive Systems for More Electric Aircraft

Skawinski, Grzegorz

Award date:
2010

Awarding institution:
University of Bath

FUEL PUMP MOTOR-DRIVE SYSTEMS FOR MORE ELECTRIC AIRCRAFT

Submitted by Grzegorz Skawinski
for the degree of
Doctor of Philosophy
of the University of Bath
Department of Electronic and Electrical Engineering
August 2010

Abstract

The fuel systems fitted to the current generation of civil transport aircraft are rather complicated, due to the presence of multiple tanks, pumps, valves and complex pipeline systems. During fuel transfer between the tanks, when controlling the aircraft centre of gravity or engine feed and refuel operations, a number of pumps and valves are involved resulting in complex pressure and flow interactions. In order to minimise the pressure surges during sudden system changes and flow overshoot during fuel transfer and refuelling, different motor drive system control strategies have been investigated. It is proposed that the current control method of electrically driven centrifugal-type pumps could be replaced by improved open and closed loop strategies where the flow overshoot can be minimised and pressure surges reduced. Steady-state and dynamic models of an AC induction motor drive and typical aircraft fuel system pipework components have been developed. The validation of these models has been performed using experimental data obtained from a fuel test rig constructed at the University of Bath using water as the working fluid. The simulation results have been shown to agree well with those from experimentation. In addition, the induction motor has been modelled based on its physical properties using the Finite Element Method software MEGA. The investigated fuel system has been described in linear terms and its behaviour has been identified. It is shown that the system dynamic behaviour can be controlled/improved using well established closed loop proportional-integral control. An open loop technique of simultaneous pump and valve control has been proposed and validated using experimental results, resulting in a reduction of both the transient pressure surges and flow overshoot during sudden valve closures, showing significant performance improvements. Improved closed loop control strategies for the pump drive system have also been developed in simulation. These are based on adaptive proportional-integral-derivative and fuzzy logic control strategies.

Acknowledgements

This work is the result of a collaboration between the Electrical Engineering and Mechanical Engineering Departments at the University of Bath. The research was supported by Airbus UK and Parker Aerospace, which is gratefully acknowledged.

I would first of all like to express my gratitude to the people who made this work possible in the first place. My most sincere thanks go to my supervisors, *Dr. Francis Robinson*, *Dr. Derek Tilley*, *Dr. Nigel Johnston* and former supervisor *Prof. David Rodger* for their expert advice, their commitment and support throughout the project.

Furthermore I owe thanks to the laboratory support staff during these years, especially *Vijay Rajput*, for the practical help given on conducting the measurements and technical experiments.

I am also grateful to my colleagues from the project, *Lewis Boyd* and *Andrew Roberts*, for their kindness and help they have given me during the work.

Finally, I would like to thank my wife *Jolanta*. Her love, support and encouragement during this work were invaluable.

Contents

List of Figures

List of Tables

Nomenclature

SUBSCRIPTS

$a,\ b,\ c$	phase variables expressed in *abc* stationary coordinates
br	blocked rotor variable
$d,\ q,\ 0$	phase variables in expressed in *dq0* rotary coordinates
dc	direct current variable
in	input variable
m	magnetising variable
nl	no load variable
out	output variable
r	rotor variable
$rated$	rated variable
rs	rotor to stator coupled variable
s	stator variable
sr	stator to rotor coupled variable
th	Thevenin variable

NOTATION OF VARIABLES

$\tilde{X}$	complex variable
$\|X\|$	absolute value of variable
$\mathbf{X}$	vector/matrix variable
X'	rotor variable refereed to stator frame
X^T	transpose of variable
$X(s)$	variable s-domain transfer function
$X(z)$	variable Z-domain transfer function
$X(n)$	variable discrete time function

VARIABLES

$\mathbf{A}$	magnetic vector potential
A	cross sectional area
A_v	valve cross-sectional flow area
a	filter coefficient
$\mathbf{B}$	magnetic field vector
B	effective Bulk modulus including cavitation
B_d	load viscous-friction damping coefficient
B_f	fluid Bulk modulus
B_{pf}	fluid-pipework Bulk modulus
C	fluid capacitance
C_q	flow coefficient
C_{air}	air content in fluid
cv	inverter control signal
$cos\ \varphi$	power factor
d	pipe diameter
de	derivative of pressure control error
d_v	valve internal diameter
d_{rl}	return pipe diameter
$\mathbf{E}$	electric field vector
E	Young's modulus
e	pressure control error
e_1	pressure control error (adaptive gain controller)
e_2	pressure performance error (adaptive gain controller)
F	force
f	friction factor
f_e	supply frequency
f_t	blocked-rotor test supply frequency
g	gravity acceleration

$\mathbf{H}$	magnetic field strength vector
h	elevation height
h	digital filter kernel
h_f	head loss
h_m	minor losses
$\mathbf{I}$	identity matrix
I	current RMS
$\mathbf{J}$	current density vector
J	total moment of inertia
J_l	pump moment of inertia
J_m	motor moment of inertia
j	complex operator ($\sqrt{-1}$)
$\mathbf{K}$	Park's transform matrix
$\mathbf{K}^{-1}$	inverse Park's transform matrix
K	minor losses coefficient (K factor)
K_b	back calculation gain (anti-windup)
K_D	derivative gain
K_I	integral gain
K_i	inverter gain
K_P	proportional gain
k_Ψ	inverter proportionality constant (V/f)
L	fluid inertance
L	inductance
L_{lr}	rotor leakage inductance
L_{ls}	stator leakage inductance
L_{sm}	magnetising inductance
l	pipe length
l_e	equivalent length of minor losses
l_{rl}	return pipe length
$\mathbf{M}$	rotational operator

m	mass
N	speed
N	number of segments in pipe lumped model
P	active power RMS
P	pole number of motor windings
P_m	mechanical power
P_{in}	motor input power
P_{loss}	motor losses
p	pump outlet pressure (gauge)
p	differentiation operator (d/dt)
p_a	absolute pressure
p_{d1-3}	quadratic fitting coefficients for pump pressure-flow characteristic
p_m	pressure drop due to minor losses
p_v	valve upstream pressure
p_{sat}	saturation pressure
p_{vap}	vapour pressure
Q	volumetric flow rate
Q	reactive power RMS
R	fluid resistance
R_c	core losses
R_r	rotor resistance
R_s	stator resistance
Re	Reynolds Number
r	resistance
r	pump impeller radius
S	apparent power RMS
s	slip
s	s-domain operator
s_{max}	breakdown slip

T	torque
T	sampling time
T_e	electrical torque
T_l	load torque
T_t	tracking time (anti-windup)
T_{max}	electrical breakdown torque
t_i	inverter dominant time constant
t_w	pipe wall thickness
V	voltage RMS
V	volume
V_{air}^{sat}	air volume at the saturation pressure
V_{boost}	inverter boost voltage
V_{diss}	volume of dissolved gas at pressure p
v	velocity
v_{c1-6}	polynomial fitting coefficients for valve flow coefficient characteristic
v_{a1-6}	polynomial fitting coefficients for valve area characteristic
w	width
X_m	magnetising reactance
X_r	rotor leakage reactance
X_s	stator leakage reactance
Z	impedance

GREEK VARIABLES

α	valve angle
α_T	material temperature coefficient
β	compressibility factor
β	convergence factor
β_{1-6}	polynomial fitting coefficients for pump pressure-flow characteristic
Δp	pressure difference across valve
δp	pressure drop (difference)

ΔT	temperature difference
Δu	voltage change (fuzzy logic)
ϵ/d	pipe relative roughness
η	efficiency
γ	polytropic index
γ_{1-6}	polynomial fitting coefficients for pump torque-hydraulic power characteristic
γ_{l1-2}	linear fitting coefficients for pump torque-hydraulic power characteristic
λ	flux linkage
μ	dynamic viscosity
μ	magnetic permeability
ν	kinematic viscosity
ω	shaft angular speed
ω	angular speed of arbitrary reference frame
ω_r	angular rotor mechanical speed
ω_s	angular synchronous speed
ϕ	non-dimensional flow coefficient
ψ	non-dimensional pressure coefficient
ρ	density
σ	electrical conductivity
τ	non-dimensional torque coefficient
τ_f	stress force (shear force)
θ	stator angle
θ_r	rotor angle
θ_t	variable transformation angle
υ	pump equivalent displacement factor
φ	phase angle
ζ	dimensionless head-loss

ABBREVIATIONS

AC	Alternating Current
AMB	Active Magnetic Bearing
APU	Auxiliary Power Unit
AVPT	Active Valve and Pumping Technologies
CFD	Computational Fluid Dynamics
DC	Direct Current
DSP	Digital Signal Processing
DTC	Direct Torque Control
EHA	Electro-Hydraulic Actuation
EMA	Electro-Mechanical Actuation
FIR	Finite Impulse Response
FBW	Fly-By-Wire
FEM	Finite Element Method
FLC	Fuzzy Logic Controller
FOC	Field Oriented Control
IIR	Infinite Impulse Response
IGBT	Insulated Gate Bipolar Transistor
MF	Membership Function (Fuzzy Logic)
MEA	More Electric Aircraft
PI	Proportional and Integral
PID	Proportional, Integral and Derivative
PMSM	Permanent Magnet Synchronous Motor
PWM	Pulse Width Modulation
RFI	Radio Frequency Interference
RMS	Root Mean Square
SRM	Switched Reluctance Machine
THD	Total Harmonic Distortion
TRU	Transformer Rectification Unit
V/f	Volt per Frequency
VI	Virtual Instrument (Labview)
VSI	Voltage Source Inverter

Chapter 1

Introduction

1.1 More Electric Aircraft

Since the 19th century, when the first aircraft were developed [1], the aerospace industry has contributed to improving and expanding technological development and high living standards throughout the world, and the long-term outlook for air travel continues to be very positive. The number of air-traffic passengers is likely to increase significantly in the future. Furthermore, cargo traffic is gaining in popularity due to resulting reductions in time and cost.

Nowadays an aircraft has a number of subsystems supplied by one or more sources of power such as hydraulic, pneumatic, electrical, and mechanical. These power sources are derived from the main engines using mechanically coupled shafts and engine driven compressors to feed pneumatic lines. Mechanical power is distributed by gearboxes to drive hydraulic pumps, fuel pumps, and electrical generators. Generated in this way, electrical power is used for avionics and to supply the utility and control systems. Hydraulic power, which is distributed throughout the aircraft, feeds actuation subsystems such as flight control actuators, landing gear and utility actuators. Pneumatic power drives the air-turbine motors for engine-start systems and the environmental control systems such as pressurisation, ice protection and air-conditioning systems.

The ongoing carrier demands for improvements in efficiency, reliability and ease of maintainability pressure aircraft manufacturers to develop new technologies to extend current performance and requirements. To improve the overall performance of future aircraft, the replacement of existing non-electric power systems with electrically-driven equivalents, in so called "More Electric Aircraft" (MEA) [2, 3], has been the subject of discussion for the

last two decades. The MEA concept has resulted in many research programmes [4, 5], including the Fly-By-Wire (FBW) program [6] supported by Airbus, and it is expected that this will lead to the development of new technologies to improve aircraft performance, especially to meet greater efficiency and flexible control requirements in future aircraft.

To realise this goal, many different techniques have been discussed in the literature [4, 6–10]. The important part of this programme is the development of electrical power systems and power electronic components to enhance reliability, fault-tolerance, power density and overall performance. The increase in aircraft electrically powered systems is likely to produce volume and weight savings as well as allow more sophisticated control [11].

The electrical power systems used nowadays on most commercial aircraft consist of power generation, distribution, conversion and battery storage stages [7]. The aircraft electrical systems are supplied from one or more power sources including engine driven AC generators, auxiliary power units (APUs), external power stages and ram air turbines. The generated power is regulated and distributed throughout the aircraft by primary and secondary power distribution systems. Furthermore, an emergency power source is mounted on board in case of failure of the main engine generators. A simple main electrical power channel is shown in figure 1.1.

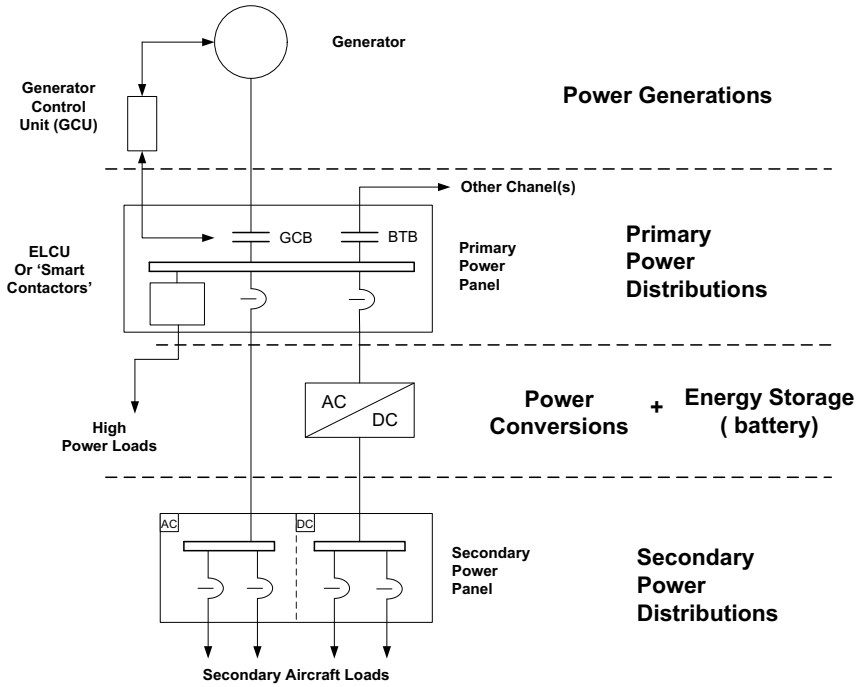

Figure 1.1. Aircraft electrical power system [7]

The power generation plays an essential role in the aircraft electrical systems. Since the power demand in future aircraft will increase, it is necessary that the power density also increases and more sophisticated load management is implemented. Both AC and DC supply systems, used in the aerospace industry nowadays [7], are the subject of research within the MEA program.

The most common supply system employed in current aircraft is 115V AC 400Hz constant frequency power systems. This historically-proven system, however, has some drawbacks in terms of weight and reliability. This arises due to the mechanical conversion assemblies required to change the varying speed of the engine shaft into a constant speed to drive the electrical generators. Due to MEA power requirements this system is unlikely to be considered in the future.

The 115V AC variable frequency system called "frequency wild" is gaining more acceptance and has been employed on the largest commercial aircraft in use today: the Airbus A380. The electrical starter/generator is fed mechanically directly from the main engine, avoiding the need for mechanical speed conversion, resulting in weight savings. However, in order to supply the secondary power levels, the power electronics converting stage requires a more complex conversion approach as the frequency varies from 350 to 800Hz. This system is more flexible than the constant frequency approach, although to reduce wiring weight, limit distribution losses and deliver higher power density, 230V AC "frequency wild" is also being considered. The higher voltage level, however, already restricts the use of this system due to discharge and arcing problems. Careful design of the electrical system, development of proper isolation and switching assemblies could contribute to the widespread adaptation of this system in the next generation of aircraft.

In contrast to AC, direct current systems have been adopted in military aircraft. The 270V high-voltage DC system has many advantages including ease of parallel DC-bus connection. In addition, inverter-fed motors can be directly connected to DC buses for an AC power distribution system, although additional power conversion stages are required resulting in additional weight. However, safety requirements necessitate the demonstration of safe insulation of power buses in the event of over-current fault conditions. As a consequence, high voltage DC systems are restricted to the military aircraft, although use of these systems for civil aircraft is a current area of study/research. Low voltage, 28V DC systems are also used, mainly for emergency power and for battery storage. In addition to the above, hybrid configurations are being investigated incorporating AC generation and primary distribution with local secondary DC distributions [12].

The power generated within aircraft is forecasted to rise dramatically (approximately up to 500kVA) due to the fact that more and more aircraft systems will be powered electrically in the future. Since existing technology is unlikely to meet these high-power requirements, a new starter/generator is under development [13, 14] which will replace existing three-phase wound-field synchronous generators.

To improve overall performance the next generation of starter/generators are likely to be embedded directly into advanced gas turbine engines [15]. Consequently, the machines will work in a harsh environment, where the temperature possibly exceeds 300 ℃. Thus, high temperature magnetic materials will be necessary. Even so proper cooling systems will have to be employed. Since the MEA concept assumes high electrical power usage, the high power generation will require high speed machines to achieve weight and volume savings.

Switched Reluctance Machines (SRM) are predicted to be the next generation of aircraft starter/generators [14]. The SRMs, with recent advancements in power electronic component technologies, high temperature wire insulation, high temperature and hard magnetic materials, are expected to satisfy the required operating conditions. The SRM offers a robust, fault tolerant solution suitable for the harsh jet-engine environment. For emergency power generation, permanent magnet machines are likely to be employed.

Power distribution systems play a key role in the aircraft electrical network. It is required that these systems are fault tolerant, meet power quality demands and be capable of delivering uninterruptible power, especially to critical flight loads [16]. For safe operation of the distribution network, smart protection systems including over-current, differential current and ground fault protection are required and high-current intelligent power contactors and controllers will be essential. In addition, the development of arc detection circuits is also necessary. An example of a future distribution system is MADMEL [17] which describes the possible electrical system of aircraft.

The use of power electronics in aerospace technologies is widespread and the trend is for greater use as sophisticated power conversion stages are required to fully implement the MEA concept. The application of power electronic devices and converters is present on all stages of electric systems. The starter/generator machines use power conversion and conditioning units, the electrical loads are supplied from the converters and power level conditioners/converters are present in the system [18]. Depending on the electrical power generation system chosen, different types of converters are employed in the distribution system and conventional solid-state converters and Transformer Rectification Units (TRU) are used [19, 20]. Since the loads connected to secondary distribution systems are DC and AC supplied, and work at different voltage levels, a number of AC/DC, DC/AC and DC/DC converters are required [21, 22]. In addition, separate converters are used as the battery chargers, providing an isolation stage between the battery banks and the main network. The power electronic converters also constitute an important part of the motor drive technologies applied to electrical-controlled actuators, fuel pump drives and other loads where electrical-mechanical power conversion is required.

A number of different power-converter topologies and control strategies can be found in the literature [22, 23] and it seems that this field of research can significantly improve

the overall performance of aircraft. The PWM and SVPWM techniques are extensively used for voltage source inverter (VSI) and current source inverter (CSI) systems. However this hard switching employed in the power semiconductor devices highly stresses them during on/off transitions and consequently the operating frequency is limited. Application of proper snubber circuits limits transition losses, reduces commutation stresses and protects the converter from an inrush current and over voltage. However, the additional components reduce overall converter reliability.

The resonant DC-link and resonant AC-link converters represent the next generation of inverters. An additional resonant tank is incorporated, resulting in a soft transition characteristic for the switching devices. Zero-current switching (ZCS) and zero-voltage switching (ZVS) have gained popularity due to an increased switching frequency range as switching occurs during low current and low voltage conditions. In addition, small switching losses and reduced electromagnetic interference makes them an attractive alternative in the aerospace industry.

The newest alternative to the inverter in motor drives is the matrix converter [24]. This bi-directional topology does not require DC-link storage components and consequently the lack of large electrolytic capacitors, one of the biggest causes of failure in electronic systems, and inductors offers significant advantages. The size of the converter is greatly reduced in relation to conventional technologies since intermediate storage components are not present. However, the complex control systems involved and the need to use a higher number of switches are major disadvantages. The matrix converter constitutes a good alternative when the power quality requirements are high, because with a proper control scheme the converter can operate with a unity power factor and draw relatively undistorted sinusoidal currents.

The advent of new technology power semiconductor devices such as Metal-Oxide- Semiconductor Field Effect Transistor (MOSFET), Insulated Gate Bipolar Transistor (IGBT) and Mos-Controlled Thyristor (MCT) contribute to a wide range of power electronics in the aerospace industry. These fully controllable switching devices offer significant improvements in power density and high efficiency, resulting in a considerable reduction in the weight and size of the converters. It is expected that the development of Silicon Carbide based (SiC) power devices, working at greater current and voltage ranges (above 1000 V) and operating at higher temperature (up to 400℃), will further enhance the efficiency and reliability of power electronics converters [25]. With other advances in thermal management technologies and control electronics such as the Digital Signal Processor (DSP) and Field Programmable Gate Arrays (FPGA), power converters will be able to be more flexibly controlled in future aircraft electrical technology.

Passive components constitute the weakest link in aircraft electrical systems. They contribute significantly to the overall mass of power electronic devices and play a major role in

achieving reliability improvements. To make MEA the preferred option, the development of new insulation, dielectric and magnetic materials for components such as capacitors and inductors is necessary. For insulation materials, higher operating temperatures (up to or above 300 ℃) are required. Traditional Kapton based insulation is likely to be replaced with advanced polymer insulation materials such as Eymyd and Upilex S, which offer superior electrical and thermal properties [8].

The improvement of capacitor technology is essential for realising further improvements in power conditioning devices in terms of volumetric and weight reductions. As a result, new organic and inorganic based capacitor technologies are currently under development. The use of high dielectric strength materials such as PBZT polymer is also being investigated. The Fluorene Polyester (FPE) and Diamond Like Carbon (DLC) capacitor technologies, which have a twofold increase in temperature capability and up to three times improvement in energy density, are also the subject of research. Diamond has the highest thermal conductivity of any known material and a very high dielectric strength. In addition, it has better electric-breakdown strength compared to classical polycarbonate capacitors. Other promising dielectric materials and construction techniques, including silicon carbide, barium titanate, multilayer diamond capacitor [8] and high temperature (up to 300℃) multilayer ceramic capacitor, are also being developed. The latter offers a tremendous volumetric density compared to other capacitor technologies. The use of super capacitors for the aircraft industry is also under consideration [26] as this technology can significantly improve energy storage capability and enhance the voltage regulation of electrical systems.

Over recent years, there has been much activity in magnetic materials and subsystems improvement. The development of high permeability, large saturation and remnant induction magnetic materials capable of operating at high temperatures (up to 500℃) is underway [9]. The use of soft magnetic material such as current state-of-the-art iron-cobalt (Co-Fe) alloys is also being investigated [21]. The overall reliability and maintainability of machines can be additionally improved by Active Magnetic Bearings (AMB) utilisation. The conventional oil lubricated bearing systems can be replaced with this contactless technology, resulting in a reduction in the weight due to the elimination of the lubrication system [15]. In addition, higher rotor speeds can be achieved as this non-contact system reduces friction. However, AMBs are limited in their load capacity and may not be able to prevent contact under high-g manoeuvres.

To meet MEA requirements, most of the aircraft loads are likely to be supplied by electrical means. Thus, the largest loads present on current aircraft, including flight control systems, utility actuation, compressors for cooling aircraft systems and fuel pumps, will all be driven by electrical motors. Since motor drive systems form an integral part of the utilisation equipment and provide the interface between the electrical power system and the loads, then reliable, high power density motor drive systems with power ratings ranging from fractional kW up to hundreds of kW are required [8].

The electrical motor plays a significant role in the motor drive system since its operating characteristics depend largely on the type of motor used [23, 27, 28]. The motor selection process depends mainly on the application and is based on the speed, power, fault tolerance and thermal capability requirements.

Historically, DC motors with excellent drive performance were employed as adjustable speed drives (ASD) in the aerospace industry. However, due to poor reliability as a consequence of mechanical maintenance (commutator and brushes), brushless motors operated from variable frequency drives (VFD) are more popular nowadays. The induction motor (IM) and permanent magnet synchronous motor (PMSM) are used on modern aircraft and brushless DC motors are now being used on Airbus aircraft. High speed, high performance switch reluctance motors (SRM) and stepper motors are also being considered as the electric drive for servo and variable speed applications in the next generation aircraft. Due to the move to "frequency wild" supply systems, the adaptation of motor drives to this system has already started and the use of induction motors fed directly from a varying supply frequency is being developed. In addition, the development of lower cost, high reliability, high-speed electric machines is underway.

Recent improvements in power drive electronics have led to the development of new efficient control techniques for motor drive systems. Consequently, more convenient and efficient speed and torque control has been achieved, resulting in higher torque/inertia ratios and power density capabilities. For ordinary applications, the widespread Volts per Hertz (V/f) strategy is frequently used. In more precise control applications, closed loop V/f control is implemented by employment of feedback sensors. For high precision and performance operation Field Oriented Vector (FOC) control methods are used [6]. These inherently closed loop systems are implemented by either direct feedback sensors or indirect rotor position estimation, offering strong system robustness although their performance is limited by the accuracy with which motor parameters are known. The Direct Torque Control (DTC) technique is gaining more acceptance as high precision control is possible using simpler control algorithms than with FOC control. However, high precision sensors are required and fast microprocessor controllers have to be used.

In order to meet the MEA requirements, all conventional hydraulic and pneumatic actuators used for primary flight and utility control, such as braking and flight control surfaces [29], are to be replaced by electrically-driven counterparts. The research into the comparisons between different actuator topologies is ongoing [23]. Currently, two options are being investigated that involve the combination of electrical subsystems with either mechanical power technologies, including accessory drive gear boxes, or hydraulic subsystems [4]. Electro-mechanical actuation (EMA) employs an electric motor drive for direct control of actuators via mechanical gearing. The second option is electro-hydrostatic actuation (EHA), where an electrical motor is used to supply mechanical power to dedicated hydraulic pumps, which in turn provide hydraulic power to actuator output stages.

The optimisation of fuel distribution and pumping systems is important since correct fuel management contributes significantly to aircraft performance. The in-flight centre of gravity control, developed by Airbus, forms an essential part of fuel distribution management since aircraft efficiency is improved due to drag reduction. Research into pump and valve technology is being conducted to improve in-flight fuel transfer operations and engine feed systems as well as ground refuelling. The conventional pump system configuration, composed of a constant speed electric motor and fixed displacement pump, offers efficient use of electrical power. However it suffers from pressure and flow distribution problems such as pressure overshoot in the case of sudden valve closure. Thus, the development of appropriate control strategies for such systems can enhance the overall fuel distribution system performance. The development of intelligent valves and valve control systems can also be beneficial as this can also improve fuel distribution.

In light of the above, a research project has been undertaken at the University of Bath in conjunction with Airbus (UK) and Parker Aerospace concerning active valve and pumping technologies (AVPT). The project commenced in 2004 and is described in the following section. It has supported three postgraduate students and one post doctoral research officer.

1.2 Active Valve and Pumping Technology Project

1.2.1 Project overview

The Active Valve and Pumping Technology project is concerned with fuel systems for future aircraft. Such systems are of particular interest as their understanding and development can potentially improve the performance of refuel and fuel-transfer operations. This project is directed at the development of component technologies, including pumps, valves and motor drives. One of the main aims of the research is to develop intelligent components that will help to reduce fuel system complexity on the aircraft. The second focus of the project was the analysis of pressure transients in aircraft fuel systems. The research has also considered advances in aircraft system technology, such as the introduction of "frequency wild" electrical supplies.

Computer simulation has been used to model the performance characteristics of fuel systems and their components, including the fuel tanks, interconnecting pipework, control valves, pumps and electrical drives. The models have been developed and validated using test data obtained from experimental test rigs constructed in the departments of Mechanical and Electrical Engineering at the University of Bath. New control techniques have been developed for the pump, valve and motor drive systems to improve system perfor-

mance during both refuel and in-flight transfer operations. The project roles undertaken by the three postgraduate students are described in the following subsections.

1.2.2 Active Valve Control

The valve project aimed to provide information about aircraft fuel systems with respect to valve operation [30]. The refuel and fuel-transfer operations have been considered as they have an impact on the overall fuel system performance. An electrically driven ball valve has been modelled analytically and its performance has been characterised experimentally. A Computational Fluid Dynamics (CFD) model has been created in order to obtain better understanding of the flow through the valve at different valve openings and to optimise valve operation. A separate flow visualisation rig was developed for analysing the operation of the valve at different operating conditions including the on-set of cavitation. State-of-the-art flow visualisation techniques have been used to investigate the flow through the valve over a range of valve openings.

A means of minimising surge pressures during valve closure sequences was investigated and an intelligent control method has been proposed to minimise pressure overshoot during sudden valve closure. The introduction of new components and a control procedure has been suggested which would lead to the development of semi-active control valves.

1.2.3 Pumping Technology

The pumping technology project was tasked with investigating the pump performance in aircraft fuel systems and to explore new opportunities in pumping technology [31]. An investigation of variable speed pumps was conducted as these could be beneficial in reducing the power consumption during a flight by matching the fuel demand, preventing pressure surges and reducing component wear. In addition, an investigation into the benefits of variable fuel transfer rate between internal aircraft tanks, at both the component and aircraft level, was conducted. The fuel transfer to control the centre of gravity was also proposed.

A three-degree of freedom simulation of flight was performed, looking at fuel consumption and overall fuel system performance. Health monitoring and fault detection tools for aircraft fuel systems were also proposed and discussed, which could be accomplished by developing an accurate system performance prediction model.

1.2.4 Electric Motor Drive Technology

The Electric Motor Drive Technology project is reported in this thesis. The project, jointly undertaken between the Mechanical and Electrical Engineering Departments at the University of Bath, is directed at the electric motor drive technology for future aircraft. This includes a review of conventional and future electrical technologies. Since an induction motor is one of the most reliable motors, its control options are also investigated and mathematical models of the induction machine are presented. In addition, a Finite Element Model is developed allowing traditional analytical methods to be compared with numerical solutions.

Since the project forms part of the Active Valve and Pumping Technology Project, the computer modelling of the aircraft fuel system components forms part of the research. The models will be validated using separate electric motor and fuel test rigs, that will allow both individual component behaviour and overall system performance to be evaluated. Furthermore, a motor drive system control technique will be investigated to minimise the pressure surges during sudden system changes and flow overshoot during fuel transfer and refuelling. The development and validation of a motor drive system controller for future generation aircraft will be investigated by comparing a conventional analogue controller with a digital equivalent.

1.3 Objective of the Thesis

The objectives of the research described in this thesis are:

- ◇ The characterisation and modelling of the AC induction motor drive used on the fuel system rig at the University of Bath.
- ◇ The modelling of the hydraulic components of the fuel system rig and integration with the electric models for the overall fuel rig modelling.
- ◇ The development and validation of an AC motor control system suitable for fuel pump pressure control of future aircraft.

1.4 Outline of the Thesis

The work presented in this thesis is divided into nine chapters as indicated below:

Chapter 1 provides a general literature review dealing with new trends and technologies in the field of aircraft electrical subsystems. The background of the Active Valve and Pumping Technology project is given, the thesis objectives and the outline of the thesis are presented.

Chapter 2 includes a description of the fuel and induction motor test rigs and details regarding dimensional and physical properties are listed.

The principles of the mathematical modelling of an AC induction machine are presented in Chapter 3. The analytical models are described for both steady state and dynamic modelling, respectively. The motor steady state and transient characteristics are depicted and analysed. In addition, the motor-parameter evaluation method is presented and the results are listed.

A finite element model of the rotor cage induction motor is presented in Chapter 4. The results obtained from the finite element method analysis and the analytical calculations are compared with measured data.

Chapter 5 deals with the hydraulic component modelling including the models for the pump, valve and pipes. The approach is based on well-established hydraulic modelling techniques. Different ways of implementing the hydraulic components are discussed and simulation data is validated using test rig data.

Chapter 6 describes the validation of the mathematical models developed for the fuel test rig and induction motor. The simulation result from two different simulation packages are compared and validated against the test rig data.

A linear model of the fuel test rig is developed in Chapter 7. The open loop characteristics are determined for different system input conditions. An analogue PID based controller design is described and closed loop simulation responses are given along with the experimental fuel rig validation data. A technique for simultaneous pump and valve control is presented to reduce pressure surges and minimise overflow during fast valve closure.

Chapter 8 covers the digital controller design. This chapter is focused on the implementation of a fixed gain PID, gain scheduled PID, an adaptive PID and a Fuzzy Logic based controllers for the induction motor. The digital control strategies are described and the simulation results presented. The performance of a classical PID controller is compared with adaptive PID and Fuzzy Logic based control strategies.

The conclusions are drawn in Chapter 9 and the areas of work to be completed in the future are described.

Chapter 2

Experimental Test Rigs

In order to validate the modelling methods undertaken under the Active Valve and Pumping Technology Project, two test rigs were developed. The overall system behaviour and a control strategy are studied and the results validated using these rigs. The main fuel rig and the electrical motor rig are described in detail in the following sections.

2.1 Fuel system rig

The fuel test rig at the University of Bath was designed to investigate the pressures and flows occurring during fuel transfer, distribution and refuelling operations. The operation of the test rig assists the research in several areas of interest related to the project 'active valve control', 'motor drive systems' and 'pumping technology'.

In this thesis, the test rig was used primarily to investigate the performance of a centrifugal pump and a variable speed motor. The effects of sudden valve closure on the system response was also investigated. Data obtained from the test rig was used to validate the component models developed for the centrifugal pump, motor drive, pipelines and aircraft fuel system ball valve.

The hydraulic test rig incorporates a motor operated ball valve, typical of those used in Airbus fuel systems. This allowed the response of the system at different valve closure times to be studied. A sensorless vector control strategy was also implemented for the induction motor control, allowing an assessment of the centrifugal pump dynamic response to be undertaken.

The fuel test rig consists of hydraulic and electrical components. The rig's modular construction allows fast and easy rearrangement of the components and pipe configurations depending on the focus of the tests. Photographs of the fuel rig components are presented in figures 2.1(a) and 2.1(b), and a schematic diagram of the test rig is presented in figure 2.2.

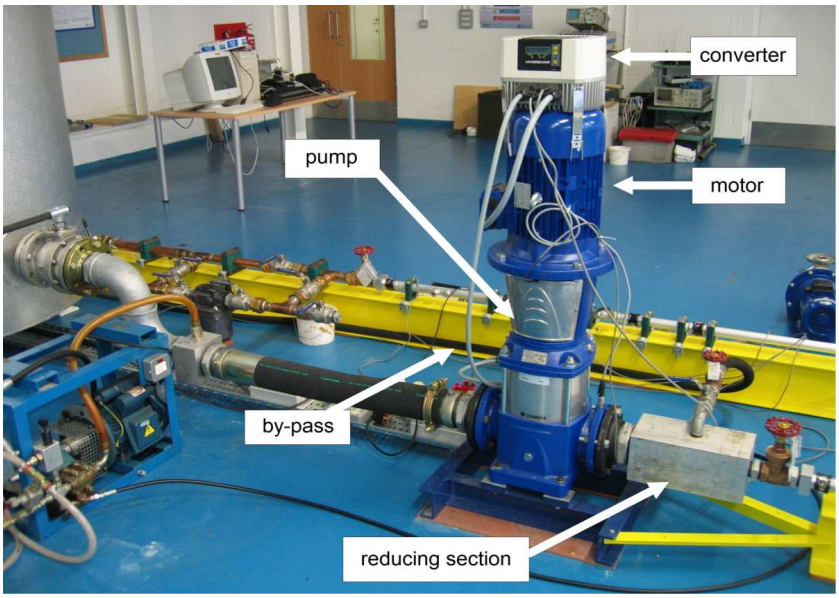

(a) Fuel rig - pump and motor drive system

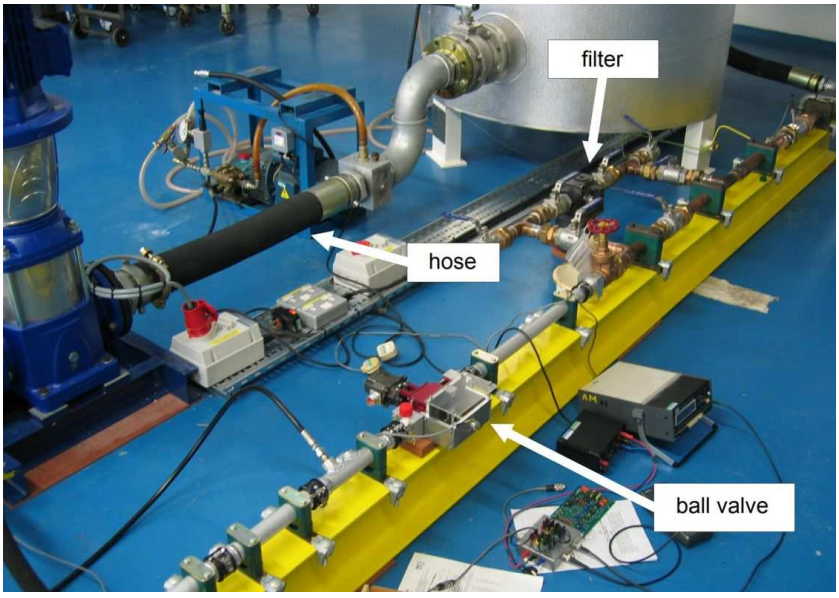

(b) Fuel rig - valve and pipeline

Figure 2.1. Fuel test rig

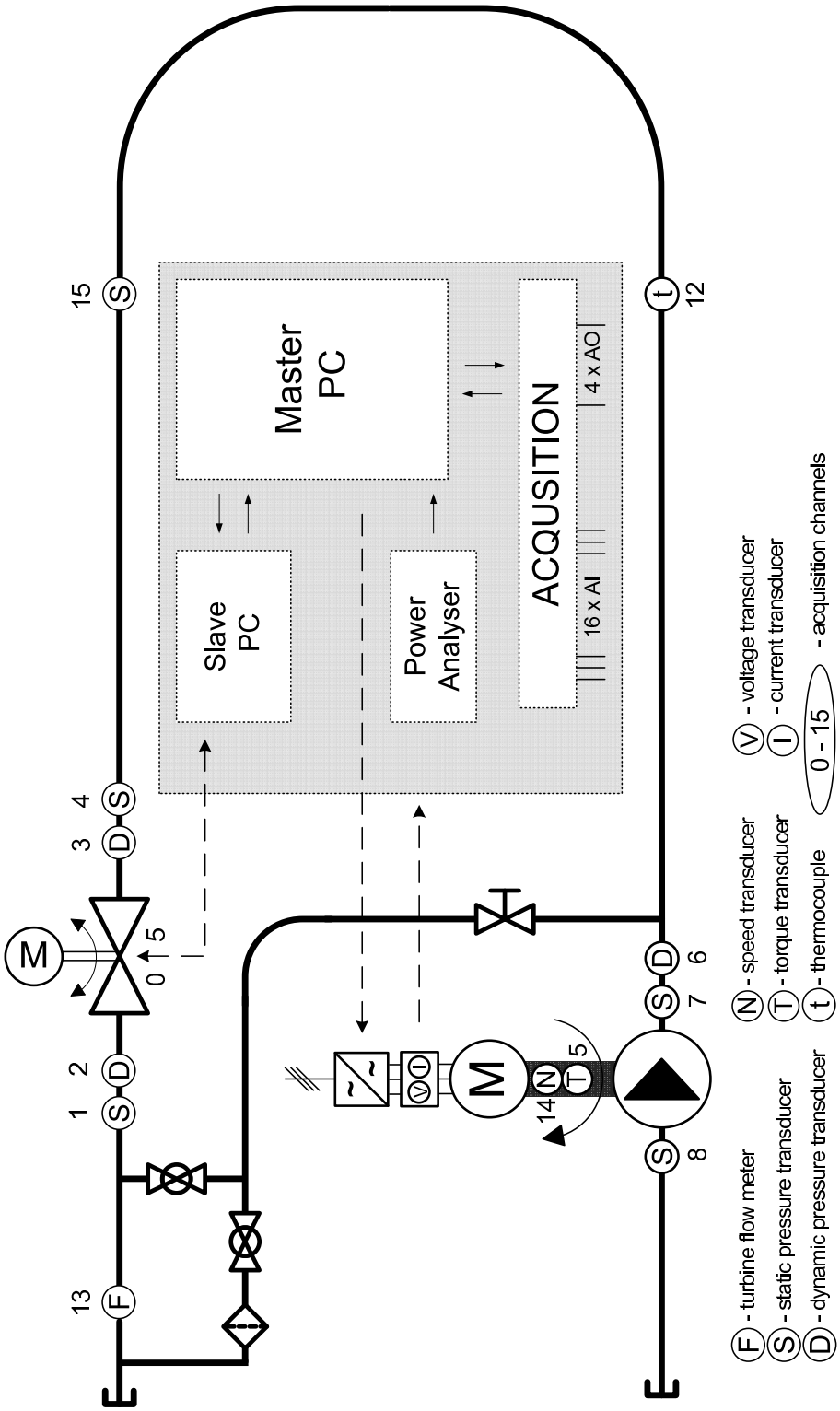

Figure 2.2. Fuel test rig at Bath University

2.1.1 Fuel Rig Hydraulic Components

For safety reasons, water rather than aviation fuel was used as the working fluid [32]. Different aircraft fuel substitutes were considered but none of them was suitable to meet health and safety requirements. Two chemicals, FERNOX CH-3 and FERNOX AF-10, were added to the water to prevent bacterial and fungal growth and to help avoid corrosion. They also helped to protect the system against limescale damage.

The water was stored in a large 2000L heated pressure vessel (tank). The temperature of the fluid could be controlled up to 70℃ using an internal heater. An external control card was designated for this purpose and was located in the main data acquisition and control rack. It was also possible to reduce the pressure in the tank to -0.5 bar to allow the effect of altitude to be investigated.

The tank was connected to the pump by a 0.9m long section of 4" diameter flexible hose and the return line was connected to the tank by a 2m long section of 3" bore flexible hose. Ball valves were fitted in the pump suction and return line for isolation purposes.

A commercial centrifugal pump manufactured by Lowara was used to represent the fuel pump. This vertical two-stage centrifugal pump (model Lowara SV66) could produce up to 6 bar pressure rise and deliver up to 1300L/min depending on the system pressure/flow requirements. The pump could be operated at constant or variable speed. The pump was driven by a three-phase 11kW AC electrical motor drive system described later.

An aluminium reducing section was used to connect the 4" diameter outlet port of the pump to the 1.5" diameter pipeline. A by-pass line was attached to the reduction block to allow flow to be passed directly back to the tank when low flow rates were required in the piping system. The flow rate through the bypass was controlled by a shut-off ball valve or varied by a gate valve.

The pipe sections were connected to each other by the Gamah couplings manufactured by Stanley Aerospace. These standard aircraft couplings acted as flexible joints between pipe segments, allowing the flexibility needed for fuel pipes installed in aircraft wings and fuselage during flight operations. In order to avoid generating significant pressure losses and transient pressure reflections, a single 180 degree bend, with a radius of approximately 0.5m, was incorporated into the pipeline.

A Parker Aerospace aircraft ball valve was located approximately 7m downstream of the bend. The operation of the valve was controlled by a remotely-controlled DC servo motor. An external controller was employed to control the position, speed and operation time of the valve. Generic user-defined operation profiles could be applied to the valve, to give a range of control possibilities. The motor-valve assembly was designed to reproduce typical aircraft component behaviour.

2.1.2 Fuel Rig Electrical Components

A schematic electrical diagram of the motor drive system connections employed in the fuel rig is presented in figure 2.3.

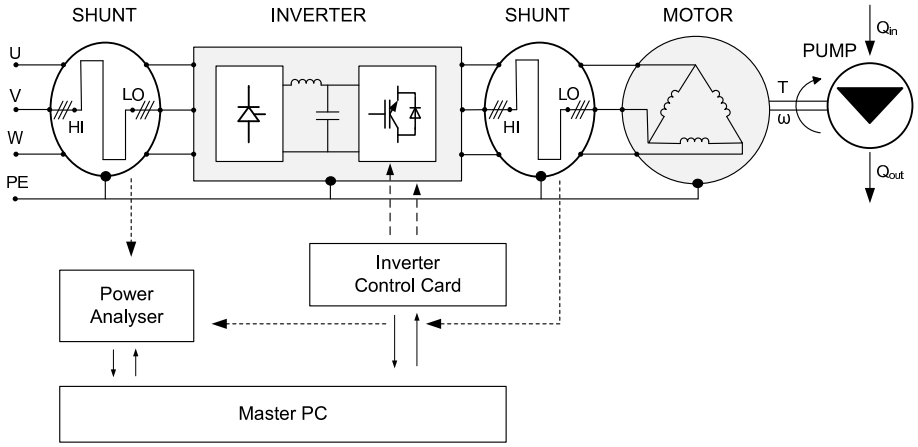

Figure 2.3. Electrical connections at fuel rig

The motor drive system consisted of an 11kW 3-phase AC induction motor and a variable frequency drive. The motor windings were delta connected in order to deliver higher output current for the same supply voltage comparing to a star connection. The star connection was also used but higher supply voltages were required to deliver the torque required by the pump.

The motor input power was controlled by adjustable frequency converters and two commercially available converters were used for this purpose. A Hydrovar converter was purchased as part of the pump system whereas a Moeller converter was purchased later in order to improve the behaviour of the pump and motor. Both converters consist of controllable thyristor rectifier bridges, DC-link filters with braking resistor branches and IGBT-based inverters. The internal controllers generate the output signals according to the specified control levels.

The control card was designed to control the converters by supplying an analogue signal to the analogue inputs on the converters. The Hydrovar converter required a 4-20 mA current source as an input control signal, whereas the Moeller accepted a voltage control signal in the range of 0-10 V. Both current and voltage maximum control signals correspond to the maximum operating voltage and frequency which could be set by the user at the time of converter configuration. In this way it was possible to control the shaft speed within the range of 300-3000 rev/min. The control signals could be generated in manual or feedback modes. A precision multi-turn rotary potentiometer was used for manual control whereas feedback control was implemented by a specially designated PID-based controller card.

Additionally, an external analogue signal could be implemented on the card for computer control and a PC-based speed controller was incorporated into the Labview-based main acquisition-control software developed for this purpose.

Both converters operate under the 'Volt per Hertz' control strategy and were controlled by external open loop voltage/current signals. The manufacturer's version of the closed loop option was implemented on the converters' control boards. Additionally, the Moeller converter was programmed to operate under a sensorless vector control regime to achieve better and faster motor response. In the latter converter, online auto-tuning of motor parameters was possible, further minimising the losses and improving motor behaviour.

For safety reasons two external emergency switches were located in proximity to the motor drive system and on the main data acquisition-control framework box.

A Norma 5000 power analyser was used to assess the efficiency of the electrical components and measure electrical power quality. As the current and voltage ranges exceeded the maximum measurement ranges, external shunts were employed. The first three-phase shunt was connected between the AC mains supply and the converter, allowing for mains supply condition monitoring. The second set of shunts was located between the converter and the motor. This arrangement allowed the motor supply condition to be determined, which is of prime importance. The electrical powers, voltages and currents were all measured. In addition, the electrical power quality parameters such as harmonic distortion, crest and form factors for both current and voltage were determined. The lack of the appropriate software did not allow direct access to sampled data, so only steady-state average values were available.

2.1.3 Data Acquisition & Post-Processing

The sensors installed on the rig are shown on figure 2.2. All sensors were connected to the PC-based acquisition software through intermediate stages. Post-processed data from the sensors was used for the model validation and real time control.

The pressure in the rig was measured by static (strain-gauge) and dynamic (piezo-resistive) pressure transducers. Both types of sensors were mounted in close proximity to record steady - state and dynamic system behaviour at each point of interest. The pump input and output pressures were measured by two pair of pressure transducers mounted close to the inlet and outlet flanges of the pump. A similar sensor arrangement was also employed at both sides of the valve. Additionally the pressure downstream of the bend was recorded for the pipeline pressure loss analysis.

A special shaft arrangement was designed and installed between the pump and electric motor that allowed speed and torque to be measured. The shaft speed was recorded by a Hall Effect device and a toothed wheel sensor fitted in the pump casing. Using sixty teeth

on the wheel allowed moderate speed accuracy to be obtained. The torque generated by the motor was measured by a vertically mounted in-line strain-gauge torque transducer mounted between the pump and the motor. Two rigid couplings were fitted on either side of the torque meter to account for any misalignment of the drive shaft between the pump and the motor.

The flow rate through the main pipe section was measured by a turbine flow meter which had a measurement range from 50 to 1100 L/min. Fluid temperature was measured at a position along the pipeline using a thermocouple. The density and viscosity of the fluid were determined by means of standard densometers and viscometers [31].

The data from all the transducers and valve position signal were recorded on the PC via a data acquisition card and post-processed online using Labview software (virtual panels) created for this purpose. The raw signals from the pressure transducers, thermocouple, pump speed sensor, flow meter and valve angle encoders were conditioned and filtered using signal conditioning cards developed in-house by the Department's instrumentation section.

Low-noise data cables were used to supply the raw signals from the transducers to the acquisition rack. These twisted two-conductor cables were screened to provide better suppression of noise with the screen grounded at one end (rack end) to avoid earth looping. The single acquisition channels for both voltage and frequency output transducers are shown in fig 2.4.

The voltage signals from transducers were passed through a two stage amplifier card with a second order low pass filter, fitted between the stages, having a 1kHz cut-off frequency. The signals from the frequency-output sensors (Hall effect transducers) were conditioned using a frequency-to-voltage conversion card with a low-pass output filter to smooth the DC output voltage.

A Data Translation high speed acquisition board was used as the acquisition card. This system was capable of measuring up to 16 signals at a maximum total sampling rate of 512kHz. The signals were multiplexed resulting in a maximum of 32kHz sampling frequency per channel. In normal operating conditions a 10kHz sampling frequency was used. Four analogue outputs were available for continuous use and the pump speed control and valve position signals were generated in this way. To minimise acquisition noise the conditioned sensor signals were connected to the acquisition channels using quasi-differential connections. Full details of the data acquisition card can be found in appendix B.

The data acquisition process was controlled by the PC operating under Windows XP using Labview software. Labview virtual instruments (VIs) were developed (mainly by the author) for different operational tasks and linked to each other in the main virtual instrument. The task-orientated VIs were implemented for board configuration, acquisi-

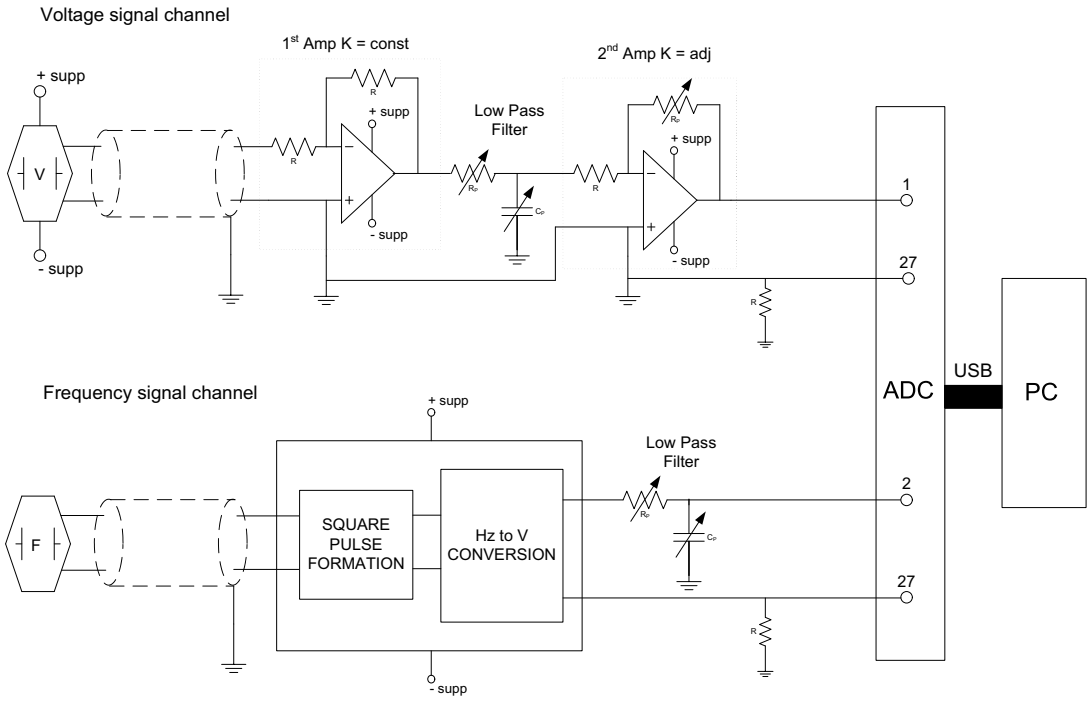

Figure 2.4. Single acquisition channels for voltage and frequency output sensors-schematic diagram

tion and control, valve and pump controlling, steady-state and transient data recording, time-averaging and signal error correction for steady-state analysis, filtering and Fourier analysis, and real-time signal monitoring. The master virtual instrument also acted as the master controller for the ball valve control instrument based on a second network-connected slave PC. This separate PC was needed as time interactions between the VIs caused significant time delays resulting in data capturing problems. The valve control VI was implemented in a way that allowed different operating modes of control to be applied, including manual controls, valve position self-checking, user-defined valve opening and closing profile operation.

The pump control was realised using a computer output mode implemented on the pump control card. A time control signal was included in the pump control VI to allow precise speed regulation. The combination of all the control subsystems allowed the complete control of the test rig within the data acquisition software. The front-end of the software is depicted in figure 2.5.

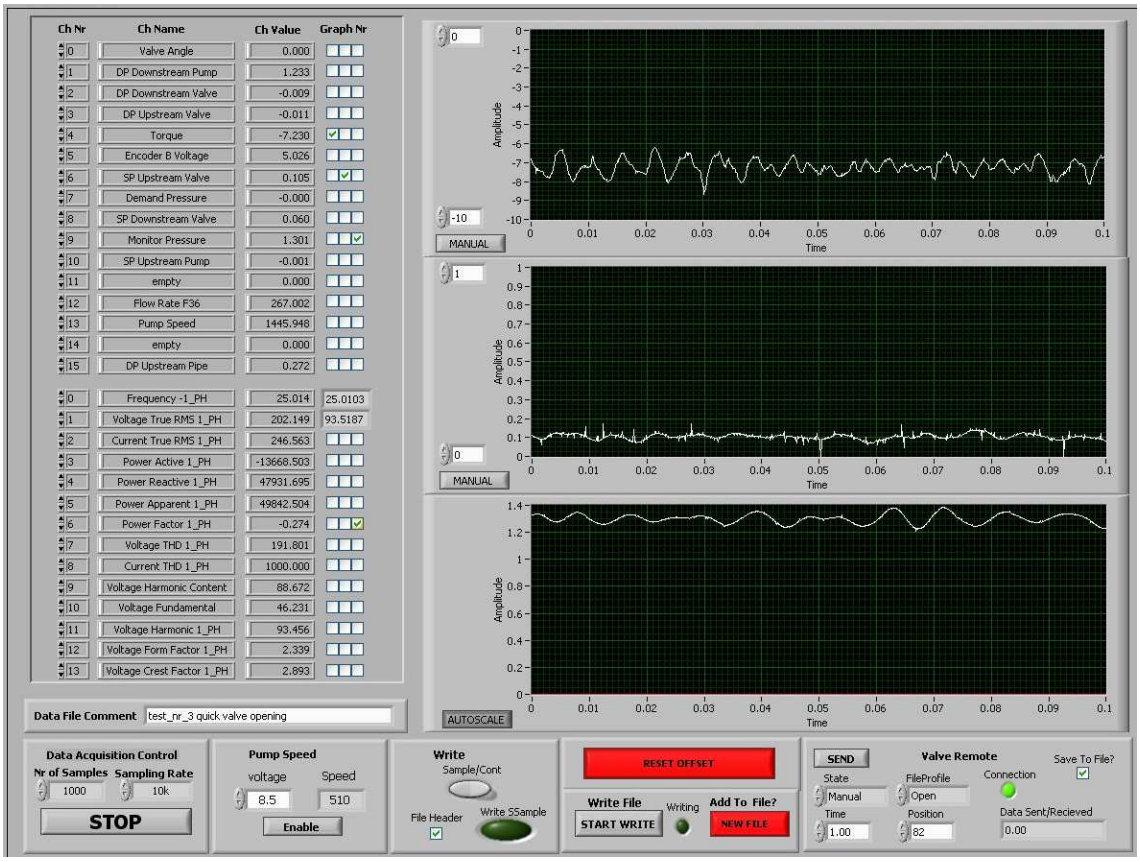

Figure 2.5. Labview data acquisition layout

2.2 Induction motor test rig

The induction motor test rig was designed and built to validate the induction motor models. The schematic diagram of the rig is presented in figure 2.6 and the actual rig is shown in figure 2.7.

In order to assess the performance of the induction motor, the motor was connected to the electrical supply through a three-phase star connected variable voltage transformer (Variac). The regulated voltage supplied to the induction motor was then controlled by means of knob potentiometer over a range from 0 to 250V. The Variac output current was limited to 60A. This configuration allowed different types of test to be undertaken including constant voltage and current tests.

The three-phase induction motor, purchased from Lowara, was the subject of test work. Different motor winding connections were tested. Delta connection allowed the motor models to be validated whereas the star configuration was useful in determining the motor parameters. To validate the modelling work a number of tests were performed including

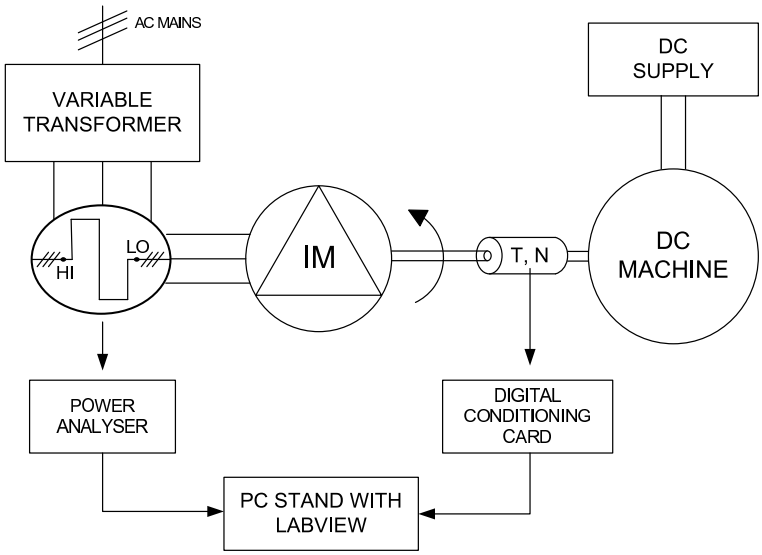

Figure 2.6. Induction motor rig - schematic layout

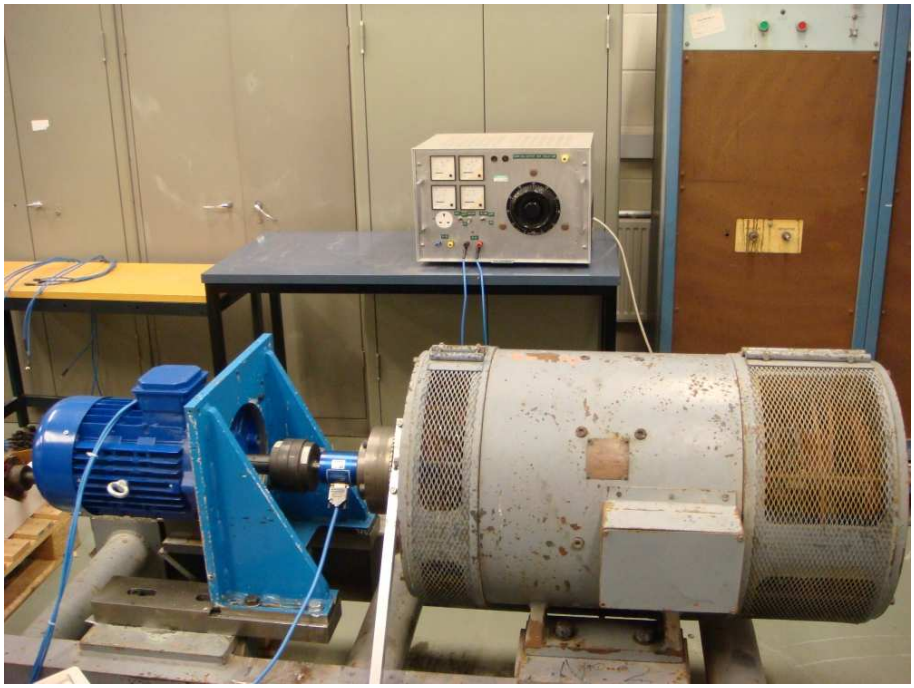

Figure 2.7. Induction motor test rig

constant voltage tests, constant current tests, reduced voltage full speed-torque characteristics, no-load and synchronous speed proximity tests. The motor parameterisation tests allowed the transient behaviour to be analysed.

The induction motor was mechanically coupled to a separately excited DC machine for the purpose of speed regulation. The speed of the DC machine was regulated by the armature voltage to provide the desired conditions and allowed the electrical torque produced by the

induction motor to be recorded. By delivering mechanical rotational power to the shaft, the induction motor could also be operated as a power receiver. As the armature current of the DC machine was large, a separate Ward-Leonard motor control system capable of 100A generation was used. Special connection leads were used and the armature current was measured to avoid current overload. For safety reasons a mechanical emergency switch was used to disconnect the armature current. The field winding was supplied from a separate controlled DC supply. Due to the high current obtained at high slip operation, and consequently motor heat generation, the tests could only be conducted for a short time as the motor parameters are highly temperature dependent.

A torque-speed transducer was mounted between the induction motor and the DC machine. Two flexible Fenner couplings were used to avoid substantial angular shaft misalignment which could induce inaccuracies in the torque measurement and in extreme cases damage the transducer. A commercial optical rotary torque transducer E300 RWT1 was used for the torque measurement with a range of 0 to 100Nm and an accuracy of 0.15%. An optical rotary speed sensor was fitted to the same transducer casing allowing speed measurement of up to 15000rpm to be obtained with an accuracy of 0.15%. Due to the inaccuracy of the speed sensor, a small 6-pole DC machine was mounted to the end of the shaft to obtain precise speed measurement. The voltage output from this generator was connected to the power analyser and recorded.

The E300 RWT1 shaft transducer was supplied and controlled from an E201 Display Interface and could be operated as a stand alone device or be controlled from a remote PC using the TorqView software. This Labview-based platform supplied by the manufacturer was used for data acquisition, recording and monitoring. In the stand alone mode of operation, data were captured and displayed on a digital instrumentation display. An external analogue output was used to acquire the data from the E201 interface before it was transferred to a PC via RS232-based connection where in-house acquisition and post-processing software was installed. Bespoke data acquisition software was created for this purpose using Labview by the author. A Labview virtual instrument (VI), working under the Windows XP operating system, was used to obtain data from the torque sensor and speed transducer fitted to the test rig. In addition, the power analyser was connected to the PC via the Ethernet and operated by the acquisition virtual instrument.

The electrical parameters were determined using the Norma 5000 power analyser to measure the voltages, currents and electrical powers. Due to the high currents generated a set of three-phase shunts were positioned between the variable transformer and the induction motor to monitor the motor supply condition. In addition, electrical power quality parameters such as the power factor and displacement power factor were recorded.

Chapter 3

Mathematical Models of Induction Machine

The induction motor modelling and analysis are presented in this chapter. The three-phase, two-pole, 11kW commercial induction motor has been the object of investigation. A short description of the investigated motor is given along with pictures of the motor rotor and stator geometry. The modelling techniques used to analyse steady-state and dynamic behaviour are described and compared to show model suitability and accuracy. In addition, the motor parameter determination method is explained and simulated motor responses and characteristics are presented.

3.1 Introduction

An induction motor is the most widely used electrical machine in industrial, commercial and residential applications. It is a rotating electric machine designed to work as an electro-mechanical energy conversion device. Like other electrical machines, induction machines can be operated as either generators (e.g. in wind turbines) or motors. However, they are most frequently used as motors. The low-cost manufacturing process and robust geometry are the two underlying reasons, for their common usage, especially as pump and fan drives. A high percentage of induction machines are designed for three-phase AC mains operation. Induction machines designed for single-phase AC operation are less efficient, and operate with a pulsatory torque component which produces greater vibrations and audible noise that the better balanced three-phase machine.

An induction motor consists of a relatively simple stator and rotor geometry. The stator is usually constructed from stacked laminations with a number of shaped slots into which windings are inserted to establish a rotating sinusoidal magneto-motive wave to establish a rotating air-gap magnetic flux. The rotor is the rotating part of the induction machine, which comprises a stack of steel laminations with a number of evenly-spaced conductor slots around the circumference. Cast-aluminium bars are placed in the slots in the case of cage type rotor and windings are placed in the case of wound rotor configuration. The ends or windings are short-circuited at both ends allowing induced currents to circulate. The wound rotor has connection terminals at one end, to which the external circuit can be connected through slip-rings, allowing external control of the machine. The conductors in the rotor are constructed with a one bar pitch "skew" to reduce torque vibrations and noise. The stator and rotor are shown in figure 3.1. Figure 3.1(b) shows the stator construction with the laminations and windings. The rotor assembly is shown in figure 3.1(a) where skewing is clearly visible.

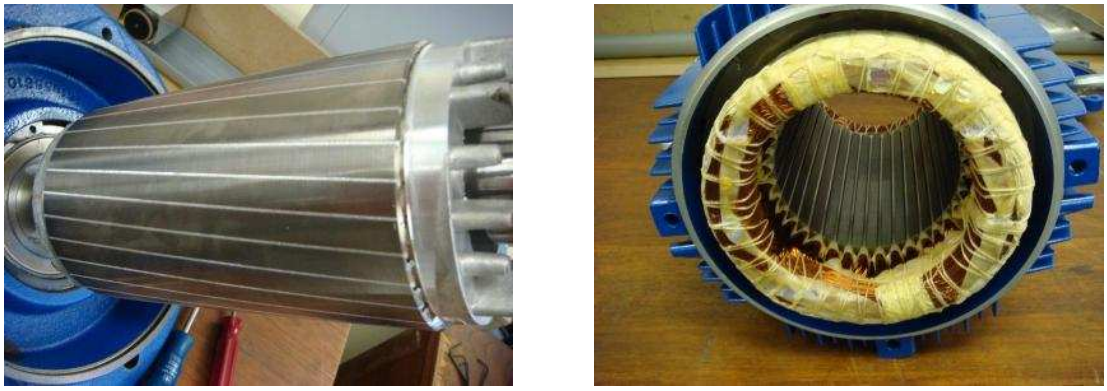

(a) Rotor (b) Stator

Figure 3.1. Induction motor assembly

Similar to other AC machines, the speed of rotation of the stator magnetic field is termed the synchronous speed ω_s in *rad/s* given by equation (3.1),

$$\omega_s = \frac{4\pi f_e}{P} \tag{3.1}$$

where the f_e is the electrical frequency and P is the pole number of the windings.

When a three-phase supply is connected to the stator winding, currents flow in the windings producing a radially-directed, spatially-rotating magnetic flux density. The magnetic flux density wave passes conductors on the rotor and consequently a voltage is induced in the conductors. Because the rotor bars are short circuited axial current flows through them, resulting in a rotor bar current wave rotating at synchronous speed and interacting with the stator magnetic field. The interaction of the rotor bar axial currents and stator

radial field rotating at constant synchronous speed generates the electrical torque on the rotor, which acts in the direction of the rotating field.

In actual motor operation, the rotor always slips behind and rotates slower than the air-gap rotating field due to motor windage/friction losses and the load connected to the shaft. This speed difference allows the rotor bars to be cut by the magnetic field and produce useful torque. The speed difference is called the slip speed and its relative value is known as slip s. It can be expressed as a measure of the relative speed difference between the synchronous stator field speed and the actual rotor mechanical speed. The slip as a percentage value is defined in equation 3.2, where ω_r is rotor mechanical speed. The slip increases with load since a higher rotor current is required for higher torque production.

$$s(\%) = \frac{\omega_s - \omega_r}{\omega_s} \times 100 \tag{3.2}$$

The performance of an induction machine is dependent on many motor parameters. It is a function of the operating speed, supply voltage and frequency. It is affected by several factors, including the level of magnetic saturation in machine 'iron', thermal effects such as increased copper and iron losses, and, if the slip is relatively high > 10% the skin effect in rotor bars which increases their resistance.

The acceleration produced in the rotor is directly related to the developed electromagnetic torque and is a function of the total inertia being accelerated by the motor and the load torque connected to the shaft. The acceleration torque, at any speed, is the difference between the torque produced by the motor and required by the load, as given in

$$T_e - T_l = J \frac{d\omega_r}{dt} + B_d \omega_r \tag{3.3}$$

where J is total moment of inertia of the motor rotor and shaft-connected load system, T_l is a load required torque and B_d is the viscous-friction damping coefficient.

The efficiency of the induction machine can be expressed by a power relationship as follows

$$\eta = \frac{P_{in} - P_{loss}}{P_{in}} = \frac{P_m}{P_{in}} \tag{3.4}$$

where P_{in} is the input power and P_{loss} is the power loss due to stator and rotor copper heating, the core or iron losses and windage and friction losses. The P_m is a mechanical power which the motor delivers to the load and can be written as follows

$$P_m = T_e \omega_r \tag{3.5}$$

3.2 Induction Motor Parameter Testing

To predict the steady-state and dynamic response of an induction motor an accurate model is required. An induction motor can be described in terms of a lumped-parameter equivalent circuit model, where the elements in the model represent the motor physical properties. The per-phase equivalent circuit model supplied by a balanced supply is presented in figure 3.2.

Experimental determination of the lumped-parameter element values, such as stator R_s and rotor R_r resistances, stator X_s and rotor X_r leakage reactances and magnetising reactance X_m, is the subject of this section. The motor internal losses represented by the parallel resistance R_c will also be calculated from measurements.

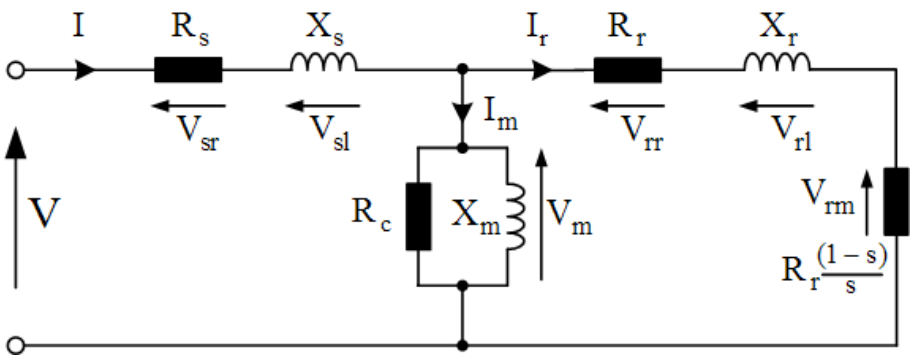

Figure 3.2. Induction machine equivalent circuit

The standard procedures for induction motor testing were employed, where the motor windings were star connected. [33]. The equivalent-circuit values were obtained from the results of a no-load test, a blocked-rotor test, and measurement of the DC resistances of the stator windings [34].

3.2.1 No-Load Test

No-load tests were conducted to measure the internal and rotational losses of the motor. The results, in conjunction with other tests, were used to determine model values. The tests were performed by applying a balanced rated 3-phase voltage at rated frequency to the stator windings. The measurements of powers, line voltages and currents were taken at the motor input.

During a no-load test the input real power P_{nl} is the sum of stator copper, windage, friction and core losses as given in

$$P_{nl} = 3I_{nl}^2 R_s + P_{loss} \tag{3.6}$$

where I_{nl} is phase current at no-load condition and P_{loss} is represented by equivalent

resistance R_c in the motor modelling and has been calculated by

$$P_{loss} = P_{nl} - 3I_{nl}^2 R_s \tag{3.7}$$

Because under no-load conditions the power factor of an induction machine is very poor, typically less than 0.2, the machine consumes largely reactive power from the mains. Therefore, the input impedance can be approximated by the sum of the magnetising and stator leakage reactances, since under no-load conditions little current flows in the rotor bars and a rotor leakage reactance can be neglected.

$$|Z_{nl}| \cong X_s + X_m \tag{3.8}$$

Then, the magnetising reactance can be estimated using

$$X_m = \frac{V_{nl}}{\sqrt{3} I_{nl}} - X_s \tag{3.9}$$

and the values of R_s and X_s may be determined using direct current and blocked-rotor tests, described in the following subsections.

3.2.2 Direct Current Test

The purpose of the DC test was to compute the stator winding resistance R_s and then to evaluate the stator copper losses. When a direct current flows through stator windings and the rotor shaft is not subject to external forces, then the stator magnetic field is stationary and the rotor does not impact the stator operation. Because, during the DC test, current is unchanging, the skin effect does not occur, motor reactance seen from the mains is zero and only the winding resistance limits DC current.

To determine the stator resistance, rated current was supplied to the two stator terminals and voltmeter and ammeter readings were taken. An adjustable DC source was used for current control and adjustment. Since the current flows through two stator windings the stator resistance measured at ambient temperature is given by

$$R_s = \frac{1}{2} \frac{V_{dc}}{I_{dc}} \tag{3.10}$$

The winding resistance during DC tests was determined at an ambient temperature of 20℃, but at a different operating temperature the resistance may be corrected using

$$R = R_{20} (1 + \alpha_T \Delta T) \tag{3.11}$$

where R_{20} is resistance at 20℃, α_T is the temperature coefficient of the copper winding and ΔT is the temperature change from 20℃.

3.2.3 Blocked Rotor Test

To complete the estimation of induction motor model values a blocked rotor test was performed. The rotor was blocked by clamping the shaft to prevent rotation and balanced voltages were applied to the stator terminals. To prevent high standstill current the supply voltage was reduced and adjusted so that rated current flowed through the stator windings. To minimise the effect of rotor skin-effect, which would be significantly higher at 50Hz than at the rotor-bar current frequency, typically between 1-5Hz, that would be produced during normal operation, the motor was supplied during measurement from an inverter at 25 percent of the rated frequency f_t [33]. This improved the accuracy of rotor resistance R_r estimation from an input power measurement. The readings of resulting currents, voltages and powers were recorded at the motor input.

The motor impedance seen during the test may be expressed as

$$|Z_{br}| = \frac{V_{br}}{\sqrt{3}I_{br}} = R_{br} + jX_{br}^{f_t} \tag{3.12}$$

where $X_{br}^{f_t} = X_s^{f_t} + X_r^{f_t}$ is the blocked rotor reactance at the test frequency f_t, I_{br} is average phase current and $R_{br} = R_s + R_r$. The stator resistance R_s was found from the DC test.

The blocked-rotor resistance and reactance were found as follows

$$R_{br} = |Z_{br}| \cos \varphi_{br} \tag{3.13a}$$

$$X_{br}^{f_t} = |Z_{br}| \sin \varphi_{br} \tag{3.13b}$$

where the phase angle was calculated using

$$\cos \varphi_{br} = \frac{P_{br}}{\sqrt{3}V_{br}I_{br}} \tag{3.14}$$

Since reactance is proportional to frequency, and the supply frequency was different from rated value f_e, scaling was applied, as follows

$$X_{br} = \frac{f_e}{f_t} X_{br}^{f_t} = X_s + X_r \tag{3.15}$$

The investigated motor was assumed to be of type NEMA Design Class C, and so the stator and rotor leakage reactances were found by dividing X_{br} in proportions of $X_s = 0.3X_{br}$ and $X_r = 0.7X_{br}$ [35].

3.2.4 Induction motor parameter evaluation

The previously described lumped-parameter measurement methods were applied to a Lowara induction motor used in the experimental test rig. For measurement purposes the motor was connected in a star configuration. A number of tests were performed at day intervals to obtain sets of independent measurements. The results of the no-load, blocked-rotor and direct-current tests are shown in following tables. The motor parameter evaluation was performed for each set of test data.

The direct-current tests were conducted using an adjustable DC voltage source. The rated current was applied to the stator winding and direct resistance measurements for three phase windings were taken and are presented in table 3.1. In addition, a DC measurement test was performed just after a blocked rotor test to show the impact of temperature change on the stator resistance.

	R_a	R_b	R_c
	Ω	Ω	Ω
Test I	0.779	0.780	0.782
Test II	0.778	0.776	0.782
Test III	0.774	0.772	0.773
Test IV (after BR)	0.812	0.808	8.10

Table 3.1. Induction motor DC test

The no-load tests were performed after the DC tests. The motor was accelerated directly from the AC mains supply via a variable transformer to limit high starting current. Once the motor speed settled down the readings of line voltage, three phase currents and phase active powers were recorded and RMS values are given below

	f_e	V_{ab}	I_a	I_b	I_c	P_a	P_b	P_c
	Hz	V	A	A	A	W	W	W
Test I	50.01	401.61	7.2734	7.7263	6.9634	53.193	189.31	230.93
Test II	49.98	401.57	7.2617	7.7916	6.945	47.333	197.31	239.75
Test III	49.97	399.56	7.431	7.42	6.697	79.36	134.55	252.4

Table 3.2. Induction motor no-load test

The locked-rotor tests were performed last to eliminate the impact of temperature change on motor parameters. The motor was supplied from a three-phase inverter delivering a 12.5Hz output so the rotor current frequency is closer to the operating slip frequency which

gives more accurate results than 50Hz measurements which would include skin effect. The rated current was fed to the stator and the measurements were taken. The following data were obtained from the locked rotor tests.

	f_t	V_{ab}	I_a	I_b	I_c	P_a	P_b	P_c
	Hz	V	A	A	A	W	W	W
Test I	12.526	25.418	21.995	21.532	21.582	269.27	266.08	264.16
Test II	12.514	25.345	21.987	21.521	21.57	269.29	265.97	264.08
Test III	12.069	24.077	21.262	20.789	20.882	247.84	244.91	242.55

Table 3.3. Induction motor blocked rotor test

Using the described measurement techniques the motor model values were estimated. The resulting sets of parameters are shown in table 3.4. The determined motor values from all the conducted tests have been averaged and constitute the measured set of parameters used in further motor modelling. Along with the measured motor parameters the data obtained directly from the manufacturer is presented. Two data sets were received from the manufacturer for loaded and no-load tests. The lab measurement conditions correspond more closely compared with no-load conditions and Lowara's no-load values. The two sets of values are in relatively good agreement (error 0.9 - 12.2%), comparing plotted further characteristics.

	R_s	R_r	X_s	X_r	X_m	P_{loss}
	Ω	Ω	Ω	Ω	Ω	W
Test I	0.779	0.921	1.775	2.663	93.26	432.23
Test II	0.773	0.898	1.784	2.676	94.56	426.15
Test III	0.775	0.907	1.781	2.664	94.01	430.34
Test (avg)	0.776	0.908	1.780	2.667	93.94	429.57
Lowara (load)	0.783	0.984	1.808	2.040	75.60	364
Lowara (no load)	0.783	0.984	1.808	2.544	105.73	377

Table 3.4. Lowara induction motor parameters

3.3 Steady State Analysis

An induction motor exhibits similar behaviour to a transformer as the rotor voltages are induced due to the stator field operation. Therefore, an induction motor can be represented as the rotating transformer where the stator can be treated as a primary winding and the rotor as secondary [36].

To describe the operation of an induction machine in steady-state operation the transformer equivalent circuit approach has been used [37]. The elements in the model are expressed as lumped quantities, and represent the motor equivalent circuit elements where all the rotor variables are referred to the stator frame. The per-phase equivalent circuit model supplied by a balanced three-phase supply is given in figure 3.2.

The individual elements comprising the equivalent circuit represent the motor's physical properties. The stator elements are represented by stator winding resistance R_s and the leakage reactance X_s. The field establishing element is modelled as a shunt connected magnetising reactance X_m, whereas the core/windage/friction losses are represented as a parallel resistor R_c. The referred rotor elements are represented by the rotor winding resistance R_r and winding leakage reactance X_r. In addition, the rotor circuit has a slip dependent resistance $R_r(1-s)/s$, equivalent to the mechanical power generation.

In order to drive the load, the induction motor is accelerated from standstill to an operating speed. The acceleration time is a function of the motor and load quantities presented in equation 3.3. When a balanced three-phase voltage is supplied, both the electromagnetic torque and the current drawn from the AC mains tend to alter with the rotor speed. To describe an induction motor behaviour during steady-state operation both quantities are plotted against the operating speed. The resulting torque-speed (also the current-speed characteristic) is slip s dependent and when compared with a load torque-speed requirements constitutes a reference point for users during the process of motor selection.

3.3.1 Torque versus Speed Characteristic

From the mechanical power relationship given in equation 3.5 the motor electromagnetic torque can be expressed as

$$T_e = \frac{P_m}{\omega_r} \tag{3.16}$$

The mechanical power developed by the motor can be written in terms of the power dissipated by a slip dependent variable resistor as

$$P_m = 3\left|\tilde{I}_r\right|^2 R_r\left(\frac{1-s}{s}\right) \tag{3.17}$$

Then, the electromagnetic motor torque can be expressed as a function of the rotor current by

$$T_e = \frac{3\left|\tilde{I}_r\right|^2 R_r\,(1-s)}{s\omega_r} \tag{3.18}$$

Rotor speed ω_r can be described as a function of the slip and the synchronous speed, using $\omega_r = \omega_s\,(1-s)$.

In order to express the torque in terms of supply voltage Thevenin's theorem may be

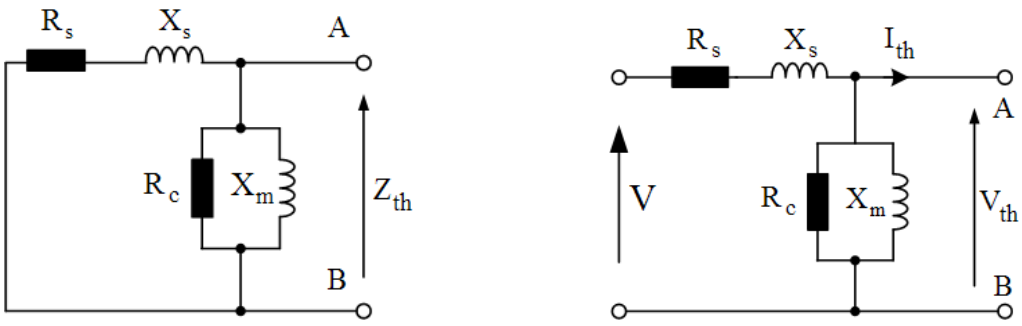

(a) Thevenin impedance circuit (b) Thevenin voltage circuit

Figure 3.3. Thevenin circuits

applied [35, 38]. The Thevenin impedance $\tilde{Z}_{th}$ and Thevenin voltage $\tilde{V}_{th}$ equivalent circuits of figure 3.2 are shown in figures 3.3(a) and 3.3(b), respectively. The Thevenin voltage, seen across terminals A and B, equals the voltage drop across the magnetising branch. The voltage division equation gives the Thevenin voltage as

$$\tilde{V}_{th} = \tilde{V}\frac{\tilde{Z}_m}{R_s + jX_s + \tilde{Z}_m} \tag{3.19}$$

where the magnetising branch impedance can be written as follows

$$\tilde{Z}_m = \frac{jR_cX_m}{R_c + jX_m} = \frac{R_cX_m^2 + jR_c^2X_m}{R_c^2 + X_m^2} \tag{3.20}$$

The motor iron losses are sometimes neglected because they are generally low. Then the magnetising branch impedance $\tilde{Z}_m$ is approximated by the magnetising reactance as follows

$$\tilde{Z}_m = jX_m \tag{3.21}$$

Both cases, with and without losses, have been modelled to show the impact of the iron loss equivalent resistance R_c on the machine model performance.

The Thevenin impedance is the impedance seen across terminals A and B as shown in figure 3.3(a) and is given by

$$\tilde{Z}_{th} = \frac{\tilde{Z}_m\,(R_s + jX_s)}{R_s + jX_s + \tilde{Z}_m} = R_{th} + jX_{th} \tag{3.22}$$

where the R_{th} and X_{th} are real and imaginary components of the Thevenin generator impedance $\tilde{Z}_{th}$, respectively.

The rotor current can be written as a function of the Thevenin voltage and Thevenin impedance as follows

$$\tilde{I}_r = \frac{\tilde{V}_{th}}{\tilde{Z}_{th} + \tilde{Z}_r} \tag{3.23}$$

where the rotor impedance $\tilde{Z}_r$ is expressed by relationship given in

$$\tilde{Z}_r = \frac{R_r}{s} + jX_r = R_r + R_r\left(\frac{1-s}{s}\right) + jX_r \tag{3.24}$$

An expression for the rotor current $\tilde{I}_r$ presented in equation 3.23 can be rewritten in terms of the Thevenin quantities as

$$\tilde{I}_r = \frac{\tilde{V}_{th}}{\left(R_{th} + \frac{R_r}{s}\right) + j\left(X_{th} + X_r\right)} \tag{3.25}$$

Recalling equation 3.18 and substituting the relationship for $\tilde{I}_r$ from the equation 3.25 the induction motor torque expression is given by

$$T_e = \frac{3}{s\omega_s} \frac{\left|\tilde{V}_{th}\right|^2 R_r}{\left(R_{th} + \frac{R_r}{s}\right)^2 + \left(X_{th} + X_r\right)^2} \tag{3.26}$$

The torque expression presented in equation 3.26 is used with manufacturer and test data listed in table 3.5, to plot the motor torque-speed graphs. The calculations have been performed assuming a 400V supply voltage and 50Hz supply frequency.

Motor parameters		Unit	Lowara (No Load)	Lowara (Load)	Test (avg)
Stator resistance	R_s	Ω	0.783	0.783	0.776
Stator leakage reactance	X_s	Ω	1.808	1.808	1.780
Rotor resistance	R_r	Ω	0.984	0.984	0.908
Rotor leakage reactance	X_r	Ω	2.544	2.040	2.667
Magnetizing reactance	X_m	Ω	105.73	75.60	93.94
Core losses	R_c	W	377	364	429.57

Table 3.5. Induction motor parameters

The torque versus speed characteristics for the investigated induction motor over the complete range of speed are presented in figure 3.4. The averaged test data gives one set of motor parameters which will be used in future motor modelling.

The resulting torque-speed characteristics in figure 3.4 all exhibit a similar pattern of variation, although the starting and pullout torques differ. However, in the linear region between 2500 and 3000rpm, where the motor is generally used, the slopes of the derived characteristics remain very similar. It can be also seen that iron loss resistance R_c, does not significantly affect motor performance in the linear region and can be neglected.

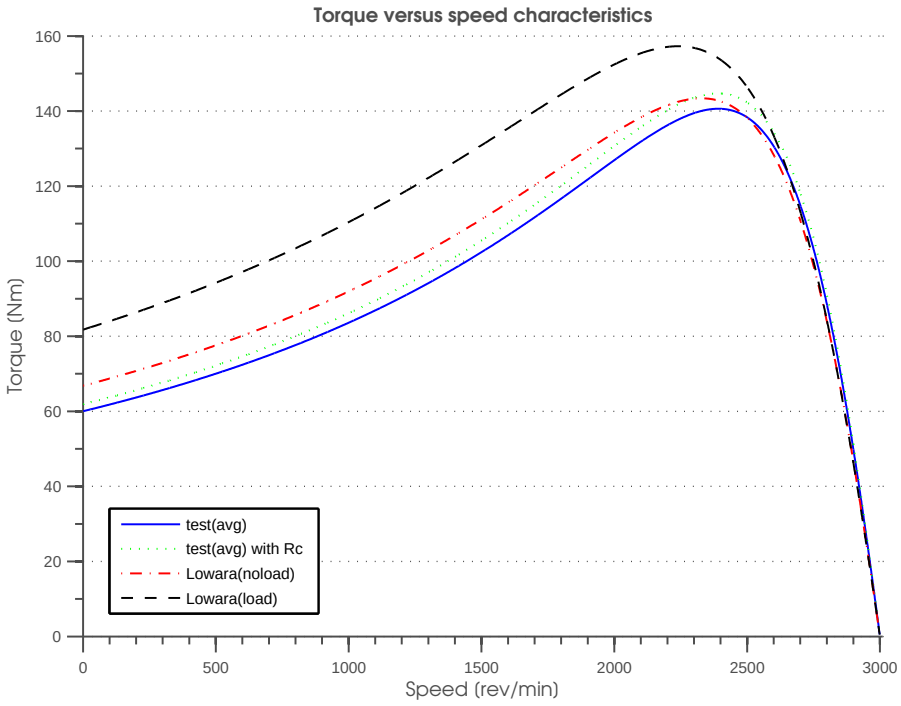

Figure 3.4. Induction machine torque-speed characteristics

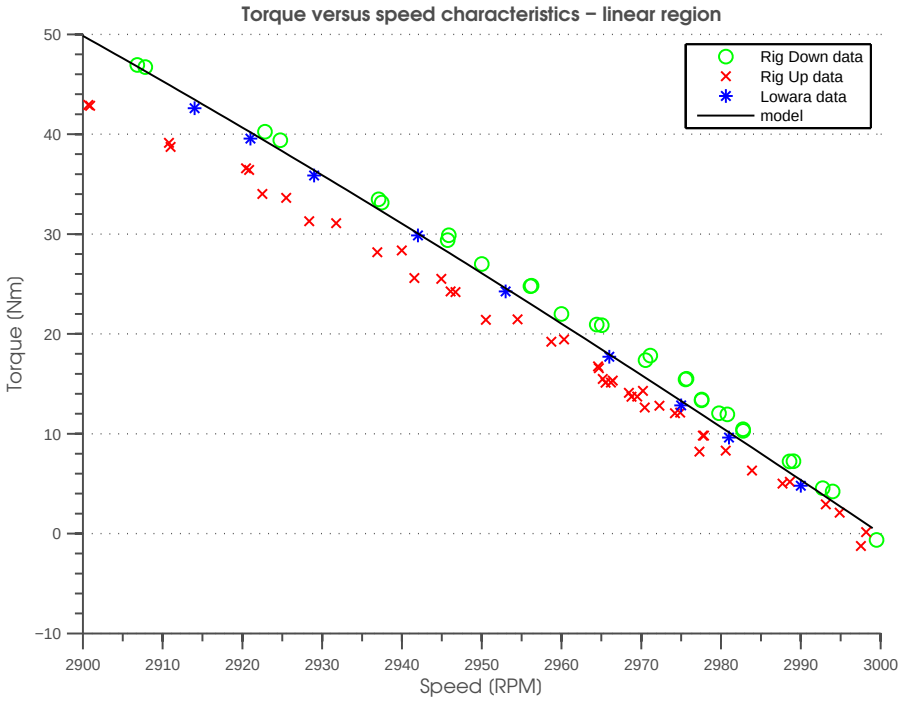

Figure 3.5. Induction machine linear region torque-speed characteristics

In order to validate the developed torque steady-state model, the tests were performed on the induction motor rig described in section 2.2. The data were recorded during steady-state operation for rated motor conditions (400V, 50Hz) and are presented in figure 3.5 along with the model predictions. The two sets of test data are presented for spin-down and spin-up tests performed one after another in the range from 2900 to 3000rpm. It can be seen that during prolonged high-slip motor operation the motor parameters are affected by higher rotor temperature, resulting in the lower torque production capability. In addition, the data obtained from the motor manufacturer is also plotted. As seen in figure 3.5 the model prediction shows good agreement (error < 10%) with both test rig results and the manufacturer's data.

Since induction motor performance is very sensitive to supply voltage level, the supply line voltage was first reduced to 345V, and then to 295V to investigate the motor performance during reduced voltage operation. The motor torque-speed characteristics have been recorded and are compared with the model predictions as shown in figure 3.6. Similar to the rated supply condition results, the model predictions for the reduced voltage supply show good agreement with the recorded data, what is evident from the graph.

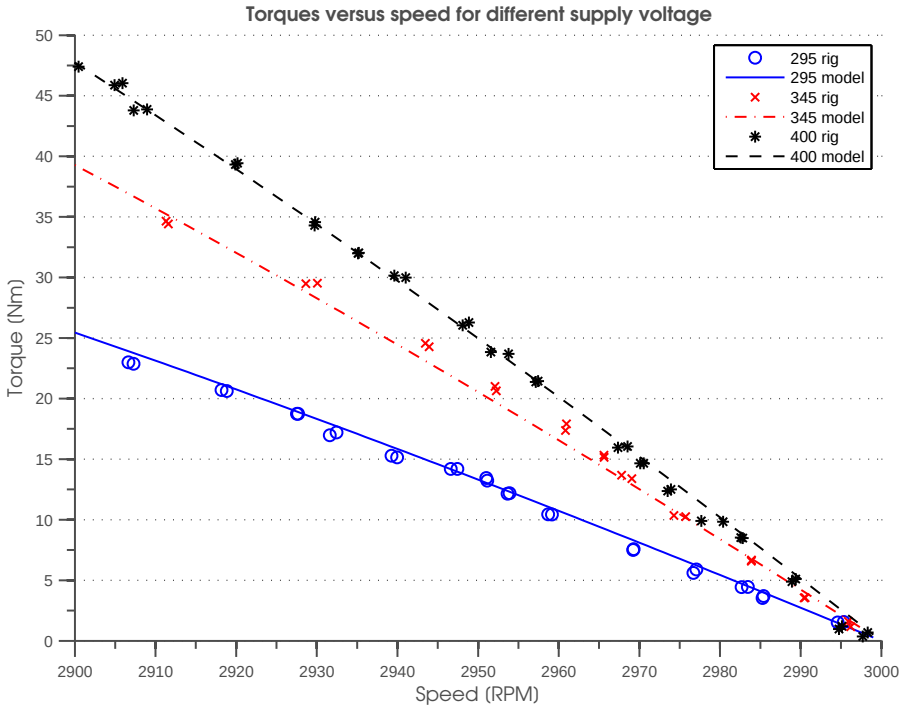

Figure 3.6. Lowara induction motor torque versus speed characteristics for supply voltages of 295V, 345V and 400V

3.3.2 Current variation with speed

When an induction motor is connected directly to a balanced 3-phase source, it draws a relatively high current when it starts. As the motor speed rises towards the synchronous speed the current drops because it is a function of slip [39]. The actual steady-state current-speed characteristic for an induction motor can be calculated using the equivalent circuit shown in figure 3.2.

When motor windings are connected in a delta configuration, the motor line current can be written in terms of a supply voltage and the per-phase impedance, $\tilde{Z}_z$ as follows

$$\tilde{I}_s = \sqrt{3}\frac{V}{\tilde{Z}_z} \tag{3.27}$$

The per-phase impedance is a function of slip and can be determined from

$$\tilde{Z}_z = R_s + jX_s + \frac{\tilde{Z}_m\left(\frac{R_r}{s} + jX_r\right)}{\frac{R_s}{s} + jX_r + \tilde{Z}_m} \tag{3.28}$$

The line input current versus operating speed characteristics for both the manufacturer's and the measured data are plotted in figure 3.7.

It is evident from figure 3.7 that R_c has relatively little effect on machine current, especially at modest slip $\leq$ 10% and may be omitted from the model. In the linear region the performance difference is hardly noticeable. The model based on the manufacturer's data exhibits the highest starting current.

The current model of the investigated induction motor has been validated on the developed motor test rig. The current in the linear region was recorded during spin-down (3000-2900rpm) and spin-up tests and the results are presented in figure 3.8. The data obtained form the manufacture is depicted on the same graph. It can be seen that the simulated results obtained show acceptable data agreement (error < 10%) with the measured and manufacturer's data, although some differences do exist due to model assumptions and limitations. The effect of current temperature change also becomes noticeable when motor operation at high slip is sustained rather than transient.

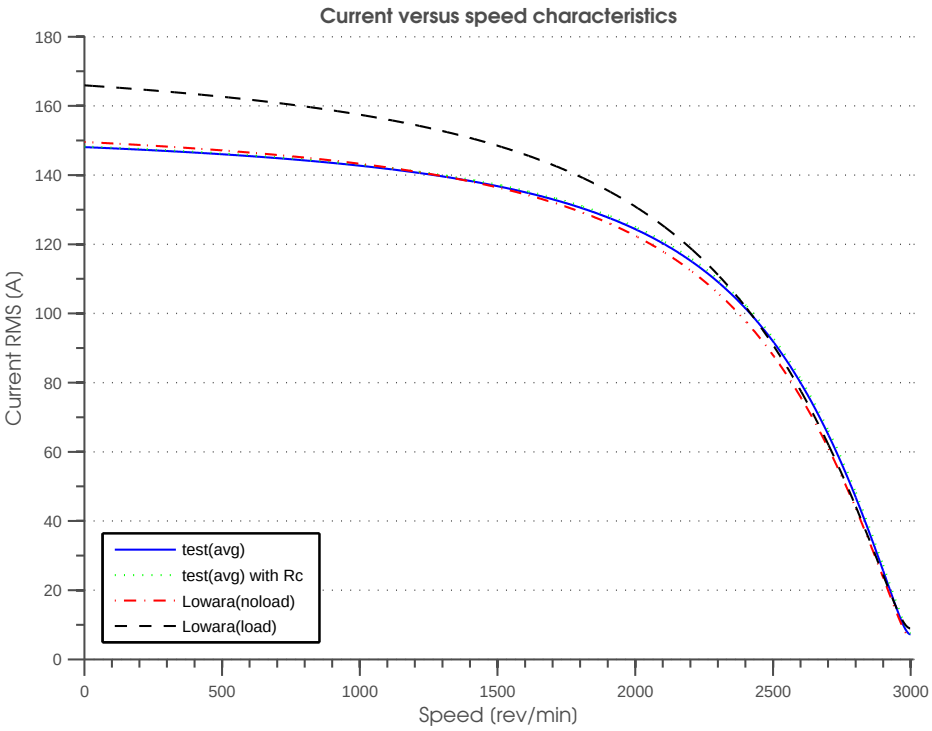

Figure 3.7. Induction machine current versus speed characteristic

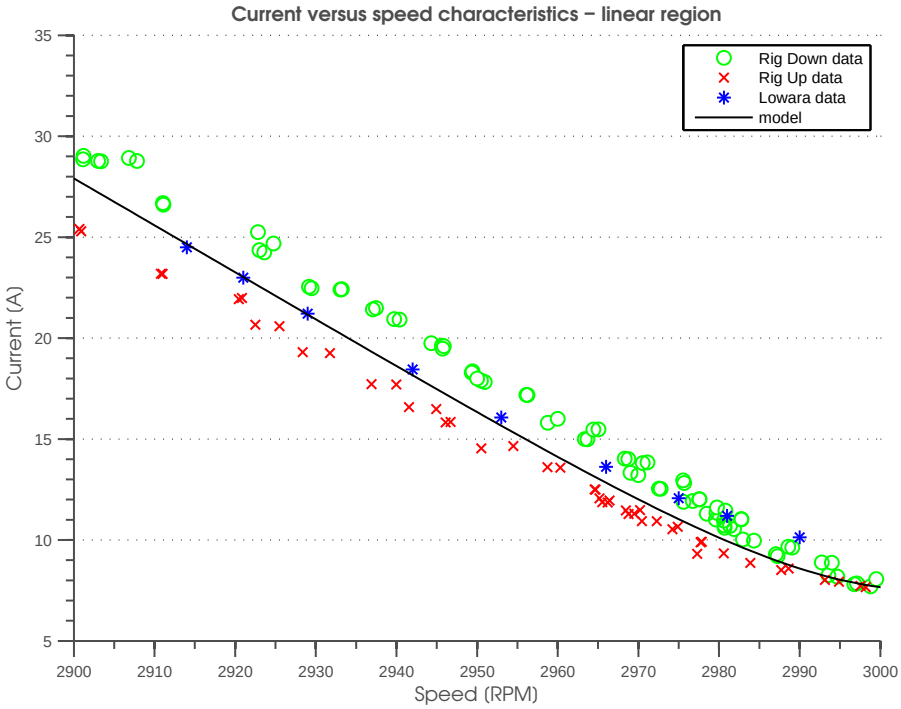

Figure 3.8. Induction machine current versus speed characteristic in linear region

3.3.3 Power and Internal Variables Distribution Models

Based on the equivalent circuit approach the powers, power factor and efficiency models have been defined and computed for the investigated Lowara induction motor. The true power P, reactive power Q and apparent power S models have been calculated only for the fundamental frequency component of supply voltage as

$$P_{(1)} = V_{(1)}I_{(1)}\cos(\varphi_{(1)}) \tag{3.29}$$

$$Q_{(1)} = V_{(1)}I_{(1)}\sin(\varphi_{(1)}) \tag{3.30}$$

$$S_{(1)} = \sqrt{P_{(1)}^2 + Q_{(1)}^2} \tag{3.31}$$

The power components have been plotted over the full range of speed and are shown in figure 3.9. The power components for the model have been validated using data obtained from tests performed on the motor test rig. The predicted results as shown in figure 3.10 seem to have close agreement (error < 10%) with measured data.

The power factor has been calculated as the ratio between the real power P delivered to the system or machine and the apparent power S absorbed by this system. Because the power factor model has been based on the calculated powers for sinusoidal operating condition, the displacement power factor $\cos\varphi_1$ may be used, as presented in equation 3.32. A graph of displacement power factor against operating speed for the investigated motor is plotted in figure 3.11. It can be seen that under light loading the induction machine exhibits poor power factor because as it approaches the no-load condition only the magnetising current is drawn from the AC mains [38]. The model validation is shown in the figure 3.12 where the simulated data is compared with the test rig results.

$$\cos\varphi_{(1)} = \frac{P_{(1)}}{V_{(1)}I_{(1)}} \tag{3.32}$$

$$\eta = \frac{P_m}{3P_{(1)}} \tag{3.33}$$

To show how effectively an induction motor converts electrical power the relationship presented in equation 3.33 is used. The efficiency of the tested motor is given on the power factor graph as the second scale plot in figure 3.11. It starts at zero and rises nearly in direct proportion to the speed until max η is reached. It then drops sharply as the motor approaches no-load conditions. The efficiency model is validated in the figure 3.12.

Based on the steady-state model of an induction machine the current and voltage internal distribution models have been developed. The rotor variables have been referred to the stator frame to allow comparison of the magnitudes and terms. The motor internal current versus operating speed are shown in figure 3.13(b) whereas the voltage quantities are depicted in figure 3.13(a).

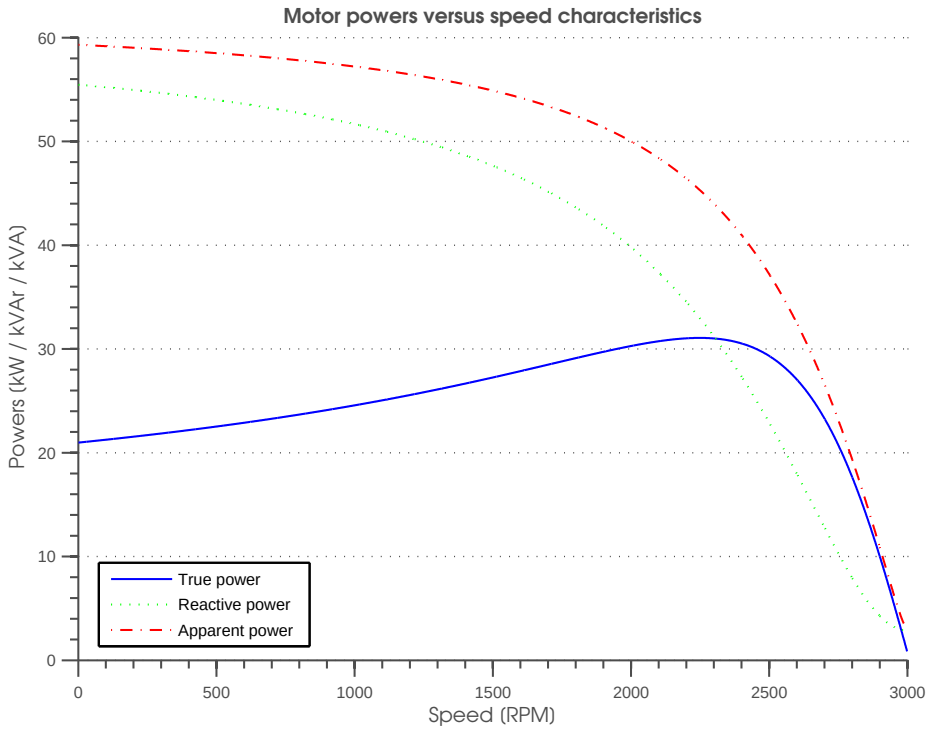

Figure 3.9. Induction machine powers versus operating speed

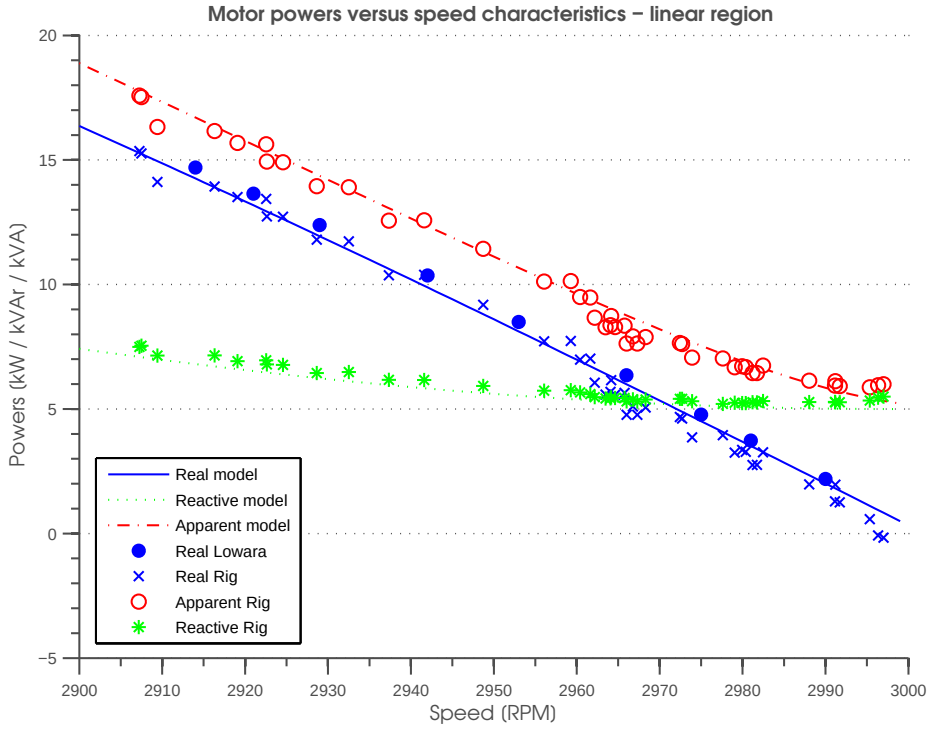

Figure 3.10. Induction machine powers versus operating speed in linear region

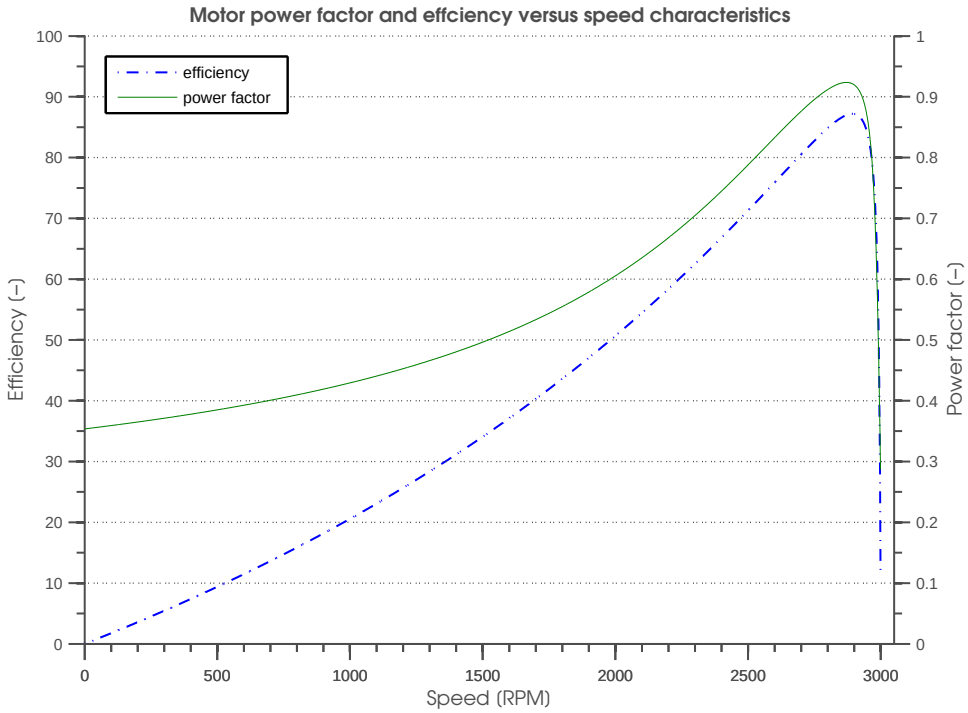

Figure 3.11. Induction machine power factor and efficiency versus operating speed

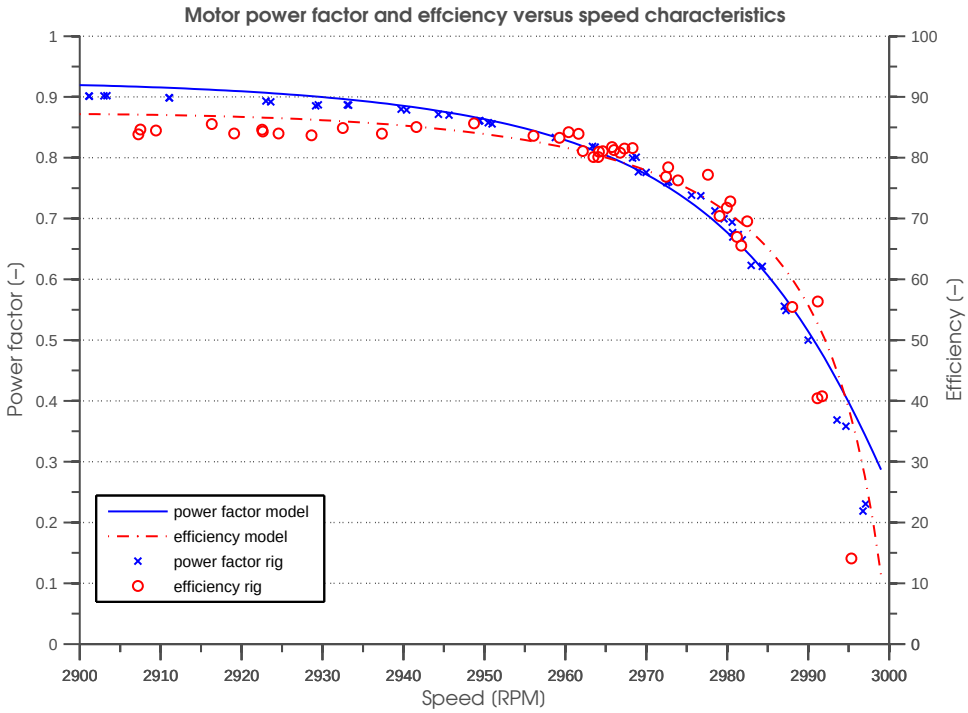

Figure 3.12. Induction machine power factor and efficiency versus operating speed - validation in linear region

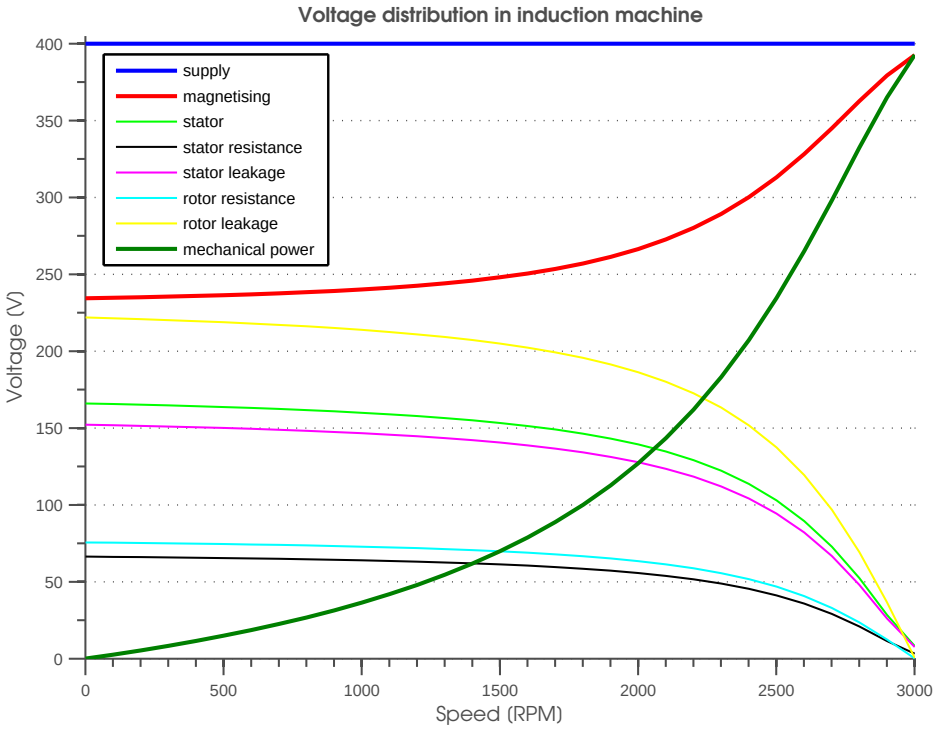

(a) Voltage distribution

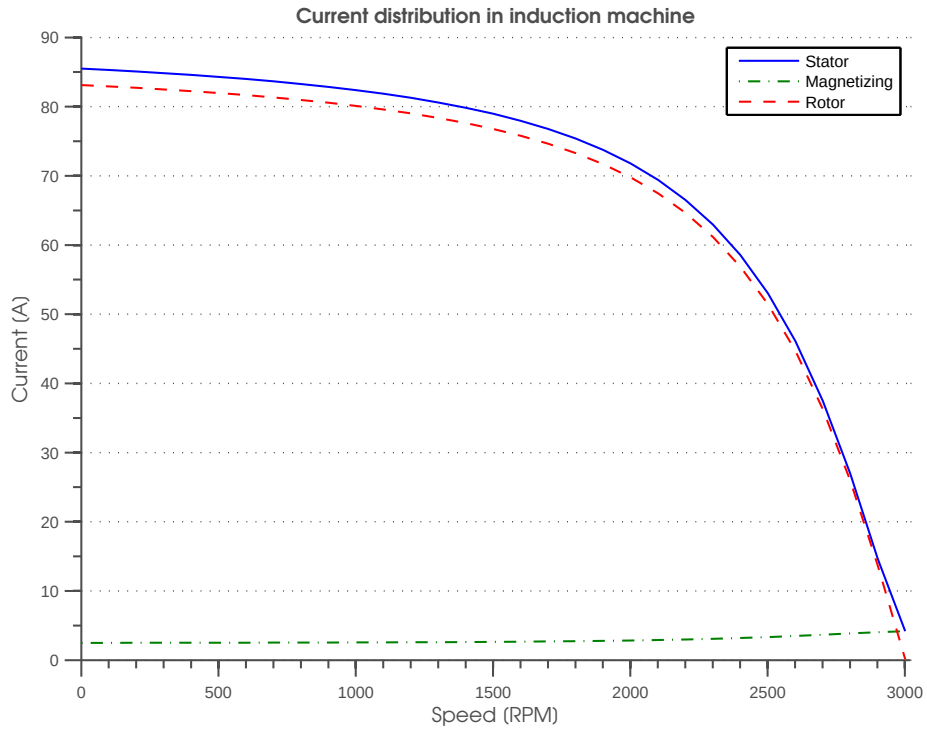

(b) Current distribution

Figure 3.13. Voltage and currents distribution in an induction machine versus operating speed

3.3.4 Standstill Torque

To predict the motor starting torque a locked rotor model was created. The model is based on the equivalent circuit and the torque equation presented in (3.26), where it has been assumed that when an induction motor is stationary the slip equals to 1. For the stationary conditions the line voltage has been adjusted from 0 to rated conditions (400V) to obtain the starting torque versus voltage and current characteristics. The obtained model data is validated with the electrical rig results and is given in figure 3.14. The rig results have been obtained only up to 160V since the high starting current limited the full range validation.

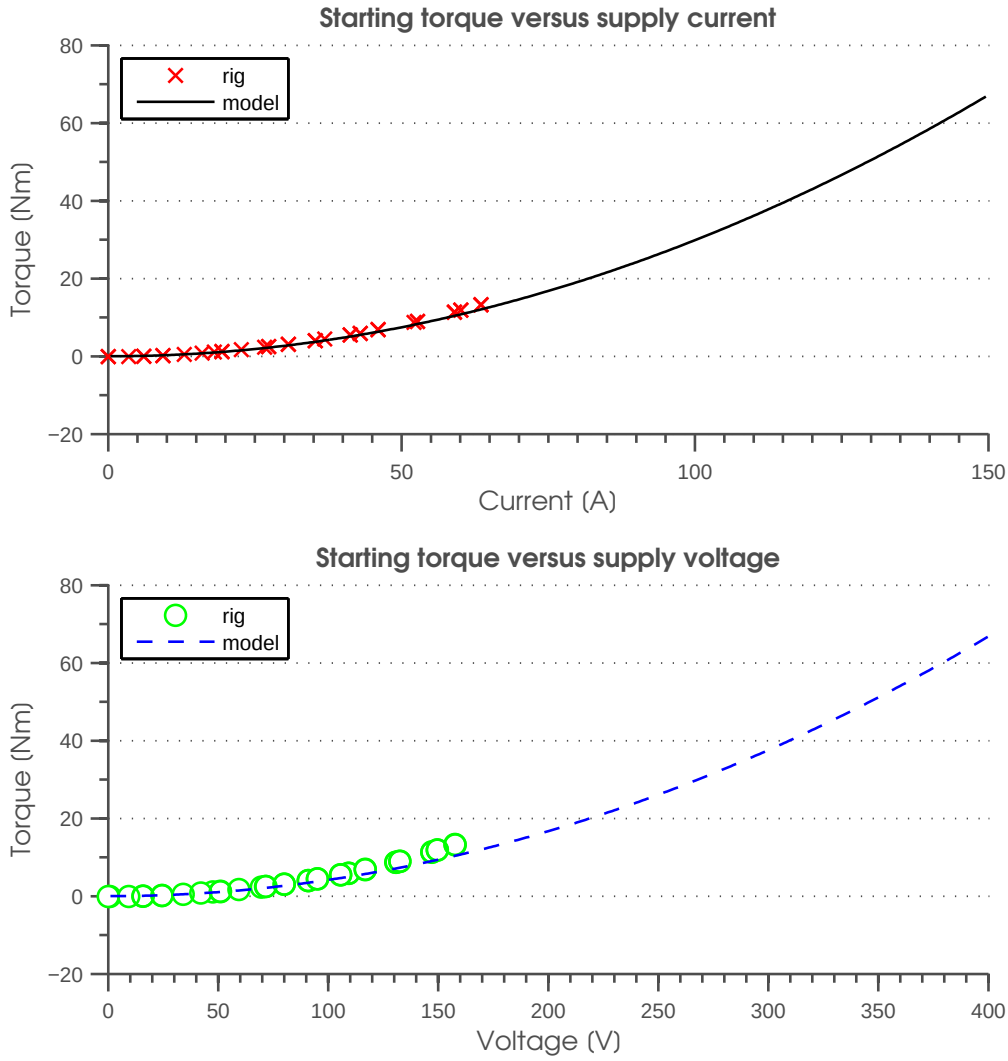

Figure 3.14. Locked rotor tests

3.3.5 Reduced-Voltage Behaviour

Due to the current constraints, the validation of the torque and current model has not been possible over the full range of speed. Therefore, torque and current tests for the complete speed range were performed under reduced voltage conditions. The two tests were conducted and the supply conditions are shown in figure 3.15. Due to the high starting current the voltage drop in the starting region is noticeable.

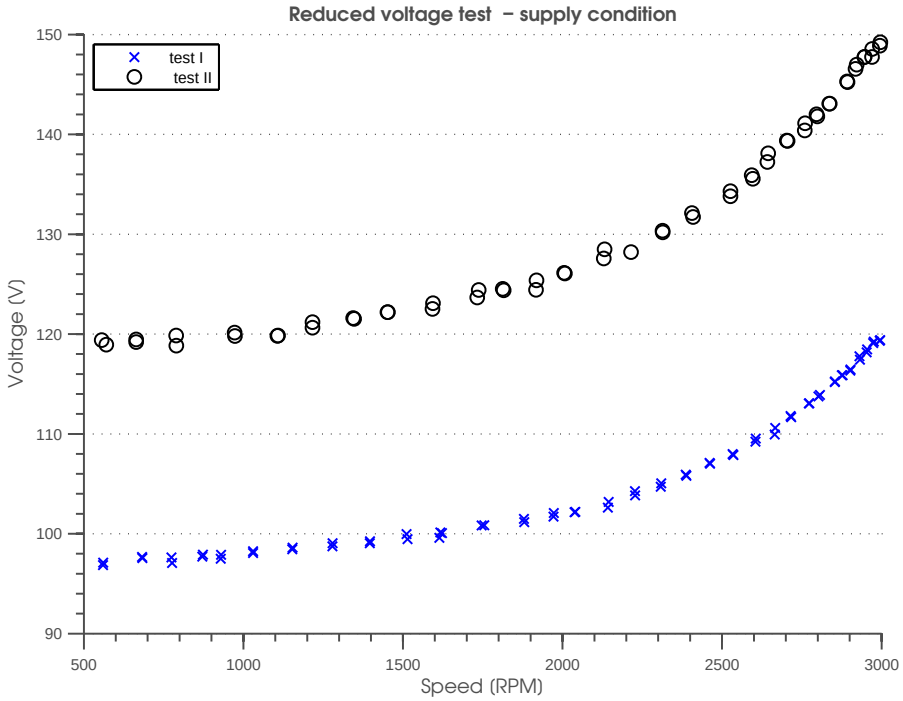

Figure 3.15. Supply condition during reduced voltage tests

The torque and current versus operating speed characteristics were recorded and are shown in figures 3.16 and 3.17, respectively. Along with the test rig results, the simulated data is presented. The simulations were performed with the recorded supply voltage as the input to the model.

The obtained results show the accuracy of model prediction varies. This is due to the assumptions made during modelling, such as that the effect of magnetic saturation and skin effect are negligible over a wide operating range. The current results differ slightly from the measurements. As a consequence the torque developed by the motor also differs slightly, although the error is less significant. The torque model predicts higher breakdown torque.

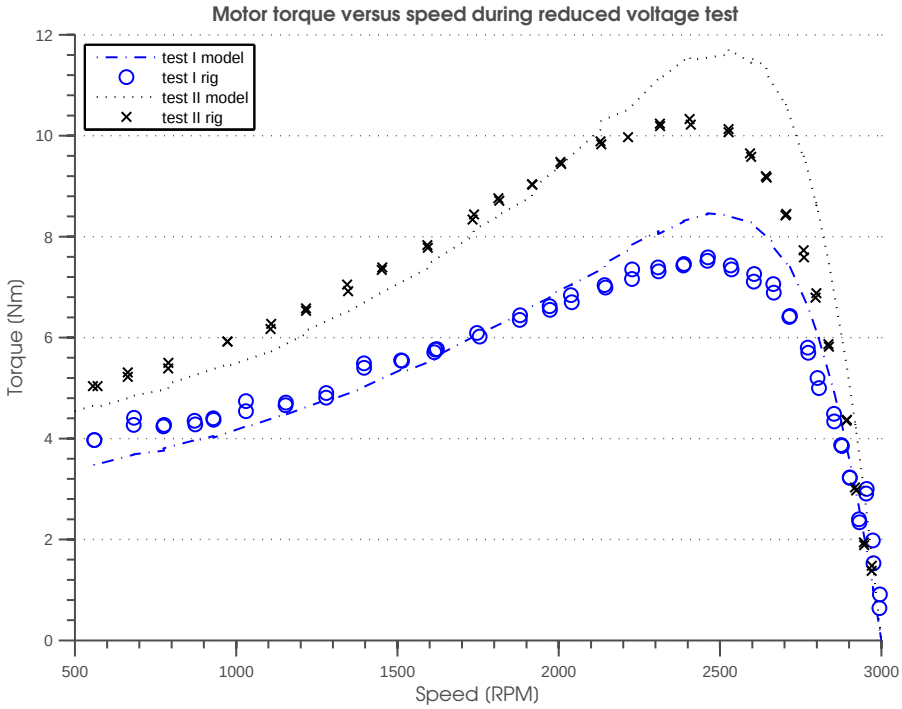

Figure 3.16. Torque versus speed during reduced voltage tests

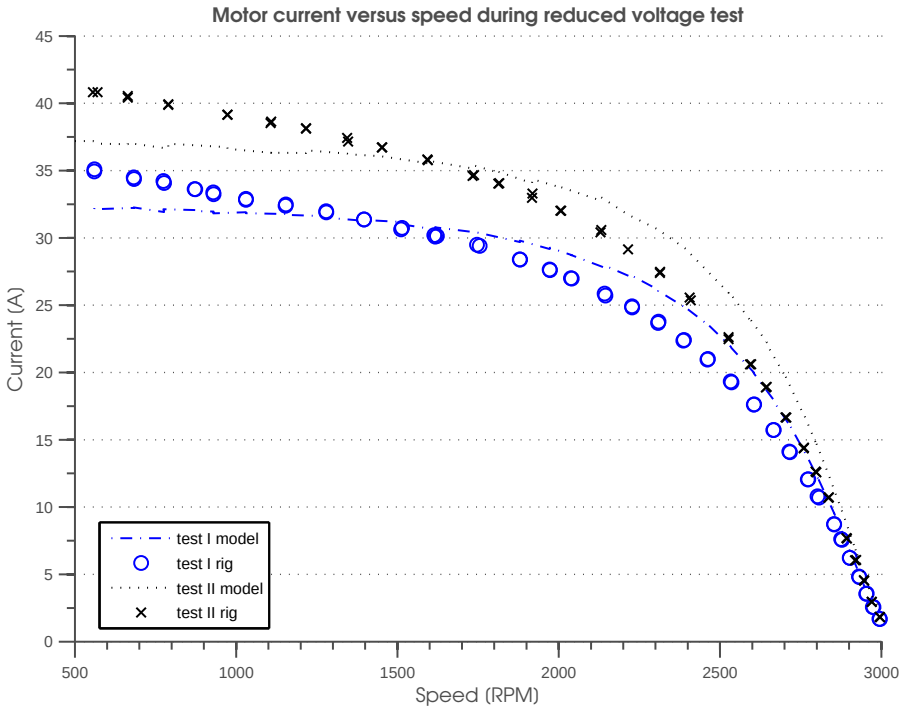

Figure 3.17. Current versus speed during reduced voltage tests

3.3.6 Torque Approximation Formula

Under balanced supply conditions the electromagnetic torque of an induction motor is slip dependent as shown in equation 3.26. Its maximum called breakdown torque can be found by taking the first derivative with respect to the slip [38] and setting it to zero as follows

$$\frac{\partial T_e}{\partial s} = 0 \tag{3.34}$$

Solving for the slip, the breakdown slip is obtained and is given by

$$s_{max} = \frac{R_r}{\sqrt{R_{th}^2 + (X_{th} + X_r)^2}} \tag{3.35}$$

By substituting the slip to equation 3.26, the breakdown torque is obtained as given in

$$T_{max} = \frac{3}{2\omega_s} \frac{V_{th}^2}{R_{th} + \sqrt{R_{th}^2 + (X_{th} + X_r)^2}} \tag{3.36}$$

To show the motor parameters impact onto the motor performance, the breakdown torque along with the corresponding slip, current and speed have been calculated for all the sets of motor parameters considered and are given in table 3.6.

Motor parameters		Unit	Lowara (No Load)	Lowara (Load)	Test (avg)
Breakdown torque	T_{max}	Nm	143.39	157.28	140.62
Breakdown slip	s_{max}	–	0.224	0.253	0.202
Speed at T_{max}	$N_{T_{max}}$	rev/min	2328	2240	2391
Current at T_{max}	$I_{T_{max}}$	A	103.79	115.98	102.15

Table 3.6. Induction motor parameters

Unlike the electromagnetic torque, the maximum torque does not vary with the rotor resistance and the slip [35] and is machine construction dependent. Dividing the expression for electromagnetic torque by the breakdown torque gives

$$\frac{T_e}{T_{max}} = \frac{\frac{3}{s\omega_s} \frac{V_{th}^2 R_r}{\left(R_{th} + \frac{R_r}{s}\right)^2 + \left(X_{th} + X_r\right)^2}}{\frac{3}{2\omega_s} \frac{V_{th}^2}{R_{th} + \sqrt{R_{th}^2 + (X_1 + X_r)^2}}} \tag{3.37}$$

This yields an expression for torque approximation called the Kloss formula [40, 41]. It is of value because, when the breakdown torque and corresponding slip are known, the operating torque for any slip can be obtained. The Kloss relationship is presented in equation 3.38.

$$\frac{T_e}{T_{max}} = \frac{2\,(1+\epsilon)}{\frac{s}{s_{max}} + \frac{s_{max}}{s} + 2\epsilon} \tag{3.38}$$

where

$$\epsilon = \frac{R_{th}}{\sqrt{R_{th}^2 + (X_{th} + X_r)^2}} \tag{3.39}$$

In the linear region of an induction machine operation where the mechanical power equivalent resistance dominates the rest of the impedances, the Kloss expression may be approximated by

$$T_e = \frac{2T_{max}}{\frac{s}{s_{max}} + \frac{s_{max}}{s}} \tag{3.40}$$

To illustrate the validity of the torque approximation formula, the torque steady-state curve detailed in section 3.3.1 has been plotted with the Kloss torque approximation. The resulting characteristics are presented in figure 3.18. It may be seen that the Kloss formula allows quick and accurate (in the linear region) torque prediction at any arbitrary speed by knowing only the motor breakdown values.

3.3.7 Variable Frequency Operation

An induction machine shaft speed depends upon the synchronous speed and the load torque applied to the shaft [42]. The former defined in equation 3.1 is the function of supply frequency and winding pole number. For a standard motor construction the pole number cannot be changed instantly and the speed regulation cannot be achieved in a simple way. For efficient motor operation the slip should be minimised to lower rotor current losses, and so motor speed regulation is best implemented by supply frequency control.

The torque generation capability of an induction motor is proportional to the magnetic flux density in the air gap. Therefore, to ensure consistent peak torque capability it is necessary to maintain the flux density of the air gap at its rated value over the operating frequency range. If the air gap flux of the machine is kept at the rated value, the torque per ampere will be high.

The induction machine presents a highly inductive load to the supply, so its impedance increases directly with applied supply frequency. Therefore, it is required to increase the applied voltage in direct proportion to the increase of frequency. The ratio of volts to frequency, known as Volts per Hertz (V/f), must be kept constant to maintain constant

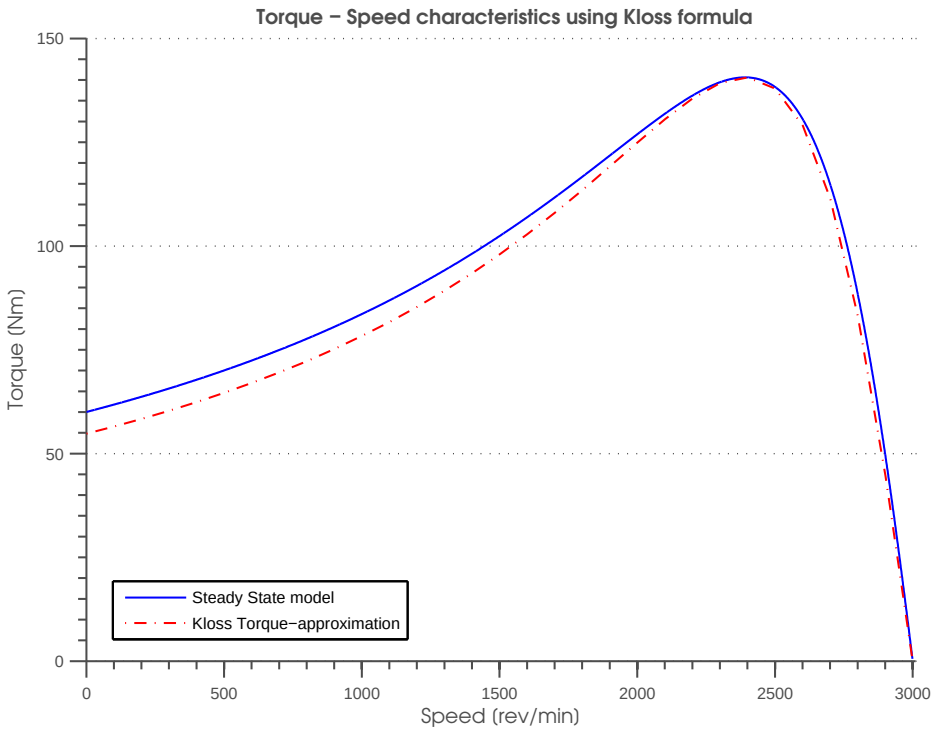

Figure 3.18. Induction machine Kloss torque approximation

flux operation. However, beyond the rated frequency the supply voltage cannot be further increased, resulting in field weakening operation while the rotor speed rises. Consequently, the region beyond base frequency provides reduced torque but constant power capability.

For low frequency operation the voltage drop across the stator impedance is significant compared to the air-gap magnetising voltage, resulting in weaker magnetising field and torque deterioration. In order to improve steady-state performance, boost voltage compensation is required. The boost voltage has been calculated according to the following formula

$$V_{boost} = |I_{rated}\,(R_s + jX_s)| \tag{3.41}$$

Based on the input current and stator impedance measurements, the initial boost compensation voltage was set up to 35V for Lowara motor modelling, and then increased in linear proportion to the supply frequency as shown in figure 3.19. The complete V/f relationship is given in equation 3.42.

$$V = V_{boost}\,(f_e) + k_\Psi f_e \tag{3.42}$$

where k_Ψ is inverter proportionality constant.

Results for a supply frequency range from 0 to 65Hz with the rated (base) frequency of 50Hz have been plotted in figure 3.19. The corresponding supply voltage varies from its minimum value to 400V, the rated voltage of the machine. The V/f control technique may

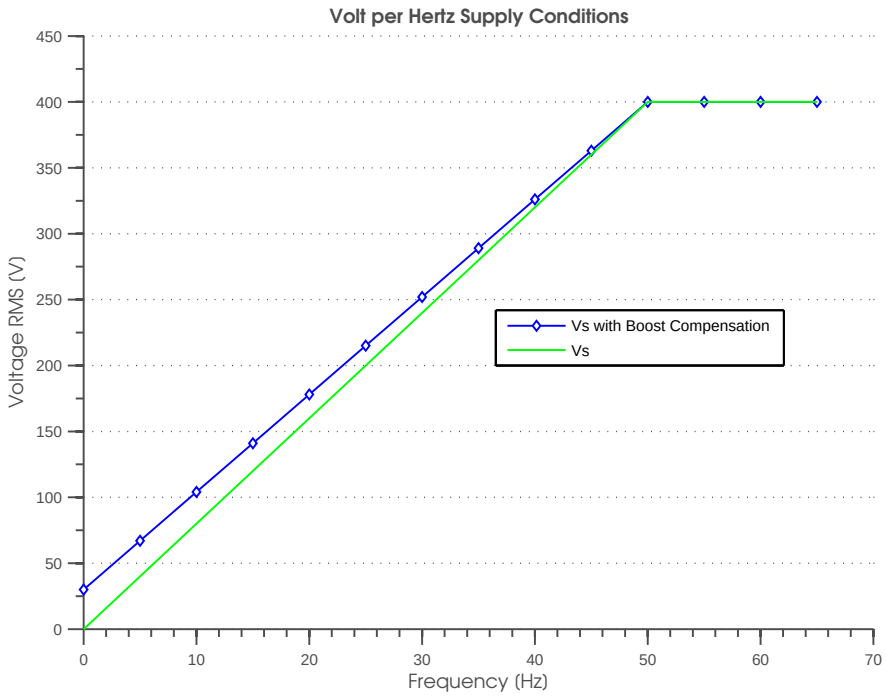

Figure 3.19. Supply condition under constant volts per hertz operation

be implemented using a voltage source inverter (VSI) employing Pulse Width Modulation (PWM) control.

The steady state torque characteristics for the investigated motor under constant V/f operation have been developed, based on the torque expression given in equation 3.26, over the range of supply conditions presented in figure 3.19. The developed torque-speed family of curves under constant V/f operation without boost compensation are depicted in figure 3.20.

The breakdown torque is reduced when the supply frequency decreases because of the stator voltage drop. Beyond the base frequency the field weakening operation is clearly visible, because the breakdown torque decreases with supply frequency. The family of motor torque versus operating speed characteristics with boost voltage compensation is shown in 3.21. It can be seen that progressively boosting the supply voltage at the supply frequency is reduced from 65Hz, improving the peak torque capability since the stator voltage drop becomes progressively more significant.

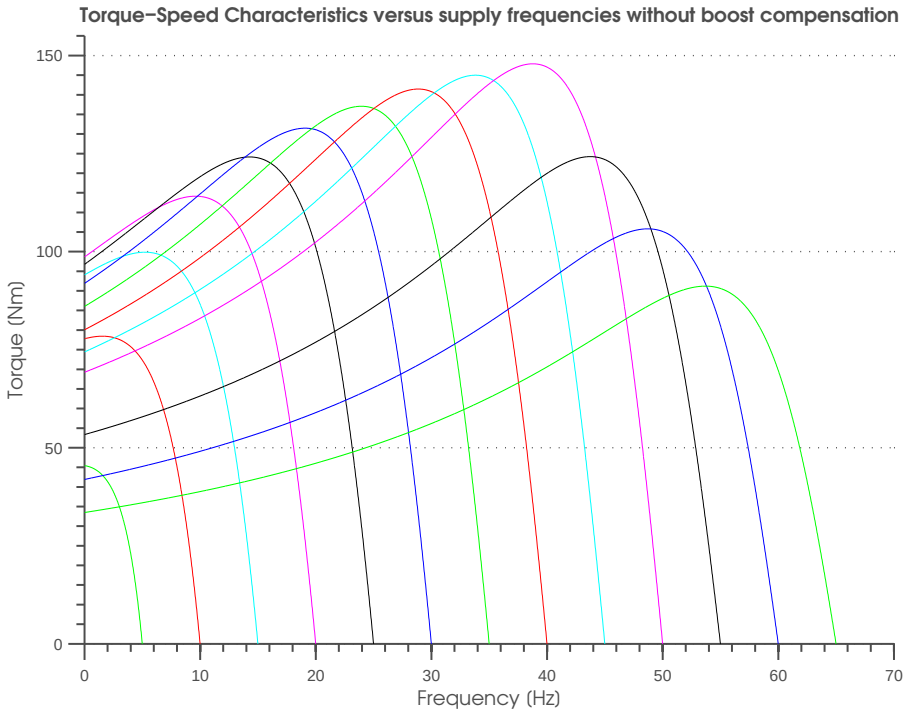

Figure 3.20. Torque-speed characteristics for the Lowara induction motor under constant volts per hertz operation without boost voltage

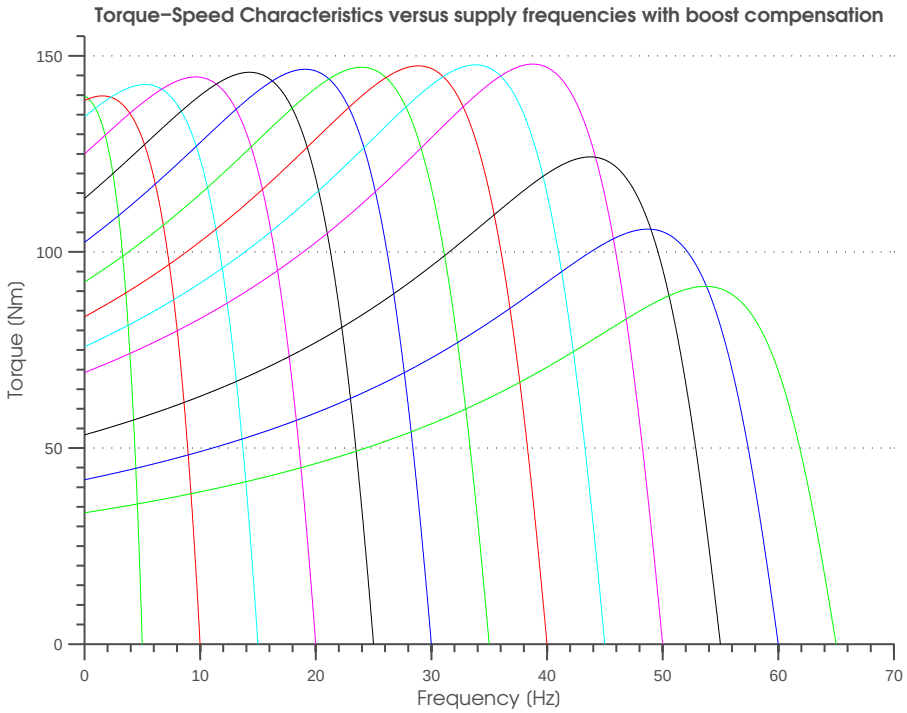

Figure 3.21. Torque-speed characteristics for the Lowara induction motor under constant volts per hertz operation with boost voltage

3.4 Transient Model of Induction Machine

Per-phase equivalent circuit models of induction machines are applicable when performance during steady state conditions of the motor is being investigated. However, when using induction machines in closed-loop control applications it is necessary to model and consider their transient behaviour. A dynamic model is then required, so that the instantaneous effects of varying voltages/currents, stator frequency, and torque disturbance may be analysed.

Because of the motor's complex internal inter-variable relationships, certain assumptions must be made to derive a dynamic model. It was assumed that the stator and rotor windings were balanced with sinusoidally distributed magnetomotive force (mmf), inductances vary sinusoidally with rotor position, the motor possesses a uniform air gap around its circumference and magnetic circuit saturation was negligible.

The induction motor behaviour may then be described by differential equations expressed in terms of machine variables. These equations are then transformed to arbitrary reference-frame coordinates, which allows the motor to be represented by a two-phase model using direct and quadrature axes, to clearly separate torque and air gap-flux producing currents.

3.4.1 Voltage Equations In Machine Variables

An induction machine involves magnetically coupled stator and rotor circuits whose coupling coefficient continuously changes with the rotor position. The terminal voltages of the stator and rotor windings can be expressed in terms of the voltage drops across winding resistances r and rates of change of flux linkages λ. Using a stationary motor reference frame abc, the stator and rotor voltage relationships can be expressed by six first-order differential equations [39] as follows

Stator voltage equations

$$v_{as} = i_{as}r_s + p\lambda_{as} \tag{3.43a}$$
$$v_{bs} = i_{bs}r_s + p\lambda_{bs} \tag{3.43b}$$
$$v_{cs} = i_{cs}r_s + p\lambda_{cs} \tag{3.43c}$$

Rotor voltage equations

$$v_{ar} = i_{ar}r_r + p\lambda_{ar} \tag{3.44a}$$
$$v_{br} = i_{br}r_r + p\lambda_{br} \tag{3.44b}$$
$$v_{cr} = i_{cr}r_r + p\lambda_{cr} \tag{3.44c}$$

where $p = d/dt$ and subscripts s and r denote stator and rotor quantities, respectively.

To express the motor equations in machine variable form it is convenient to refer all rotor variables to stator coordinates using an appropriate turns ratio [43]. Then the voltage

equations for the stator and rotor may be represented by vector notation as follows

$$\begin{aligned} \mathbf{v}_{abcs} &= \mathbf{r}_s \mathbf{i}_{abcs} + p\boldsymbol{\lambda}_{abcs} \\ \mathbf{v}'_{abcr} &= \mathbf{r}'_r \mathbf{i}'_{abcr} + p\boldsymbol{\lambda}'_{abcr} \end{aligned} \tag{3.45}$$

where $(\mathbf{f}_{abc})^T = \begin{bmatrix} f_a & f_b & f_c \end{bmatrix}$, the superscript T denotes the transpose of the vector and the rotor referred variables are denoted with a prime e.g. $\mathbf{r}'$.

In the symmetrical induction machine the stator and rotor resistances are time invariant and per-phase values are equal. Consequently $\mathbf{r}_s$ and $\mathbf{r}'_r$ are diagonal matrices defined by $\mathbf{r}_s = r_s\mathbf{I}$ and $\mathbf{r}'_r = r'_r\mathbf{I}$ for the stator and rotor, respectively where $\mathbf{I}$ is the identity matrix.

Since inductance is flux-linkage per amp, the instantaneous flux linkages of the stator and the rotor windings may be described in terms of the winding inductances and currents by

$$\begin{bmatrix} \boldsymbol{\lambda}_{abcs} \\ \boldsymbol{\lambda}'_{abcr} \end{bmatrix} = \begin{bmatrix} \mathbf{L}_s & \mathbf{L}'_{rs} \\ (\mathbf{L}'_{sr})^T & \mathbf{L}'_r \end{bmatrix} \begin{bmatrix} \mathbf{i}_{abcs} \\ \mathbf{i}'_{abcr} \end{bmatrix} \tag{3.46}$$

where $\mathbf{L}_s$ and $\mathbf{L}'_r$ are stator-to-stator and rotor-to-rotor inductance, and $\mathbf{L}'_{sr}$ and $\mathbf{L}'_{rs}$ are equivalent stator-to-rotor and rotor-to-stator mutual inductances, defined below:

$$\mathbf{L}_s = \begin{bmatrix} L_{ls} + L_{ms} & -\frac{1}{2}L_{ms} & -\frac{1}{2}L_{ms} \\ -\frac{1}{2}L_{ms} & L_{ls} + L_{ms} & -\frac{1}{2}L_{ms} \\ -\frac{1}{2}L_{ms} & -\frac{1}{2}L_{ms} & L_{ls} + L_{ms} \end{bmatrix} \tag{3.47}$$

$$\mathbf{L}'_r = \begin{bmatrix} L'_l + L_{ms} & -\frac{1}{2}L_{ms} & -\frac{1}{2}L_{ms} \\ -\frac{1}{2}L_{ms} & L'_l + L_{ms} & -\frac{1}{2}L_{ms} \\ -\frac{1}{2}L_{ms} & -\frac{1}{2}L_{ms} & L'_{lr} + L_{ms} \end{bmatrix} \tag{3.48}$$

and L_{ls} and L'_{lr} represent per-phase stator and rotor leakage inductances, whereas L_{ms} is the stator magnetising inductance.

The mutual inductances $\mathbf{L}'_{sr}$ between stator and rotor are also a function of rotor position θ_r as given by

$$\mathbf{L}'_{sr} = \mathbf{L}'_{rs} = L_{ms} \begin{bmatrix} \cos\theta_r & \cos\left(\theta_r + \frac{2\pi}{3}\right) & \cos\left(\theta_r - \frac{2\pi}{3}\right) \\ \cos\left(\theta_r - \frac{2\pi}{3}\right) & \cos\theta_r & \cos\left(\theta_r + \frac{2\pi}{3}\right) \\ \cos\left(\theta_r + \frac{2\pi}{3}\right) & \cos\left(\theta_r - \frac{2\pi}{3}\right) & \cos\theta_r \end{bmatrix} \tag{3.49}$$

The induction motor voltage equations expressed in terms of currents may then be written as follows [44]

$$\begin{bmatrix} \mathbf{v}_{abcs} \\ \mathbf{v}'_{abcr} \end{bmatrix} = \begin{bmatrix} \mathbf{r}_s + p\mathbf{L}_s & p\mathbf{L}'_{sr} \\ (p\mathbf{L}'_{sr})^T & \mathbf{r}'_r + p\mathbf{L}'_r \end{bmatrix} \begin{bmatrix} \mathbf{i}_{abcs} \\ \mathbf{i}'_{abcr} \end{bmatrix} \tag{3.50}$$

The complete six voltage equations for the induction machine given in (3.43) and (3.44) can also be represented by a single matrix relationship as follows

$$\begin{bmatrix} v_{as} \\ v_{bs} \\ v_{cs} \\ v'_{ar} \\ v'_{br} \\ v'_{cr} \end{bmatrix} = \begin{bmatrix} r_s + L_{ss} & pM_s & pM_s & pM_{sr}\cos\theta_0 & pM_{sr}\cos\theta_1 & pM_{sr}\cos\theta_2 \\ pM_s & r_s + L_{ss} & pM_s & pM_{sr}\cos\theta_2 & pM_{sr}\cos\theta_0 & pM_{sr}\cos\theta_1 \\ pM_s & pM_s & r_s + L_{ss} & pM_{sr}\cos\theta_1 & pM_{sr}\cos\theta_2 & pM_{sr}\cos\theta_0 \\ pM_{sr}\cos\theta_0 & pM_{sr}\cos\theta_2 & pM_{sr}\cos\theta_1 & r'_r + L'_{rr} & pM_s & pM_s \\ pM_{sr}\cos\theta_1 & pM_{sr}\cos\theta_0 & pM_{sr}\cos\theta_2 & pM_s & r'_r + L'_{rr} & pM_s \\ pM_{sr}\cos\theta_2 & pM_{sr}\cos\theta_1 & pM_{sr}\cos\theta_0 & pM_s & pM_s & r'_r + L'_{rr} \end{bmatrix} \begin{bmatrix} i_{as} \\ i_{bs} \\ i_{cs} \\ i'_{ar} \\ i'_{br} \\ i'_{cr} \end{bmatrix} \tag{3.51}$$

where the inductances are defined by $L_{ss} = L_{ls} + L_{ms}$, $M_s = -L_{ms}/2$, $M_{sr} = L_{ms}$, $L'_{rr} = L'_{lr} + L_{sm}$ and angles as $\theta_0 = \theta_r$, $\theta_1 = \theta_r + 2\pi/3$ and $\theta_2 = \theta_r - 2\pi/3$

The torque of an induction machine is a function of energy stored in the coupled magnetic fields and rotor position [44]. Because only the mutual stator-to-rotor inductances are functions of rotor angle the torque equation may be expressed as

$$T_e\left(i_j, \theta_r\right) = \left(\frac{P}{2}\right)(\mathbf{i}_{abcs})^T \frac{\partial}{\partial\theta_r}\left[\mathbf{L}'_{sr}\right]\mathbf{i}'_{abcr} \tag{3.52}$$

Equation 3.52 can be expressed [44] in terms of the instantaneous currents and expanded version is given as follows

$$\begin{aligned} T_e &= -\left(\frac{P}{2}\right)L_{ms}\left\{\sin\theta_r\left[i_{as}\left(i'_{ar} - \frac{1}{2}i'_{br} - \frac{1}{2}i'_{cr}\right)\right.\right. \\ &+ \left. i_{bs}\left(i'_{br} - \frac{1}{2}i'_{ar} - \frac{1}{2}i'_{cr}\right) + i_{cs}\left(i'_{cr} - \frac{1}{2}i'_{br} - \frac{1}{2}i'_{ar}\right)\right] \\ &+ \left.\frac{\sqrt{3}}{2}\cos\theta_r\left[i_{as}\left(i'_{br} - i'_{cr}\right) + i_{bs}\left(i'_{cr} - i'_{ar}\right) + i_{cs}\left(i'_{ar} - i'_{br}\right)\right]\right\} \end{aligned} \tag{3.53}$$

3.4.2 Transformation Of Variables to Arbitrary Reference Frame

The operation of an induction machine can be described by non-linear differential relationships as shown in equation 3.50. The coupled fields described by mutual inductances are the function of rotor position and furthermore vary with time during machine motion. Consequently, the operation of an induction machine is described by complex relationships which are difficult to analyse.

To simplify the induction machine analysis a change of variables is employed. The machine variables, expressed in a stationary reference frame, are transformed to a rotating reference

frame where the inductances become constant values regardless of rotor position. The schematic relations between coordinates and frames are shown in figure 3.22.

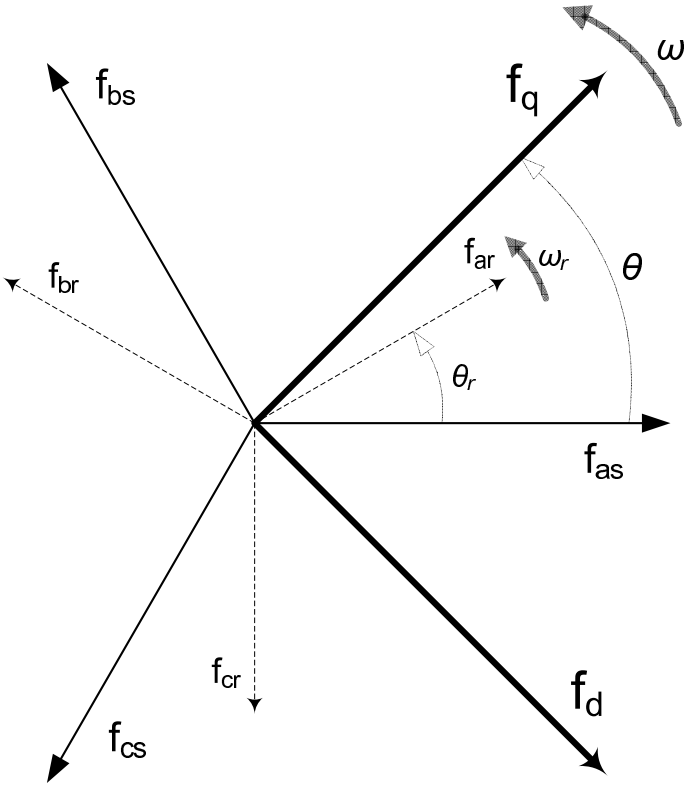

Figure 3.22. Variable transformation

The transformation of motor variables from the 3-phase stationary reference frame *abc* to a rotating 2-phase arbitrary reference frame *qd*0 may be expressed using *Clarke's* and *Park's* transformations [45] as follows

$$\mathbf{f}_{qd0} = \mathbf{K}(\theta_t)\,\mathbf{f}_{abc} \tag{3.54}$$

where $\left(\mathbf{f}_{qd0}\right)^T = \begin{bmatrix} f_q & f_d & f_0 \end{bmatrix}$, $(\mathbf{f}_{abc})^T = \begin{bmatrix} f_a & f_b & f_c \end{bmatrix}$ and θ_t is the transformation angle.

The transformation matrix $\mathbf{K}(\theta_t)$ is valid both for stator and rotor variables and is given as

$$\mathbf{K}(\theta_t) = \frac{2}{3}\begin{bmatrix} \cos\theta_t & \cos\left(\theta_t - \frac{2\pi}{3}\right) & \cos\left(\theta_t + \frac{2\pi}{3}\right) \\ \sin\theta_t & \sin\left(\theta_t - \frac{2\pi}{3}\right) & \sin\left(\theta_t + \frac{2\pi}{3}\right) \\ 1/2 & 1/2 & 1/2 \end{bmatrix} \tag{3.55}$$

where $\theta_t = \theta$ and $\theta_t = \theta - \theta_r$ is to be set for stator and rotor variables transformation, respectively.

The transformation angle is a function of rotating speed and can be expressed for both stator and rotor variables as

$$\theta = \int_0^t \omega(t)\,dt + \theta(0) \tag{3.56}$$

$$\theta_r = \int_0^t \omega_r(t)\,dt + \theta_r(0) \tag{3.57}$$

where ω is angular velocity of an arbitrary reference frame.

The inverse transformation valid for both stator and rotor is given as

$$\mathbf{f}_{abc} = [\mathbf{K}(\theta_t)]^{-1}\,\mathbf{f}_{qd0} \tag{3.58}$$

where

$$[\mathbf{K}(\theta_t)]^{-1} = \begin{bmatrix} \cos\theta_t & \sin\theta_t & 1 \\ \cos\left(\theta_t - \frac{2\pi}{3}\right) & \sin\left(\theta_t - \frac{2\pi}{3}\right) & 1 \\ \cos\left(\theta_t + \frac{2\pi}{3}\right) & \sin\left(\theta_t + \frac{2\pi}{3}\right) & 1 \end{bmatrix} \tag{3.59}$$

The analysis of induction motor operation can be performed in a number of reference frames depending on the analysis needs. However, the three common reference frames are used for induction machine description. The stationary reference frame is employed when the rotating speed is equal to zero, $\omega = 0$; for the rotor reference frame, rotor speed is the base of rotation speed, $\omega = \omega_r$; and the synchronously rotating reference frame is obtained if the rotation speed is set to angular speed of the stator field, $\omega = \omega_e$. Regardless of the reference frame used the machine equations have to be transformed appropriately to and from the employed reference frame.

The total power before and after transformation has to be preserved. The total instantaneous power in *abc* variables may be expressed as

$$P_{abc} = v_a i_a + v_b i_b + v_c i_c \tag{3.60}$$

After performing the transformation of variables the total power in an arbitrary reference frame is obtained using

$$P_{qd0} = \frac{3}{2}\left(v_q i_q + v_d i_d + 2v_0 i_0\right) \tag{3.61}$$

Regardless of the reference frame used the power waveform is unchanged [44].

3.4.3 Voltage Equations In Arbitrary Reference Frame

The induction motor model based on arbitrary reference frame coordinates can be derived by applying transformation (3.54) to motor voltage equations expressed in the machine coordinates. Then

$$\begin{aligned} \mathbf{v}_{qd0s} &= \left[\mathbf{K}_s \mathbf{r}_s \left(\mathbf{K}_s\right)^{-1}\right] \mathbf{i}_{qd0s} + \mathbf{K}_s p \left[\left(\mathbf{K}_s\right)^{-1} \boldsymbol{\lambda}_{qd0s}\right] \\ \mathbf{v}'_{qd0r} &= \left[\mathbf{K}_r \mathbf{r}'_r \left(\mathbf{K}_r\right)^{-1}\right] \mathbf{i}'_{qd0r} + \mathbf{K}_r p \left[\left(\mathbf{K}_r\right)^{-1} \boldsymbol{\lambda}'_{qd0r}\right] \end{aligned} \tag{3.62}$$

where transformation matrix $\mathbf{K}$ subscripts denote the association with stator and rotor variables, respectively. Because of phase resistance symmetry $\mathbf{r} = r\mathbf{I}$ so the $\mathbf{K}r\mathbf{I}\left(\mathbf{K}\right)^{-1} = \mathbf{r}$ and is valid for both stator and rotor resistance matrices.

Thus, the motor voltage equation for an arbitrary reference frame can be expressed in the form of

$$\begin{aligned} \mathbf{v}_{qd0s} &= \mathbf{r}_s \mathbf{i}_{qd0s} + \omega \boldsymbol{\lambda}_{dqs} + p\boldsymbol{\lambda}_{qd0s} \\ \mathbf{v}'_{qd0r} &= \mathbf{r}'_r \mathbf{i}'_{qd0r} + \left(\omega - \omega_r\right) \boldsymbol{\lambda}'_{dqr} + p\boldsymbol{\lambda}'_{qd0r} \end{aligned} \tag{3.63}$$

where $\left(\boldsymbol{\lambda}_{dqs}\right)^T = \begin{bmatrix} \lambda_{ds} & \lambda_{qs} & 0 \end{bmatrix}$ and $\left(\boldsymbol{\lambda}'_{dqr}\right)^T = \begin{bmatrix} \lambda'_{dr} & \lambda'_{qr} & 0 \end{bmatrix}$

To complete variable transformation, the flux linkages have to be transformed to an arbitrary reference frame. Applying *Clarke's* and *Park's* transformations (3.54) to the flux linkage relationships given in equation 3.46 yields

$$\begin{aligned} \boldsymbol{\lambda}_{qd0s} &= \left[\mathbf{K}_s \mathbf{L}_s \left(\mathbf{K}_s\right)^{-1}\right] \mathbf{i}_{qd0s} + \left[\mathbf{K}_s \mathbf{L}'_{sr} \left(\mathbf{K}_r\right)^{-1}\right] \mathbf{i}'_{qd0r} \\ \boldsymbol{\lambda}'_{qd0r} &= \left[\mathbf{K}_r \left(\mathbf{L}'_{sr}\right)^T \left(\mathbf{K}_s\right)^{-1}\right] \mathbf{i}_{qd0s} + \left[\mathbf{K}_r \mathbf{L}'_r \left(\mathbf{K}_r\right)^{-1}\right] \mathbf{i}'_{qd0r} \end{aligned} \tag{3.64}$$

the flux linkage equations expressed in $qd0$ coordinates have been obtained as

$$\begin{aligned} \boldsymbol{\lambda}_{qd0s} &= \mathbf{L}_{qd0s} \mathbf{i}_{qd0s} + \mathbf{L}'_{qd0m} \mathbf{i}'_{qd0r} \\ \boldsymbol{\lambda}'_{qd0r} &= \left(\mathbf{L}'_{qd0m}\right)^T \mathbf{i}_{qd0s} + \mathbf{L}'_{qd0r} \mathbf{i}'_{qd0r} \end{aligned} \tag{3.65}$$

where the inductance matrices have been defined as follows

$$\mathbf{L}_{qd0s} = \mathbf{K}_s \mathbf{L}_s \left(\mathbf{K}_s\right)^{-1} = \begin{bmatrix} L_{ls} + \dfrac{3}{2} L_{sm} & 0 & 0 \\ 0 & L_{ls} + \dfrac{3}{2} L_{sm} & 0 \\ 0 & 0 & L_{ls} \end{bmatrix} \tag{3.66}$$

$$\mathbf{L'}_{qd0r} = \mathbf{K}_r \mathbf{L'}_r (\mathbf{K}_r)^{-1} = \begin{bmatrix} L'_{lr} + \frac{3}{2}L_{sm} & 0 & 0 \\ 0 & L'_{lr} + \frac{3}{2}L_{sm} & 0 \\ 0 & 0 & L'_l \end{bmatrix} \tag{3.67}$$

$$\mathbf{L'}_{qd0m} = \mathbf{K}_s \mathbf{L'}_{sr} (\mathbf{K}_r)^{-1} = \mathbf{K}_r (\mathbf{L'}_{sr})^T (\mathbf{K}_s)^{-1} = \begin{bmatrix} \frac{3}{2}L_{sm} & 0 & 0 \\ 0 & \frac{3}{2}L_{sm} & 0 \\ 0 & 0 & 0 \end{bmatrix} \tag{3.68}$$

The motor flux linkage relationships may be expressed by a single matrix as

$$\begin{bmatrix} \lambda_{qs} \\ \lambda_{ds} \\ \lambda_{0s} \\ \lambda'_{qr} \\ \lambda'_{dr} \\ \lambda'_{0r} \end{bmatrix} = \begin{bmatrix} L_{ls} + \frac{3}{2}L_{sm} & 0 & 0 & \frac{3}{2}L_{sm} & 0 & 0 \\ 0 & L_{ls} + \frac{3}{2}L_{sm} & 0 & 0 & \frac{3}{2}L_{sm} & 0 \\ 0 & 0 & L_{ls} & 0 & 0 & 0 \\ \frac{3}{2}L_{sm} & 0 & 0 & L'_l + \frac{3}{2}L_{sm} & 0 & 0 \\ 0 & \frac{3}{2}L_{sm} & 0 & 0 & L'_{lr} + \frac{3}{2}L_{sm} & 0 \\ 0 & 0 & 0 & 0 & 0 & L'_l \end{bmatrix} \begin{bmatrix} i_{qs} \\ i_{ds} \\ i_{0s} \\ i'_{qr} \\ i'_{dr} \\ i'_{0r} \end{bmatrix} \tag{3.69}$$

The voltage equation describing the induction machine in an arbitrary rotating reference frame can be presented in matrix form as follows

$$\begin{bmatrix} v_{qs} \\ v_{ds} \\ v_{0s} \\ v'_{qr} \\ v'_{dr} \\ v'_{0r} \end{bmatrix} = \begin{bmatrix} r_s + pL_{ssq} & \omega L_{ssq} & 0 & \frac{3}{2}pL_{sm} & \frac{3}{2}L_{sm}\omega & 0 \\ -\omega L_{ssq} & r_s + pL_{ssq} & 0 & -\frac{3}{2}L_{sm}\omega & \frac{3}{2}pL_{sm} & 0 \\ 0 & 0 & r_s + pL_{ls} & 0 & 0 & 0 \\ \frac{3}{2}pL_{sm} & \frac{3}{2}L_{sm}\omega_t & 0 & r'_r + pL'_{rrq} & \omega_t L'_{rrq} & 0 \\ -\frac{3}{2}L_{sm}\omega_t & \frac{3}{2}pL_{sm} & 0 & -\omega_t L'_{rr} & r'_r + pL'_{rrq} & 0 \\ 0 & 0 & 0 & 0 & 0 & r'_r + pL'_{lr} \end{bmatrix} \begin{bmatrix} i_{qs} \\ i_{ds} \\ i_{0s} \\ i'_{qr} \\ i'_{dr} \\ i'_{0r} \end{bmatrix} \tag{3.70}$$

Where $L_{ssq} = L_{ls} + 3/2L_{sm}$, $L'_{rrq} = L'_{lr} + 3/2L_{sm}$ and $\omega_t = \omega - \omega_r$

The electromagnetic torque expressed in $qd0$ variables can be obtained using *Clarke's* and *Park's* transformations of the torque relationship developed in *abc* coordinates

$$T_e = \left(\frac{P}{2}\right)\left[(\mathbf{K}_s)^{-1}\,\mathbf{i}_{qd0s}\right]^T \frac{\partial}{\partial\theta_r}\left[\mathbf{L'}_{sr}\right](\mathbf{K}_r)^{-1}\,\mathbf{i'}_{qd0r} \tag{3.71}$$

This torque expression can be presented in terms of the currents as

$$T_e = \left(\frac{3}{2}\right)\left(\frac{P}{2}\right)\left(\frac{3}{2}L_{sm}\right)\left(i_{qs}i'_{dr} - i_{ds}i'_{qr}\right) \tag{3.72}$$

It is also possible to express torque either in terms the rotor quantities as given in (3.73) or by the stator quantities as shown in (3.74)

$$T_e = \left(\frac{3}{2}\right)\left(\frac{P}{2}\right)\left(\lambda'_{qr}i'_{dr} - \lambda'_{dr}i'_{qr}\right) \tag{3.73}$$

$$T_e = \left(\frac{3}{2}\right)\left(\frac{P}{2}\right)\left(\lambda_{ds}i_{qs} - \lambda_{qs}i_{ds}\right) \tag{3.74}$$

3.4.4 Induction Motor Transient Model Implementation

A transient model of an induction machine was developed using the Matlab/Simulink environment. The model was based on the machine equations expressed in an arbitrary rotating reference frame described in section 3.4.3. The behaviour of a symmetrical induction machine was studied in the synchronously rotating reference frame and the simulated induction motor voltage equations were obtained from these in the arbitrary reference frame by setting the angular velocity of the arbitrary reference frame to the angular speed of supply network $\omega = \omega_e$.

Because the investigated induction motor is of the squirrel-cage type then rotor input voltages are set to zero $\mathbf{v'}_{qd0r} = 0$. Then, the simulated voltage equations are given as

$$\begin{aligned} \mathbf{v}_{qd0s} &= \mathbf{r}_s\mathbf{i}_{qd0s} + p\boldsymbol{\lambda}_{qd0s} + \omega\mathbf{M}\boldsymbol{\lambda}_{qd0s} \\ 0 &= \mathbf{r'}_r\mathbf{i'}_{qd0r} + p\boldsymbol{\lambda'}_{qd0r} + (\omega - \omega_r)\,\mathbf{M}\boldsymbol{\lambda'}_{qd0s} \end{aligned} \tag{3.75}$$

where $\mathbf{M}$ is a rotational operator expressed as

$$\mathbf{M} = \begin{bmatrix} 0 & -1 & 0 \\ 1 & 0 & 0 \\ 0 & 0 & 0 \end{bmatrix} \tag{3.76}$$

The investigated induction motor was connected in a delta configuration and supplied from symmetrical and balanced supply voltages so there is no need to take the zero component

in $qd0$ coordinates into account. The resulting voltage equations modelled in Simulink are presented as follows

$$\begin{aligned} \mathbf{v}_{qds} &= r_s \mathbf{i}_{qds} + p\boldsymbol{\lambda}_{qds} + \omega \mathbf{M}\boldsymbol{\lambda}_{qds} \\ 0 &= r'_r \mathbf{i}'_{qdr} + p\boldsymbol{\lambda}'_{qdr} + (\omega - \omega_r)\,\mathbf{M}\boldsymbol{\lambda}'_{qds} \end{aligned} \tag{3.77}$$

where $\left(\mathbf{f}_{qd}\right)^T = \begin{bmatrix} f_q & f_d \end{bmatrix}$ and $\mathbf{M} = \begin{bmatrix} 0 & -1 \\ 1 & 0 \end{bmatrix}$. The motor supply voltage as the input to the model is the vector of quadrature v_{qs} and direct v_{ds} voltages so the instantaneous voltages v_{as}, v_{bs} and v_{cs} were transformed to rotating qd coordinates.

The flux linkages and currents are interdependent, and the flux linkages were chosen as the reference variables. Choosing the currents as the reference variables results in two derivatives in the voltage equations, making the machine voltage equations more difficult to implement. The implemented flux linkage relationships are presented as follows

$$\begin{aligned} \boldsymbol{\lambda}_{qds} &= \left(L_{ls} + \frac{3}{2}L_{sm}\right)\mathbf{i}_{qds} + \frac{3}{2}L_{sm}\mathbf{i}'_{qdr} \\ \boldsymbol{\lambda}'_{qdr} &= \frac{3}{2}L_{sm}\mathbf{i}_{qds} + \left(L'_{lr} + \frac{3}{2}L_{sm}\right)\mathbf{i}'_{qdr} \end{aligned} \tag{3.78}$$

The instantaneous values of stator and rotor currents expressed in qd coordinates were found by inverse flux-current relationship as follows

$$\begin{aligned} \mathbf{i}_{qds} &= G_s\boldsymbol{\lambda}_{qds} - G_m\boldsymbol{\lambda}'_{qdr} \\ \mathbf{i}'_{qdr} &= -G_m\boldsymbol{\lambda}_{qds} + G_r\boldsymbol{\lambda}'_{qdr} \end{aligned} \tag{3.79}$$

where

$$\begin{aligned} G_s &= \frac{L_{lr} + L_{sm}}{L_{ls}L_{lr} + L_{lr}L_{sm}} \\ G_r &= \frac{L_{ls} + L_{sm}}{L_{ls}L_{lr} + L_{lr}L_{sm}} \\ G_m &= \frac{L_{sm}}{L_{ls}L_{lr} + L_{lr}L_{sm}} \end{aligned} \tag{3.80}$$

The instantaneous currents expressed in the synchronously rotating reference frame qd were then transformed to machine reference frame abc by the inverse transformation given in (3.59).

The motor electromagnetic torque model was based on equation 3.72 and calculated according to

$$T_e = \left(\frac{3}{2}\right)\left(\frac{P}{2}\right)\left(\frac{3}{2}L_{sm}\right)\left(\mathbf{M}\mathbf{i}'_{qdr} \bullet \mathbf{i}_{qds}\right) \tag{3.81}$$

The complete transient diagram-model of the induction motor was developed in Matlab/Simulink and is shown in figure 3.23, where the transformation of variables is also depicted. The dq0-based transient model of an induction motor is highlighted in figure 3.24. Each variable is modelled by the two-element vectors with quadrature q and direct d components, respectively.

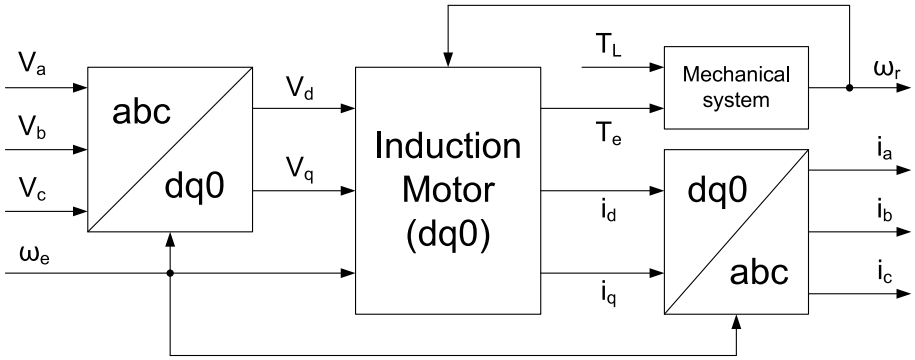

Figure 3.23. Induction motor model

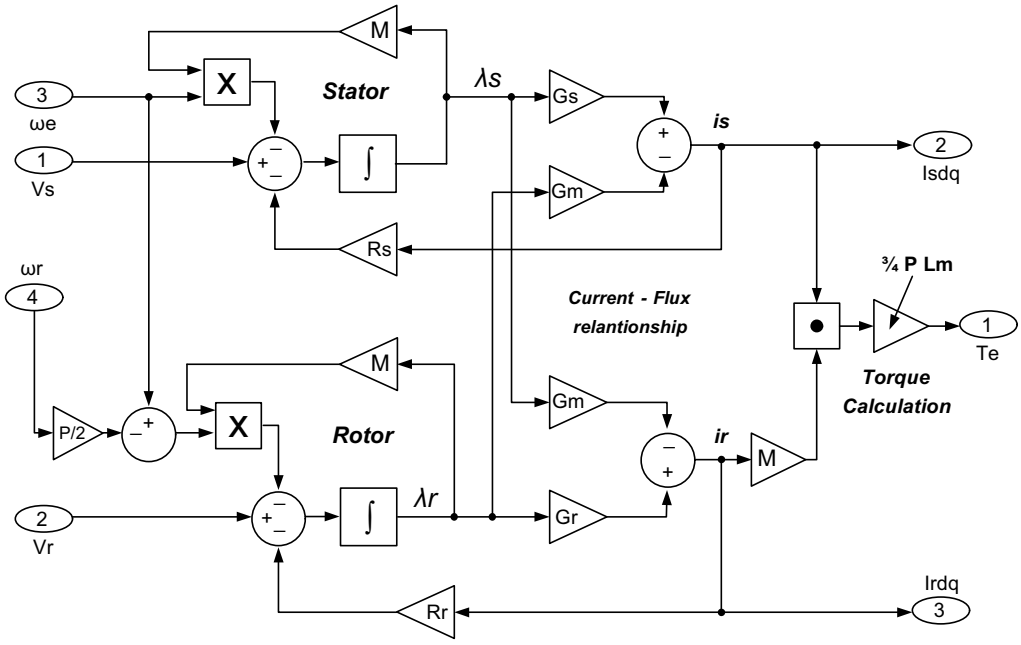

Figure 3.24. Induction motor dq0-based transient model

In order to validate the developed transient model the four different sets of induction motor parameters were taken from [44] and the dynamic behaviour of these motors has been modelled. The investigated sets of motor parameters are given in table 3.7. The resulting torque versus speed load-free starting characteristics are plotted in figure 3.25.

P	V_{rated}	N	T_e	I_{rated}	R_s	X_s	X_m	R_r	X_r	J
hp	V	rpm	Nm	A	Ω	Ω	Ω	Ω	Ω	kgm^2
3	220	1710	11.9	5.8	0.435	0.754	26.13	0.754	0.816	0.089
50	460	1705	198	46.8	0.087	0.302	13.08	0.302	0.228	1.662
500	2300	1773	1980	93.6	0.262	1.206	54.02	1.206	0.187	11.06
2250	2300	1786	8900	421	0.029	0.226	13.04	0.226	0.022	63.87

Table 3.7. Krause induction motor parameters [43]

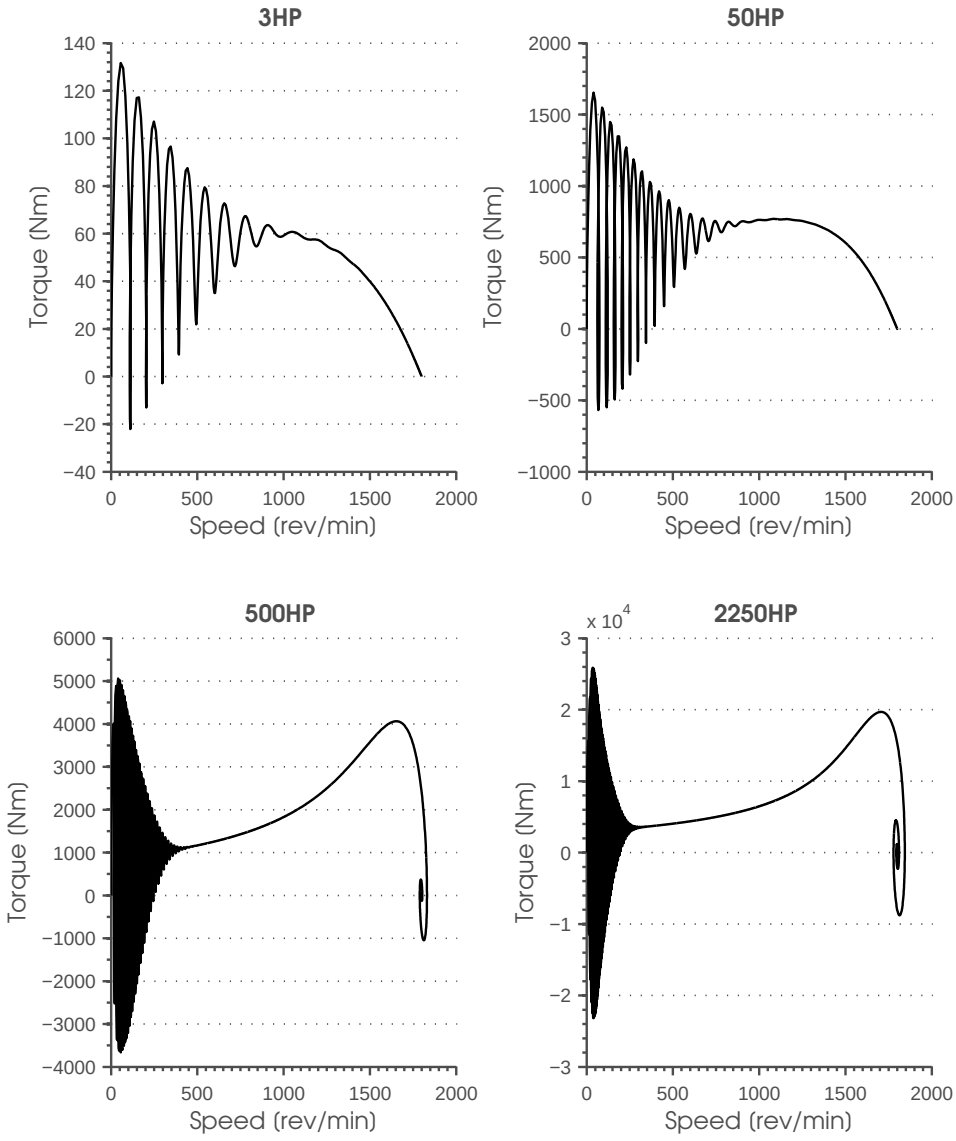

Figure 3.25. Torque versus speed characteristics for Krause motors [43] generated to validate Matlab model

3.4.5 Lowara motor transient characteristics

The Lowara induction motor transient behaviour was modelled according to equations presented in section 3.4.4. In addition, the steady-state behaviour curves were added to show the differences between the steady-state and dynamic models. Using the motor parameters given in table 3.8, a number of characteristics were obtained for different load conditions.

Motor parameters			
Stator resistance	R_s	Ω	0.776
Stator leakage reactance	X_s	Ω	1.779
Rotor resistance	R_r	Ω	0.909
Rotor leakage reactance	X_r	Ω	2.669
Magnetizing reactance	X_m	Ω	93.91
Core losses	R_c	W	429.07
Motor Inertia	J_m	kgm^2	0.019
Load Inertia	J_l	kgm^2	0.020

Table 3.8. Induction motor parameters

The torque versus speed characteristics for both free-acceleration and with load on the shaft are shown in figure 3.26. Along with the transient curve, the steady-state curve was plotted to show the differences between dynamic and steady-state motor behaviour. During load-free spin-up the motor accelerates above synchronous speed but eventually settled down at that speed. The loaded-motor conditions are given with corresponding load characteristics to show the impact of increased load on motor behaviour. The Lowara centrifugal pump and the hydraulic system described in section 5 were modelled as a quadratic type of load. The shape of torque characteristic depends on the motor internal parameters and the motor-load system inertia. During free-spin up the inertia is defined only by the rotor assembly components, so the unloaded motor characteristic has a different shape compared to the loaded cases. The effect of additional load inertia is clearly visible as additional oscillations during motor spin-up.

Since the investigated induction motor was fed from the inverter it is useful to show how the motor torque behaves during start-up under the inverter supply conditions. The same set of motor starting torque characteristics were obtained for motor under the Volts per Hertz supply operation. The resulting characteristics are given in figure 3.27. Because of the current limitation, the developed peak-torque of the motor was reduced for both free-spin and loaded motor conditions, resulting in different shapes of torque-speed characteristics. The load curve was added to show how the motor adapts to changing load conditions. It is clear that the motor produces the torque required for driving the load and rotational losses.

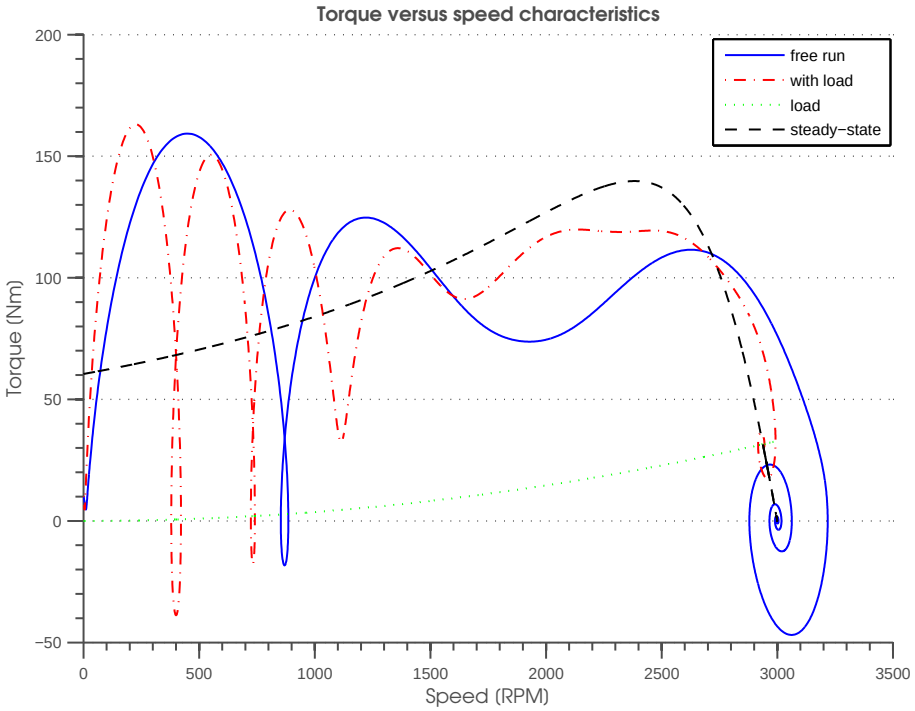

Figure 3.26. Lowara motor torque versus speed characteristics

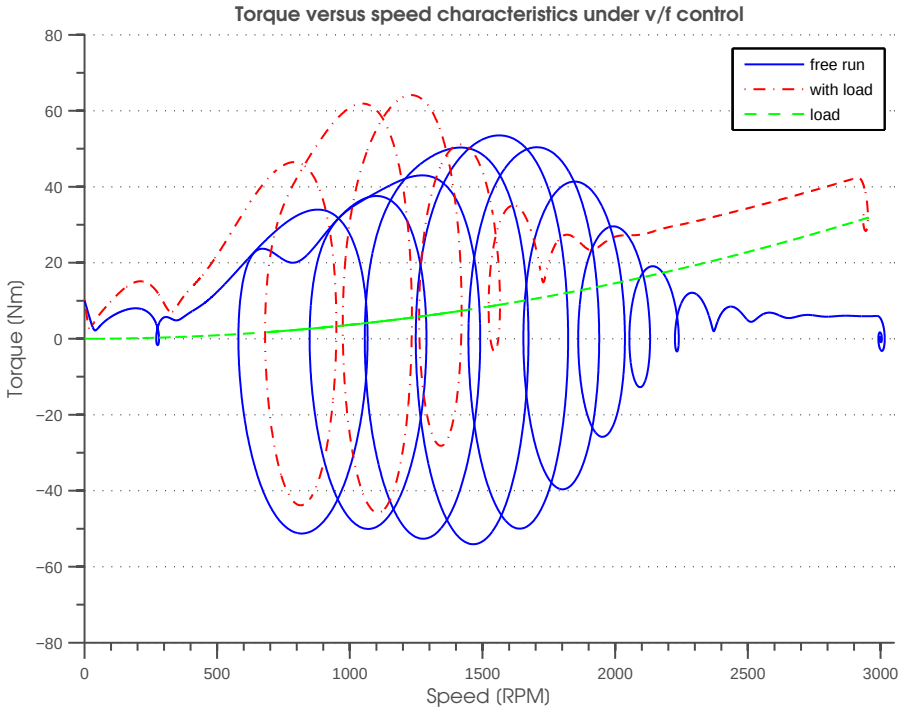

Figure 3.27. Lowara motor torque versus speed characteristics under V/f control

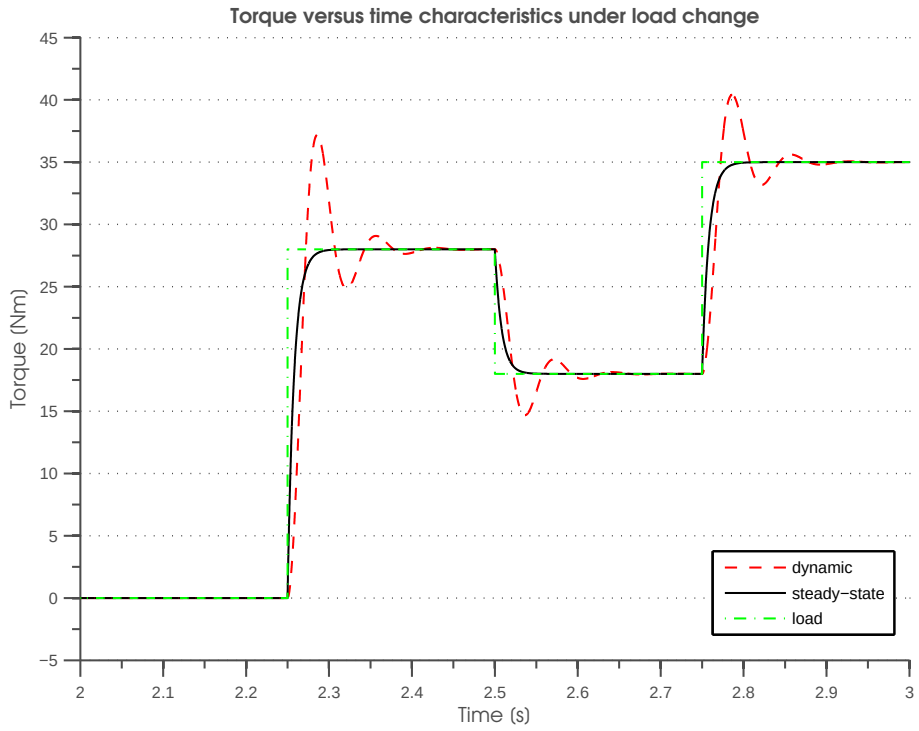

Figure 3.28. Lowara motor torque versus time characteristics under load changes

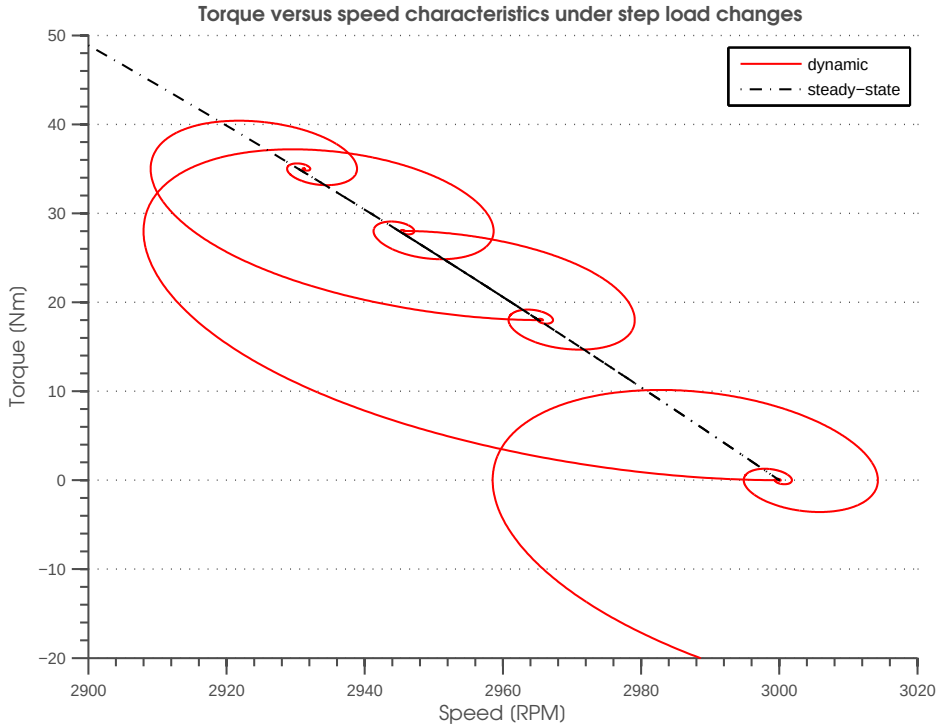

Figure 3.29. Lowara motor torque versus speed characteristics under load changes

In order to investigate motor transient behaviour a step load was applied to the shaft. The motor time responses for both steady-state and transient conditions are shown in figure 3.28. Following the load profile the motor produces the torque required for driving the load. The steady-state and dynamic characteristics are related to each other, to show the motor dynamics. The differences between steady-state and transient conditions are clearly visible.

The torque versus speed behaviour for applied step load changes are given in figure 3.29. Following the load changes the motor torque adapts to the changes by producing transient oscillations and eventually reaches the steady state operating point, which can be predicted using the steady-state model. When a higher torque is applied on the shaft the motor decelerates, whereas during load torque release the motor accelerates above the operating point to release some energy and follows a circular path on the torque-speed graph before reaching the steady-state operating point as in figure 3.29.

3.5 Closure

In order to simulate the complete fuel pump system, detailed knowledge of the steady-state and dynamic behaviour of an induction motor is required to construct a complete model. The modelling methods were discussed in this chapter and the results are validated using data obtained from the developed test rig.

A method of estimating the lumped parameter circuit model for an induction machine is described. The method was applied to the Lowara induction motor which was used in the fuel test rig, and two sets of test data were obtained. The measured data was compared to the values obtained from the manufacturer. The two sets were shown to be in relatively good agreement (max error 12.1%).

A steady-state AC induction motor model was developed using the equivalent circuit lumped-parameter approach. The model can predict torque, current, power components, power factor and efficiency. The model was applied to the motor in the test rig. Using the parameters obtained from the manufacturer and measured on the developed test rig, the motor steady-state characteristics were determined. The simulated results were validated using the data obtained from the induction motor test rig. It was shown that model and the test rig data are in close agreement with error less than 10%. However, it was also noted that model predictions are limited to the linear region of the induction motor characteristics due to the assumptions made, such as lack of saturation in the magnetic circuit and skin effect in windings. The simple torque approximation equation called the Kloss formula was presented and validated with the developed steady-state torque model.

The method of simulating the dynamic behaviour of an induction motor was investigated. Generalised machine theory was applied to analyse the transient behaviour of an AC

induction motor. The transient model of an induction machine developed in an arbitrary rotating reference frame is described. The model was validated using the motor details taken from Krause [43]. The motor's transient characteristics were evaluated and when compared with graphs in [43], show the same graph shapes and similar peak values. Based on the measured parameters the transient torque-speed characteristics of the Lowara motor was developed. The steady-state and dynamic behaviour were compared with experimental results. The model differences are visible but the models seem sufficiently accurate to allow complete fuel system modelling.

It was shown that both the steady-state and transient model predict the behaviour of the investigated induction motor and will therefore be used for more complete modelling of the fuel pump drive system.

Chapter 4

Finite Element Model of an AC Induction Motor

4.1 Introduction

4.1.1 Finite element method

An AC induction motor can be analysed in a number of ways. The modelling technique based on the equivalent circuit presented in chapter 3 is a useful approach for analysing the behaviour under different operating conditions. However, due to the complex and non-linear nature of magnetic circuits in the motor, the accuracy of the predictions obtained is limited.

An alternative to the equivalent circuit approach is the Finite Element Method (FEM) analysis of the magnetic field conditions within the motor. The finite element method is a numerical technique that is widely used to obtain solutions for a wide variety of engineering problems. Although the approach is computationally challenging, it does allow a highly accurate prediction of motor performance to be obtained.

The development of a FEM model of an induction motor requires a knowledge of the machine's geometry and material properties [46]. The stator winding supply variation and the motion of the rotor can be also taken into account. In this way, steady-state and dynamic characteristics can be determined with good accuracy.

4.1.2 MEGA - Finite Element Method Software

To perform the FEM analysis of the Lowara AC induction motor fitted on the fuel system rig, MEGA in-house developed simulation software was used. The MEGA package [47] is a Finite Element Method Software package developed in the Department of Electronic and Electrical Engineering at the University of Bath as part of the on-going research in the field of modelling electromagnetic devices. It is designed to solve a variety of 2D and 3D problems, depending on the type of problem and material/device being modelled.

MEGA is designed to solve low frequency electromagnetic problems, where the displacement currents can be neglected. It is based on the electromagnetic field equations (i.e. Maxwell's equations), which are implemented in MEGA as follows

$$\nabla \times \mathbf{H} = \mathbf{J} \tag{4.1}$$

$$\nabla \times \mathbf{E} + \frac{\partial\, \mathbf{B}}{\partial t} = 0 \tag{4.2}$$

$$\mathbf{J} = \sigma \mathbf{E} \tag{4.3}$$

$$\mathbf{B} = \mathbf{B}\,(\mathbf{H}) \tag{4.4}$$

where σ is the electrical conductivity, **B**, **E**, **H**, **J** are the magnetic field, the electric field, the magnetic field strength and the current density vectors, respectively.

The solution presented in the thesis is based on the magnetic vector potential **A** formulation [46] based on the equation

$$\nabla \times \frac{1}{\mu} \nabla \times \mathbf{A} + \sigma \frac{\partial\, \mathbf{A}}{\partial t} = \mathbf{J} \tag{4.5}$$

When a two-dimensional problem is considered, the formulation (4.5) solves for a single component (in z-axis) of the magnetic vector potential

$$\mathbf{A} = A_z \hat{z} \tag{4.6}$$

then the governing PDE deduced from Maxwell's equations can by expressed as [47]

$$-\nabla \cdot \frac{1}{\mu} \nabla A_z + \sigma \frac{\partial\, A_z}{\partial t} = J_z \tag{4.7}$$

The MEGA package consists of a pre/post processor MEGAVIEW and MEGASOLVE solver. The MEGAVIEW is the interactive environment where the problem formulation, definition and post processing analysis are defined and analysed, whereas the MEGASOLVE uses the described equations to determine a numerical solution for the specified problem.

4.2 Motor Geometries and Model Derivation

In order to characterise the induction motor used in the fuel test rig, a second identical motor was purchased and used in the experimental testing and theoretical analysis.

4.2.1 Motor geometries and material properties

When the motor testing, undertaken for model validation, was completed the motor was disassembled and the motor physical properties determined. The dimensions of the stator and rotor assemblies were determined and used to generate the model mesh. In addition, the motor material properties were identified.

The Lowara induction motor is a 2-pole, three-phase, 11kW induction machine. The motor stator and rotor assembly were previously shown in figure 3.1. The stator has 36 symmetrical slots, with a 10° span, where the three-phase windings are situated. A total of 41 turns sit inside each slot. The windings are arranged in a single layer and three slots are connected in series. Each phase occupies 12 slots, where two parallel paths (per phase) between both ends of the motor are placed. Each path (half-phase winding) has 123 strands of copper wire. The complete geometry of the stator slot is shown in figure 4.1(a).

The rotor cage of the motor consists of active rotor bars and end ring segments where the bars are short-circuited. There are a total of 30 bars on the rotor, with each rotor bar being positioned 12° apart. The rotor bar is a double-cage type NEMA design class C and the rotor dimensions and the whole bar geometry are given in figure 4.1(b). The rotor is made from 0.5mm thick lamination and is 180mm long. The rotor end-rings are 10mm wide with an internal ring radius of 27.36mm and an external ring radius of 56.56mm.

The air-gap was estimated from the stator and rotor radius measurements. The stator external diameter is 200.05mm, whereas the internal stator diameter is 109.982mm. The diameter of the rotor is 109.12mm and the shaft diameter was measured as 44.73mm. The clearance between the rotor and stator was estimated to be 0.431mm around the rotor circumference. The table 4.1 summarises the important dimensions for the motor.

The motor magnetic material properties were determined from visual inspection and assumptions made for this class of motor. The stator and rotor lamination was assumed to be made from the TRANSIL 315 magnetic material and its magnetisation B-H characteristic is plotted in figure 4.2. The stator windings are made from copper and a conductivity of 59.6 MS/m is used in the analysis and the rotor bars are modelled as aluminium alloy LM6 with a conductivity of 21.46 MS/m. The relative permeability of both the stator wiring and the rotor bars was set to 1.

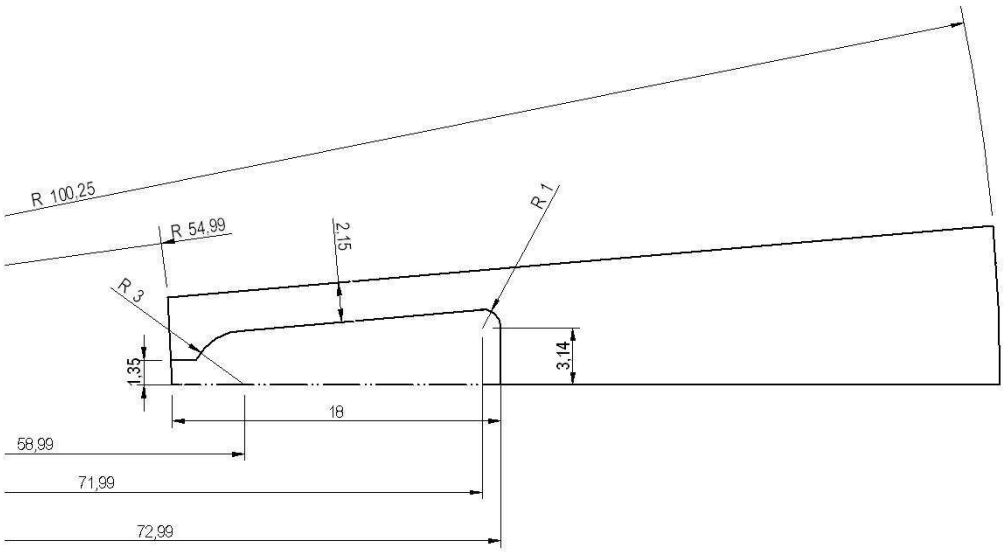

(a) Stator half-slot

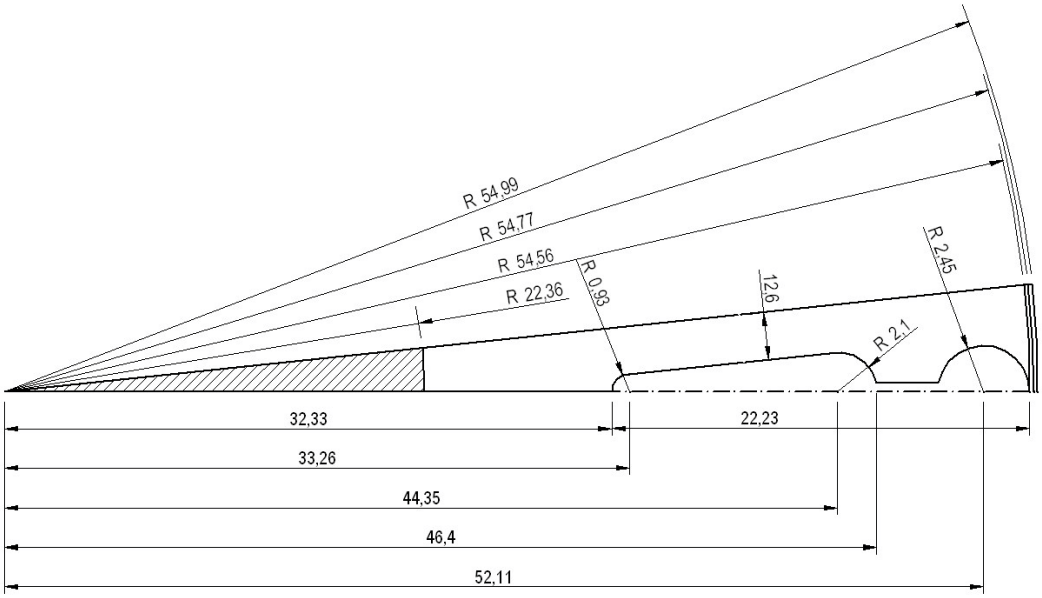

(b) Rotor half-bar

Figure 4.1. Lowara induction motor stator and rotor dimensions

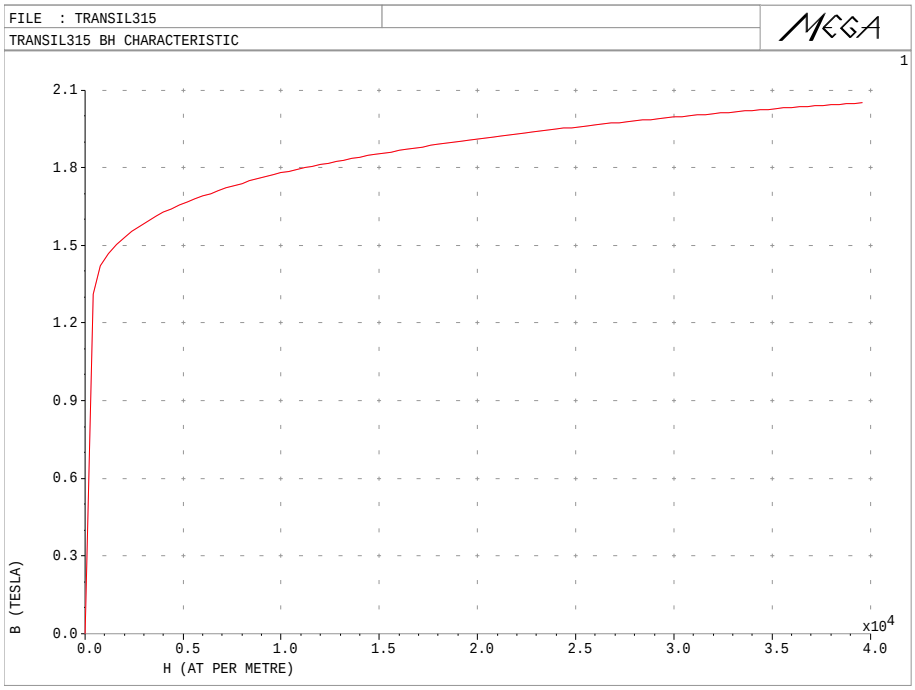

Figure 4.2. B-H characteristic of Lowara motor lamination material - TRANSIL 315

Name	value	unit
shaft diameter	44.730	mm
rotor diameter	109.120	mm
rotor length	180	mm
stator internal diameter	109.982	mm
stator external diameter	200.050	mm
air gap clearance	0.431	mm
number of stator slots	36	-
stator slot angular displacement	10	deg
number of rotor bars	30	-
rotor slot angular displacement	12	deg
rotor end-ring width	10	mm
rotor end-ring external radius	56.560	mm
rotor end-ring internal radius	27.360	mm

Table 4.1. Lowara induction motor dimensions

4.2.2 Mesh generation

The FEM mesh for the motor was developed in MEGAVIEW. This program generates a finite element mesh for the cross sectional geometry of the motor directly from the dimensional data. In order to allow the motor mesh to rotate, the motor was meshed

separately for the stator and rotor assemblies. Stator slot and rotor bar symmetry was used to simplify development of base models for one stator tooth and one rotor bar. These were created, using the measured dimensions given in figure 4.1 and table 4.1. The meshes obtained for the base models are presented in figures 4.3(b) and 4.3(a) for the rotor and stator, respectively.

In the complete motor model, the separately meshed stator and rotor models are joined together using Lagrange multipliers [48, 49]. A magnified cut view of the stator-rotor arrangement in the surroundings of the air-gap is shown in figure 4.3(c), where the geometries of important elements are visible. The air-gap clearance was modelled on both the stator and the rotor meshes as half of the air-gap value for each mesh, and a value of 0.2155mm was used.

The complete MEGA FEM model consists of 85219 nodes, which were used to create 90060 elements and constitutes one two-dimensional (2D) disc/slice of the model. A complete 2D motor mesh is described by 85362 equations and in conjunction with configuration files represents the 2D model used in the analysis. The model is solved as a 2D cartesian problem.

4.2.3 Model configuration

In order to predict the motor behaviour using MEGA, the FEM model of the motor mesh has to be configured, boundary conditions set and all elements assigned to region identifiers (ids), where the actual material characteristics, such as permeability and conductivity, can then be associated with each region id. Each physically distinct material should coincide with a set of elements with a unique region id. The stator is described by 12 coil regions and one lamination region, whereas the rotor is represented by 30 bar regions, the lamination and shaft regions. The air-gap also has its own unique id number.

Boundary conditions have been imposed onto the stationary and the rotating parts of the motor. Since the rotor mesh is rotated with respect to the stator mesh, the magnetic vector potential was set to zero at the stator external diameter, allowing the stator flux tangential conditions to be determined. The magnetic scalar potential was also set to zero at the centre of the rotor in order to prevent flux from flowing into the shaft. Non-linear magnetising B-H curves, as shown in figure 4.2, were used for the stator and the rotor core lamination materials.

As stated earlier, the stator has 36 slots where the three-phase winding is placed. Each phase occupies the 12 slots and it is divided into two six-slot groups (lower-input and upper-output). The input and output groups are further divided into two symmetrical sub-groups. The slot windings within each sub-group are series connected and two parallel paths constitute the complete phase coil arraignment. Therefore, the winding for one phase

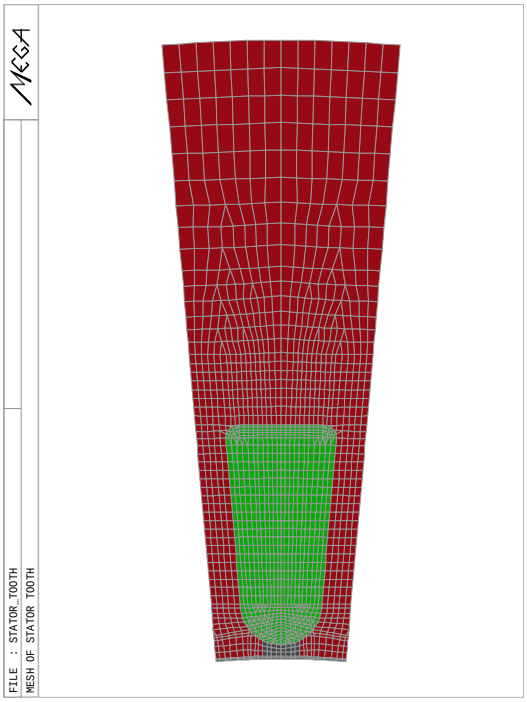

(a) Stator slot mesh

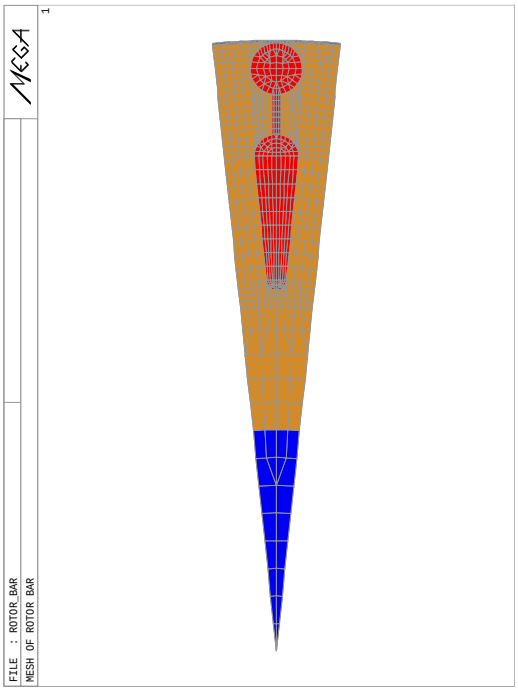

(b) Rotor bar mesh

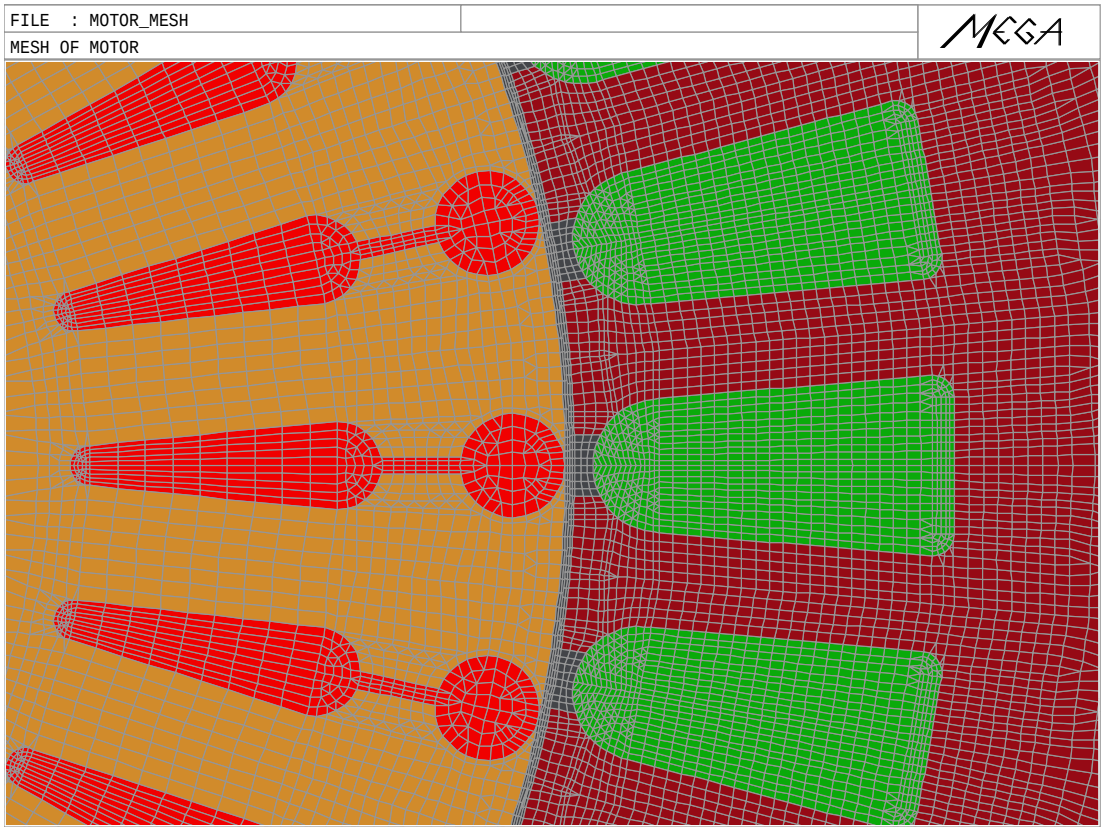

(c) Lowara motor combined mesh - cut view

Figure 4.3. Lowara induction motor FEM meshes

(e.g. R) is described in the FEM model by 4 regions, which were split into 2 parallel paths as shown in figure 4.4. The figure depicts also the one phase slot physical connection with the corresponding slot numbers and region ids. The complete three-phase stator windings

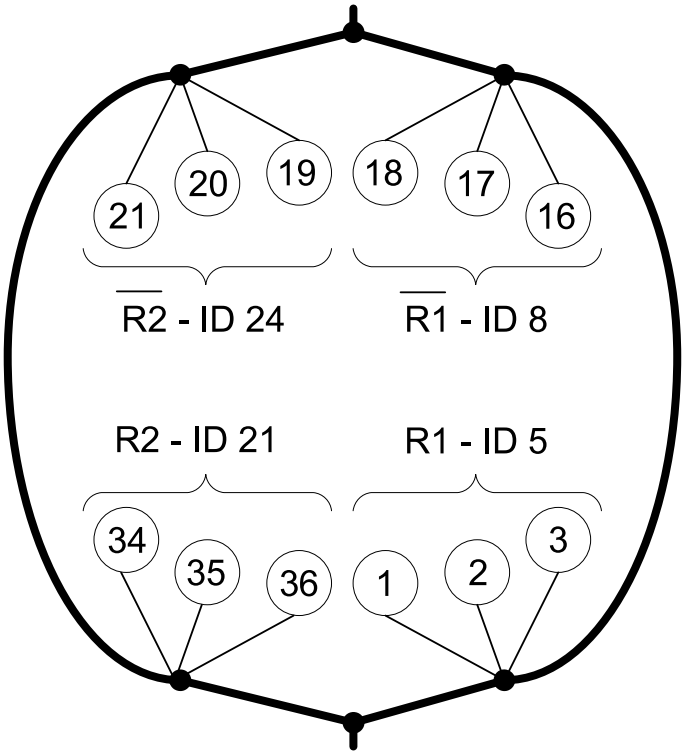

Figure 4.4. Stator phase coil- one phase slot arrangement

slot arrangement with respect to the slot numbers, slot-regions and phase assignments and internal id's connections is given in table 4.2. The stator lamination is described by a separate region to take into account the core properties.

The rotor FEM model was described by 32 regions. Each rotor bar was represented by a unique region label and number to model each bar separately. A similar approach was applied to the rotor core material and shaft. The nonlinear magnetising characteristic (fig. 4.2) was assigned to the rotor lamination id. The shaft was modelled using the carbon steel B-H properties.

In MEGA, all model elements are connected via ports [50, 51]. In this way it was possible to connect the coils to each other and to any external circuit containing resistors, inductors and/or different types of supply sources. A number of ports were created to allow all the regions and the external circuits to be connected. In this way the motor supply and the motor external parameters are connected to the mesh model as described later.

The external supply was connected to the model via stator main phase ports (R,B,Y). The inputs to the model are instantaneous voltages at the input terminals. A per-phase

Slot number	Phase	Region name	Region ID (number)	Region connection
1,2,3	R, R, R	R1	5	$5 \rightarrow 8$
4,5,6	$\overline{\text{B}}, \overline{\text{B}}, \overline{\text{B}}$	$\overline{\text{B1}}$	6	$6 \rightarrow 25$
7,8,9	$\overline{\text{B}}, \overline{\text{B}}, \overline{\text{B}}$	$\overline{\text{B2}}$	22	$22 \rightarrow 9$
10,11,12	Y, Y, Y	Y1	7	$7 \rightarrow 10$
13,14,15	Y, Y, Y	Y2	23	$23 \rightarrow 26$
16,17,18	$\overline{\text{R}}, \overline{\text{R}}, \overline{\text{R}}$	$\overline{\text{R1}}$	8	$8 \rightarrow 5$
19,20,21	$\overline{\text{R}}, \overline{\text{R}}, \overline{\text{R}}$	$\overline{\text{R2}}$	24	$24 \rightarrow 21$
22,23,24	B, B, B	B1	25	$25 \rightarrow 6$
25,26,27	B, B, B	B2	9	$9 \rightarrow 22$
28,29,30	$\overline{\text{Y}}, \overline{\text{Y}}, \overline{\text{Y}}$	$\overline{\text{Y2}}$	26	$26 \rightarrow 23$
31,32,33	$\overline{\text{Y}}, \overline{\text{Y}}, \overline{\text{Y}}$	$\overline{\text{Y1}}$	10	$10 \rightarrow 7$
34,35,36	R, R, R	R2	21	$21 \rightarrow 24$

Table 4.2. Lowara induction motor stator slot arrangement

stator circuit model was created permitting the coils to be connected to the supply source. The model contains the wiring resistance R_s and end-stator leakage reactance L_{le}. The resistance was determined from the DC test described in section 3.2, whereas the end-stator leakage inductance was calculated from an end ring stator model described later. Both external elements are connected to the surrounding elements via ports.

The complete stator phase connection model (e.g. R phase as shown in figure 4.5) was described using the regions and external elements as follows. The external supply is connected to the stator main phase port R, from where the phase is supplied. The external passive elements are connected between the main phase port R and the coil input port LR. The phase resistance R_s is connected between the main port R and internal port RR to where the end-stator leakage inductance L_{le} is also connected. At the far-end L_{le} is connected to the LR port. The second end of the coil mesh is the branch output and depends on the stator winding configuration connected either to ground (G) or the second phase input (B). The regions inside the mesh are connected by the internal ports $R1X$ and $R2X$, one for each path, respectively. The complete stator phase-ports configuration is given in table 4.3. The other phases are modelled in the same way. Since the Lowara motor used in the fuel test rig has the stator windings connected in delta mode, the MEGA model is configured in the same manner. The complete three-phase stator arrangement including regions, ports and external elements connection is shown in figure 4.5.

The squirrel-cage type rotor has 30 axial bars which are short-circuited by end-rings. Each rotor bar was described as a separate region and, as a consequence, the rotor was modelled as the parallel connection of the bars. An external circuit elements were connected to

Input port	Element	Element type	Output port
R	V_s	phase supply	G
R	R_s	resistance	RR
RR	L_{le}	inductance	LR
LR	$R1$	region	R1X
LR	$R2$	region	R2X
R1X	$\overline{R1}$	region	B
R2X	$\overline{R2}$	region	B

Table 4.3. Lowara induction motor stator port arrangement

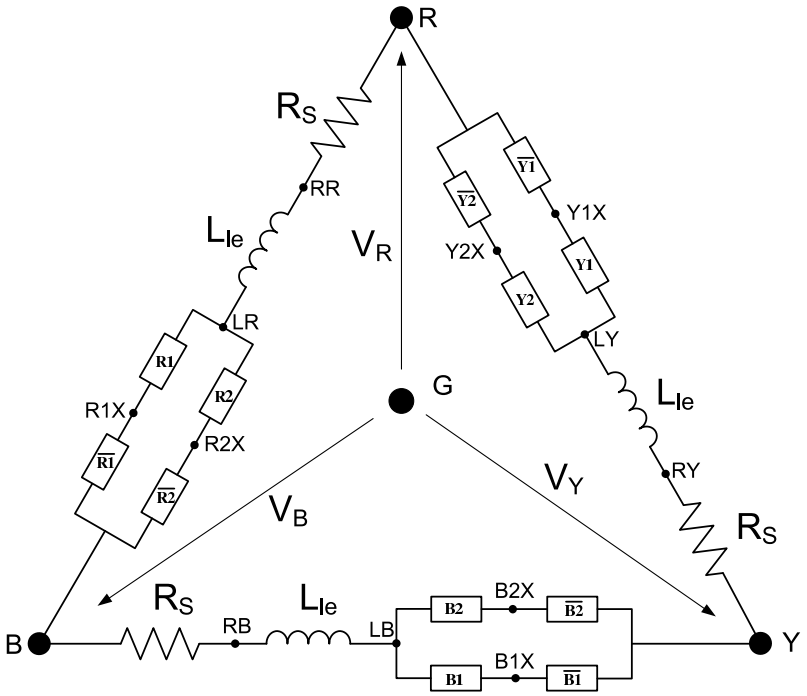

Figure 4.5. Stator FEM model with external circuit configuration

the rotor to model the end-ring properties. The end-ring was modelled as an in-series connection of the resistance R_{rl} and the leakage inductance L_{rl} between the two surrounding rotor bars. The connection of the end-ring elements and the rotor bars was made via ports. The one bar port arrangement is depicted in table 4.4, whereas the complete rotor connection diagram is shown figure 4.6, where the consecutive rotor bars and the end-ring parameters are depicted. Since the rotor model is symmetric only three bars are shown.

Input port	Element	Element type	Output port
P1	BAR1	rotor bar ID	G
P1	R_{rl}	resistance	PR1
PR1	L_{rl}	inductance	P2

Table 4.4. Lowara induction motor rotor port arrangement

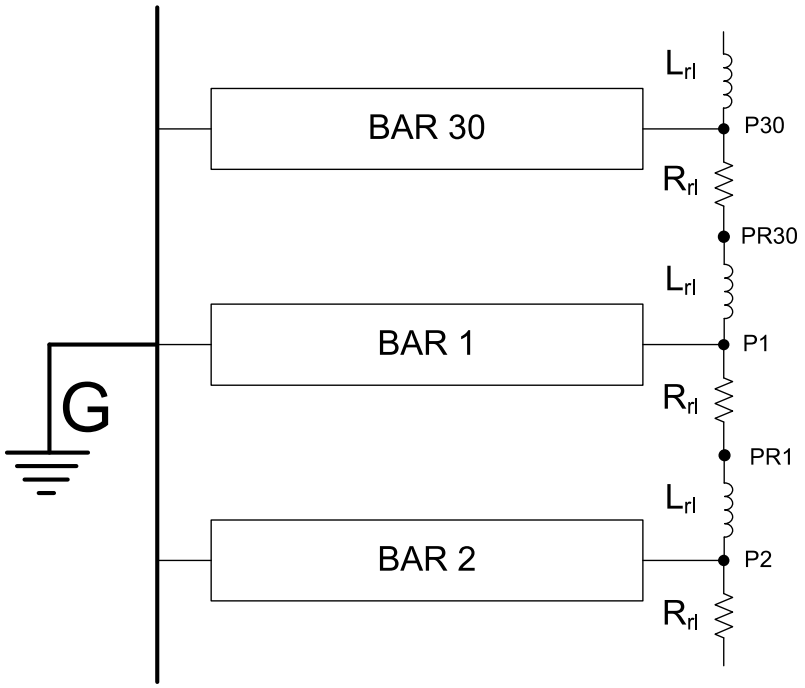

Figure 4.6. Rotor external circuit model

4.2.4 End-motor-model parameter determination

To take into account an induction motor end-effect, which includes the rotor end-ring and end winding impedance, external parameters are used to model this problem [52]. In order to determine the external circuit parameters required by the MEGA software, a separate FEM model of the motor end-side was created. The model is based on the measured Lowara motor geometries. This allows the calculation of the stator end-turn leakage and the rotor end-bar leakage inductances. The model was solved separately for the stator and rotor as an axi-symmetric problem, where the results obtained had a value per circumference. Examples of the resulting flux-line plots obtained for both the stator and rotor solutions are shown in figure 4.7.

A rated current density of 8000A/m^2, at different supply frequencies (0-50Hz), was supplied to the rotor end-bar to obtain the rotor end-ring resistance and leakage inductance. The

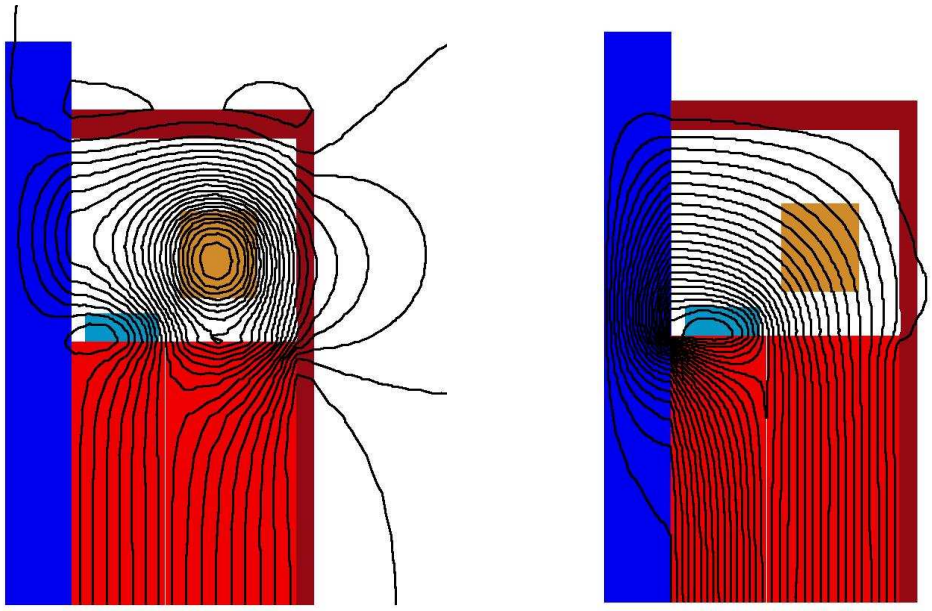

(a) Stator end turn model (b) Rotor end ring model

Figure 4.7. External parameters models

voltage excited on the end-ring was recorded and used for the parameters determination using *Ohm's Law*. Figure 4.8 shows the parameters obtained with changes in the supply frequency.

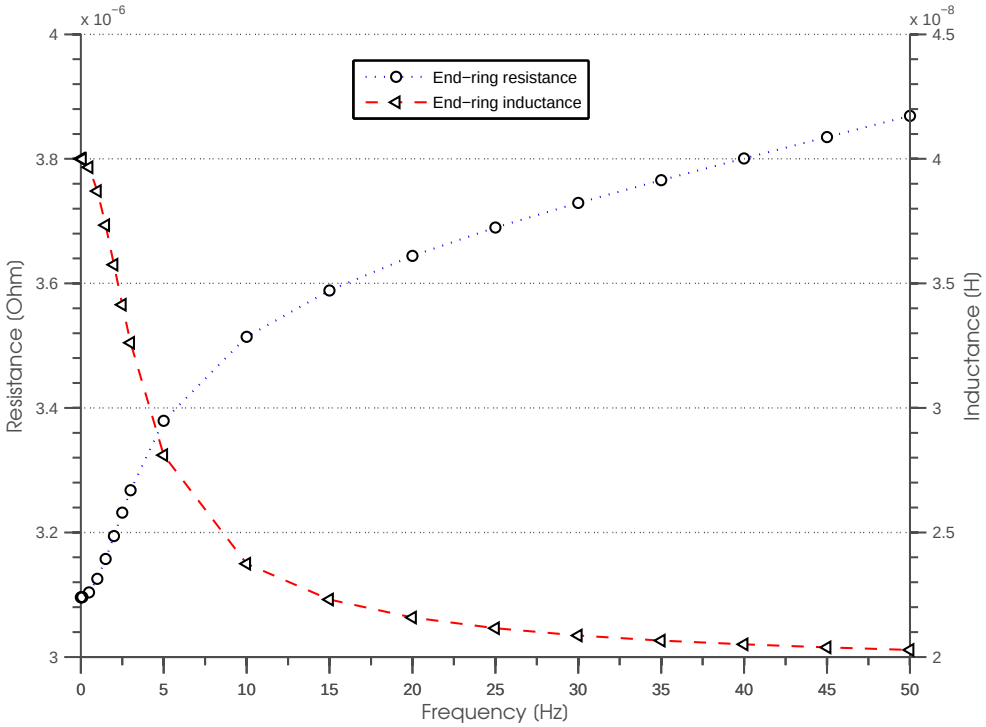

Figure 4.8. End ring rotor parameters

The rotor end-ring resistance was also modelled using an analytical approach, where the resistance was determined from the physical rotor geometries as follows

$$R_{rl} = \frac{1}{30} \frac{(r_1 + r_2)\,\pi\rho}{(r_2 - r_1)\,w} \tag{4.8}$$

The end-ring radii were measured and values of 27.36mm (r_1) and 56.56mm (r_2) used in the calculation. The end-ring width (w) was set to 10mm with an end-ring material resistivity (ρ) of $4.66 \times 10^{-8}\Omega$m, giving a value of $3.02 \times 10^{-6}\Omega$ for R_{rl}. Although the calculated resistance is only an approximation, where the skin effect is neglected, the FEM results show good agreement with the analytical solution values.

For the stator end-turn modelling, a rated current of 22A was supplied to the winding and the reactive voltage measured. The per circumference stator leakage reactance was then found using *Ohm's Law*. The length of windings, which protrude from the stator slots, was determined by measurement. The leakage reactance was calculated using

$$L_{le} = \left(\frac{L_{axi}}{2\pi r}\right) * 2\,(2l_1 + 2l_2 + 2l_3) \tag{4.9}$$

where the length of outside-protruded windings is given as follows: l_1=20cm, l_2=22cm and l_3=24cm. The radius (r) used in the calculation was 73mm, also obtained from measurement. The value obtained for the leakage inductance was 0.0013H, which is used in FEM modelling. The stator wiring resistance was found from the Lowara induction motor parameter determination test and a value of 0.776 Ω is used in the simulation.

The stator and rotor external circuits parameters are presented in table 4.5. For the rotor simulation two sets of parameters are given, since during start-up (locked rotor test) the skin effect impacts on the values and consequently affects motor performance.

Name		value	unit
stator phase resistance	R_s	0.783	Ω
stator end-turn leakage inductance	L_{le}	1.3×10^{-3}	H
rotor end-ring resistance (50Hz)	R_{rl}	3.85×10^{-6}	Ω
rotor end-ring resistance (1Hz)	R_{rl}	3.1×10^{-6}	Ω
rotor end-ring resistance analytical (DC)	R_{rl}	3.02×10^{-6}	Ω
rotor end-ring inductance (50Hz)	L_{rl}	2.05×10^{-8}	H
rotor end-ring inductance (1Hz)	L_{rl}	3.95×10^{-8}	H

Table 4.5. Lowara induction motor FEM external parameters

4.3 Finite Element Model Analysis

Since the FEM model was created in two-dimensions (2D), the predicted electromagnetic field and the model predictions (torque and current) are also two-dimensional.

4.3.1 Flux and flux density of the motor

The 2D FEM model was used to determine the magnetic field density and the flux line distribution in the cross-section of the induction machine. As the non-linear material magnetic property B-H for the laminations are taken into account, realistic magnetic field conditions are obtained. The magnetic field distribution is symmetrical in the case of a healthy squirrel-cage induction machine. The resulting magnetic field density and flux lines, when the motor is stationary under the rated supply conditions, are shown in figure 4.9. It can be seen from this figure that the flux penetrates the rotor surface and, as a consequence, an electromagnetic torque is produced. An extended vector plot of the magnetic field density in the proximity of the rotor bars is depicted in figure 4.10.

From figure 4.9 it is evident that some regions near the stator teeth, and deeper into, the stator and the rotor core, are magnetically saturated. The operating point of the machine is therefore located in the saturated 'knee' part of the B-H characteristic shown in figure 4.2.

4.3.2 Rotor 'skewed' model

Two-dimensional AC analysis of an electromagnetic force was performed for the stationary motor. The torque was determined using the Maxwell stress tensor [47], computed along a line within the air-gap of the motor. It was discovered that the computed force differs with rotor position for the same supply condition, resulting in torque variations with the rotor angular displacement. This cogging torque is likely to be due to the slotting formed in the stator.

AC analysis was performed assuming that the rotor was rotated in clock-wise direction. This allowed the torque to be determined at different rotor positions. The angle of rotor movement was 0.5° (first test) and 1° (second test) and the results are plotted in figure 4.11.

As can be seen from figure 4.11, the torque variations are periodic with a 12° span. Hence, the electromagnetic torque can be approximated by an average value as follows

$$T_e = \frac{1}{N} \sum_{N=\theta}^{12/\theta} T_N \tag{4.10}$$

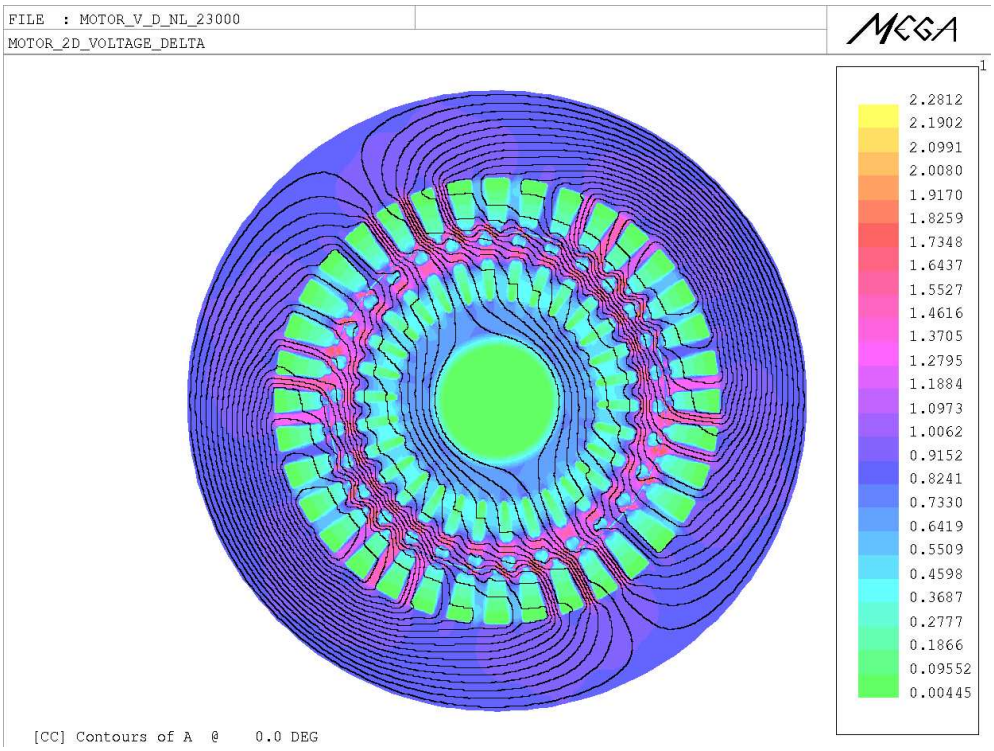

Figure 4.9. Magnetic field density and flux line distribution in Lowara induction motor at standstill

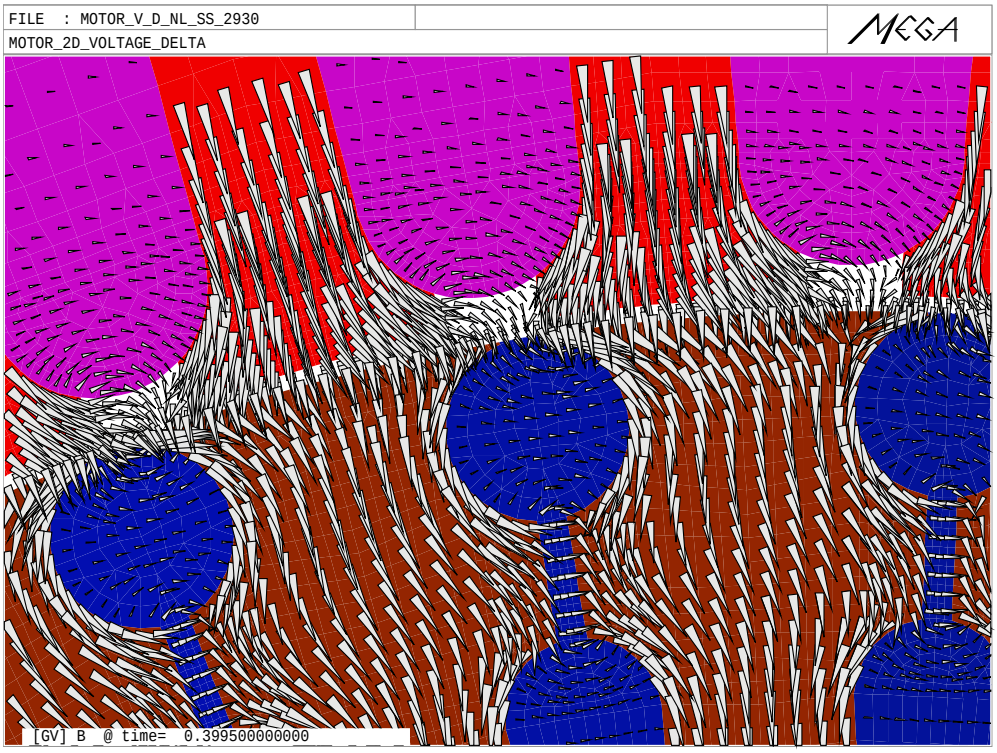

Figure 4.10. Magnetic field vector distribution

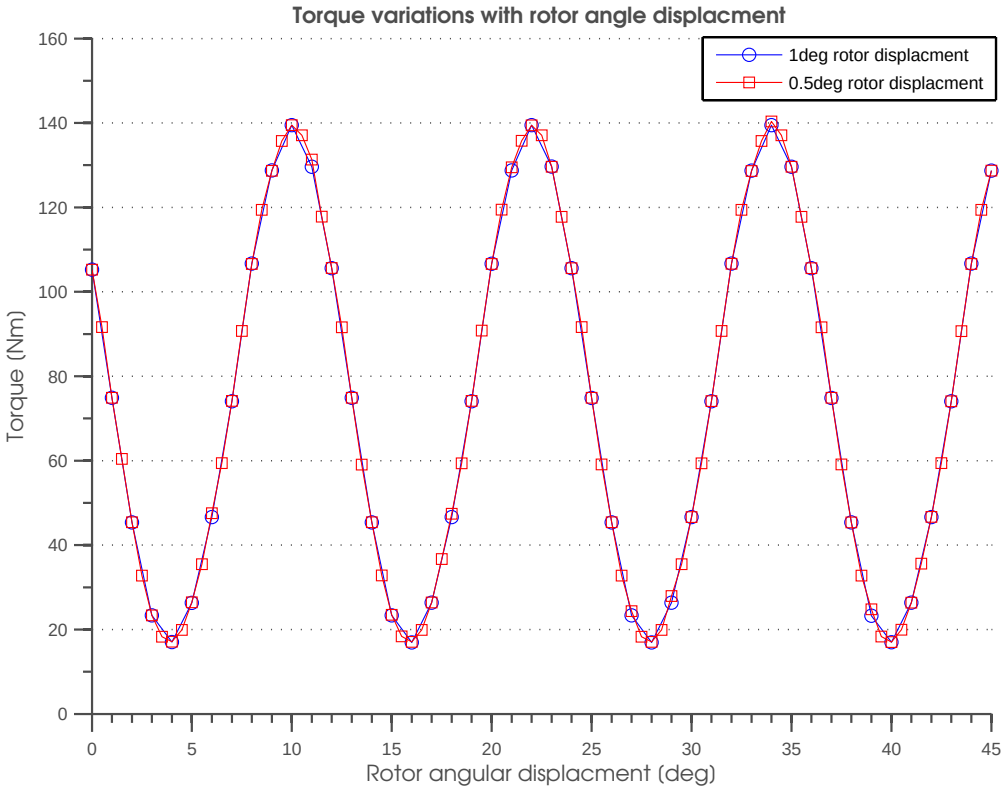

Figure 4.11. Torque variation with rotor angle of the Lowara induction motor

Owing to the fact that the 2D FEM model cannot predict accurately torque and current, a 2D multi-slice FEM model ($2\,^1/_2\,\mathrm{D}$) was created [52, 53] . As a consequence, this allowed a 'skewed' rotor model to be developed. This method assumes that a motor is modelled by a certain number of cross sections N, at different positions along the shaft. Each cross-section is displaced θ° and the windings are segmented into elementary conductors associated with the slices. Therefore, the rotor bars that appear in each of the slices are replaced with 'stepwise' skewed bars. The multi-section method, also known as the $2\,^1/_2\,\mathrm{D}$ model, consists of replacing a full 3D analysis by a number of 2D analysis. The greater the number of cross-sections, the higher the model accuracy, although the resulting increase in the CPU run time is a significant drawback. The 2D slices are not magnetically connected so the model only provides an approximation to the 3D model. The other disadvantage of this approach is that, when the machine is voltage supplied, it is necessary to solve different problems (one for each cross-section) simultaneously due to the fact that the current is the same in all the sections.

Taking into account the calculation time and the accuracy of the solution the 4-slice $2\,^1/_2\,\mathrm{D}$ FEM model, with 12° rotor bar pitch where each slice cross-sections is 4° angle-displaced, was developed and used in the Lowara motor analysis. The developed $2\,^1/_2\,\mathrm{D}$ model for 4 slices is presented in figure 4.12.

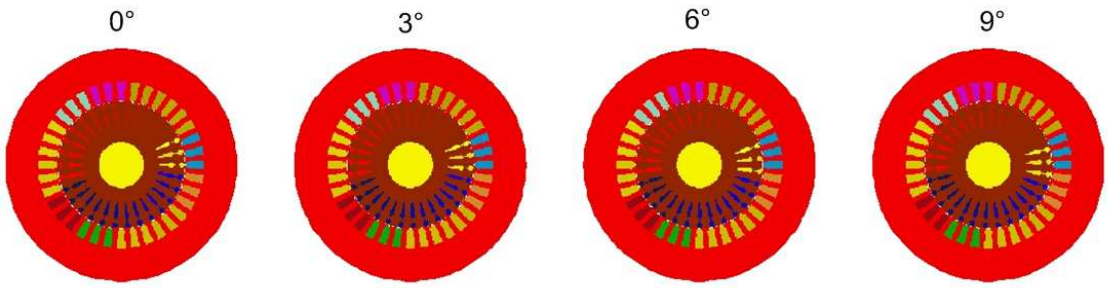

Figure 4.12. Multislice model of the Lowara induction motor

Since the Maxwell stress on each surface has different values, the total torque in the $2\,^1/_2$ D model is calculated using a value at each slice, where the rotor position is displaced by θ° and the torque is calculated from equation 4.11 as the sum of the torques at each slice. The current is the same in each slice since the same voltage is applied to each cross-section model.

$$T_e = \sum_{N=0}^{12/\theta} T_N \tag{4.11}$$

A full 3D model of Lowara induction motor was also created in MEGA. A number of cross-sections (slices) were joined together in the z-axis, allowing the model to be magnetically connected. However, due to the model complexity and consequently very long simulation times, the 3D model was not considered to be a practical solution. Hence the $2\,^1/_2$ D model was used, as this allows an approximate solution to the complex 3D model.

4.3.3 Locked rotor analysis

The steady state behaviour of the Lowara induction motor was investigated using MEGA. Based on the $2\,^1/_2$ D , model the locked rotor characteristics were determined. The locked rotor tests were conducted as a steady-state AC problem where the rotor was prevented from movement. A set of external parameters, obtained from a 50Hz supply condition, was used in the blocked rotor predictions of the motor.

The simulations were conducted at different supply conditions, where the supply voltage was changed from 0 to the full rated 400V line voltage. Both the starting current and torque were recorded during the voltage changes. The torque obtained from the simulations was calculated using equation 4.11, since all the slices have different values.

The locked rotor results are shown in figure 4.13 along with the data obtained from the test rig. The Simulink model predictions are also presented to allow model comparisons. It is evident that both the simulated results deviate slightly from the measured data. From

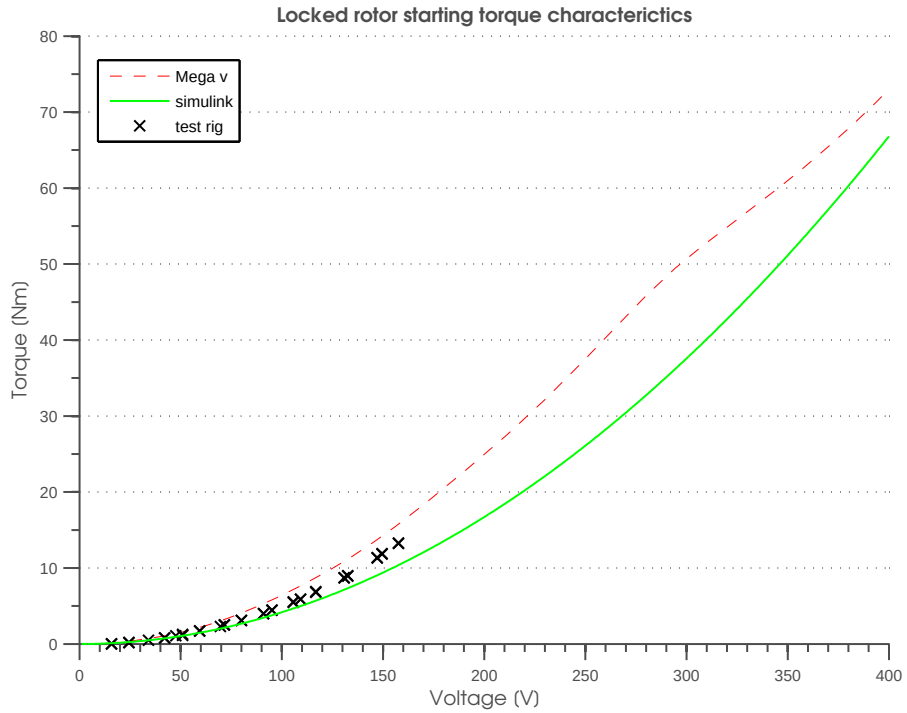

Figure 4.13. Starting torque versus supply voltage for the locked rotor condition

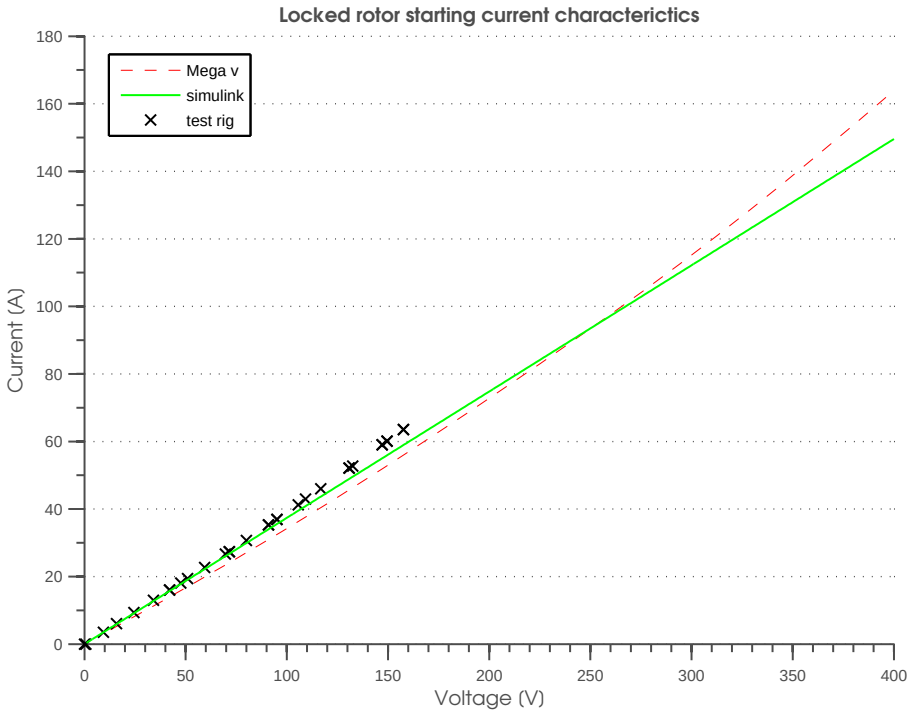

Figure 4.14. Starting current versus supply voltage for the locked rotor condition

the MEGA model, magnetic saturation is visible. Above a voltage of 280V, the torque is affected by motor-iron saturation. The starting torque at the rated motor voltage is around 73Nm from the MEGA model, whereas the Simulink prediction is about 67Nm for the same supply condition. Both simulated data is close to the test rig results, which were performed only for limited range of supply voltage, due to starting current limitations.

Similar to the torque, the starting current was also investigated and the results obtained are shown in figure 4.14. The starting current is plotted versus supply voltage at the rated supply frequency of 50Hz. The MEGA model shows some current-voltage non-linearity, which is not visible in Simulink predictions, due to the lack of magnetic saturation and skin effect modelling in the Simulink. The test rig data, obtained for limited range up to 60A, shows relatively good agreement (error < 10%) with both simulated results. For the rated voltage (400V) the predicted starting current for the MEGA model is 163A, whereas from the Simulink model 150A is obtained, resulting in 8% error.

4.3.4 Steady state analysis

Steady-state analysis was performed using the $2^1/_2$ D FEM model. The steady-state torque versus speed and the current versus speed characteristics were evaluated as a transient problem, at constant rotor speeds. The time step was set to 0.5ms and 400 steps were simulated. Examples of the MEGA torque versus time plots for different operating speeds at the rated supply condition are shown in figure 4.15.

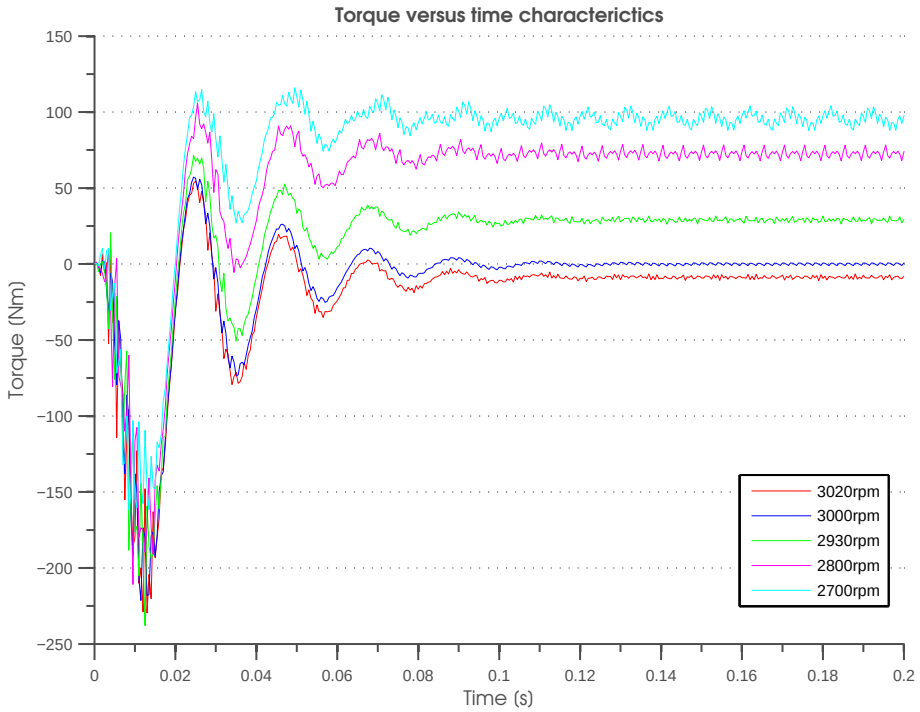

Figure 4.15. Torque versus time during constant-speed time-step simulations used to determine steady-state torque

The steady-state torque versus speed characteristics were evaluated for a number of operating speeds as shown in figure 4.16. The test rig results and the steady-state prediction from Simulink model are included along with the MEGA data. The characteristics obtained have slightly different shapes over the speed range, due to the different assumptions made in modelling. The MEGA model predicts higher starting torque (17% error) and lower breakdown torque (7% error). Nonetheless the difference over whole range of speed is less than 15Nm. However, in the linear region where the motor normally operates the both predicted data shows good correlation with the experimental results. The shape difference is likely due to the parameters used in the models, since both models used externally evaluated variables for internal calculations. It is thought that the MEGA model better predicts the motor behaviour, since saturation and skin effect are taken into account. However it is limited by the $2\,^1/_2\,\mathrm{D}$ approximation.

The steady-state current variations with speed were also investigated and the results obtained are presented in figure 4.17. As with the torque graph, the test rig and Simulink model data are also included on this figure. The current-speed graphs show slight shape differences and the MEGA model predicts a higher starting current. Although the results show slight differences, the linear region prediction for both the developed models agree well with the data obtained from the test rig.

4.3.5 Transient analysis

In order to evaluate the transient characteristics of the Lowara motor the time-stepping method was used. This requires the simulation of the rotation of the rotor, in which the rotor rotation is modelled as an angular movement through a couple of degrees at each time step using the $2\,^1/_2\,\mathrm{D}$ FEM model. The transient $2\,^1/_2\,\mathrm{D}$ FEM model was set up, with the time step set to 0.5ms and simulations were made at 500 steps, resulting in a total simulation time of 0.25s.

The MEGA simulation for a free-run test was also performed. In this case, the motor was accelerated without load and the torque-speed characteristic obtained. The MEGA transient torque prediction is shown and compared with the Simulink results in figure 4.18. It is evident that both the developed models show similar shape patterns, although the peak values are different. It is thought that the differences are due to the assumptions made in the Simulink model and inaccuracies of the material properties in the MEGA model. In addition, the MEGA model is based only on a two-dimensional approximation, which may result in an additional error in torque predictions.

The transient behaviour when the motor is loaded has also been investigated using the $2\,^1/_2\,\mathrm{D}$ model. In this case the load was simulated as a simple square-law characteristic having a 40Nm peak torque at 3000rpm. The MEGA and Simulink transient predictions obtained at this condition are shown in figure 4.19. In a similar way to the free-run test, the results differ due to the limitations associated with the modelling techniques.

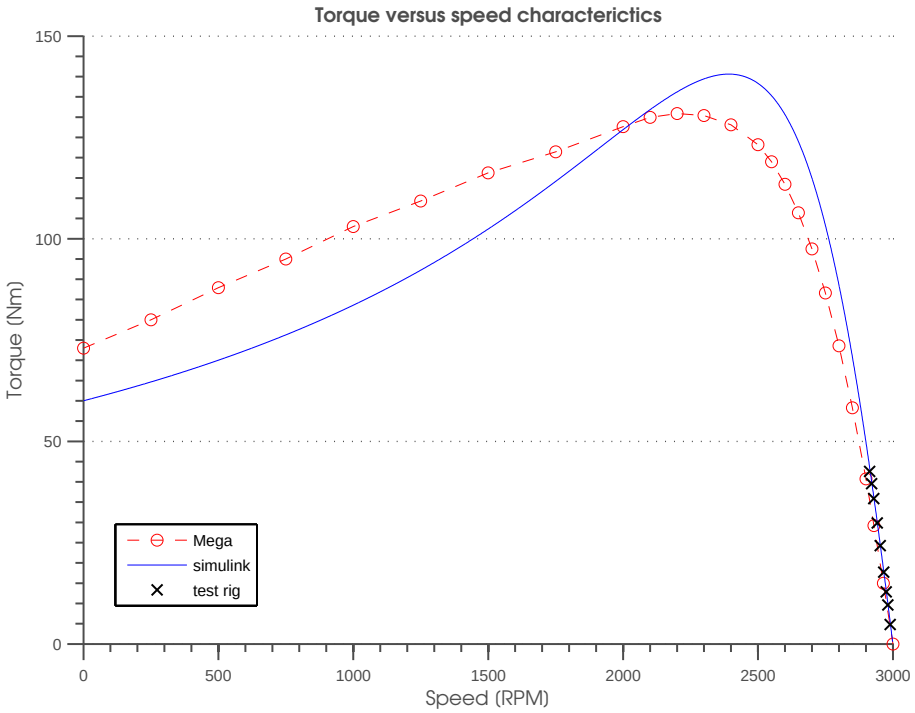

Figure 4.16. Steady state torque versus operating speed characteristics

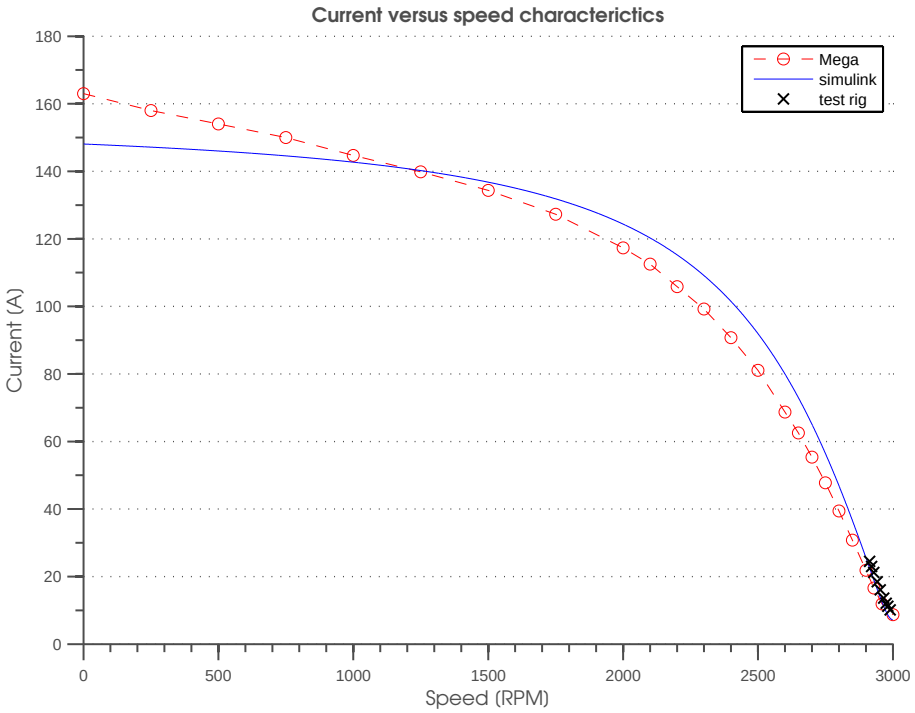

Figure 4.17. Steady state current versus operating speed characteristics

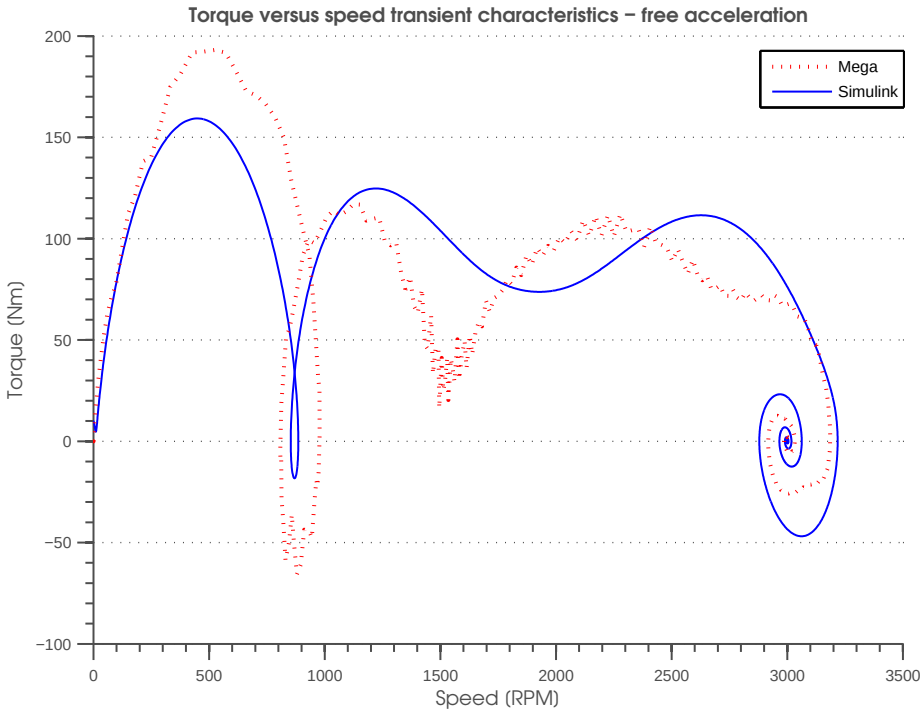

Figure 4.18. Torque versus speed characteristics during free acceleration

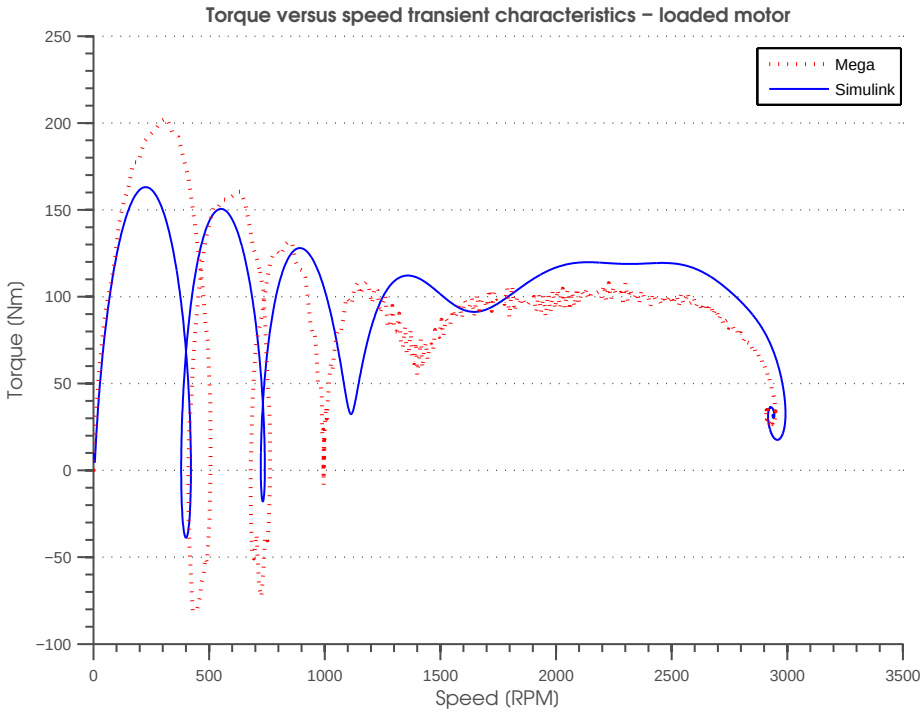

Figure 4.19. Torque versus speed characteristics during free acceleration when the motor is loaded

4.4 Closure

A Finite Element Model analysis was used to model an AC induction motor. Based on the measurements taken from a Lowara induction motor, meshes for the stator and rotor were created and joined together. The complete motor cross-section was configured and used in conjunction with the physical material properties of the motor to form a two-dimensional model of the motor. Due to torque variations with angular displacement, the 2D model was found to be insufficient to simulate the complete motor. Therefore the $2\,^1/_2\,$D version was created, where four slices were joined together and configured to obtain an approximation to a full 3D model.

In order to determine the external parameters required for the MEGA software, a FEM motor-end model was developed. This allowed the external parameters both for the locked rotor and the rated motor conditions to be determined. The steady-state motor characteristics were predicted using the $2\,^1/_2\,$D model and the results compared with the Simulink predictions and experimental data. The locked rotor characteristics of the starting current and torque at the rated conditions were determined and the data obtained from the MEGA model shows acceptable correlation with the Simulink predictions and the rig results. The steady-state torque and current versus operating speed were also determined. Although the results obtained from MEGA differ slightly from the Simulink data, relatively close agreement was obtained in the normal operating low-slip linear region when compared with the experimental results.

The transient characteristics of Lowara motor were also investigated. A free-running motor test was performed and the torque-speed characteristics obtained were compared with the Simulink predictions, showing that both characteristics show similar variation but have different peak values. The motor acceleration from standstill with a load connected to the shaft was predicted. The results were compared with the Simulink counterpart and, similar to the free-run test, the shapes are comparable although the amplitudes are slightly different. Both transient models reach the same steady state operating points, resulting in good agreement in the linear region.

The steady-state and transient characteristics of both the MEGA and Simulink models were compared. The results differ slightly although both models provide good predictions for the Lowara motor behaviour in the linear region. It is difficult to say which transient characteristic is correct, since transient experimental validation were not undertaken, due to safety constraints. The MEGA model is based on the real motor geometry, but the materials from which the motor is made are based on assumptions and estimations. Therefore a performance error can be introduced, since the induction motor is very sensitive to parameter changes. Although the MEGA results can be very helpful, when proper motor geometry and material data is used, it is difficult to incorporate the model into the complete fuel test rig model. Therefore, the results are used as alternative valida-

tion approach that have been used in the complete test rig model modelling. The second very important shortcoming is that the MEGA model implementation and development is very time-consuming, requiring relatively good FEM expertise to obtain a complete set of motor characteristics.

Chapter 5

Mathematical Models for the Hydraulic System Components

This chapter covers the hydraulic modelling of the components present in the fuel test rig. The modelling techniques used to analyse steady-state and dynamic behaviour are described. Components simulations were undertaken using Matlab/Simulink general-purpose software package and the in-house Bath*fp* hydraulic-pneumatic orientated software.

5.1 Introduction

An aircraft fuel system is a complex long-pipe system where the fuel is transferred between the tanks by means of transfer pumps. The aircraft fuel, like all fluids, is subject to the laws of mechanics. In fluid mechanics the state of fluid may be described by its density ρ, energy and velocity v at every point in space. Associated with these parameters are the following three main independent dynamical laws in continuum fluid mechanics:

- Conservation of Momentum
- Conservation of Energy - Bernoulli's Equation
- Conservation of Mass - The Equation of Continuity

5.1.1 Conservation of Momentum

The *Conservation of Momentum Law* [54] states that the time rate of change of momentum of a system is equal to the sum of external forces acting on that body.

$$\sum F = \frac{\delta}{\delta t}(mv) \tag{5.1}$$

where the fluid velocity can be determined from the volumetric flow rate Q and cross sectional flow area A.

$$v = \frac{Q}{A} \tag{5.2}$$

When fluid flows through a pipeline a force is exerted on it. This force, acting on the fluid in motion, can be split into gravity, pressure and surface stresses forces. A fluid will exert a normal force on any boundary it is in contact with. That force, which acts on a surrounding surface, is called pressure and is defined as

$$p = \frac{\delta F}{\delta A} \tag{5.3}$$

In a fluid the pressure acts equally in all directions. The fluid in motion overcomes the internal force which can be characterised as the shear required to drag one layer of fluid past another a unit distance away with unit velocity in laminar flow. This surface stress force (shear force) τ_f can be defined as the product of the dynamic viscosity coefficient μ and the velocity gradient v in a direction l perpendicular to the direction of flow as

$$\tau_f = \mu \frac{\delta v}{\delta l} \tag{5.4}$$

The dynamic viscosity μ is the property of a fluid describing the cohesion and interaction between molecules within the fluid resisting shear deformation.

The kinematic viscosity ν is introduced to relate the viscous property of the fluid with the mass and is defined as the ratio of dynamic viscosity to mass density [55].

$$\nu = \frac{\mu}{\rho} \tag{5.5}$$

Kinematic viscosity is a measure of the resistive flow of a fluid under the influence of gravity.

5.1.2 Conservation of Energy - Bernoulli's Equation

The *Conservation of Energy Law* [56] states that in an isolated system the total energy must be constant. As a consequence, energy is not permitted to enter or leave the closed system. In fluid mechanics the energy law is governed by the *Bernoulli Equation* [56].

In the fluid, subjected to steady motion, the energy is defined as potential, kinetic and pressure energy.

For a non-viscous, non-turbulent, perfect, incompressible fluid in steady flow, the sum of the mechanical energy in a fluid along a streamline is the same at all points on that streamline.

$$\frac{v^2}{2} + gh + \frac{p}{\rho} = Constant \tag{5.6}$$

where v is the fluid flow velocity at a point on a streamline, g is the acceleration due to gravity, p is the pressure at the elevation point h, and ρ is the density of the fluid. As a consequence, changes in fluid velocity produce the changes in pressure and potential energy. Assuming that a system is stationary and there are no changes in gravitational forces, the total pressure within the system is constant

$$\frac{1}{2}\rho v^2 + p = constant \tag{5.7}$$

where p is the static pressure.

5.1.3 Conservation of Mass - The Equation of Continuity

The *Conservation of Mass Law* [56] states that the amount of fluid per unit time, called the mass flow rate, is conserved within a control volume when the fluid density is constant. Thus, the total mass entering the control volume is the sum of the total mass exiting the control volume and the mass accumulating within the volume

$$\rho\, \delta A\, v = \frac{dm}{dt} = constant \tag{5.8}$$

To describe the mass property of the fluid within a volume, the mass density is defined as the mass of substance per unit volume.

$$\rho = \frac{m}{V} \tag{5.9}$$

If the fluid in the system is incompressible (ρ is constant) then the volume flow rate Q defined as

$$Q = v\, \delta A \tag{5.10}$$

For a single inlet and outlet pipe, in steady state,

$$Q_{in} = Q_{out} \tag{5.11}$$

where the indices *in* and *out* mean input and output to the system, respectively.

5.1.4 Reynolds Number

The flow in a pipeline is dependent on the flow regime. The type of flow depends upon the flow rate as well as the type of fluid and can be laminar, turbulent and transitional between the two. To determine the type of flow a non-dimensional ratio called Reynolds Number *Re* is used, where

$$Re = \frac{(velocity, v)\ d}{(kinematic\ viscosity, \nu)} \tag{5.12}$$

and is a measure of the ratio of inertial and viscous forces. Viscous stresses within a fluid tend to stabilise and organise the flow, whereas excessive fluid inertia tends to disrupt the organised flow leading to chaotic turbulent behaviour. Flow patterns can be characterised as

- laminar: Re < 2300
- turbulent: Re > 4000
- transition: $2300 <$ Re < 4000

Laminar flow refers to smooth continuous flow in which a fluid flows in parallel layers. Turbulent flow is a fluid regime characterised by chaotic, stochastic property changes with rapid variations in pressure and velocity in space and time. In the transition between the laminar and turbulent regimes, the flow is characterised by both regimes and it is possible to find sub-regions of both flow types within a given flow field.

5.2 Pipeline mathematical models

5.2.1 Lumped Parameter and Finite Element Distributed Pipe Models

Hydraulic pipelines store energy which can be divided into motion (kinetic) and strain (elastic deformation) energy. Kinetic energy is dissipated as heat through viscous friction, which is lost within the system. The losses caused by the fluid motion are fluid velocity dependent. The velocity of fluid flowing in a pipe varies with radial and longitudinal position and depends on the fluid properties, the velocity of the flow, the geometry and the surface roughness of the pipe.

An important factor when analysing a pipeline is fluid inertia. In a long pipe, where the volume can be significant, the fluid inertance can change or even determine system conditions. One way to analyse a fluid system is to express it in terms of its electrical counterpart. Since both systems have distinct behaviour similarities, it is possible to describe the fluid system using a direct analogy with a low-frequency electrical circuit. The analogy between fluid and electrical parameters is presented in table 5.1.

Electrical system	Hydraulic system
Voltage	Pressure
Current	Flow rate
Resistance	Friction
Inductance	Fluid Inertance
Capacitance	Fluid Compressibility

Table 5.1. Hydraulic-electric systems analogy

The hydraulic pipeline model can be expressed mathematically as

$$\frac{\delta p}{\delta t} = RQ|Q| + \int \left(\frac{Q_{out} - Q_{in}}{C}\right)\delta t + L\frac{\delta Q}{\delta t} \tag{5.13}$$

where R, L and C parameters are described in later subsections.

Hydraulic pipelines are inherently distributed parameter elements. Since the fluid pipework is often complex, it is convenient to represent the system using a lumped parameter model. In this case, the pipeline system is represented using capacitance, resistance and inertance terms as shown in figure 5.1. The pressure losses introduced by additional components, such as fittings, elbows, bends, etc can be accounted for using an equivalent pipe length.

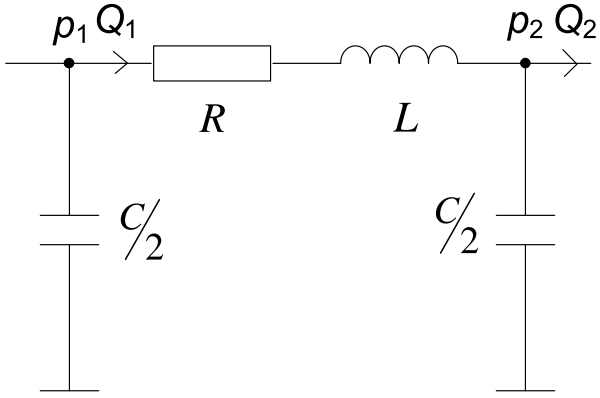

Figure 5.1. Single lumped parameter pipe model

A finite element distributed pipe model can be produced by connecting a number of lumped parameter elements in series as shown in figure 5.2. The higher the number of elements used, the closer the model becomes to its distributed parameter counterpart.

The nodes, to which constant volume blocks are connected, are assigned names $N_1, N_2, , N_n$ where n is the number of segments. The nodes represent energy interactions at the corre-

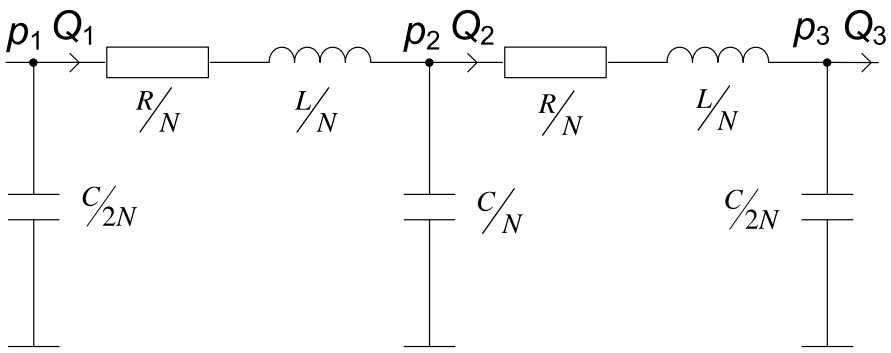

Figure 5.2. Pipe lumped parameter model

sponding inlets of the real pipe element. Pressures at the nodes $p_1, p_2, , p_n$ are assumed to be equal to average pressure of the element.

The following subsections describe the approach used to model the pipeline, which is based on the outline in [57].

5.2.2 Fluid Resistance

When fluid flows through a pipe a pressure loss will be generated. The pressure-flow relationship describing the resistive characteristic of this phenomena can be expressed by the ideal fluid resistor relationship

$$p(t) = R\,|Q(t)|\,Q(t) \tag{5.14}$$

where R is the pipework resistance.

This resistance is usually known as pipe friction and is caused by viscous shear stresses within the liquid and the turbulence that occurs along the internal walls of the pipe, created by the roughness of the pipe material. The pressure drop due to friction in a long smooth pipe is a function of the average flow velocity, fluid density and viscosity, pipe length and diameter.

The relationship for the frictional resistance in a pipeline can be determined using the *Darcy-Weinsbach* equation [56] which provides a measure of the head loss of the fluid as an equivalent resistance as shown in equation (5.15). Thus the term head loss is also used to express the resistance to flow.

$$h_f = f\frac{l}{d}\frac{v^2}{2g} \tag{5.15}$$

where f is a friction factor described later. The pipe-head loss can also be expressed as

$$h_f = \frac{\delta p}{\rho g} \tag{5.16}$$

Substituting (5.16) to (5.15) allows the pipeline pressure loss to be expressed in terms of the pipeline dimensions and fluid properties as follows

$$\delta p = f \frac{l}{d} \rho \frac{v^2}{2} \tag{5.17}$$

Since the volumetric flow rate Q, in circular pipes, can be expressed in terms of the fluid velocity (5.2), the pressure losses can written in terms of volumetric flow rate as

$$\delta p = f l \rho \frac{8Q^2}{\pi^2 d^5} \tag{5.18}$$

The friction factor and the pipeline system behaviour depends on the flow regime determined by Reynolds Number. The friction factor can be determined graphically using a Moody diagram. Using this approach, the friction factor can be determined for different pipe internal roughness ϵ/d at a particular value of Reynolds number.

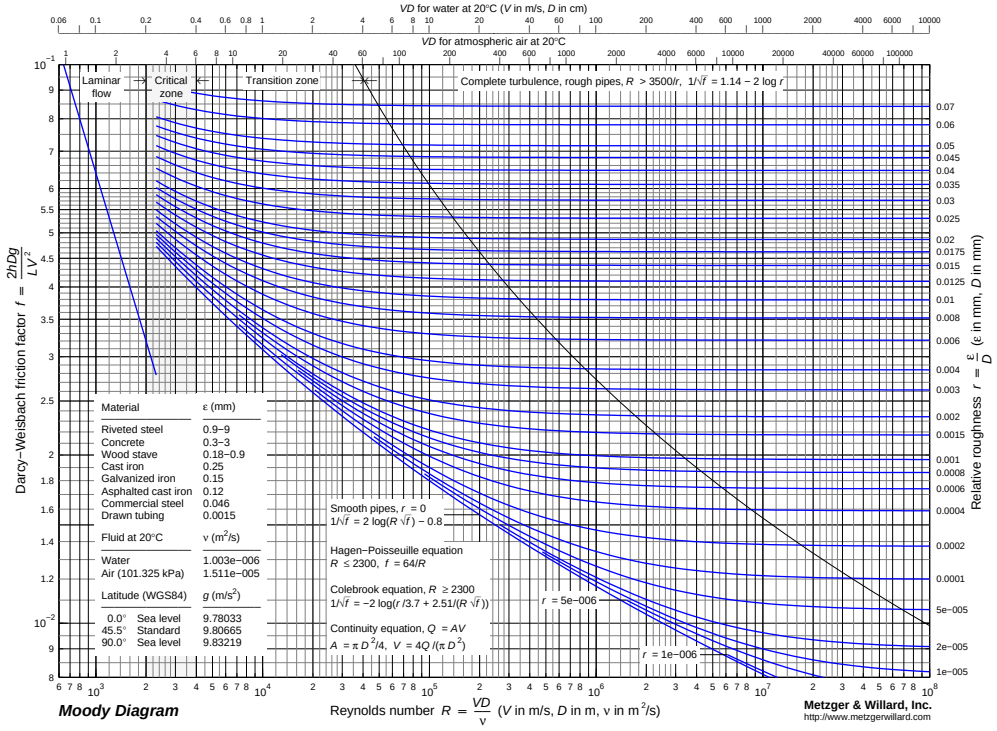

Figure 5.3. Moody diagram [58]

An alternative method is the explicit solution of the pipe friction equations given later. As the friction factor is a function of Reynolds number, the solution to the pressure loss has to take into account the flow regime.

For laminar flow, the friction coefficient can be expressed [59] as

$$f = \frac{64}{Re} \tag{5.19}$$

The pressure loss for laminar flow can then be determined by substituting (5.19) into (5.17).
The pressure loss relationship can then be expressed using system specific parameters as

$$\delta p = \frac{32\nu l \rho v}{d^2} = \frac{128\nu l \rho Q}{\pi d^4} \tag{5.20}$$

From (5.20) it can be concluded that in laminar flow the losses are proportional to volumetric flow rate Q or fluid average velocity v.

The friction factor calculation for the turbulent flow regimes is much more complicated. Since the hydraulic system can be analysed from different points of interest, different solution can be used. The commonly encountered situations in the pipeline models can be split between

- ◇ determination of pressure-loss using flow input
- ◇ determination of flow-rate using pressure inputs

According to the nature of the problem different solution approaches have to be chosen.

The pressure-loss related problems can be analysed using the *Colebrook* equation [59]. Using this approach the *Darcy* friction factor f can be calculated from

$$\frac{1}{\sqrt{f}} = -2.0 \log\left(\frac{\epsilon/d}{3.7} + \frac{2.51}{Re\sqrt{f}}\right) \tag{5.21}$$

Due to the implicit nature of the Colebrook equation, the determination of a friction factor requires some iteration or a numerical solving method.

An estimation for f can be achieved using an explicit formula known as the *Haaland* equation [59]

$$\frac{1}{\sqrt{f}} = -1.8 \log\left[\frac{6.9}{Re} + \left(\frac{\epsilon/d}{3.7}\right)^{1.11}\right] \tag{5.22}$$

The solution of this formula gives an estimation which in most cases is sufficient to determine the pressure loss.

The flow-rate can be determined by knowing the dimensionless head-loss as a function of dimensionless velocity.

$$\zeta = f(Re) \tag{5.23}$$

where ζ is dimensionless head-loss and is a function of head loss h_f. The complete rela-

tionship combining all mentioned functions is given by [59]

$$\zeta = \frac{gd^3 h_f}{lv^2} = \frac{fRe^2}{2} \tag{5.24}$$

Since the dimensionless velocity is to be found, the *Colebrook* interpolation given in (5.21) can be rewritten in term of (5.24) allowing Re to be solved. The explicit Reynolds number solution is given by

$$Re = -\sqrt{(8\zeta)}\log\left(\frac{\epsilon/d}{3.7} + \frac{1.775}{\sqrt{\zeta}}\right) \tag{5.25}$$

Thus, the volumetric flow rate can be found directly from the Reynolds number relationship (5.12).

$$Q = \frac{\nu Re \pi d}{4} \tag{5.26}$$

Both methods are used, where the appropriate technique is based on the use of model with flow rate or pressure as input variables.

5.2.3 Fluid Capacitance

The ideal fluid capacitance can be characterised as a physical element in which a fluid volume is a function of the pressure within the element.

$$V(t) = Cp(t) \tag{5.27}$$

where C is fluid capacitance. Equation (5.27) can also be expressed as the pressure-flow relationship given by

$$Q = C\frac{\delta p}{\delta t} \tag{5.28}$$

In fluid mechanics, all fluids have some degree of compressibility. The compressibility is a measure of the relative volume change of a fluid as a response to the pressure change applied to it. The relative change in fluid volume can be related to a change in pressure by a compresibility factor β.

$$\beta = -\frac{1}{V}\frac{\delta V}{\delta p} \tag{5.29}$$

The compresibility is a fluid dependent characteristic and the reciprocal of compressibility is called bulk modulus [60]. The bulk modulus B is a measure of the fluid's resistance to uniform compression and it is defined as the pressure increase needed to cause a given relative decrease in volume.

$$B = -V\frac{\delta p}{\delta V} \tag{5.30}$$

To find a fluid capacitance relationship, equations (5.27) and (5.30) have to be compared.

Thus the fluid capacitance can be expressed as

$$C = \frac{V}{B} \tag{5.31}$$

5.2.4 Fluid Inertance

When a fluid flows through a pipe section the force acting on it is due to acceleration of the fluid. The force, distributed over the volume, corresponds to a pressure difference and is called an inertia force. An ideal fluid inductor can be defined by the linear relation between pressure and flow through the pipe [61] as given by

$$\delta p = L\frac{\delta Q}{\delta t} \tag{5.32}$$

where p is the inductor pressure, Q is the inductor volume flow-rate, and the constant parameter L is the fluid inductance of the fluid inductor, or fluid inertance. By considering the unsteady frictionless flow of an incompressible fluid in a non-accelerating pipe segment the fluid inertance can be defined. The visualisation of the fluid inductance concept is shown in figure 5.4.

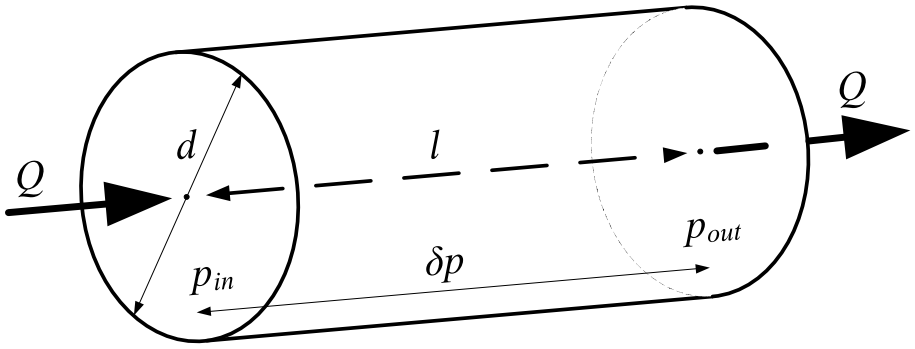

Figure 5.4. Pipe fluid inertia

If the pipe has constant area cross-section A and the velocity v of the fluid is uniform across any cross section of the pipe, then every fluid particle has the same velocity v and hence the same acceleration dv/dt. Thus, the force F necessary to produce an acceleration dv/dt of the fluid mass in the pipe is given by

$$F = A(p_{in} - p_{out}) = \rho A l\frac{\delta v}{\delta t} \tag{5.33}$$

Applying the flow-velocity relationship (5.10) to (5.33) it is possible to express the ideal fluid inductor relationship presented in (5.32) as a function of pipe diameters and fluid

properties.

$$\delta pA = \rho l \frac{\delta Q}{\delta t} \tag{5.34}$$

Thus the fluid inductance of the flow in the pipe may be expressed as

$$L = \rho \frac{l}{A} \tag{5.35}$$

The derived fluid inertance relationship is satisfied only when the pipe is not being accelerated. If the pipe itself has an acceleration, an additional pressure difference effect between the inlets of the pipe segment will have to be taken into account.

5.2.5 Fluid Minor Losses

In addition to pipe friction losses, the fluid system has additional energy losses that occur due to bends, changes in cross sections, joints, couplings and others elements, called *Minor losses*. As the fluid system has to be consistent, the method used to incorporate these additional losses to the pipework system need to be considered.

The Minor losses h_m, defined as the head loss due to all fittings in a system [56], are given by

$$h_m = K \frac{v^2}{2g} \tag{5.36}$$

where K is the minor loss coefficient and is a measure of all fitting losses in the system. Substituting (5.16) into (5.36) yields the pressure losses p_m caused by the fitting components

$$p_m = \rho K \frac{v^2}{2} \tag{5.37}$$

Minor losses may be expressed in terms of an equivalent length l_e of straight pipe that would have the same head loss for the same discharge flow rate. This relationship can be found by equating (5.15) and (5.37) as follows;

$$\rho K \frac{v^2}{2} = f \frac{l_e}{d} \rho \frac{v^2}{2} \tag{5.38}$$

This allows the K loss factor to be expressed in terms of the friction factor, length and diameter of the pipeline.

$$K = f \frac{l_e}{d} \tag{5.39}$$

Rearranging (5.39) allows the equivalent length of the minor losses l_e to be determined as

$$l_e = K \frac{d}{f} \tag{5.40}$$

The main rig minor losses were measured by Boyd [31] and then converted to K loss factors

as presented in table 5.2. The K factors were measured at 20 ℃. A scaling factor should be applied if the temperatures differ as the fittings loss depends on fluid mass density ρ as presented in (5.37).

Name	K factor	internal diameter
	[-]	[mm]
Reducing section	1.087	34.3
Inlet line	3.5503×10^{-3}	100
Couplings (stretched)	0.11	34.3
Couplings (compressed)	0.08	34.3
Bend	0.2222	34.3
Return line	0.729	34.3

Table 5.2. K loss factors for the main rig

5.2.6 Cavitation

Cavitation is defined as the phenomenon of formation of vapour bubbles in a flowing liquid in a region where the pressure of the liquid falls below its vapour pressure [60]. Vapour bubbles will be released from the liquid as the consequence of the pressure reduction. In a long pipeline with significant friction losses a transient caused by rapid valve closure may cause negative pressure waves sufficient to give rise to cavitation and the appearance of liquid vapour.

The pressure reduction process and its consequences can be summarised as:

- ◇ $p > p_{sat}$ In this case, in the steady state, the fluid consists only of pure liquid, not containing any vapour or free gas.
- ◇ $p \leq p_{sat}$ If the local pressure reduces below the saturation pressure air starts to be released due to the air dissolved in the liquid.
- ◇ $p \leq p_{vap}$ A further drop of the local liquid pressure allows more air release within the fluid and after reaching the vapour pressure p_{vap} the fluid becomes saturated resulting in local vapour bubbles and cavity formation.

The following analysis is based on [57] where the gauge pressure p in bar can be expressed in absolute units as

$$p_a = p + 1; \tag{5.41}$$

The air volume at the saturation pressure is given by

$$V_{air}^{sat} = C_{air} V \tag{5.42}$$

The volume of dissolved gas at pressure p_a can be found using Henry's law

$$V_{diss} = V_{air}^{sat} \left(\frac{p_a}{p_{sat}} \right) \tag{5.43}$$

Assuming that the free air content at saturation pressure is $1 - V_{diss}/V$, the actual released air volume at pressure p can be expressed by

$$V_{air}^{p} = V_{air}^{sat} \left(1 - \frac{p_a}{p_{sat}} \right) \left(\frac{p_{sat}}{p_a} \right)^{1/\gamma} \tag{5.44}$$

where γ is the polytropic index and a value of 1 is taken for the analysis (ie. isothermal conditions).

The effective bulk modulus B can be calculated from

$$\frac{V}{B} = \frac{V - V_{air}^{p}}{B_{pf}} + \frac{V_{air}^{p}}{\gamma p_a} \tag{5.45}$$

where B_{pf} is the effective fluid-pipework bulk modulus calculated from

$$B_{pf} = \frac{B_f}{1 + \dfrac{B_f d}{t_w E}} \tag{5.46}$$

where B_f is the fluid bulk modulus, t_w is the pipe wall thickness and E is the Young's modulus of the pipe material. The time derivative of pressure p can be found using

$$\frac{\delta p}{\delta t} = B \, \frac{Q_{out} - Q_{in}}{V} \tag{5.47}$$

The bulk modulus of a liquid can be affected by gas or vapour content in the liquid. The effective bulk modulus B is reduced as absolute pressure falls to zero as illustrated in figure 5.5.

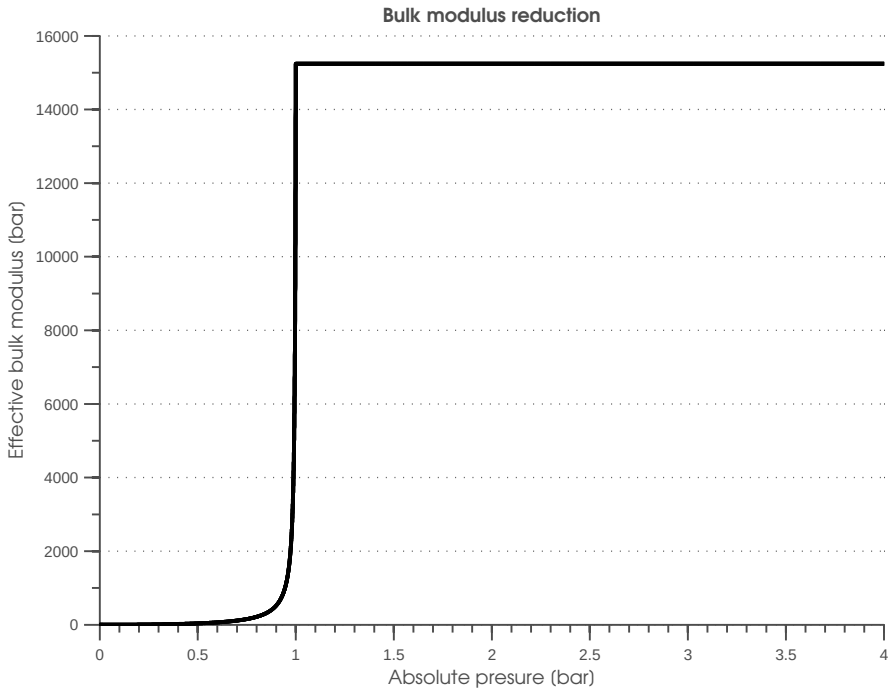

Figure 5.5. Bulk modulus reduction

5.3 Centrifugal Pump

The two stage commercial centrifugal pump is the source of hydraulic power in the main test rig. The pump uses two rotating impellers to increase the pressure of the fluid. The pressure rise across the pump is given by (5.48) and is a function of flow rate and pump shaft speed.

$$\delta p = p - \rho g h \tag{5.48}$$

where p is the pump outlet pressure, $\rho g h$ is the pressure at the pump input port and is expressed by the hydrostatic pressure caused by the tank head, neglecting losses in the inlet line.

Centrifugal pumps can be characterised in terms of a pressure-rise versus flow rate relationship. Since the fluid inertia is a dominant factor in the rig and is much larger than the pump inertia, a model based on the pump steady-state characteristic is sufficient to describe the rig behaviour [31].

The steady-state performance of the Lowara centrifugal pump has been investigated on the test rig at Bath University by Boyd [31] where the pump drive supply frequency was change from 20 to 50Hz in steps of 2.5Hz. This corresponded to the motor's synchronous speed being changed in the range of 1200-3000rpm in steps of 150rpm. The system flow rate, the pump pressure rise, the shaft speed and the torque were recorded and analysed

and the steady-state performance curves obtained at different operating conditions are shown in figures 5.6 and 5.7.

From figure 5.6, it can be seen that the pattern of variation for different speeds is the same. Hence, the pump performance could be described as a family of similar curves. It was shown that all of the curves could be condensed into a single curve [31], thus allowing the behaviour of the pump at different operating speeds to be determined from a single dimensionless steady-state characteristic.

The normalisation is performed by means of Affinity laws, which state that the flow rate through the pump varies in proportion to the shaft speed as in (5.49), the steady-state pressure varies as the square of the shaft speed (5.50) and the power-speed relationship is a cubic function of speed as shown in (5.51).

$$Q_2 = Q_1\left(\frac{\omega_2}{\omega_1}\right) \tag{5.49}$$

$$p_2 = p_1\left(\frac{\omega_2}{\omega_1}\right)^2 \tag{5.50}$$

$$P_2 = P_1\left(\frac{\omega_2}{\omega_1}\right)^3 \tag{5.51}$$

For a full description of the pump's behaviour, the pressure-rise, flow rate and torque were reduced to non-dimensional parameters, based on the affinity laws using a pressure coefficient ψ, flow coefficient ϕ and torque coefficient τ as defined in (5.52-5.54);

$$\psi = \frac{\delta p}{\omega^2} = \frac{\delta p}{\frac{1}{2}\rho\,(\omega r)^2} \tag{5.52}$$

$$\phi = \frac{Q}{\omega \upsilon} \tag{5.53}$$

$$\tau = \frac{T}{\frac{1}{2}\rho\,(\omega r)^2\,\upsilon} \tag{5.54}$$

where υ is the "equivalent displacement factor" of the pump and is equal to the ratio of maximum possible flow rate and maximum possible speed.

$$\upsilon = \frac{Q_{max}}{\omega_{max}} \tag{5.55}$$

The measured flow rate, torque and pump pressure-rise have been normalised by the above method and the resulting dimensionless curves describing the pump behaviour are presented in figures 5.8 and 5.9.

The mathematical description of the characteristic presented in figure (5.8) is obtained by polynomial approximation. Two polynomial functions are used for this purpose. For

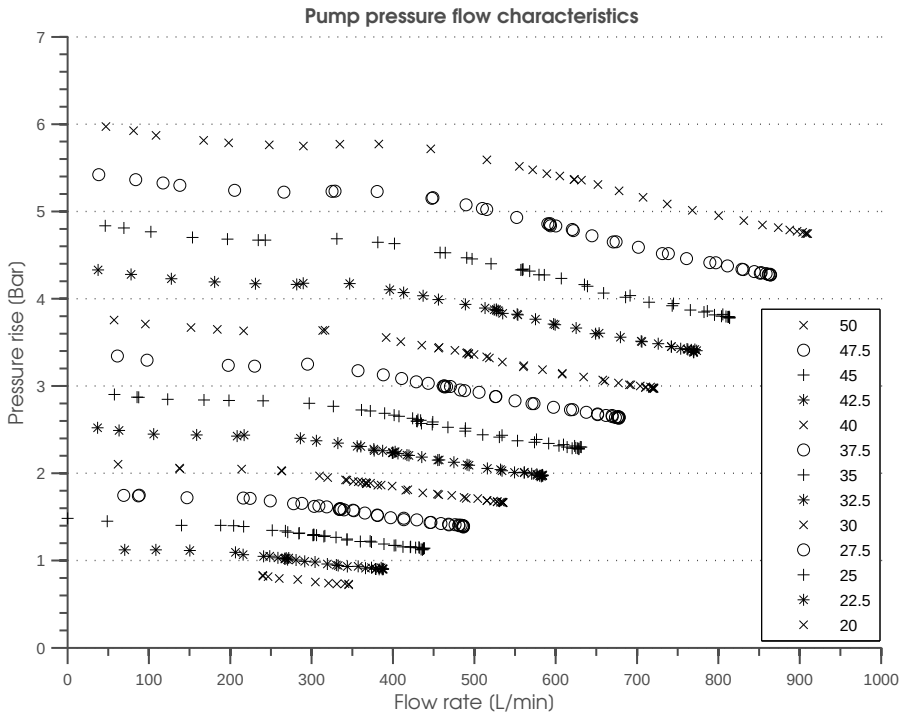

Figure 5.6. Lowara pump pressure flow characteristics at different supply frequencies (20-50Hz)

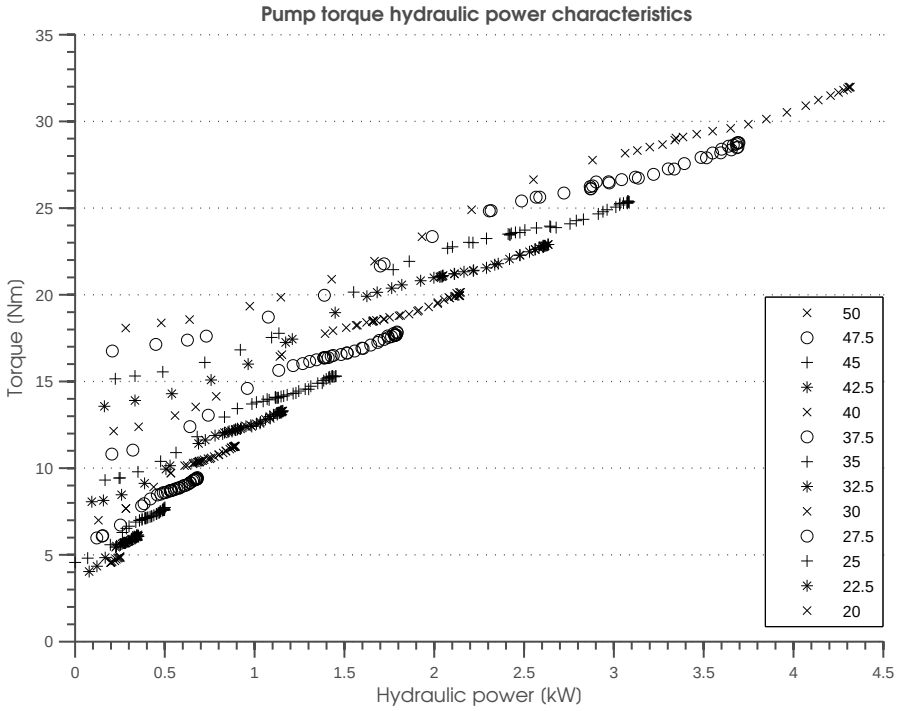

Figure 5.7. Lowara pump torque hydraulic power characteristics at different supply frequencies (20-50Hz)

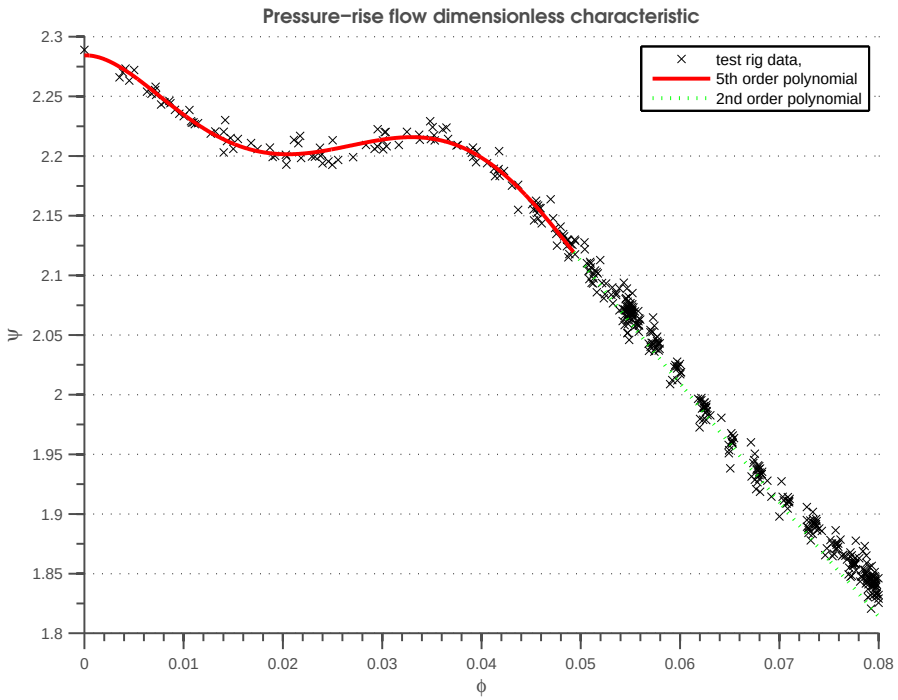

Figure 5.8. Pressure-rise flow dimensionless characteristic

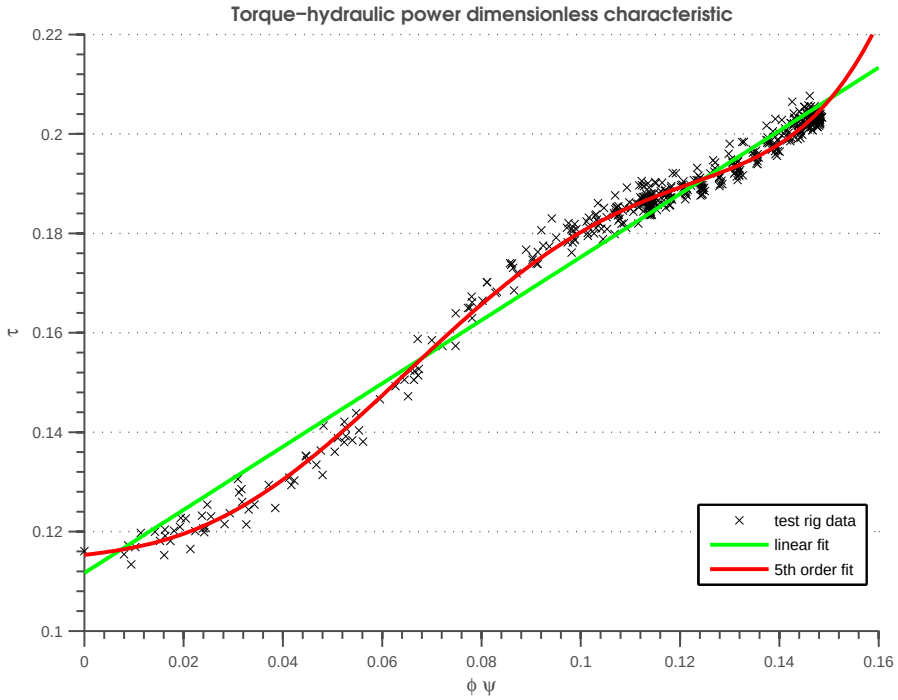

Figure 5.9. Torque-hydraulic power dimensionless characteristic

the low flow rates, $\phi \leq \phi_0$, to capture the dip in the characteristic a 5th order polynomial fitting is used and at higher flow rates, $\phi \geq \phi_0$, a 2nd order polynomial approximation is used. The threshold ϕ_0 is the point at which the two approximation curves meet. The dimensionless pressure-flow relationship can therefore be described as in (5.56)and (5.57);

$$\psi = \beta_1 \phi_e^5 + \beta_2 \phi_e^4 + \beta_3 \phi_e^3 + \beta_4 \phi_e^2 + \beta_5 \phi_e + \beta_6 \tag{5.56}$$

$$\psi = \beta_4 \phi_e^2 + \beta_5 \phi_e + \beta_6 \tag{5.57}$$

where ϕ_e is a dummy variable given by $\phi_e = \phi - \phi_0$ and the fitting coefficients are given in table 5.3.

β_1	1.0835×10^7
β_2	1.1643×10^6
β_3	3.436×10^4
β_4	17.8113
β_5	−10.4845
β_6	2.1193
ϕ_0	0.0493

Table 5.3. Pump pressure non-dimensional fitting coefficients

The torque delivered by the pump can be determined by the non-dimensional curve shown in figure 5.9. The dimensionless torque-hydraulic power relationship is approximated by the linear and 5th order polynomial as given in (5.58) and (5.59), respectively. The linear approximation has been used in the Bath*fp* model, whereas the 5th order polynomial has been employed in the Simulink analysis.

$$\tau = \gamma_{l1} (\phi\psi) + \gamma_{l2} \tag{5.58}$$

$$\tau = \gamma_1 (\phi\psi)^5 + \gamma_2 (\phi\psi)^4 + \gamma_3 (\phi\psi)^3 + \gamma_4 (\phi\psi)^2 + \gamma_5 (\phi\psi) + \gamma_6 \tag{5.59}$$

The polynomial approximation coefficients are given in table 5.4.

In order to incorporate the pump model with the motor and pipeline models, the dimensionalisation has to be performed by the inverse relationships shown in (5.60-5.62).

$$\delta p = \psi \left(\frac{1}{2} \rho (\omega r)^2 \right) \tag{5.60}$$

$$Q = \phi (\omega v) \tag{5.61}$$

$$T = \tau \left(\frac{1}{2} \rho (\omega r)^2 v \right) \tag{5.62}$$

γ_{l1}	0.6355
γ_{l2}	0.1117
γ_1	9711
γ_2	−3018
γ_3	253.09
γ_4	0.3901
γ_5	0.1263
γ_6	0.1153

Table 5.4. Pump torque non-dimensional fitting coefficients

The pump geometries are given in table 5.5.

r	0.0735	m
υ	6.0686×10^{-4}	m^3

Table 5.5. Pump geometries

5.4 Ball Valve

The flow passing through the pipeline in the fuel system test rig is controlled by an electrically operated ball valve, supplied by Parker Aerospace. The ball valve consists of a body containing a flow control element attached to it and operated by an external power source. The flow control is achieved by a ball which rotates a quarter-turn allowing it to achieve a desired position within the internal valve housing. The rotating ball has a hole through one axis to connect the inlet and outlet ports within a pipeline. The full bore flow is achieved when the axis of the hole is aligned with the axis of the flow. Figure (5.10) summarises the ball valve construction.

The objective of the ball valve model is to calculate the flow rate through the valve which has been modelled as two variable-orifice restrictors. Fluid passing though an orifice constriction will experience a pressure drop across the orifice. This change can be used to predict the flow rate of the fluid. The flow rate through the valve is proportional to the valve opening position and to the pressure differential across the valve and is determined

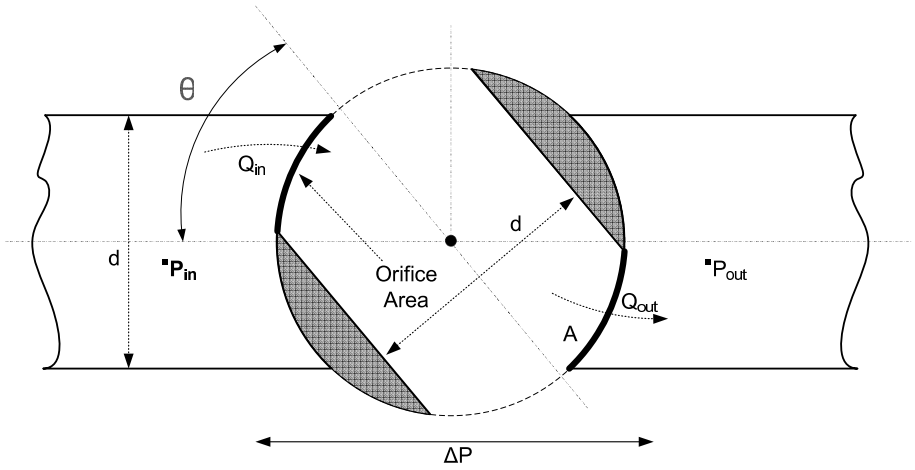

Figure 5.10. Ball valve

according to the equation (5.63).

$$Q = C_q A_v \sqrt{\frac{2\Delta p}{\rho}} \tag{5.63}$$

where Δp is the pressure drop across the orifice, ρ is the density the liquid, C_q is a flow coefficient and A_v is a cross-sectional area of the orifice.

The flow coefficient is a relative measure of its efficiency at allowing fluid flow. It is used to determine flow capacities, valve positioning and energy losses of the system. The flow coefficient can be described by the relationship between the pressure drop across an orifice and the corresponding flow rate. By varying the orifice coefficient the flow rate is controlled. Mathematically the flow coefficient can be expressed by (5.64).

$$C_q = \frac{Q}{A_v} \sqrt{\frac{\rho}{2\Delta p}} \tag{5.64}$$

Values of the coefficient were determined experimentally by Roberts [30]. For various flow rate conditions the valve angle position was adjusted allowing the value of the coefficient to be predicted. Figure 5.11 summarises the discharge coefficient characteristic.

In order to model the valve, the characteristic presented in figure (5.11) was approximated as a polynomial function. The actual angle-dependent value for C_q was approximated by means of a seventh order polynomial function [30] as equation (5.65).

$$C_q(\alpha) = v_{c1}\alpha^6 + v_{c2}\alpha^5 + v_{c3}\alpha^4 + v_{c4}\alpha^3 + v_{c5}\alpha^2 + v_{c6}\alpha + v_{c7} \tag{5.65}$$

where α is the valve angle in degrees. The values of the evaluated polynomial flow coefficients are presented in table (5.6).

The second variable parameter in (5.63) is the cross-sectional area of the valve. The shape

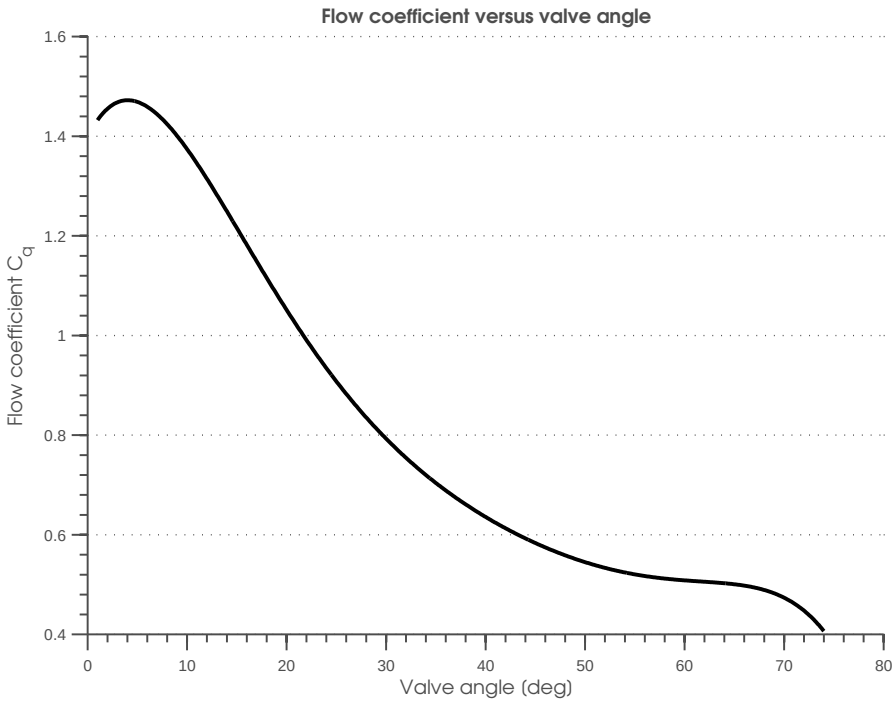

Figure 5.11. Ball valve flow coefficient

Name	value
v_{c1}	-2.192×10^{7}
v_{c2}	5.395×10^{-8}
v_{c3}	-5.326×10^{-6}
v_{c4}	2.648×10^{-4}
v_{c5}	-6.452×10^{-3}
v_{c6}	4.0456×10^{-2}
v_{c7}	1.398

Table 5.6. Flow coefficient polynomial coefficients

and value of area A_v is determined by the valve operating angle α and the orifice area is assumed to be zero when the valve is closed. In contrast, the area takes a maximum value equal to the pipe cross-sectional area when the ball valve is fully aligned with the pipe flow axis. Figure (5.12) depicts the measured cross-section area of the valve.

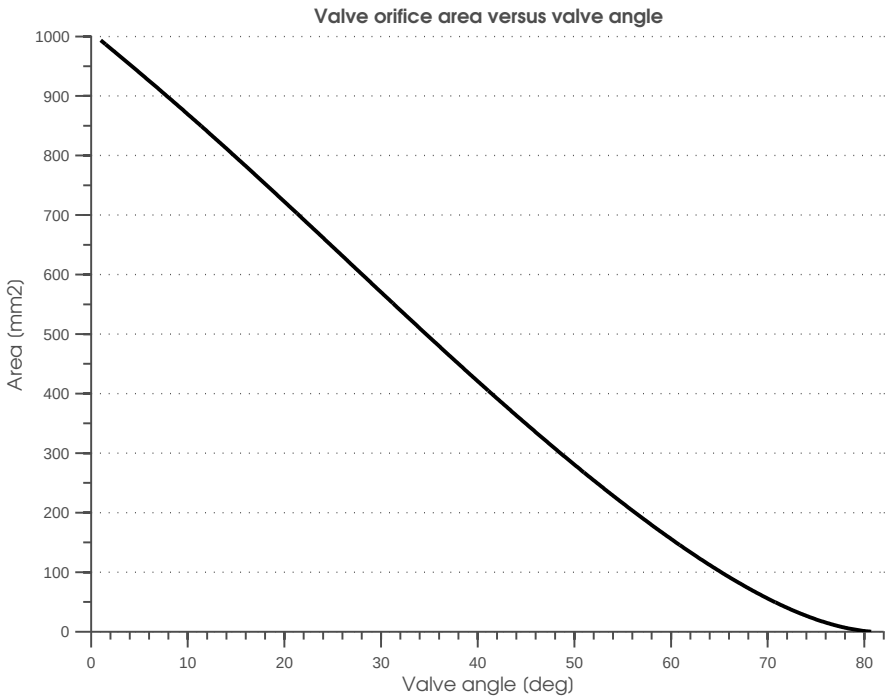

Figure 5.12. Ball valve cross-section orifice area

The measured cross-section area versus valve angle function was approximated by a 7th order polynomial function [30] presented in (5.66).

$$A_v(\alpha) = v_{a1}\alpha^6 + v_{a2}\alpha^5 + v_{a3}\alpha^4 + v_{a4}\alpha^3 + v_{a5}\alpha^2 + v_{a6}\alpha + v_{a7} \tag{5.66}$$

where the polynomial coefficients are given in table 5.7.

Name	value	unit
v_{a1}	1.564×10^{-9}	mm^2
v_{a2}	-5.328×10^{-7}	mm^2
v_{a3}	7.206×10^{-5}	mm^2
v_{a4}	-5.512×10^{-3}	mm^2
v_{a5}	2.969×10^{-1}	mm^2
v_{a6}	1.085	mm^2
v_{a7}	0	mm^2

Table 5.7. Valve orifice area polynomial coefficients

5.5 Closure

In order to model and simulate the operation of the fuel system test rig a knowledge of the system components and fluid is required. The fuel system consists of a centrifugal pump, pipeline with included minor losses and a ball valve used for the flow control. Previous described hydraulic system components, modelled in Bath*fp*, have been developed and extended in Simulink, and are used in this thesis.

A centrifugal pump model is outlined that was developed by Boyd [31]. The pump model is based on measured data and normalised dimensionless pressure-flow and hydraulic power-torque characteristics of the pump. The curves allow the pump behaviour to be predicted at different operating conditions including variable-speed drive. The pump torque model was extended to higher order accuracy. The pump model will be connected to the induction motor model developed and described in chapter 3. The ball valve modelling method [30] based on measured data is discussed and the valve flow relationship identified. The measured data is used to characterise the flow coefficient and valve area as a function of valve angle.

Models of the pipeline are presented and the flow pattern-dependent parameters are described. For low-value Reynolds numbers, a laminar flow pipe model is used. For turbulent flow, a friction model based on Halland's equation (5.22) and a dimensionless head relationship (5.24) are used. The former approach is applied to the main pipe line with flow input ports whereas the latter is used for the return line where the pressure is the input variable.

The steady-state pressure losses associated with various rig components were considered. The couplings, bend and return line measured losses are expressed using K factors and are converted to an equivalent length of straight pipe. The resulting friction model was included in the inertance and the capacitance pipe models. The compressibility of the fluid was taken into account and presented as a function of the fluid volume and the effective bulk modulus. An inertia model was also developed, where the fluid inertance is expressed in terms of the fluid properties and the pipeline dimensions. In addition, air release in the pipeline was modelled using a reduced bulk modulus.

Chapter 6

Model Validation

In order to analyse the behaviour of the fuel system test rig, a number of component models were developed as described in chapters 3 and 5. If the model predictions show good agreement with measured component behaviour, then the response at different operating conditions can be analysed and a robust control system for the electric motor can be designed.

The test rig components were modelled as individual blocks that were linked together to create a complete system model. A mixture of analytical and empirical models was used to replicate the steady state and transient behaviour of the system components. The model validation was conducted with respect to the overall system behaviour and for each component independently. Results are presented and analysed. This approach allows multi-purpose system use as the developed models could be easily linked to each other allowing complex systems to be analysed.

This chapter covers both the electrical and hydraulic modelling of the components present in the fuel test rig. The modelling environments are briefly described and steady-state and dynamic responses of the components are analysed.

6.1 Modelling and Simulation software

The components and system simulations were undertaken using Matlab/Simulink-general purpose software package and the in-house Bath*fp* hydraulic-pneumatic orientated software. The models were developed in both packages to show that the fuel rig Simulink models, developed by the author, can accurately approximate any Bath*fp*-based results, that are obtained using this fluid-power analysis software. Both simulation packages allow non-

linear system analysis and simulations were performed in the time domain. The predicted results were recorded as mat-workspaces within Simulink and as text files in Bath*fp* for post-processing operations. A variety of generic component models were created, however some library elements were also incorporated for both electrical and hydraulic component implementation. The simulation details and the specifications of the model parameters are described in subsequent subsections, for both the induction motor and the fuel test rigs respectively.

6.1.1 Bath*fp* based models

The Bath*fp* software was designed as a modular dynamic simulation package [57]. This software was originally developed for pure hydraulic and pneumatic applications and uses well-established fluid system analysis methods to simulate pipelines. All Bath*fp* components are implemented by their physical pressure and flow representation. Nonetheless, some control possibilities are also available. The user-defined control strategies and external models can be incorporated into the package through user-defined Fortran or C based subprograms.

The developed model consists of a steady state induction motor, a centrifugal pump, a ball valve and higher order pipe models as presented in fig.6.1. Existing and user-defined libraries of electrical and hydraulic components were used for this purpose.

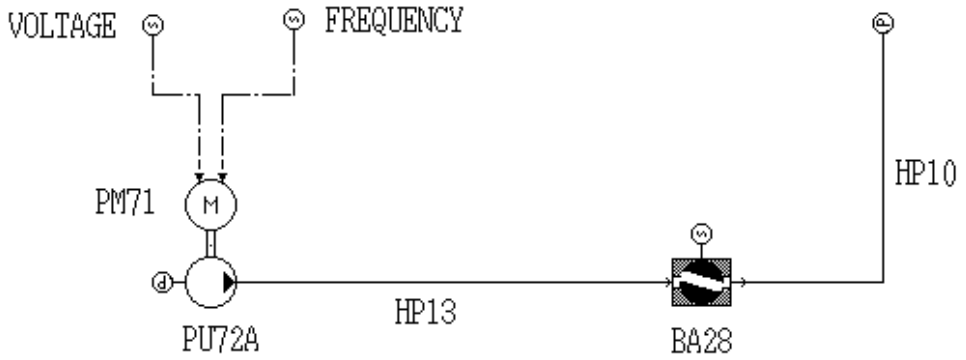

Figure 6.1. Bath*fp* fuel test rig model

The centrifugal pump PU72A subroutine implemented by Boyd [31] and the ball valve BA28 subprogram created by Roberts [30] were used. The induction motor model PM71 was developed by the author. The pipeline were modelled by 10-element generic-type pipe model that included fluid inertance, pressure losses and cavitation. The pipe models HP13 and HP10 were employed for the main fuel line and the return line, respectively. The induction motor supply voltage and frequency as well as the ball valve position are

represented using signals to allow a variety of the test rig conditions to be simulated. The fuel test rig physical dimensions and the fluid properties are specified in subsection 6.1.3 and the simulated data is validated in section 6.2.

6.1.2 Matlab/Simulink based models

Matlab/Simulink [62][63] is a block-orientated software package that provides a flexible approach to simulation. The software libraries deliver a variety of generic blocks which can be easily incorporated into user-defined models and sub-models allowing a diversity of implementation possibilities.

The test rig used as part of the research described in this thesis was modelled in Matlab/Simulink. Component models were implemented as Simulink blocks whereas the Matlab m-file based scripts were used to initialise the Simulink models. This approach provides a flexible simulation environment.

The complete Simulink-based fuel test rig model is depicted in figure 6.2 and its complete version is given in Appendix C. The component blocks were built according to the equations detailed in chapters 5 and 3. The complete model includes the transient model of the induction motor described in the subsection 3.4, the centrifugal pump, the ball valve and the 2-stage pipeline models discussed in chapter 5. The input control variables such as the motor supply condition and valve angle are initialised and controlled through use of a Matlab script file. The model internal parameters and dimensions and the fluid properties are depicted in subsection 6.1.3. The simulation results and validation discussion are covered in section 6.2 along with the hydraulic test rig data.

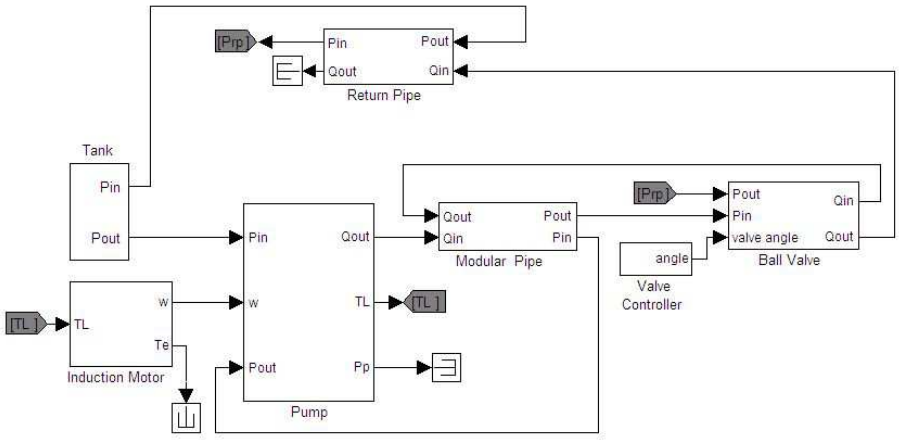

Figure 6.2. Simulink fuel test rig model

The induction motor models were developed to investigate the motor behaviour during steady-state and transient operating conditions. A number of models were created in both Matlab and Simulink with the steady-state models implemented as Matlab m-files. The

torque and current versus speed characteristics, the induction motor powers and internal parameters distribution models were analysed in this way. The transient model of the induction motor used in the validation was implemented in Simulink and the initialisation was done using a m-file script. The steady-state analysis of the induction motor were performed using Simulink model where m-file functions for torque and current were called as subroutines. The induction motor model validation results are presented and discussed in chapter 3. The motor electrical parameters used in the fuel rig validation are given in table 6.3.

6.1.3 Fuel test rig model data

The dimensional data for the fuel test rig are presented in table 6.1. The pipe lengths and diameters were measured directly from the rig. The inner diameter of the main pipe was set to 34.4mm and the length to 16.6m whereas the return line length was set to 4m with a 50mm internal diameter. The return line dimensions were averaged as this section of the rig is built from different pipe segments. The measured pipe wall thickness was set to 2.5mm. The relative roughness was estimated from tests performed by Boyd [31] and a value of 5.5×10^{-5} was used in simulations. The tank inlet and outlet heads were estimated as 0.16m and 1.38m, respectively. The fuel system models developed in both

Name	symbol	value	unit
pipe length	l	16.6	m
pipe relative roughness	ϵ/d	5.5×10^{-5}	-
return line length	l_{rl}	4	m
return pipe diameter	d_{rl}	0.05	m
pipe diameter	d	0.0344	m
valve internal diameter	d_v	0.036	m
tank head inlet	h_{in}	0.16	m
tank head outlet	h_{out}	1.38	m
pipe wall thickness	t_w	0.0025	m

Table 6.1. Fuel test rig dimensions

packages include the physical properties of water. Since a fluid additive has been added to the water, tests were conducted to assess the impact of the chemicals on fluid properties. The water density and kinematic viscosity of the fluid were measured and set to 998kg/m^3 and $1.004\times10^{-6}\text{m}^2/\text{s}$, respectively. The fluid bulk modulus was estimated to have a value of 18700bar and all the fluid properties are listed in table 6.2. The detailed analysis and the measurement details of the hydraulic rig parameters are discussed by Boyd [31]. The pump model is based on the measured pump characteristics using the method developed by Boyd

Name	symbol	value	unit
fluid bulk modulus	B_f	8.17×10^9	Pa
pipe Young modulus	E	69×10^9	Pa
fluid density	ρ	998	kg/m^3
gravity acceleration	g	9.81	m/s^2
fluid kinematic viscosity	ν	1.004×10^{-6}	m^2/s
fluid dynamic viscosity	μ	1.002×10^{-3}	kg/ms

Table 6.2. Fuel system fluid properties

[31]. The data fitting techniques detailed in section 5.3 were applied to measured data resulting in a non-dimensional pump characteristics. The obtained fitting coefficients were given previously in tables 5.3 and 5.4 for both the non-dimensional pressure-flow rate and torque-hydraulic power characteristics, respectively. Two sets of the torque coefficients (linear and 5th order polynomial) were used in the torque model analysis due to the different approaches used in the modelling, since the linear pump torque model developed by Boyd [31] turned out to be insufficiently accurate for the motor analysis as shown later. The ball valve model used in the fuel rig modelling was described earlier in section 5.4, where the valve fitting coefficients for both the flow coefficient and area evaluation were previously given in tables 5.6 and 5.7, respectively.

The Lowara induction motor, which supplies power to the centrifugal pump, is modelled using the transient model described in section 3.4. The motor parameters used in simulation were obtained from the tests undertaken on the induction motor and are given in table 6.3. These were obtained at a 50Hz supply frequency and for different operating conditions scaling was applied. The pump inertia was estimated using CAD by Boyd [31].

Name	symbol	value	unit
Stator resistance	R_s	0.776	Ω
Stator leakage reactance	X_s	1.780	Ω
Rotor resistance	R_r	0.908	Ω
Rotor leakage reactance	X_r	2.667	Ω
Magnetizing reactance	X_m	93.94	Ω
Motor moment of inertia	J_m	0.019	kgm^2
Pump moment of inertia	J_l	0.02	kgm^2

Table 6.3. Induction motor parameters

The complete set of data used for Simulink model analysis is listed in Appendix A.

6.2 Fuel rig validation

A number of tests were conducted on the rig to investigate the system's response. The simulation data for both Bath*fp* and Simulink models is given and compared with the measured data obtained from the test rig.

6.2.1 Inverter and motor supply condition

The motor drive system provides the source of mechanical power to the centrifugal pump. An inverter-based motor speed controller is connected to a three-phase symmetrical AC network through a set of circuit-breakers. The measured electrical parameters of the ac mains are given in table 6.4.

Variable	unit	test I	test II
Line voltage RMS	V	409.26	409.27
Phase voltage RMS	V	235.77	233.63
Voltage THD	%	2.86	2.54
Voltage fundamental harmonic RMS	V	235.68	233.55
Voltage fundamental content	%	99.95	99.96
Voltage crest factor	-	1.371	1.386
Voltage form factor	-	1.115	1.116

Table 6.4. AC mains supply conditions

The two pulse-width modulated (PWM) converters described in section 2.1.2 act as the source of regulated power to the motor. Since the induction motor is supplied from a frequency converter (also termed inverter system), the supply conditions are different from the mains supply conditions and influence the behaviour of the motor. Both inverter switching frequencies were set to 8kHz during the initial configuration of the inverters. The voltage per hertz control is used as the modulation strategy.

The performance of the induction motor fed from the PWM inverters was partially determined by the harmonic content of the output voltage. As the motor responds mostly to the fundamental harmonic, a higher harmonic content results in a lower operating voltage for a particular supply frequency. Variations in the supply voltage applied to the motor with supply frequency (or speed) settings are shown in figure 6.3 for both inverters.

The figure includes the RMS voltage measurements, the fundamental component and the total output voltage for the full range of investigated frequencies. It can be seen that reducing the supply frequency reduces the Volts per Hertz ratio and consequently lowers

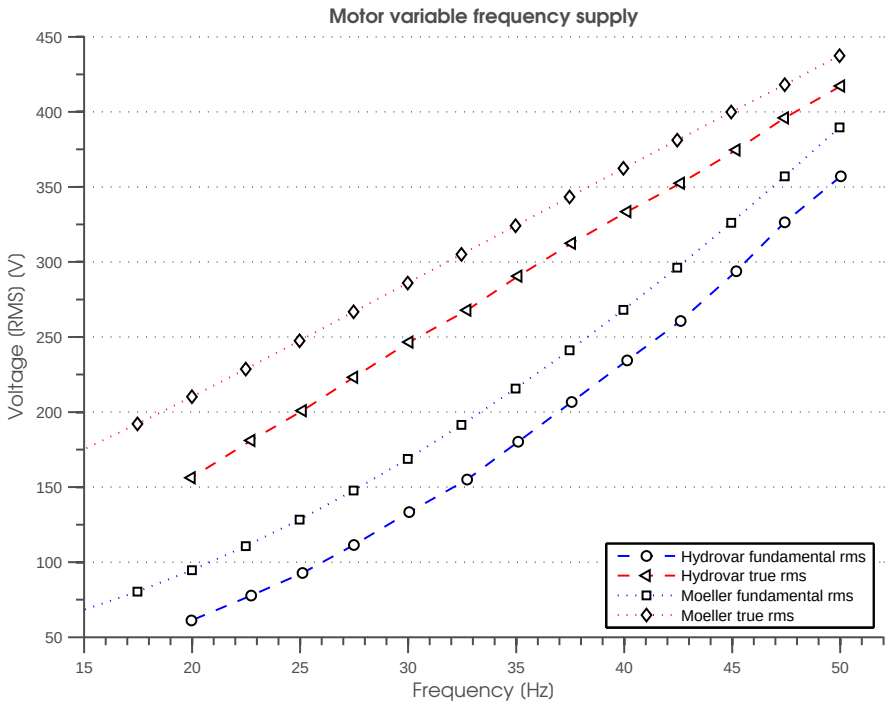

Figure 6.3. Variation in motor voltage with frequency for different inverter conditions

the motor torque production capability. The Moeller inverter seems to better utilise the input power, resulting in an improved motor performance.

The total harmonic and fundamental output voltage levels, expressed as a percentage of the RMS output voltage, are depicted in figure 6.4. It is noticeable that the presented graphs show an inverse relationship between the total harmonic and fundamental voltage levels. Hence, the higher the motor supply frequency (and hence fundamental) the lower the voltage distortion. At low supply frequencies the fundamental voltage level falls below 50%. The fundamental voltage level obtained using the Moeller inverter is approximately 5% higher than that obtained using the Hydrovar over the entire frequency range.

The inverter's output voltage total harmonic distortion (THD) defined in equation 6.1 is given in figure 6.5.

$$THD_U = \frac{\sqrt{U_{h2}^2 + U_{h3}^2 + \dots}}{U_{h1}} \tag{6.1}$$

To illustrate the relationship between the voltage THD and the voltage fundamental harmonic, the THD is shown as a second scaled plot. It can be seen that the PWM modulation techniques introduce a large harmonic distortion varying between 50 and 240 % and the content is inversely proportional to the frequency supplied to the motor. The superiority of the Moeller inverter over the Hydrovar can again be seen from this figure.

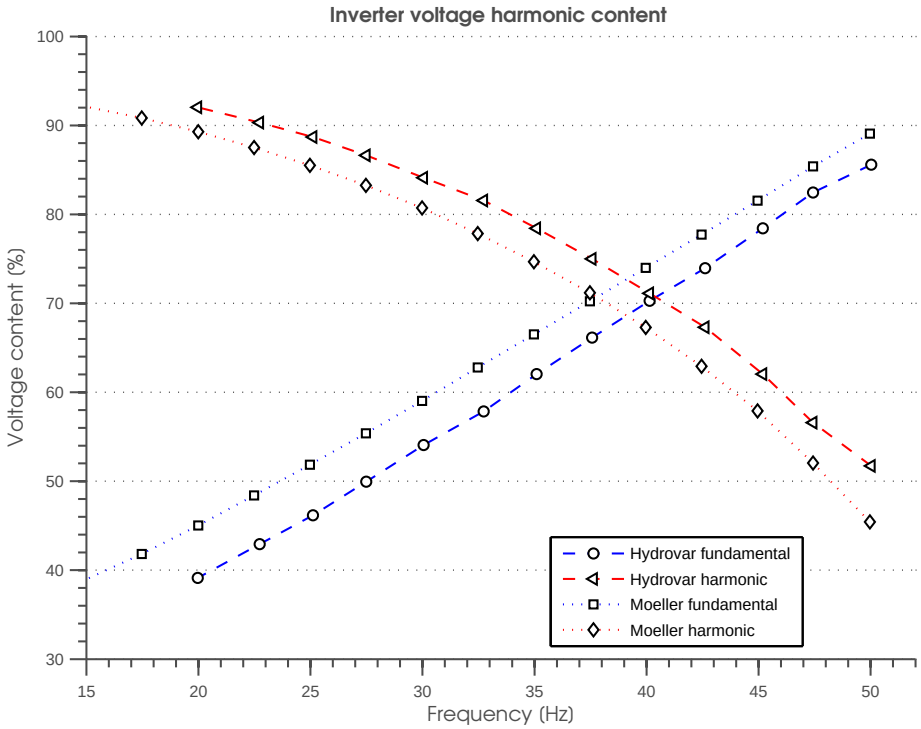

Figure 6.4. Inverters' harmonic content

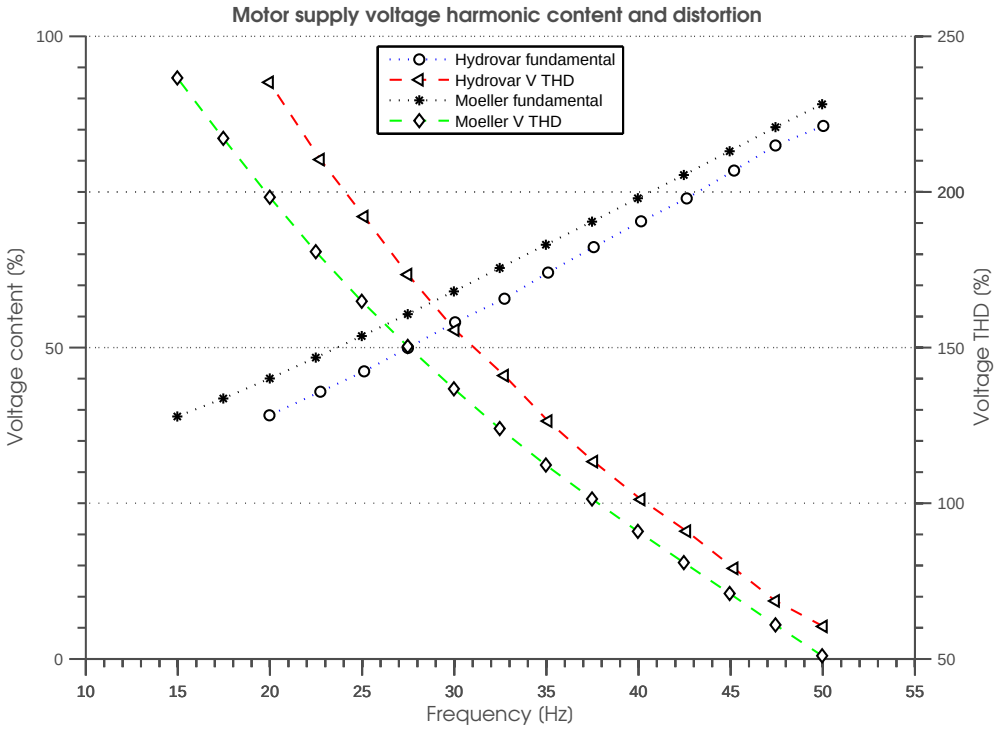

Figure 6.5. Voltage harmonic content and harmonic distortion under V/f operation

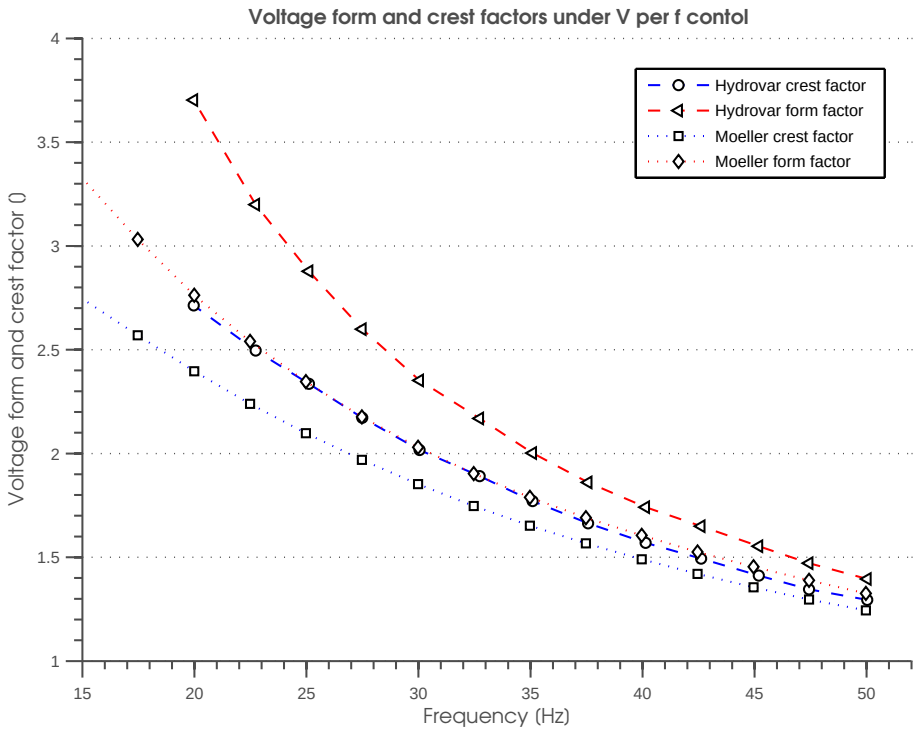

Figure 6.6. Voltage crest and form factors under V/f operation

Two power quality factors were chosen to assess the power quality of both inverters.

$$ff = \frac{U_{RMS}}{U_{avg}} \tag{6.2}$$

$$cf = \frac{|U_{peak}|}{U_{RMS}} \tag{6.3}$$

A voltage form factor and a crest factor, defined in equations 6.2 and 6.3 respectively, were recorded at different supply frequency conditions as shown in figure 6.6. The voltage crest factor and the form factor show similar trends during the tests with the values decreasing as the supply frequency is increased. The crest factor has a value of 3.5 at low supply frequencies and 1.2 at the maximum frequency. The form factor varies from 2.8 to 1.25 as the frequency was increased from 15 to 50Hz.

To complete the motor supply analysis, the efficiency of both inverters was analysed. For the same switching frequency and the same modulation technique, the Moeller inverter gives better input power utilisation. This can be seen when comparing the output voltages at the same supply frequency. The inverters' harmonic content, the total harmonic distortion and the power factor results further confirm the Moeller superiority. However, the better supply conditions provided by the Moeller inverter were produced at the expense of higher radio frequency interference (RFI) noise. The power quality and efficiency of the two inverters were linked with the faster switching device utilisation in the internal

bridge configuration. The faster switching could be the cause of the higher RFI noise as stronger ringing effects arise during shorter switching state transitions where current is bypassed through freewheel diodes creating a resonance between stray capacitances and inductances.

6.2.2 Motor and pump characteristics

The electrical motor and pump characteristics were measured and compared with those obtained from the models. A range of electrical supply conditions was applied to the motor resulting in a family of characteristics. Additionally, the hydraulic system conditions were changed by means of the ball valve and as a consequence the pump and motor operating points were changed while the data was recorded.

The pump pressure versus flow rate characteristics measured at different supply frequency conditions were compared with the simulation results in figure 6.7. This figure presents a family of characteristics for 30, 40 and 50Hz for both the tested inverters. The ball valve opening was varied to change the system flow rate and the bypass was used to allow the system flow rate to be investigated over a wide range of operating conditions.

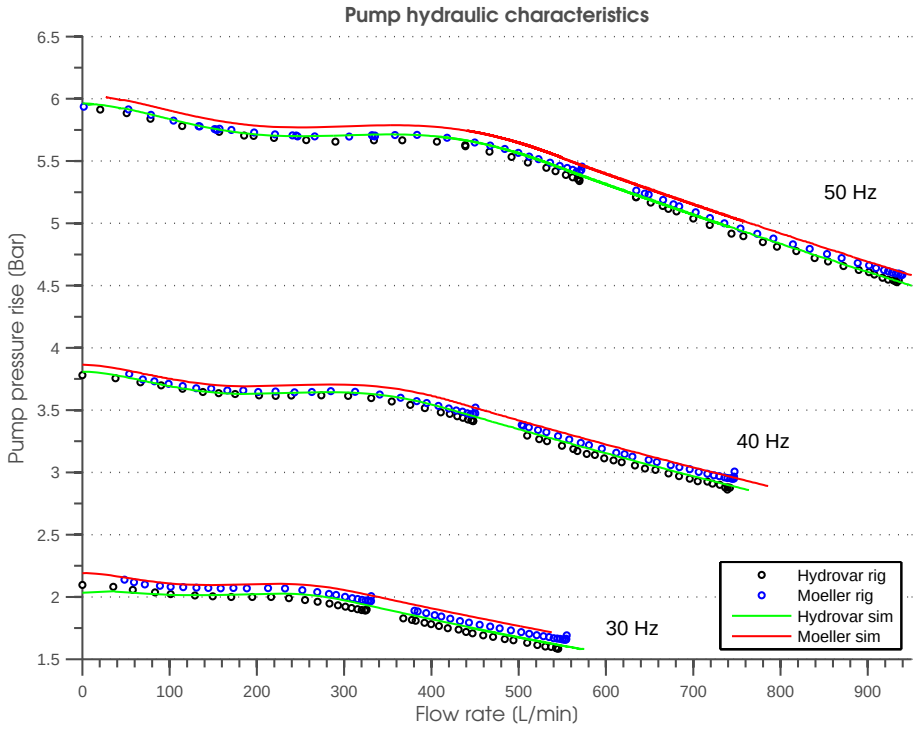

Figure 6.7. Pump pressure-rise flow characteristics

The small horizontal gaps in the pressure-rise versus flow rate characteristics, as seen on the plots, resulted from a lack of flow regulation when the bypass line was introduced. It was not possible to obtain the missing part of the pressure-flow rate characteristics even when the combined, the ball valve and the bypass, flow rate regulation was introduced. The small differences in the pump performance, when the motor was supplied from both the inverters, exist as a consequence of the shaft speed variations. The supply voltage applied to the motor input terminals was varied as shown in figure 6.3 resulting in different motor operating speeds. However, the characteristics exhibit similar trends. Because the pump maximum outlet pressure is a function of the shaft speed, the Moeller inverter characteristics are slightly shifted upwards as a consequence of higher speed for the same supply frequency. The simulation results show good agreement (5% error) for all the investigated cases. The complete pump behaviour analysis is described in the Boyd thesis [31].

The behaviour of the induction motor used as the source of mechanical power for the centrifugal pump has also been investigated. The recorded torque-speed characteristics are depicted in figure 6.8 for 30, 40 and 50Hz, respectively.

The figure includes the recorded motor torque characteristics together with the simulation results using both inverters. Different curve slopes can be seen as a consequence of the different supply conditions. The higher the supply frequency the steeper the recorded characteristic. This is due to the induction motor being very sensitive to the supply voltage changes as pointed out in the supply subsection 6.2.1. The simulated data show good correlation with the experimental results although it was necessary to adjust the model input voltage in order to minimise the errors due to the fact that the motor model was supplied from sinewave, compared to a distorted voltage on the rig. At the lower supply frequencies the simulated data deviates slightly from the test rig results due to the induction motor performance being modelled based on the motor parameters measured at 50Hz and a correction factor applied at the different supply conditions.

The induction motor current versus operating speed was also investigated. The current-speed relationship was changed by means of the load torque, the same as in the motor torque case. The measured and predicted characteristics are depicted in figure 6.9. A distinct difference between the measured and predicted results is clearly visible, especially at lower frequencies. This is due to model inaccuracies. The resistance changes caused mostly by temperature changes were not modelled as it was impossible to measure the motor internal conditions during a test. In addition the lack of modelling of motor non-linearities, such as magnetic saturation, air-gap non-sinusoidal flux distribution and skewing of the rotor bars, is also likely to have an effect on the results. Although some errors exist, the general fit between the simulated and measured data can be seen to be relatively good with error less than 10%.

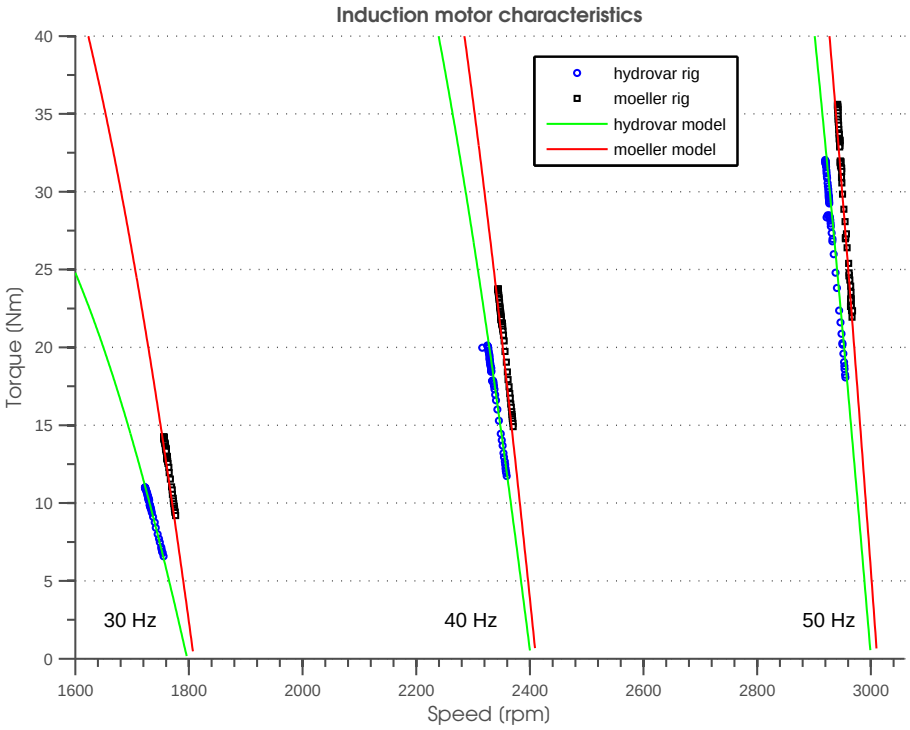

Figure 6.8. Induction motor torque versus speed characteristics

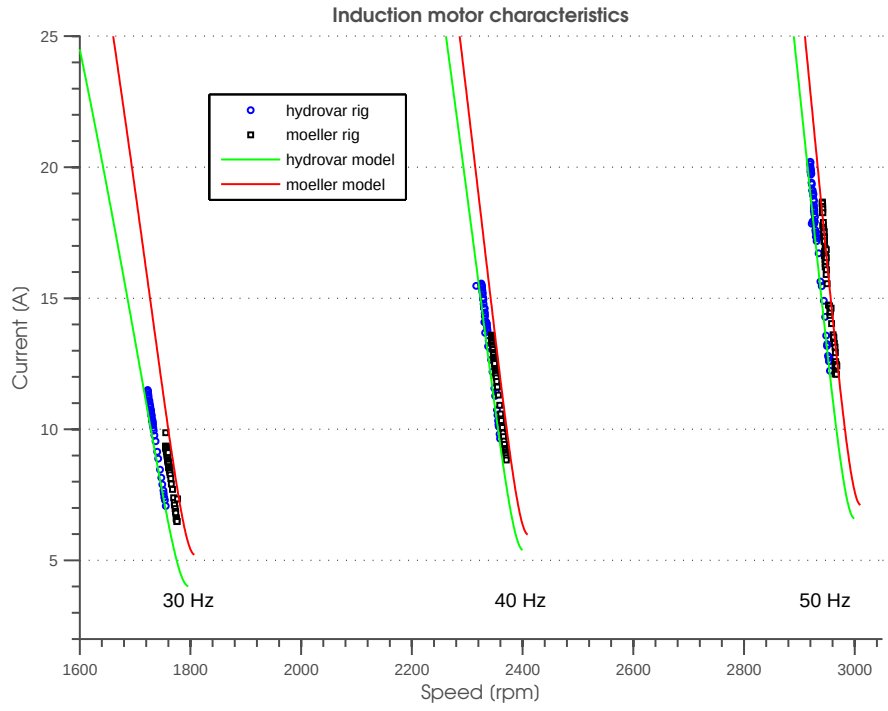

Figure 6.9. Induction motor current versus speed characteristics

6.3 Hydraulic system characteristics

The behaviour of the fuel rig was tested at different operating conditions. To analyse the system's steady-state response and transient behaviour, two parameters were varied. Because the pump performance is speed-dependent, the supply frequency to the induction motor was adjusted to control the pump shaft speed. The supply frequency was changed from 30 to 50Hz in 10Hz steps to investigate the system responses to sudden flow rate changes and the influence of fluid inertance at different shaft speeds.

The ball valve was used to introduce a disturbance into the system to change the flow rate. The valve operating time was the second variable parameter used to observe the dynamics of the system. To investigate the system response, two different modes of valve operation were used. User-defined closure and opening profiles were created and supplied to the electrically-controlled valve through a specialised controller using 0.5s and 1s operation profiles for both valve opening and closure. Each operation profile was used to investigate both steady-state and transient behaviour. The valve closure starts at 2s after the profile is started. The steady-state condition lasts 2s for a one second operation profile and 2.5s for a half second profile. The opening of the valve commences at 7s and is fully open at 7.5s or 8s depending on the profile.

To avoid unwanted and undesirable measurements, a data offsetting/compensation technique was applied to the pressure signals. At the time of the acquisition initialisation, the data from all channels was read and the channels' offset evaluated. During normal operation the offsets were subtracted from the test rig readings. In this way the steady-state rig sensor errors were removed.

The data obtained from the valve tests are presented in figures 6.10-6.15 for both 1s and 0.5s valve ramp times and both steady-state and transient behaviour are shown. To validate the system model, the simulated data is presented along with the rig results. To limit the number of figures only the 50Hz motor supply frequency case is shown as the transient responses exhibit similar trends and only the steady-state levels were found to change depending on the pump operating conditions. The steady-state responses for all recorded frequencies are given in tables 6.6 and 6.5, representing the cases where the valve was fully open and fully closed, respectively.

The data presented in all of the figures show some time-shift differences. The time offset between the rig and the simulation data is caused by the fact that the valve is controlled by a separate Ethernet-connected PC and a communication delay occurs. The communication time was found to be variable, and a time shift of up to 0.1s can be visible in the figures 6.10-6.15 for both valve operation profiles. The differences between the simulated and measured data are in most cases very small, showing very good fitting trend between the measured and predicted results.

The variation in pump pressure as the valve is closed and opened at the two different ramp times is shown in figure 6.10. When the valve is fully closed there is no flow and the pump pressure rises to its maximum value of approximately 6bar. For the fully-open valve case, the steady-state pressure oscillates around the 5.4bar level. There are some visible pressure variations caused by the system itself. It is though that pressure harmonics caused by the pump dual-stage impeller pumping characteristic are present in in the waveform. In addition, any shaft misalignment between the pump and the motor could result in an additional cogging torque which was possibly translated into an additional pressure ripple. The transient bump visible on both Simulink and Bath*fp* pressure plots is thought to be due to the system natural resonance caused by the inertance term.

When the valve is closed cavitation occurs resulting in large pressure spikes as shown in figure 6.13. Consequently a water hammer effect was created with a pressure wave travelling back and forth between the pump and the valve, affecting the fuel test rig behaviour. This travelling wave effect is amplified by the valve mounting arrangement, due to the valve being able to move. Furthermore, the Gamah couplings can allow movement of the pipework. Although the cavitation water hammer effect phenomenon was not included in the models the predicted results show similar trends to the measured data.

The variation in system flow rate versus time when the ball valve is open and closed is shown in figure 6.11. The steady-state behaviour is clearly defined and a flow of around 570 L/min is established when the valve is fully open. There is no flow when the valve is fully closed. The measured transient behaviour is characterised by the flow transition from maximum to zero flow conditions and by flow spikes that are visible just after the valve has closed. The latter phenomenon has arisen as a result of the cavitation water hammer effect in the return line and represents a negative flow as vapour column collapses. Only positive spikes are visible in the figure due to the way in which the flow readings are obtained. Although the turbine flow meter is able to measure positive and negative flow rates, a Hall-effect transducer attached to the flow sensor only provides an absolute frequency measurement. Thus a negative flow rate was measured as a positive value. This effect can be clearly seen on the flow-rate related graphs. During a 0.5s valve operation profile, the spikes have higher magnitudes due to the onset of severe cavitation. The peak flow rate reaches 325 L/min whereas during the one second closure spikes up to 120 L/min are visible. The simulated data do not show any spikes as the cavitation is modelled only as a pressure reduction.

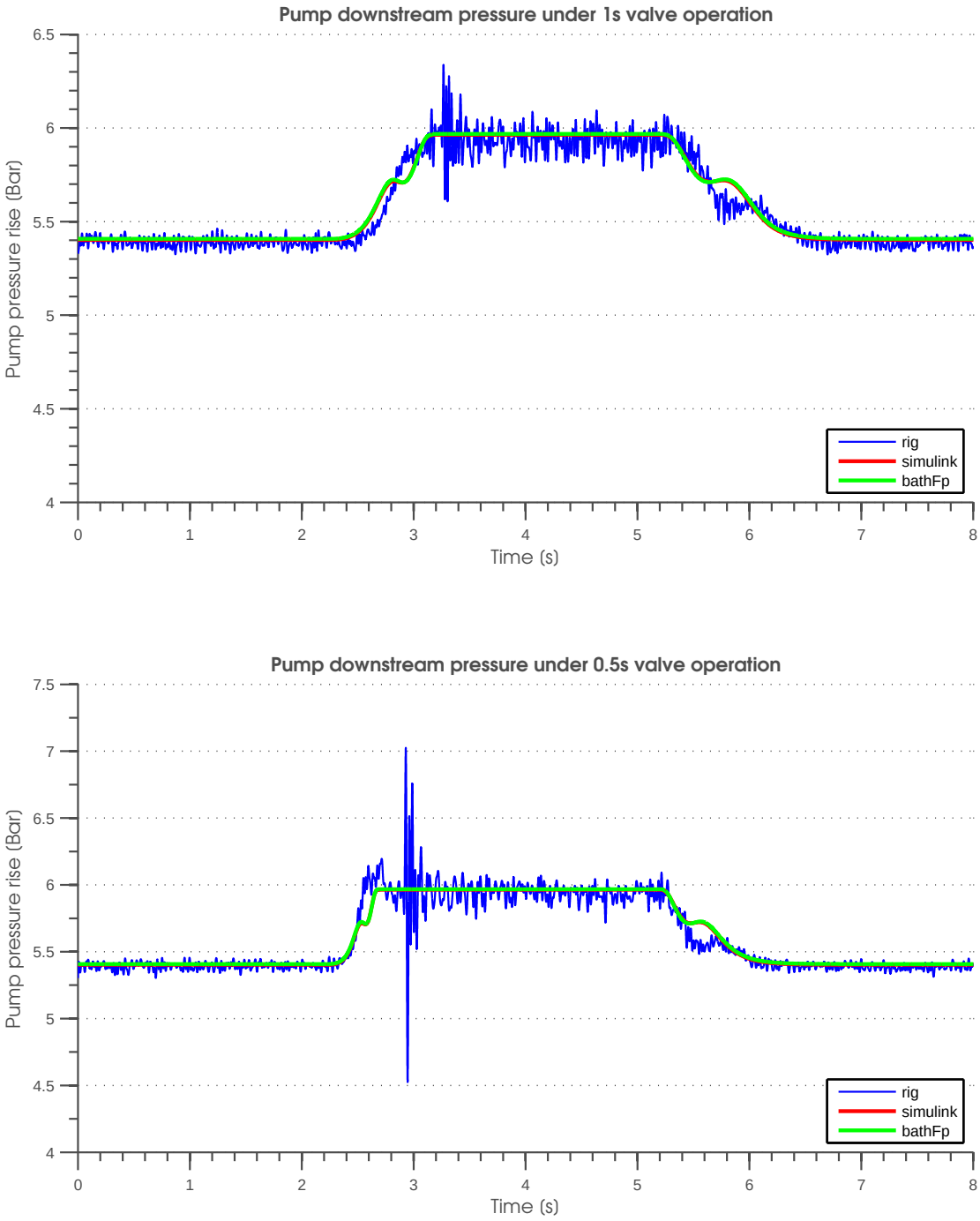

Figure 6.10. Pump downstream pressure under valve operation

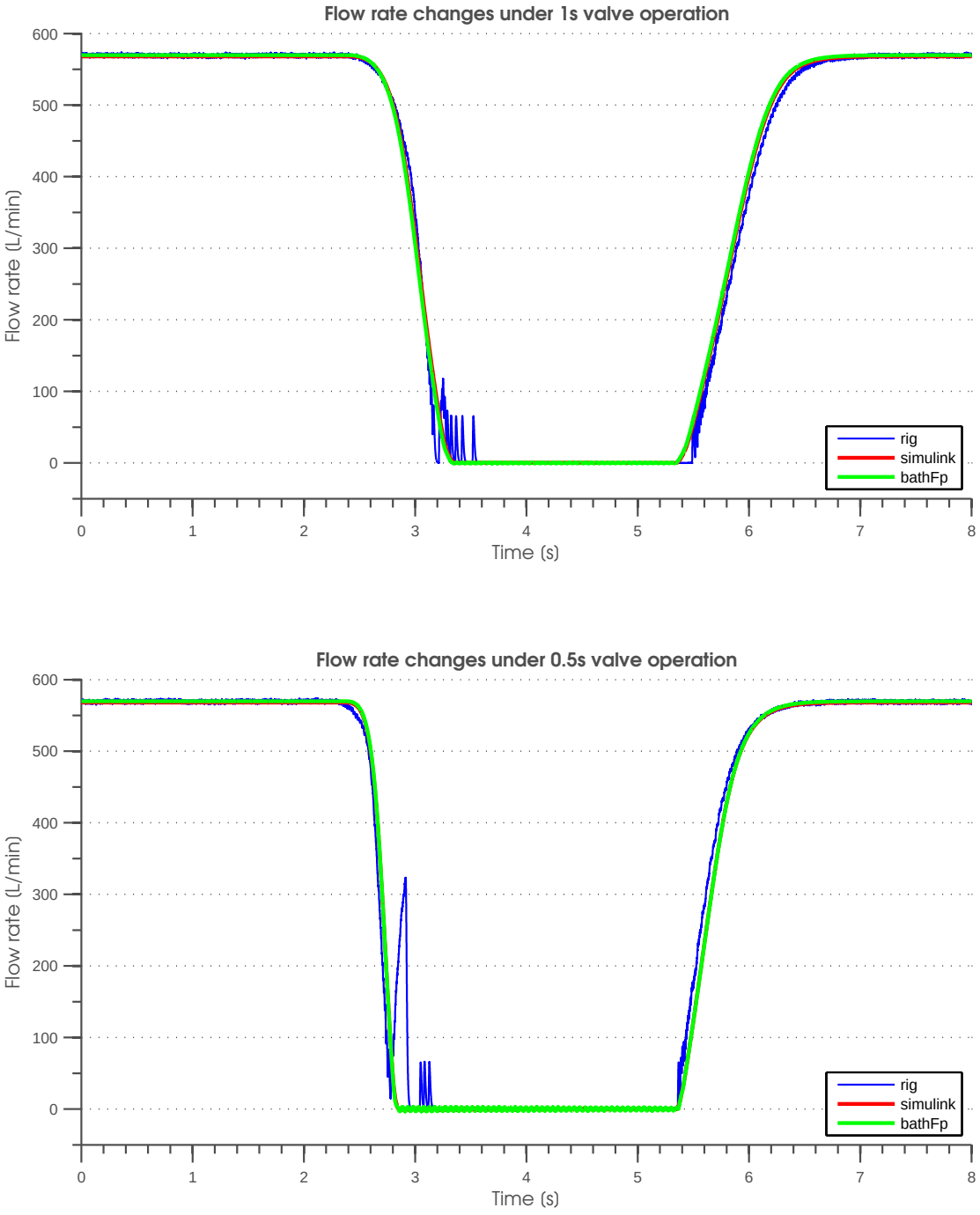

Figure 6.11. System flow rate under valve operation

The pressure at the upstream side of the ball valve is shown in figure 6.12. Due to the fast valve closure, a pressure surge was created and after a settling time the pressure returns to its steady-state value. During the no-flow condition, the steady state pressure rises to a maximum of 5.94bar. The visible oscillation on the simulated data following valve closure is caused by a numerical oscillation due to the low value of damping present. At the maximum flow condition the valve upstream pressure is around 0.43bar and due to the pressure losses at the valve (about 0.2 bar) and the pressure losses in the return pipeline. The decaying oscillation in the valve upstream pressure during valve closure is clearly visible. These oscillations are due to the cavitation water hammer effect mentioned previously.

The transient behaviour was mainly determined by the valve operation time. For a 1s valve closing time, the pressure upstream of the valve (fig. 6.12) peaked to 9bar whereas at the fast 0.5s closing the peak pressure increased to 14bar. Hence, it is possible that the resulting pressure peak could damage the system if the valve is closed too fast. The agreement between the modelled and measured results seems to have good correlation, when the relatively simple models used for the pump and the valve were taken into account. The ball valve was represented by an algebraic equation without an inertance term, while the pump inertia was expressed by a simple state variable model which was used to represent the pump transient behaviour. It was shown [31][30] that the pipework inertance is the dominant term for the system inertance, having a value of 1.84×10^7 kg/m^4, compared with the pump term of 1.35×10^5 kg/m^4 and the valve which varies between $(5.4-13)\times10^5$ kg/m^4 depending on valve angle.

The valve downstream pressure is presented in figure 6.13 where the steady-state pressure responses show good fit with the simulated results. The return line pressure losses are around 0.2bar. The transient caused by the fast valve operation is clearly visible for both the valve closure and opening profiles, respectively. The 0.5s valve closure led to the on-set of more severe cavitation compared to the one second operation. The pressure spikes (up to 35bar) seen in the lower plot were limited on the figure to 10bar since the cavitation analysis was not the prime focus of the validation.

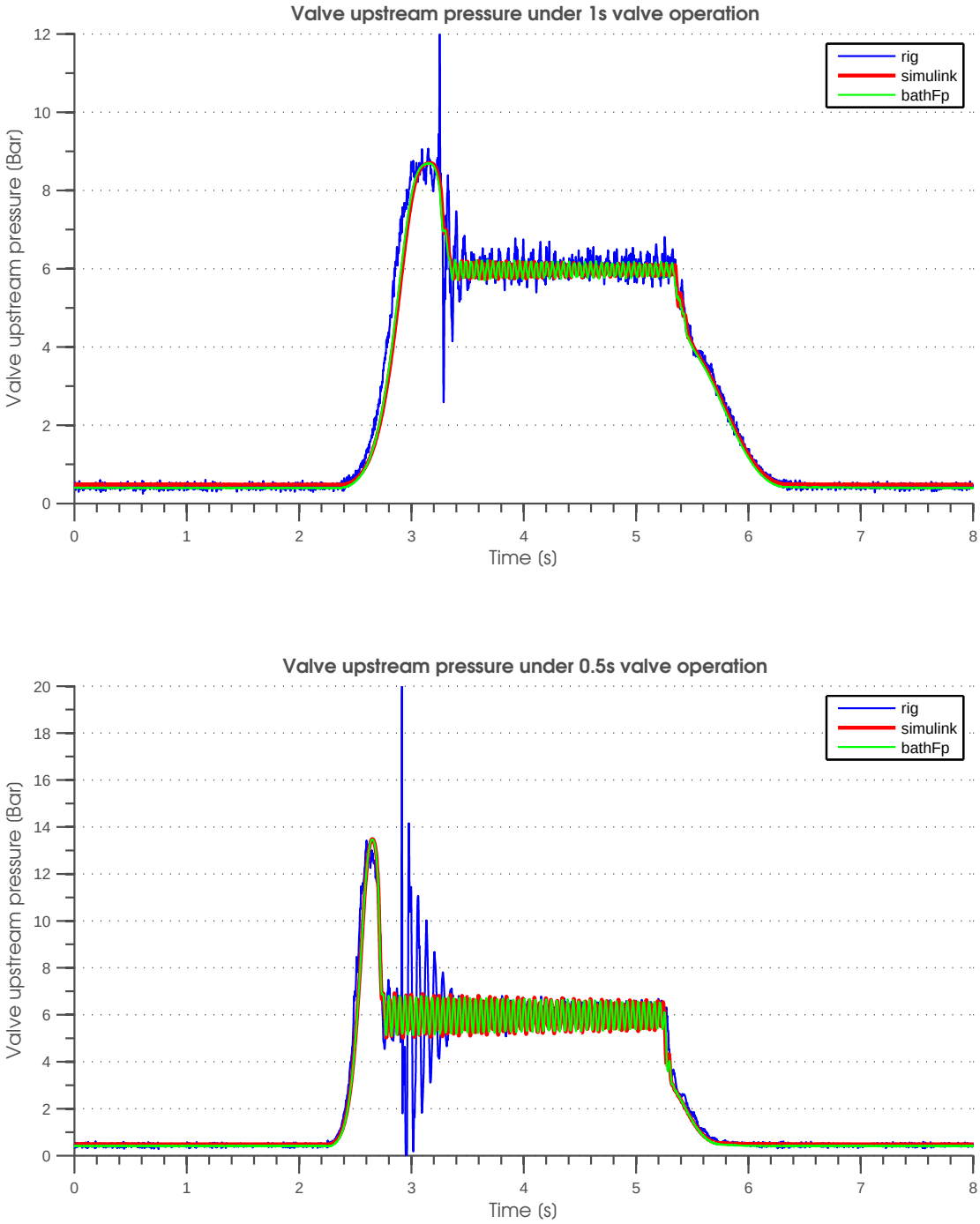

Figure 6.12. Valve upstream pressure under valve operation

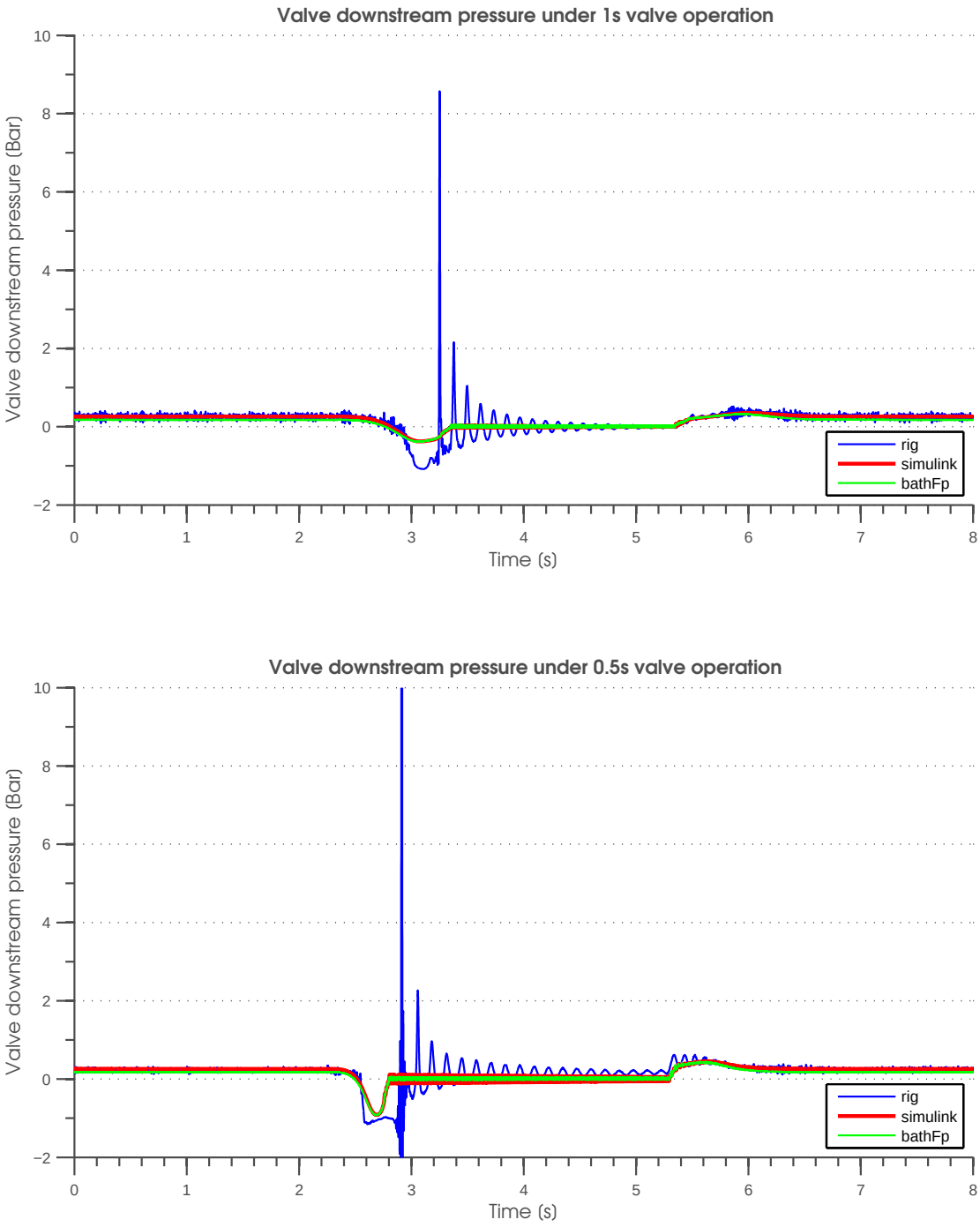

Figure 6.13. Valve downstream pressure under valve operation

Observing the transient data from the rig, the valve downstream pressure falls to below absolute zero pressure (fig.6.13). It is unlikely that such a condition would occur in reality and there are a number reasons why it occurred. The pressure sensors mounted on the rig were set to measure the gauge pressure with respect to the tank head. The transducers fitted downstream of the ball valve were calibrated for a pressure range of 35bar, and therefore at low value signals error could result and electrical noise could dominate the measured signals. The sensor offsetting technique is responsible for the pressure shift of around 0.1bar, since the stationary hydrostatic pressure was also eliminated in this way, causing the pressure signals to fall below absolute zero by this value. During cavitation, the fluid hammer phenomenon could affect the pressure transducer reading as more strain occurred at the time of water hammer propagation. Additionally, the transducer drift could have a small effect on the data reading. However the main source of error is likely to be due to the electrical noise since noise spikes could be significant compared to the low level of a pressure signal.

The motor torque versus time characteristics are depicted in figure 6.14. The steady-state torque produced by the motor is the same as the sum of pump torque demand and motor losses. A torque of 28.5Nm is required at the maximum flow condition falling to 18.5Nm when the valve is closed. The torque ripples are due to using the transducer at the bottom of its measurement range and the effect of electrical noise. The transducer has a 130Nm measurement range with 0.25% measurement accuracy error.

The model and the rig data results seem to have good correlation. However, some error can be seen as the load torque is a function of the pump pressure and system flow. The fact that the pump torque model is based on fitting equations to the measured data is the main source of inaccuracies in the simulated torque predictions. The pump measured characteristic of torque versus hydraulic power was approximated by polynomial functions. The recorded data is shown in figure 5.9 and is slightly scattered so the fitting results have small errors for different operating points. The Simulink torque versus hydraulic power model was implemented as a 5th order polynomial function. The Bath*fp* model is based only on a linear fit to the experimental torque-hydraulic power data and thus could lead to worse result accuracy. The differences in the data approximation are noticeable and the Bath*fp* simulated torque has a consistent 0.6Nm error compared to the Simulink model predictions and rig data. Furthermore, the transducer offsetting has introduced some additional measurement error.

The pump shaft speed data is shown in figure 6.15. Because the torque and speed are coupled, the speed changes as a result of the pump torque fluctuations. Thus the torque errors were propagated into the speed characteristics and vice verse. A dynamic motor model was used in the Simulink simulations and a steady-state model was used in Bath*fp*. The transient differences are visible with the Bath*fp* predictions responding quicker than the Simulink and rig data, especially when the motor speed is reduced .

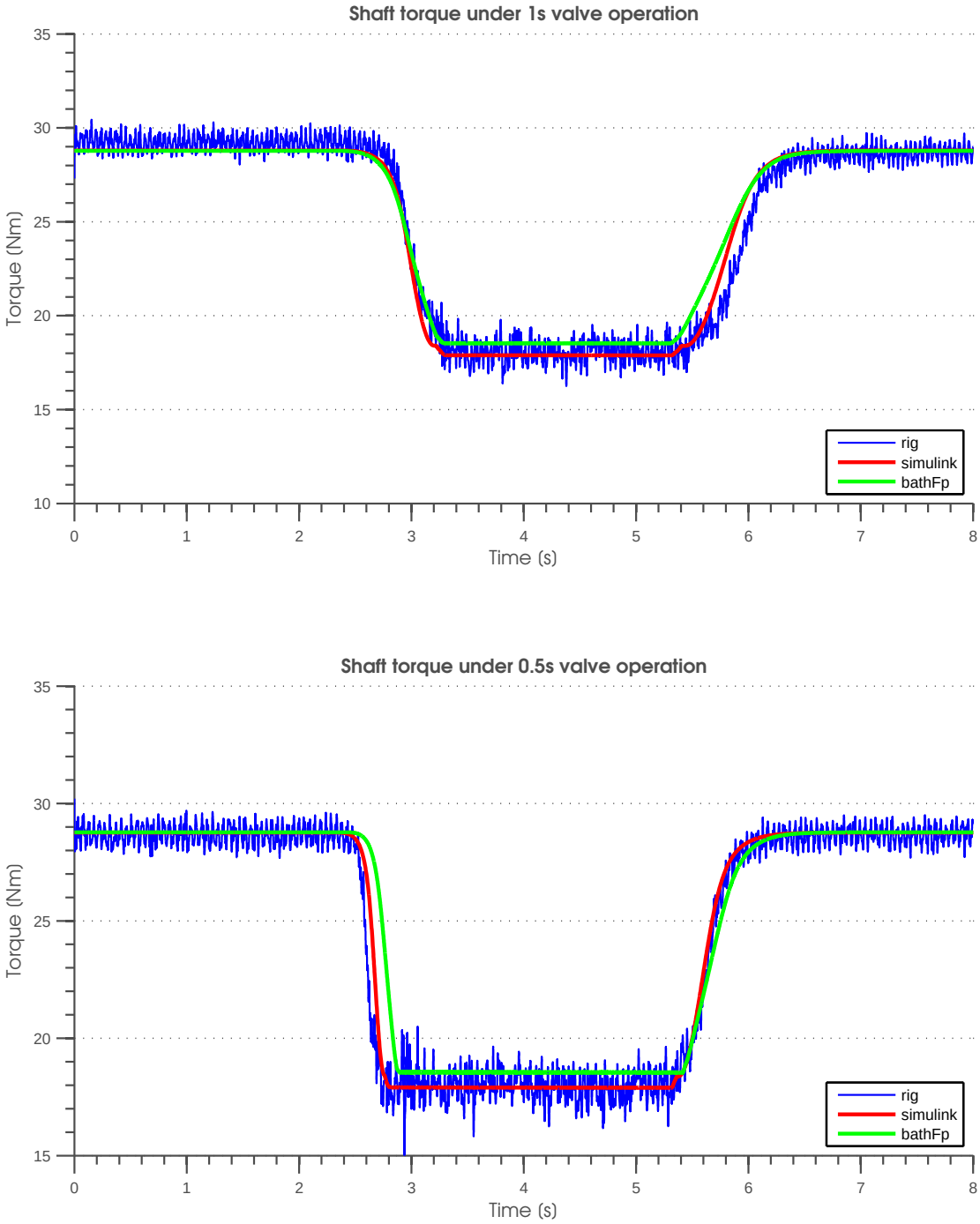

Figure 6.14. Shaft torque under valve operation

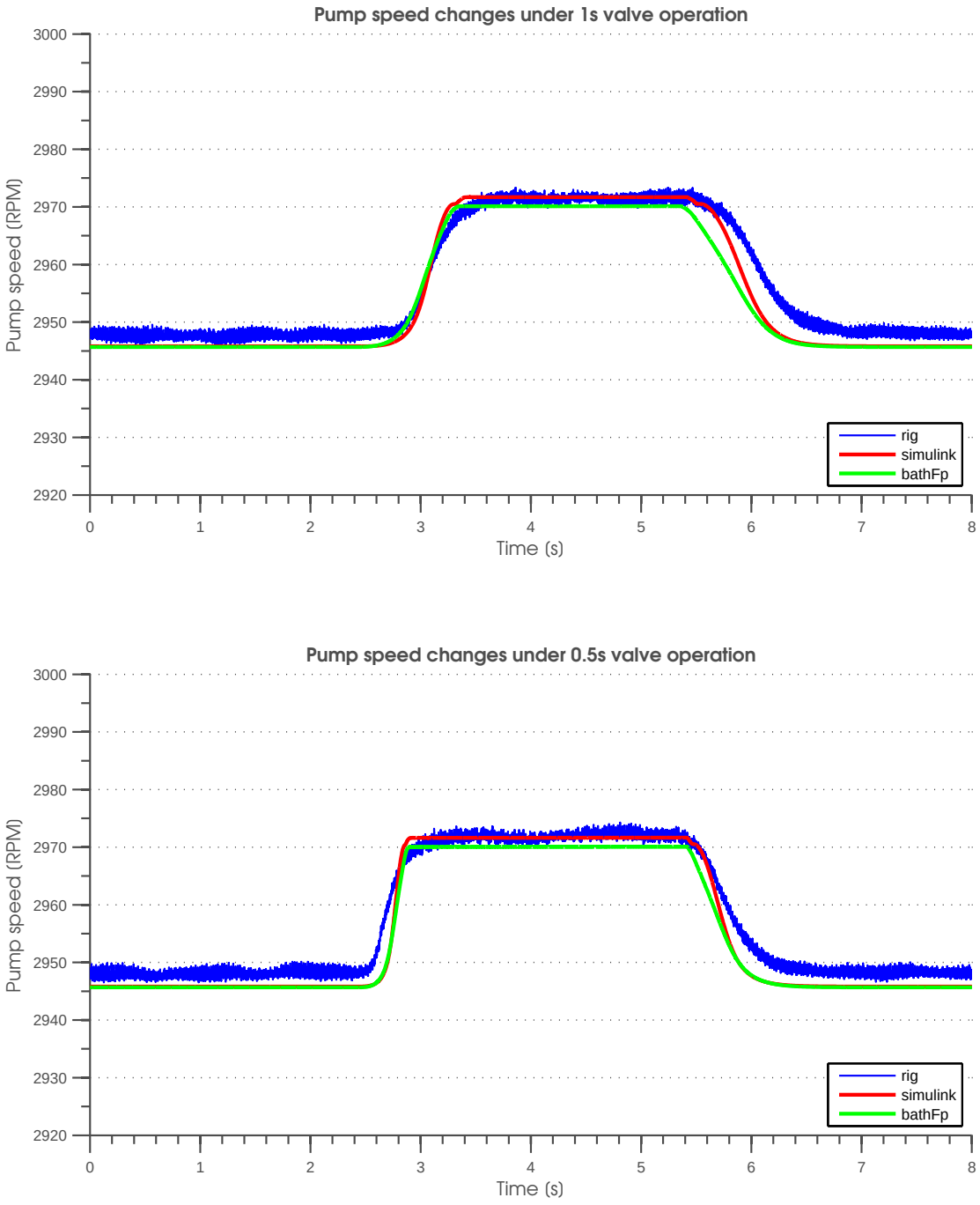

Figure 6.15. Shaft speed under valve operation

A series of tests were conducted on the fuel test rig and the data obtained were compared with model predictions, showing good general fit between them. To avoid the need for a large number of graph plots, the data is presented in tabular form. The simulation data and the results from the test rig is divided into two tables. Table 6.6 indicates the steady state readings for the case when the ball valve was fully open whereas the closed-valve operating conditions are shown in table 6.5. The transient data readings were omitted from the tables as the transient trends are the same for different supply conditions as previously discussed (figures 6.10-6.15). To show the deviations between the simulated and the measured data, the error was calculated and presented in both tables. Since the data simulated in both Simulink and Bath*fp* is consistent, the error calculation presented in tables 6.5 and 6.6 is based on the test rig results and the Simulink predictions.

The tabular data was averaged over the time when the steady state conditions occur. The results are presented in a way such that each supply frequency is separated. Good data agreement can be seen for all the investigated variables. The calculated errors were expressed as a percentage value and are typically in the range of $0 - 1\%$, although errors outside of this band are also present. When the valve is closed, no flow occurs and the flow rate and the valve downstream pressure have both been set to zero.

Both models show consistent results although small differences can be seen for the pressure upstream and downstream of the ball valve. The cause of this is that Bath*fp* uses direct iterative methods (eqn. 5.21) for a friction coefficient calculation whereas the Simulink model is based on an indirect approximation (eqn. 5.22). Slightly larger errors can be seen when the torque and speed are analysed. The sources of these errors can be explained by the fact that the motor was supplied from a PWM inverter with a significant level of harmonic distortion whereas in the models sinusoidal supply conditions were applied. An additional source of error could be introduced by changes in motor parameters, as the induction motor responses are very sensitive to the motor parameter fluctuations. The motor parameters were evaluated at the 50Hz supply frequency and later were adjusted for different supply conditions if required.

The accuracy and measurement ranges of the transducers are presented in appendix B. When the measurements are undertaken at signal levels typically below 10% of the transducer full scale range, the transducer accuracy errors can be significant compared to the measured data and the percentage errors will increase. A source of error has also been introduced by the zero-off-setting technique. In the case when a channel's offset changed the data correction method is used to compensate for the resulting error. Care must be taken when real time analysis or feedback operation is to be conducted as it can affect control techniques.

Supply frequency		Q	P_{Pdown}	P_{Vdown}	P_{Vup}	T	N
[Hz]		[L/min]	[Bar]	[Bar]	[Bar]	[Nm]	[rev/min]
50	rig	0.00	5.932	0.00	5.936	18.09	2971.4
	Simulink	0.00	5.964	0.00	5.964	18.37	2971.6
	Bath*fp*	0.00	5.968	0.00	5.968	18.36	2970.1
	error [%]	–	0.538	–	0.771	1.193	0.019
40	rig	0.00	3.712	0.00	3.744	12.07	2366.6
	Simulink	0.00	3.787	0.00	3.814	11.82	2364.8
	Bath*fp*	0.00	3.782	0.00	3.782	12.85	2363.4
	error [%]	–	0.169	–	0.579	2.075	0.074
30	rig	0.00	2.103	0.00	2.084	6.914	1769.2
	Simulink	0.00	2.115	0.00	2.094	6.842	1769.7
	Bath*fp*	0.00	2.121	0.00	2.119	6.865	1768.1
	error [%]	–	0.570	–	0.486	1.049	0.024

Table 6.5. Rig validation for closed valve operation

Supply frequency		Q	P_{Pdown}	P_{Vdown}	P_{Vup}	T	N
[Hz]		[L/min]	[Bar]	[Bar]	[Bar]	[Nm]	[rev/min]
50	rig	569.9	5.388	0.256	0.436	29.13	2947.5
	Simulink	567.8	5.403	0.259	0.484	29.26	2945.6
	Bath*fp*	569.8	5.407	0.176	0.404	29.27	2945.6
	error [%]	0.372	0.266	1.216	11.208	0.842	0.057
40	rig	446.9	3.401	0.158	0.279	18.65	2341.7
	Simulink	445.6	3.420	0.163	0.302	18.61	2340.3
	Bath*fp*	447.1	3.427	0.116	0.256	18.59	2340.2
	error [%]	0.305	0.574	3.136	8.247	0.233	0.060
30	rig	326.3	1.896	0.088	0.152	10.50	1745.3
	Simulink	328.6	1.909	0.089	0.165	10.53	1746.2
	Bath*fp*	327.9	1.920	0.070	0.145	10.53	1746.0
	error [%]	0.705	0.685	1.394	8.445	0.421	0.051

Table 6.6. Rig validation for open valve operation

6.3.1 Model comparison

The fuel rig system simulations were carried out using the Matlab/Simulink and Bath*fp* simulation packages. Data from the two packages were compared and validated against the fuel rig results. It was shown that the simulation data from both models seem to have good correlation when compared to each other, although some differences exist due to model inaccuracies and limitations.

The pipe friction factor evaluation was based on different estimation techniques in both models. The data from Bath*fp* employs the Colebrook iterative algorithm presented in equation (5.21) whereas the Simulink model uses the direct Halland-method approximation presented in (5.22). Although, the explicit Colebrook method was expected to give more accurate predictions, the Halland method gave satisfactory results. The second difference in the modelling approach was the load torque calculation. While the models were both based on test rig measurements, different fitting techniques were applied. A linear approximation of the pump torque characteristic was used in Bath*fp* and a 5th order polynomial was employed in Simulink. Consequently the Simulink model gave better accuracy.

Although the hydraulic components are better represented in the hydraulic-orientated Bath*fp* package, the control and the electrical component modelling are more easily implemented in the Simulink software. Thus the steady-state induction motor model was used in the former model and the transient model of the induction machine was implemented in the latter, resulting in small behaviour differences and showing a Simulink model advantage.

Although different numerical integration techniques were used for solving the differential equations, a stiff integration algorithm was employed in both models. In both cases a numerical artificial natural frequency with low damping occurred resulting in ripples and oscillations in pipeline models. The Bath*fp* model used a standard inertial pipe model with 10 elements whereas in Simulink only 2 stages were employed. The impact of the number of stages was investigated and it is considered that the Simulink implementation is sufficiently accurate. The higher number of pipe elements resulted in a significant slowing of simulation result computation and the Simulink model solving time was approximately 10 times faster than the Bath*fp*.

The Simulink rig model was created specially for the project by the author. The main goal of the model comparisons was to show results consistency as the Simulink is a general purpose software package whereas the Bath*fp* is hydraulic-pneumatic orientated software. The simulated results and validation data show that the Simulink-based hydraulic model gives satisfactory accuracy and system response. Having proven and validated the model, the research can be extended to include different control strategies for the electric motor.

6.4 Closure

In order to simulate the behaviour of the fuel test rig a hydraulic system model was developed. The model comprises of a tank, a centrifugal pump driven by a motor drive system, a long section of pipeline containing various bends and couplings, a motor driven ball valve and a return line. The complete model was developed in two simulation packages, Bath*fp* and Simulink, which were used to simulate performance during both steady-state and dynamic operations. The models were tested for a number of different supply conditions and under two developed valve operation profiles. It was shown that the system and component models were capable of predicting the rig performance over a variety of operating conditions despite a number of simplifying approximations made taken during modelling.

The models developed in two different modelling packages were compared. The differences between the simulation packages results were identified. It is clear that the results obtained from the models developed in both packages compare well in general and are in close agreement with the test-rig data. The Simulink model was chosen for further test-rig simulations due to the convenience of model implementation and modifications as well as due to the faster solution computation time.

Chapter 7

Open and Closed Loop Control of the Motor Drive System

7.1 Linear Model of Fuel Test Rig

The fuel test rig is a non-linear system with many independent variables. In order to analyse this system using well establish linear modelling techniques, the non-linear system was linearised over a restricted operating range. An approximate linear model of the system was used to determine system frequency responses and time constants. Control of the pump outlet pressure was then investigated using a linear PI closed loop control technique with to the motor drive system.

7.1.1 Linearisation technique

The *Small Perturbation Technique* can be used to linearise continuous non-linearities for small changes around an operating point. This approach is based on the expansion of the non-linear model using the Taylor series about the operating points, neglecting higher order terms [64].

A non-linear function defined in terms of n variables can be linearised using Taylor series [65], where the higher order terms are neglected as follows

$$f(x_1 + \Delta x_1 \ldots x_n + \Delta x_n) = f(x_{1_0} \ldots x_{n_0}) + \sum_{i=1}^{n} \left.\frac{\partial f(x_i)}{\partial x_i}\right|_{x_i = x_{i_0}} \Delta x_i \tag{7.1}$$

The linearised equation in proximity of the operating points can be then expressed as

$$f\left(x_1 + \Delta x_1 \ldots x_n + \Delta x_n\right) = c_0 + \sum_{i=1}^{n} c_i \Delta x_i \tag{7.2}$$

where c_n is the normalised coefficient for each independent variable.

7.1.2 Ball valve model

The flow through a ball valve can be expressed in terms of the flow coefficient C_q, the area A_v and the pressure drop Δp across the valve as follows

$$Q = C_q(\alpha) A_v(\alpha) \sqrt{\frac{2\Delta p}{\rho}} \tag{7.3}$$

Since the flow coefficient and the valve active area are nonlinear functions of the valve angle as shown in section 5.4, the valve angle α is the independent variable used in the linearisation.

Applying the linearisation technique to equation (7.3) yields a linear approximation of the valve flow valid around an equilibrium point Q_0 and is given by

$$Q\left(\Delta p, \alpha\right) = v_0 + v_1\left(\alpha - \alpha_0\right) + v_2\left(\Delta p - \Delta p_0\right) \tag{7.4}$$

where the linearised coefficients are calculated from

$$v_0 = Q\left(\Delta p_0, \alpha_0\right) = C_q\left(\alpha_0\right) A_v\left(\alpha_0\right) \sqrt{\frac{2\Delta p_0}{\rho}} \tag{7.5}$$

$$v_1 = \left.\frac{\partial Q}{\partial \alpha}\right|_{\Delta p_0, \alpha_0} = \sqrt{\frac{2\Delta p_0}{\rho}} \left(\left.\frac{\partial C_q(\alpha)}{\partial \alpha}\right|_{\alpha_0} A_v(\alpha_0) + \left.\frac{\partial A_v(\alpha)}{\partial \alpha}\right|_{\alpha_0} C_q(\alpha_0) \right) \tag{7.6}$$

$$v_2 = \left.\frac{\partial Q}{\partial p}\right|_{\Delta p_0, \alpha_0} = C_q(\alpha_0) A_v(\alpha_0) \sqrt{\frac{1}{2\rho\Delta p_0}} \tag{7.7}$$

where the valve angle dependent variables are as follows

$$C_q\left(\alpha\right) = v_{c1}\alpha^6 + v_{c2}\alpha^5 + v_{c3}\alpha^4 + v_{c4}\alpha^3 + v_{c5}\alpha^2 + v_{c6}\alpha + v_{c7} \tag{7.8}$$

$$A_v\left(\alpha\right) = v_{a1}\alpha^6 + v_{a2}\alpha^5 + v_{a3}\alpha^4 + v_{a4}\alpha^3 + v_{a5}\alpha^2 + v_{a6}\alpha + v_{a7} \tag{7.9}$$

$$\frac{\partial C_q(\alpha)}{\partial \alpha} = 6v_{c1}\alpha^5 + 5v_{c2}\alpha^4 + 4v_{c3}\alpha^3 + 3v_{c4}\alpha^2 + 2v_{c5}\alpha + v_{c6} \tag{7.10}$$

$$\frac{\partial A_v(\alpha)}{\partial \alpha} = 6v_{a1}\alpha^5 + 5v_{a2}\alpha^4 + 4v_{a3}\alpha^3 + 3v_{a4}\alpha^2 + 2v_{a5}\alpha + v_{a6} \tag{7.11}$$

The value of the valve coefficients have been presented previously in tables 5.6 and 5.7.

Thus the valve linear model in the s-domain can described by a simple gain term.

The pressure loss Δp across the valve is the pressure difference between the supply line outlet pressure p_v and the return line pressure p_{rl}

$$\Delta p = p_v - p_{rl} \tag{7.12}$$

where p_v and p_{rl} are described in the following subsections.

7.1.3 Pipeline model

It was shown in section 5.2 that the pipe behaviour can be described by the following set of non-linear equations that include the compressibility, resistance and inertia of the fluid,

$$Q - Q_v = C\frac{dp}{dt} \tag{7.13}$$

$$p - p_v = L\frac{dQ}{dt} + RQ\,|Q| \tag{7.14}$$

where the pipe inertance L and the capacitance C can be found from

$$L = \rho\frac{l}{A} \tag{7.15}$$

$$C = \frac{V}{B} \tag{7.16}$$

The pipe resistance R depends on the flow regime and is governed by the pressure-flow relationship given in

$$\delta p = \left(\frac{8fl\rho}{\pi^2 d^5} + \frac{8K\rho}{\pi^2 d^4}\right) Q\,|Q| \tag{7.17}$$

The fluid resistance R can be then calculated from

$$R = \frac{8\rho}{\pi^2 d^5}\,(fl + Kd) \tag{7.18}$$

where the friction factor f depends on the flow regime, and is characterised by the complex non-linear relationship described previously in section 5.2.

Since the pipe resistance is described by a non-linear relationship, this has to be linearised for use in the linear analysis.

The linear set of pipe equations are then as follows

$$Q - Q_v = C\frac{dp}{dt} \tag{7.19}$$

$$p - p_v = L\frac{dQ}{dt} + r_p\,(Q - Q_0) \tag{7.20}$$

where the linearised resistance coefficient r_p is calculated from

$$r_p = \left.\frac{\partial(\delta p)}{\partial Q}\right|_{Q_0} = 2R|Q_0| \tag{7.21}$$

7.1.4 Return pipeline model

The pressure loss across the return pipeline fitted between the ball valve and the tank, p_{rl}, is represented in the model by a non-linear function of the flow in terms of loss factor as

$$p_{rl} = K_{rl} Q|Q| \tag{7.22}$$

where the K factor K_{rl} was found experimentally and a value of 0.729 is used in the model.

The linearised equation describing the return line pressure loss is as follows

$$p_{rl} = r_0 + r_1 (Q - Q_0) \tag{7.23}$$

where the linearisation coefficients are calculated from

$$r_0 = K_{rl} Q_0^2 \tag{7.24}$$

$$r_1 = \left.\frac{\partial p_{rl}}{\partial Q}\right|_{Q_0} = 2K_{rl} Q_0 \tag{7.25}$$

7.1.5 Centrifugal pump model

The mathematical model of the centrifugal pump employed in the rig is based on the measured non-dimensional pressure-flow characteristic previously presented in figure 5.8, which can be approximated by a square function as

$$\psi = p_{d1}\phi^2 + p_{d2}\phi + p_{d3} \tag{7.26}$$

where the coefficients were experimentally determined by Boyd [31] and are presented in table 7.1.

p_{d1}	−73.659
p_{d2}	0.6569
p_{d3}	2.2476
γ_{l1}	0.6355
γ_{l2}	0.1117

Table 7.1. Pump fitting coefficients used in linear model

Using the Affinity laws and the pressure and flow non-dimensionalised equations given in section 5.3 the pump pressure-flow pump characteristics as a function of speed ω was determined as

$$p(\omega, Q) = \frac{\rho r^2}{2v^2}\left(p_{d1}Q^2 + p_{d2}vQ\omega + p_{d3}v^2\omega^2\right) \tag{7.27}$$

This non-linear equation can be approximated by a linear function as follows

$$p(\omega, Q) = p_0 + p_1(\omega - \omega_0) + p_2(Q - Q_0) \tag{7.28}$$

where the linear proportionality coefficients are calculated from

$$p_0 = p(\omega_0, Q_0) = \frac{\rho r^2}{2v^2}\left(p_{d1}Q_0^2 + p_{d2}vQ_0\omega_0 + p_{d3}v^2\omega_0^2\right) \tag{7.29}$$

$$p_1 = \left.\frac{\partial p(\omega, Q)}{\partial \omega}\right|_{Q_0, w_0} = \frac{\rho r^2}{2v^2}\left(2p_{d3}v^2\omega_0 + p_{d2}vQ_0\right) \tag{7.30}$$

$$p_2 = \left.\frac{\partial p(\omega, Q)}{\partial Q}\right|_{Q_0, w_0} = \frac{\rho r^2}{2v^2}\left(2p_{d1}Q_0 + p_{d2}v\omega_0\right) \tag{7.31}$$

The pump torque model is based on the measured hydraulic power-torque characteristic. The torque model was obtained in a similar way as the pump pressure-flow characteristic using the Affinity laws and the torque non-dimensionalised equation (5.62) and is given by

$$T_l = \gamma_{l1}\frac{Qp}{\omega} + \frac{1}{2}\gamma_{l2}\rho v\omega^2 r^2 \tag{7.32}$$

where γ_{l1} and γ_{l2} coefficients are listed in the table 7.1. The torque equation is a non-linear function of the pump pressure rise, the system flow rate and the shaft speed and therefore has to be linearised.

The pump torque can be approximated by the following linear relationship

$$T_l(Q, \omega, p) = l_0 + l_1(Q - Q_0) + l_2(\omega - \omega_0) + l_3(p - p_0) \tag{7.33}$$

where the linearisation coefficients are calculated from

$$l_0 = \gamma_{l1}\frac{Q_0 p_0}{\omega_0} + \frac{1}{2}\gamma_{l2}\rho v\omega_0^2 r^2 \tag{7.34}$$

$$l_1 = \gamma_{l1}\frac{p_0}{\omega_0} \tag{7.35}$$

$$l_2 = -\gamma_{l1}\frac{Q_0 p_0}{\omega_0^2} + \gamma_{l2}\rho v r^2\omega_0 \tag{7.36}$$

$$l_3 = \gamma_{l1}\frac{Q_0}{\omega_0} \tag{7.37}$$

7.1.6 Motor drive system model

The steady state induction motor model described in section 3.3 was used in the linear analysis because it was assumed that the motor mechanical constant (0.019s) is larger than the rotor constant (0.0085s). In addition, the inverter protection features mainly determine the motor drive system time response and the resulting signal ramping time (time constant of 0.1s) was likely to be significantly larger than either the rotor or mechanical response times.

An induction machine in the steady-state operates in the linear region where the slip s is kept at a minimum value (typically $s < 5\%$). Therefore it was also assumed that the rotor resistance term R_r/s is significant compared to the other motor impedance terms shown in equation 3.26. Ignoring smaller terms of motor impedance, the steady-state torque characteristic of an induction motor can be approximated by

$$T_e \approx \frac{3V^2}{(R_r/s)\omega_s} \approx \frac{3V^2(\omega_s - \omega_r)}{R_r\omega_s^2} \tag{7.38}$$

It can be seen that the motor torque is a function of the supply voltage V, the supply angular frequency ω_s and the motor operating speed ω_r.

The induction motor employed in the fuel rig is driven by a PWM inverter under the Volt per Hertz control strategy. The V/f proportionality coefficient k_Ψ which determines the relationship between the output voltage and supply frequency f_e, or supply angular frequency ω_s, is defined as

$$k_\Psi = \frac{V}{f_e} = \frac{2\pi V}{\omega_s} \tag{7.39}$$

Substituting (7.39) into (7.38) yields the steady-state induction motor torque approximation as a function of the motor synchronous speed and the rotor operating speed as follows

$$T_e \approx \frac{3}{2\pi}\frac{k_\Psi^2 f_e s}{R_r} \approx \frac{3}{4\pi^2}\frac{k_\Psi^2(\omega_s - \omega_r)}{R_r} \tag{7.40}$$

For small changes around the operating speed, the torque relationship can be expressed as a linear function of the synchronous and rotor speeds using

$$T_e(\omega_s, \omega_r) = m_0 + m_1(\omega_s - \omega_{s_0}) + m_2(\omega_r - \omega_{r_0}) \tag{7.41}$$

where the proportionality coefficients are calculated from

$$m_0 = T_e(\omega_{r_0}, \omega_{s_0}) = \frac{3}{4\pi^2} \frac{k_\Psi^2 (\omega_{s_0} - \omega_{r_0})}{R_r} \tag{7.42}$$

$$m_1 = \left.\frac{\partial T_e}{\partial \omega_r}\right|_{\omega_{r_0}, \omega_{s_0}} = \frac{3}{4\pi^2} \frac{k_\Psi^2}{R_r} \tag{7.43}$$

$$m_2 = \left.\frac{\partial T_e}{\partial \omega_s}\right|_{\omega_{r_0}, \omega_{s_0}} = -\frac{3}{4\pi^2} \frac{k_\Psi^2}{R_r} \tag{7.44}$$

The PWM inverter is the source of power to the induction motor. The inverter is controlled by an analogue input signal within a range of 0-10V. This highly nonlinear system determines the motor time response due to protection features which slow down the inverter response. Owing to the relatively fast response of the inverter, it was assumed that a first-order lag model would approximate the inverter dynamics adequately. The transfer function used to describe the inverter is a function of

$$I(s) = \frac{K_i}{t_i s + 1} \tag{7.45}$$

the inverter gain K_i and the inverter dominant time constant t_i, which was determined by the maximum ramp time of the analogue input control signal. The s is Laplace-domain operator.

7.1.7 Linear model of the fuel test rig

Based on the linear component models determined in the previous sub-sections, a linear model of the complete fuel test rig was developed in Simulink. The aim of the linear analysis was to determine the system transfer function, from which the system gains and time constants could be determined. The system diagram of the linear fuel test rig is presented in figure 7.1. The inputs to the system are the inverter analogue control signal and the ball valve position control signal and the model output is the pump outlet pressure. The linear model analysis is based on the physical properties of the component models listed in table 7.2.

In order to validate the fuel test rig linear model, the model was linearised about the operating points given in table 7.3 and the results compared with the non-linear fuel test rig model described in chapter 6. Unit step control signals were applied to the inputs, each at a separate time and the change in pump output pressure determined. The results obtained are shown in figure 7.2. As can be seen from the figure the linear model predictions seem to be in good agreement with its nonlinear counterpart despite the assumptions made during the model linearisation.

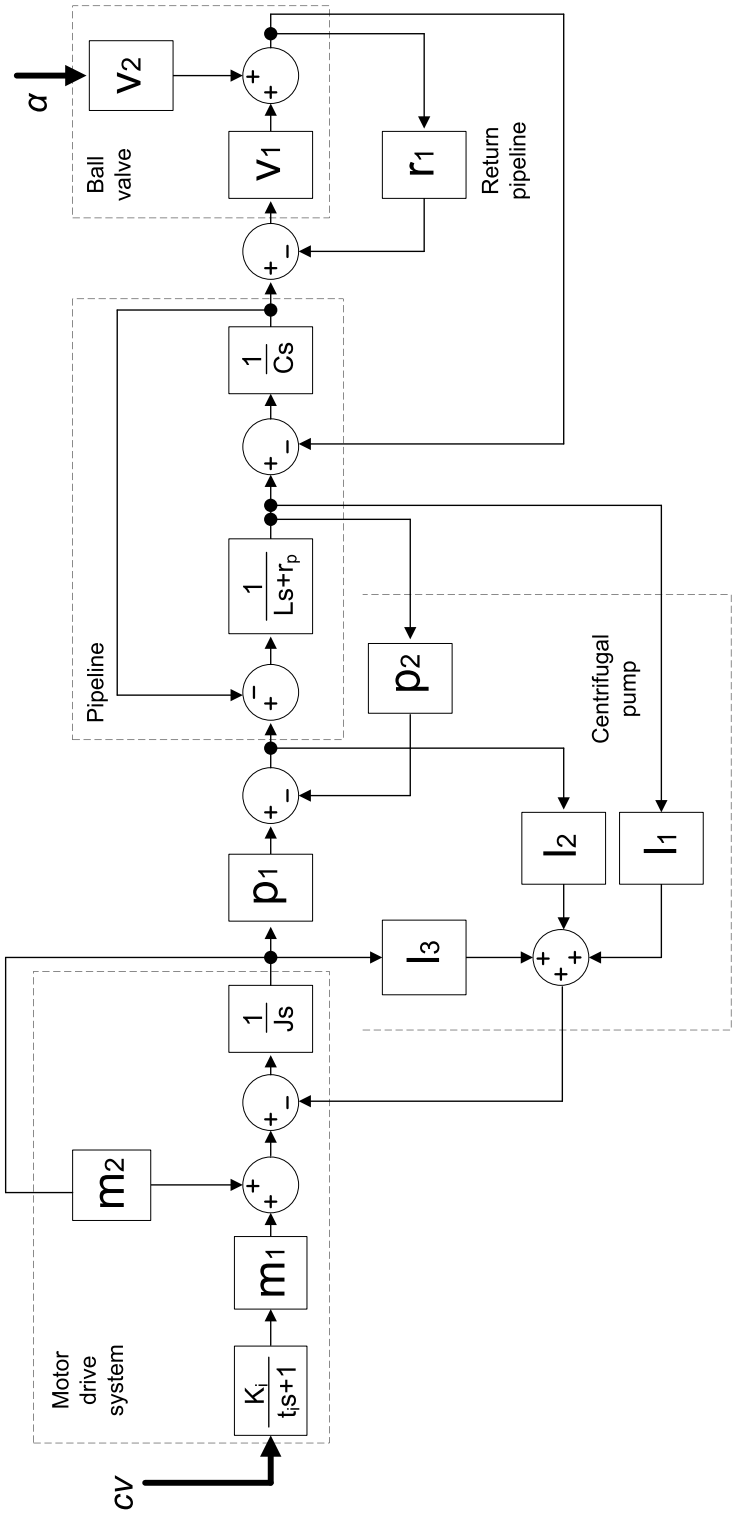

Figure 7.1. Linear model of the fuel test rig

Parameter	symbol	unit	value
Inverter gain	K_i	-	31.41
Inverter time constant	t_i	s	0.1
Inverter V/f constant	k_Ψ	V/Hz	8
Rotor resistance	R_r	Ω	0.909
Motor Inertia	J_m	kgm^2	0.019
Load Inertia	J_l	kgm^2	0.020
Pump impeller radius	r	m	0.0735
Water density	ρ	kg/m^3	998
Pump volume displacement	υ	m^3	6.0686×10^{-4}
Pipe length	l	m	16.6
Pipe relative roughness	ϵ/d	-	5.5×10^{-5}
Pipe diameter	d	m	0.0344
Fluid bulk modulus	B_f	Pa	8.17×10^9
Minor losses K factor	K	-	1.7
Return line K factor	K_{rl}	-	0.729

Table 7.2. Fuel test rig coefficients and variables used during linearisation

f_0	50	Hz
N_0	2944	rpm
Q_0	568	L/min
α_0	0	deg

Table 7.3. Operating points used for the model linearisation to validate the model

The transfer function of this system was determined from the linear model developed for the fuel test rig. Since there are two inputs to the system and one output, the transfer function can be expressed in the form of

$$P_p(s) = P_{mp}(s) + P_{vp}(s) \tag{7.46}$$

where $P_{mp}(s)$ and $P_{vp}(s)$ are the transfer functions defined between the inverter, the valve inputs and the pump output pressure, respectively.

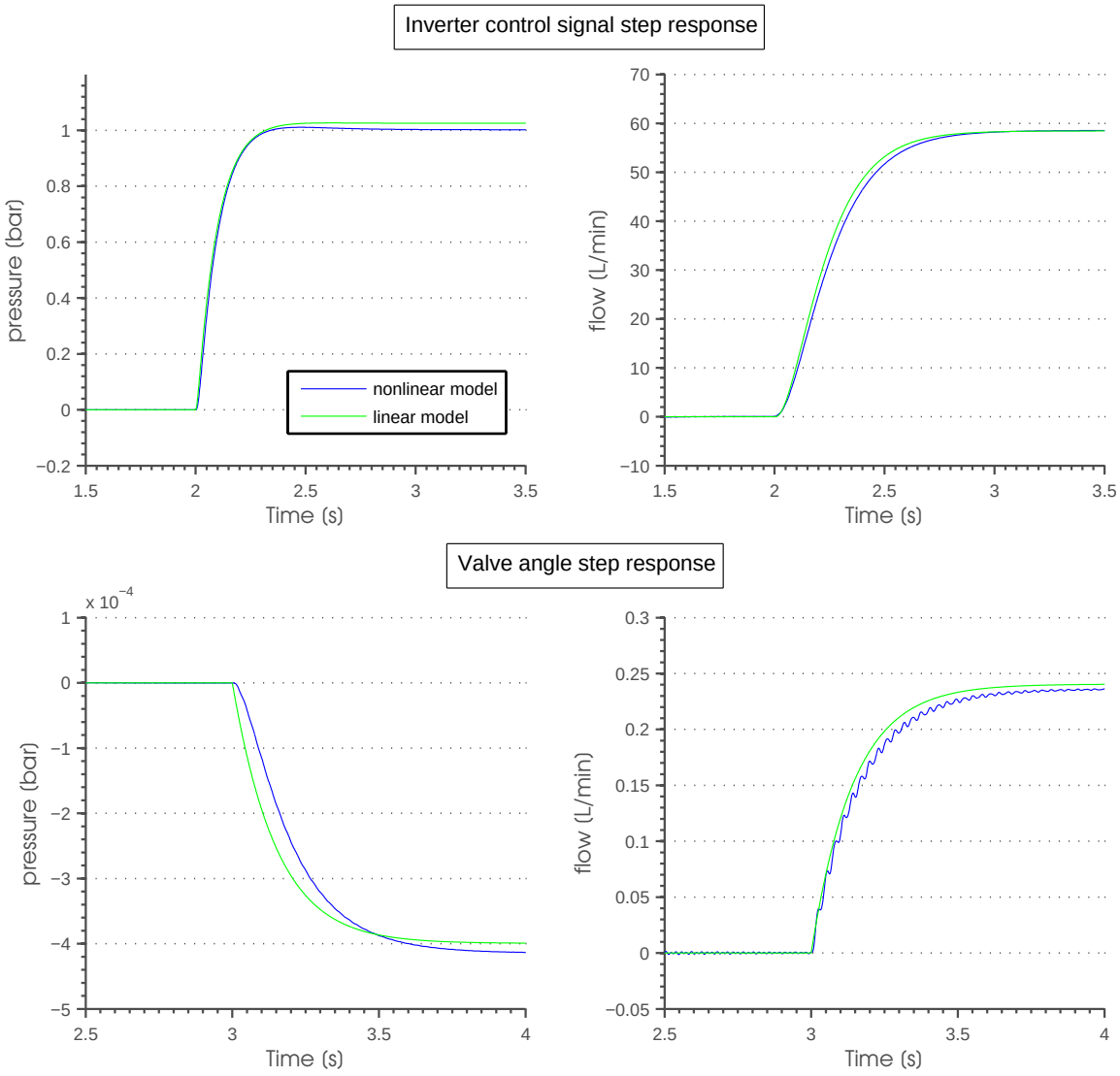

Figure 7.2. Comparison of linear and non-linear fuel rig model responses

The Simulink control system toolbox was used for the transfer function determination. By applying the appropriate linear analysis tool to the developed linear model at different operating points, both transfer functions were determined as follows

$$P_{mp}(s) = \frac{K_{mp}}{(s + p_{m1})(s + p_{m2})} \tag{7.47}$$

$$P_{vp}(s) = \frac{K_{vp}(s + z_v)}{(s + p_{v1})(s + p_{v2})(s + p_{v3})} \tag{7.48}$$

where K_{mp} and K_{vp} are the steady state (DC) gains and p and z are the poles and the zero of the transfer functions, respectively. The values for the poles and the zero are dependent on the system operating conditions.

Transfer function modelling approach was used to determine the system responses for different supply and valve angle operating conditions. Frequency response analysis was performed on each of the developed transfer functions and a dominant time constant and a DC gain were determined for each case considered. The data obtained is presented in tables 7.4 and 7.5 for the inverter-pump and valve-pump transfer functions, respectively.

From both tables it is clear that the system response exhibits similar trends, depending upon the operating conditions. The inverter-input dominant time constant is independent of the supply frequency and valve angle changes, whereas the valve-input dominant time constant increases when the supply condition decreases. The valve angle changes also affect the system time response, because the dominant time constant increases when the ball valve closes, reaching a maximum value when the valve is fully closed. The inverter-pump transfer-function steady state gain is fairly constant during valve angle changes but reduces slightly when the supply frequency is reduced. The DC gains obtained for the valve-pump transfer functions also exhibit a similar pattern. The steady-state gain increases when the motor supply frequency is reduced, however, and during valve operation the gain shows some variation with valve angle. It has its maximum value at 0°, which decreases when valve angle is increased up to 45°, when it reaches a minimum. The value then increases at larger value angles.

The families of Bode plots developed for the transfer functions at different supply conditions are presented in figures 7.3 and 7.4 for the inverter-pump and the valve-pump transfer functions, respectively. Since both families of the transfer functions exhibit similar frequency response patterns, only changes in the motor supply frequency obtained at a 0° valve angle are shown on the figures.

As can be seen from figure 7.3, the inverter-pump frequency characteristics can be modelled as two first-order lags. It is evident that the system time response is determined by a dominant time constant, which is due to the inverter. The valve-pump transfer function frequency responses (7.4) can also be described by a two first order lag model, although mathematically this system is expected to have three poles as indicated in equation 7.48. However, one pole is cancelled by the zero resulting in the response shown in figure 7.4.

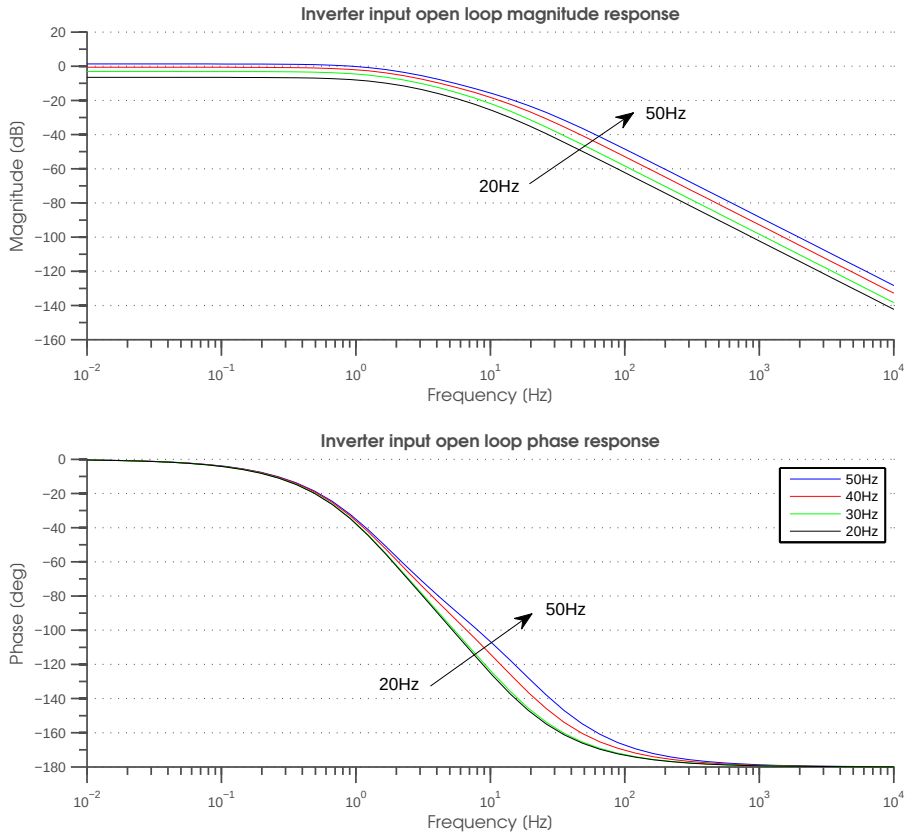

Figure 7.3. Bode plot of inverter-input transfer functions at 0° valve angle linearisation point

Supply		Valve angle [deg]			
Hz		0	30	45	60
50	Gain [dB]	1.328	1.308	1.275	1.236
	Time constant [s]	0.1	0.1	0.1	0.1
40	Gain [dB]	−0.597	−0.563	−0.584	−0.605
	Time constant [s]	0.1	0.1	0.1	0.1
30	Gain [dB]	−3.076	−3.005	−3.020	−3.0416
	Time constant [s]	0.1	0.1	0.1	0.1
20	Gain [dB]	−6.523	−6.4745	−6.4961	−6.5225
	Time constant [s]	0.1	0.1	0.1	0.1

Table 7.4. Inverter-input transfer function dominant time constants and the DC gains

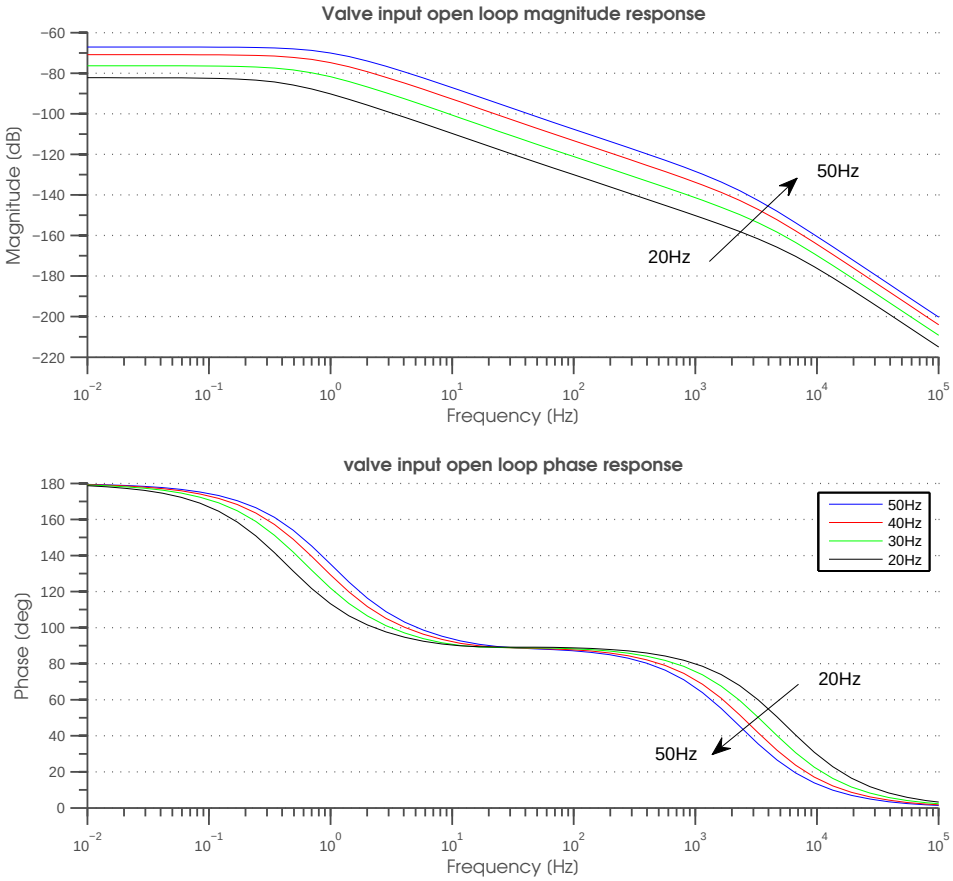

Figure 7.4. Bode plot of valve-input transfer functions at 0° valve angle linearisation point

Supply		Valve angle [deg]			
Hz		0	30	45	60
50	Gain [dB]	−67.089	−26.38	−24.352	−33.232
	Time constant [s]	0.156	0.185	0.260	0.505
40	Gain [dB]	−70.867	−30.748	−28.84	−37.96
	Time constant [s]	0.192	0.226	0.314	0.611
30	Gain [dB]	−76.31	−36.402	−32.549	−43.922
	Time constant [s]	0.251	0.293	0.406	0.779
20	Gain [dB]	−82.24	−44.003	−40.493	−52.258
	Time constant [s]	0.364	0.425	0.582	1.095

Table 7.5. Valve-input transfer function dominant time constants and the DC gains

7.2 Closed Loop Control of the Induction Motor

The prime aim of this section of the thesis is to maintain a constant pump outlet pressure irrespective of the pump speed and valve position. It is likely that the fuel rig behaviour is determined mainly by the inverter operation. Nonetheless, the system is also dependent to some extent on the position of the ball valve. In this study, changes in the valve angle control are considered to be an external disturbance to the pump controller. The control of the pump output pressure was implemented using an analogue control card and a pressure transducer connected to an external Labview-based controller.

Open-loop system responses were determined for standard control inputs including step, ramp and sinusoidal control signals. The disturbance, due to the valve operation, was introduced into the system during constant level and sine control. During sudden valve closure the pump pressure increased to a maximum.

The open-loop characteristics of the system were recorded and are shown in figure 7.5 with the non-linear simulation results. As can be seen from the figure, some noise is superimposed on the experimental results. From the step-input response it is evident that a pressure overshoot is present in the system during sudden changes. However during slower control signal changes (ramp and sine signals) the pump outlet pressure responses follow the pressure reference signal. The pump pressure change during valve closure was also recorded, where the reference signal was maintained at a constant level of 5bar. Similar valve closures, as a disturbance to the system, were implemented when a sinusoidal reference signal was applied to the inverter controller. Although the simulation data show less oscillations, the overall agreement between the measured and predicted results are generally good. A small steady state error exists between the experimental and predicted results when a constant-level reference signal is applied to the inverter controller.

The closed loop control of the pump output pressure was also implemented using the analogue control card. A Proportional plus Integral (PI) controller was used for this purpose. The main requirement for the controller was that the system must be capable of meeting the specified steady-state and dynamic characteristics whilst providing adequate stability margins. The schematic diagram of the proposed control technique is shown in figure 7.6.

Based on the linear rig model discussed in section 7.1, the transfer function was determined and used in the controller design. The optimum PI controller gain values were found based on the well-established 5% overshoot tuning method from the linear simulation model. Once the PI controller was tuned, the non-linear rig model validated in chapter 6 was used for the pump pressure control simulation. In the actual non-linear model the PI gain values were slightly changed, because of non-linearities that were not accounted for in the model. A values of 5 and 6 were used for the proportional and the integral gains.

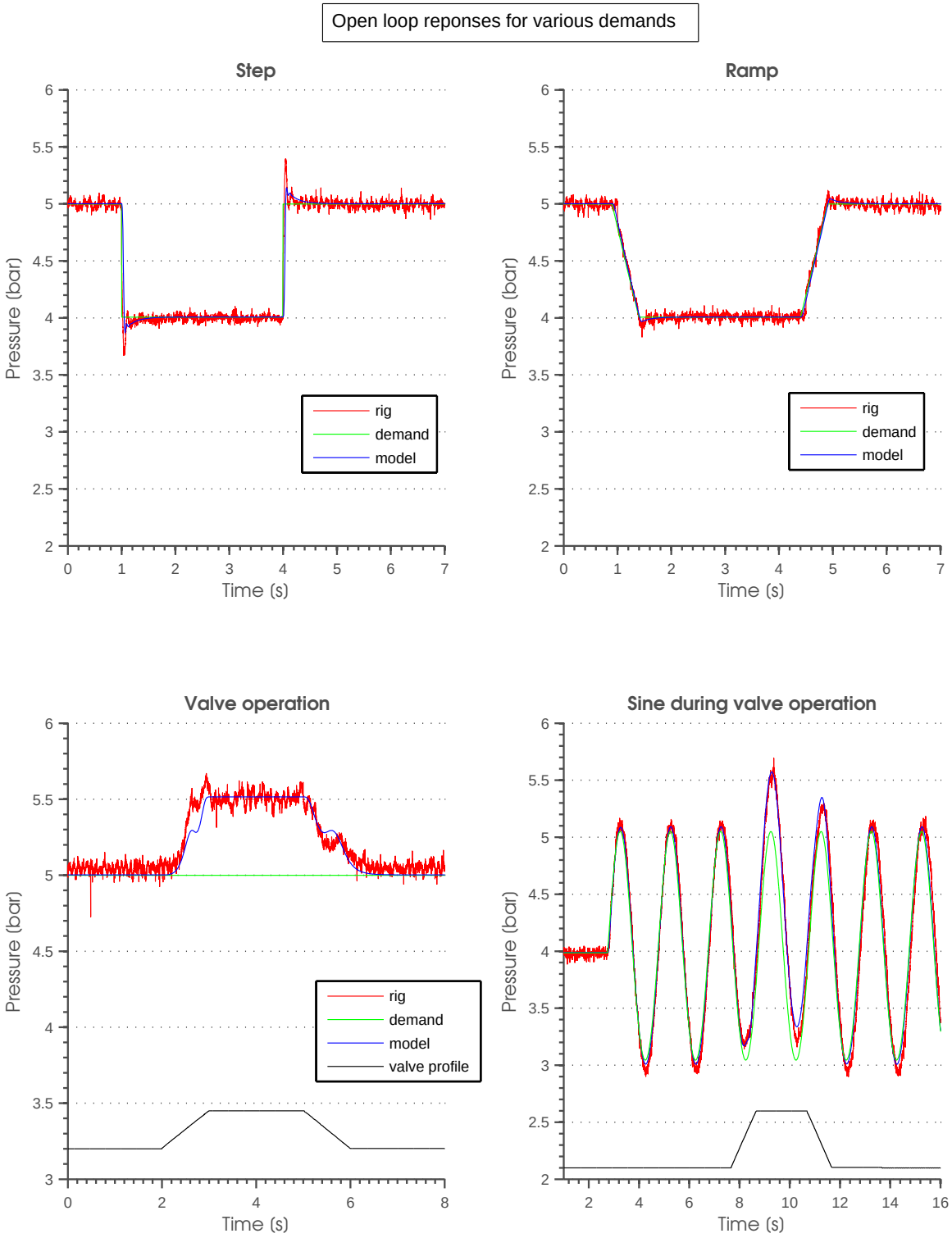

Figure 7.5. Open loop responses for various motor input demands

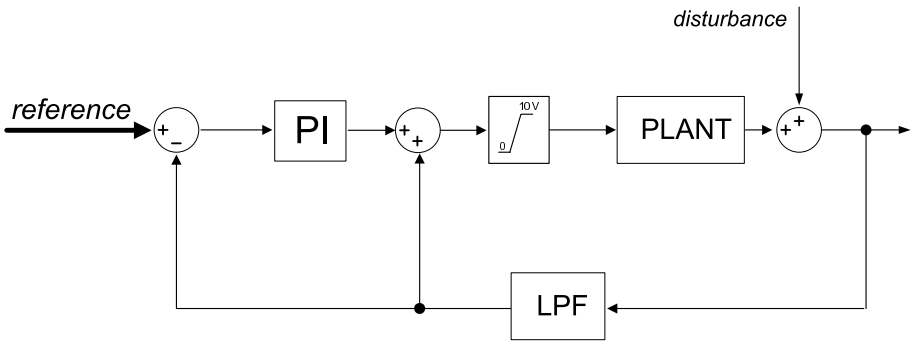

Figure 7.6. Closed loop control diagram

On the actual test rig it was impossible to use the PI controller settings obtained from the simulations as these gave unacceptable responses. The pump pressure overshoot was too large and not within the specified limit, resulting in a large controller error causing the inverter protection to be triggered. The reason for this is thought to be due to a hidden gain in the controller that was not accounted for in the model. Due to the control and acquisition system complexity, it was impossible to determine this gain and as a consequence differences between the simulation and actual controller gains are present. As significant ripples were superimposed on the measured pump outlet pressure, a 20Hz low-pass filter (LPF) was introduced into the feedback line, adding an additional delay. The simulated and actual PI controller gains are listed in table 7.6, indicating a 'hidden gain' setting of around 8.

Gain	Test rig	Model
K_P	0.6	5
K_I	0.7	6

Table 7.6. Analogue PI controller gains used in the model and the test rig

To evaluate the performance of the designed PI controller, the closed-loop responses were simulated using the full non-linear model and compared with the experimental results. The results are compared in figures 7.7 - 7.11. Each figure includes the pressure and the speed responses. The results were obtained following the introduction of change in demand pressure.

The closed loop 1bar step responses are presented in figure 7.7. The step-up and step-down control signals were implemented to show the system behaviour during positive and negative step changes, when the ball valve was fully open. It can be seen from this figure, that the pump output pressure follows the control signal with good accuracy, although pressure overshoots are present in both investigated cases. It is evident that the predicted

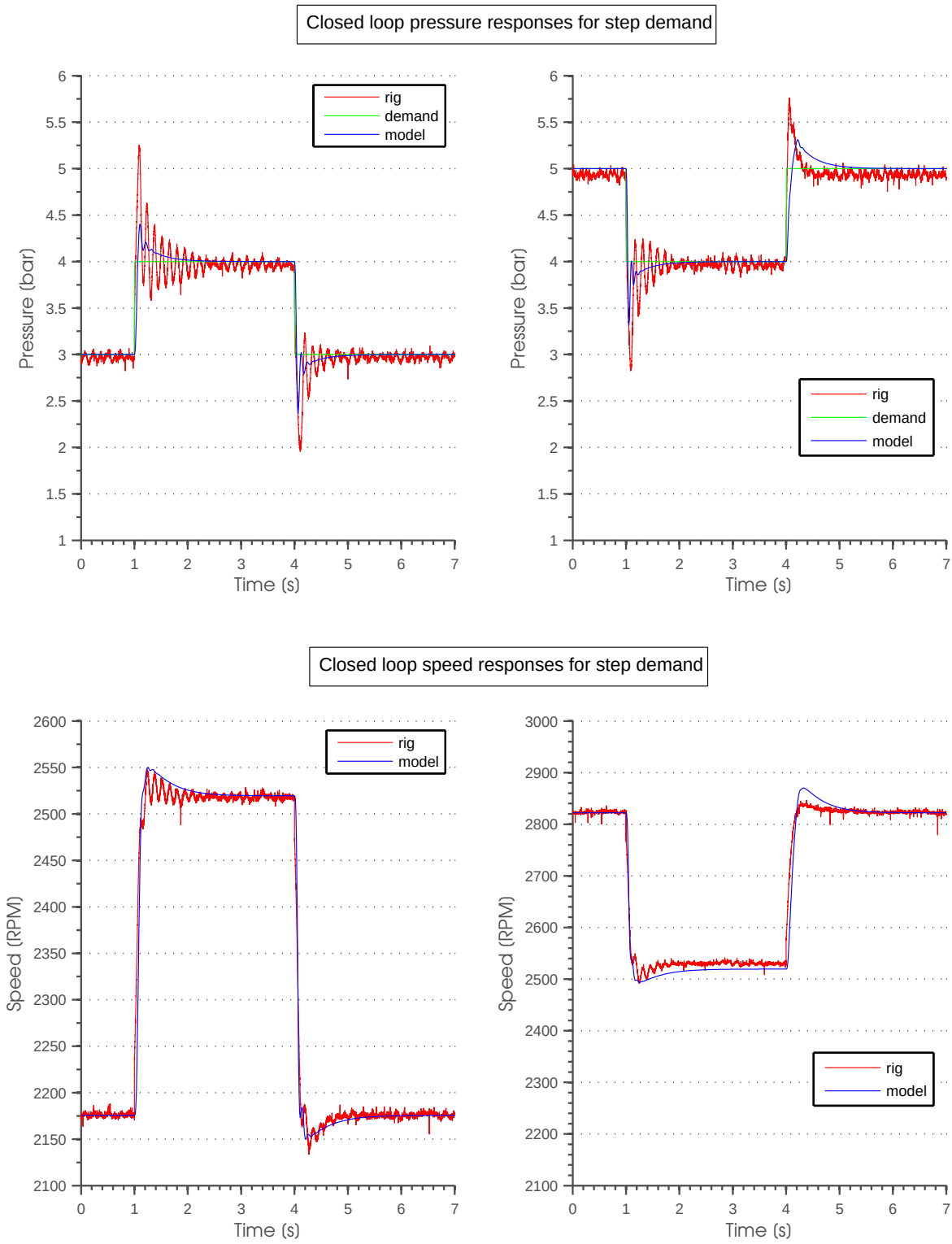

Figure 7.7. Closed loop responses for step demand at the inverter input when the valve is fully open

system response is well-damped. The test rig speed responses show also good fit with the simulated results (error < 5%).

The closed loop system responses for a unit-ramp input are given in figure 7.8. Similar to the step responses, a 1bar ramp-down and ramp-up were investigated. From the figure it is evident that the pump pressure follows the reference signal with good accuracy and, due to the fact that the system is well damped, the dynamic response is very good. The simulated results shown good agreement with the rig data for both the pressure and the speed responses.

The controller behaviour during sudden valve closure at two different reference levels of 3bar and 5bar is shown in figure 7.9. In addition, the valve signal profile is shown on the figure to give an indication of the valve angle. During valve closure, the pump outlet pressure was prevented from rising to its maximum level shown in figure 7.5, due to the controller reducing the pump speed as shown by the speed response included in figure 7.9. In this way the pump pressure is maintained at the required reference level. Again the simulation results predict the rig behaviour with error less than 5% compared to the experimental data.

The pump outlet pressure response to a sine reference signal with closed loop control is shown in figure 7.10. The left graph shows how the pressure follows a 0.5Hz sine control signal and the right graph shows the same sine reference signal when the valve was closed as indicated on figure 7.10. It is evident that the controller is capable of maintaining the pump outlet pressure at the reference signal even though a disturbance is present in the system. During valve closure, when the disturbance is entered into the system, the controller reduces the motor speed as shown on the speed responses. The simulation results show good agreement (less than 5% error) with the rig data.

To show the limitation of the controller, higher frequency sine reference signals were applied. The controller was tested using 1Hz and 2Hz control signals as shown in figure 7.11. During the 1Hz input signal the controller is at the boundary of accurate control performance, and a small steady-state pressure error is present. The 2Hz case shows that the controller is unable to maintain the pump output pressure at the reference signal. Although the system is stable, a steady-state pressure error exists with some phase shift. It can be seen from figure 7.11, that the model is unable to accurately predict the rig behaviour at this frequency. However achieving fast acting control is not main objective of this project. The model was shown to relatively accurately predict the rig behaviour with sufficient accuracy at frequencies below 2Hz.

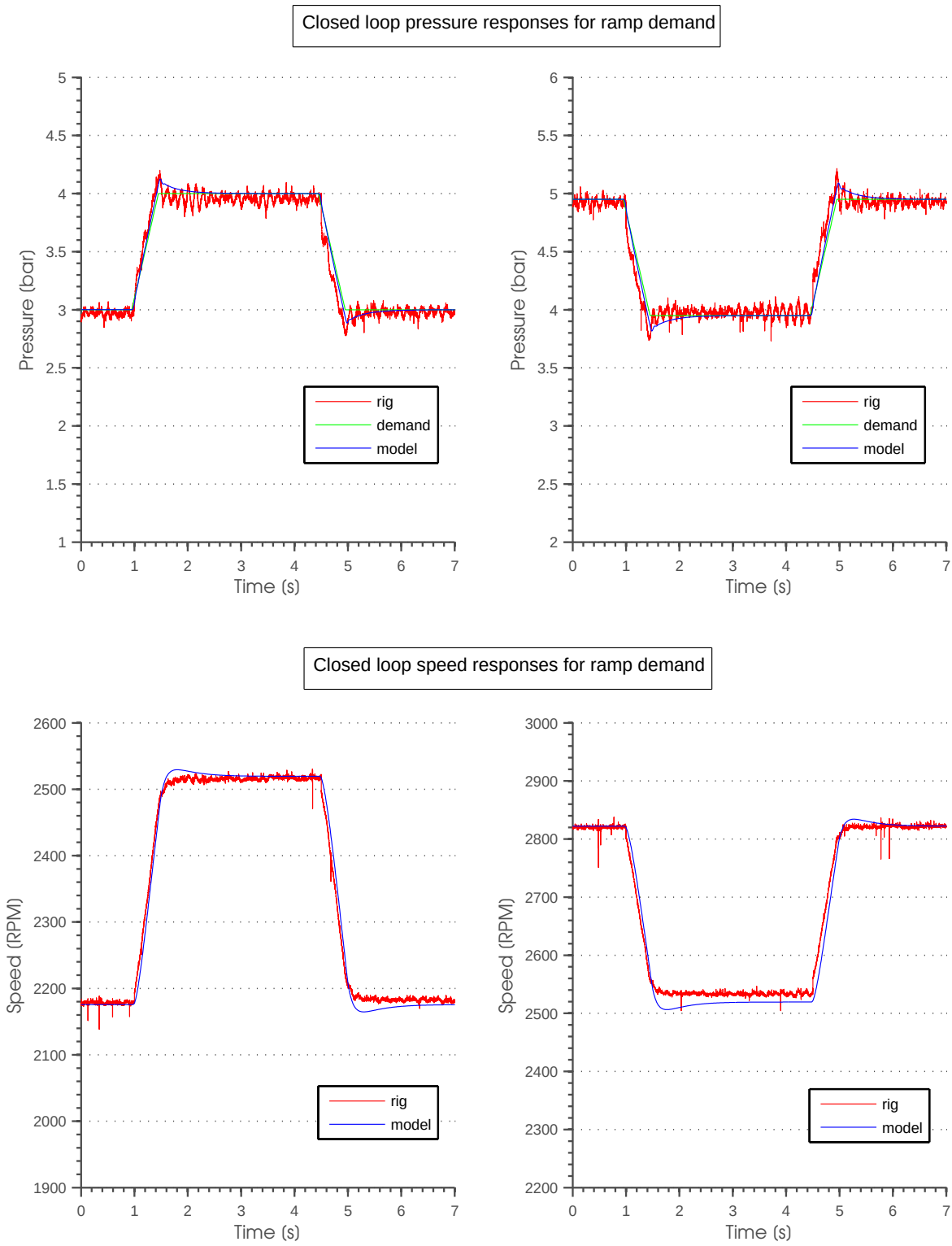

Figure 7.8. Closed loop responses for ramp demand at the inverter input when the valve is fully open

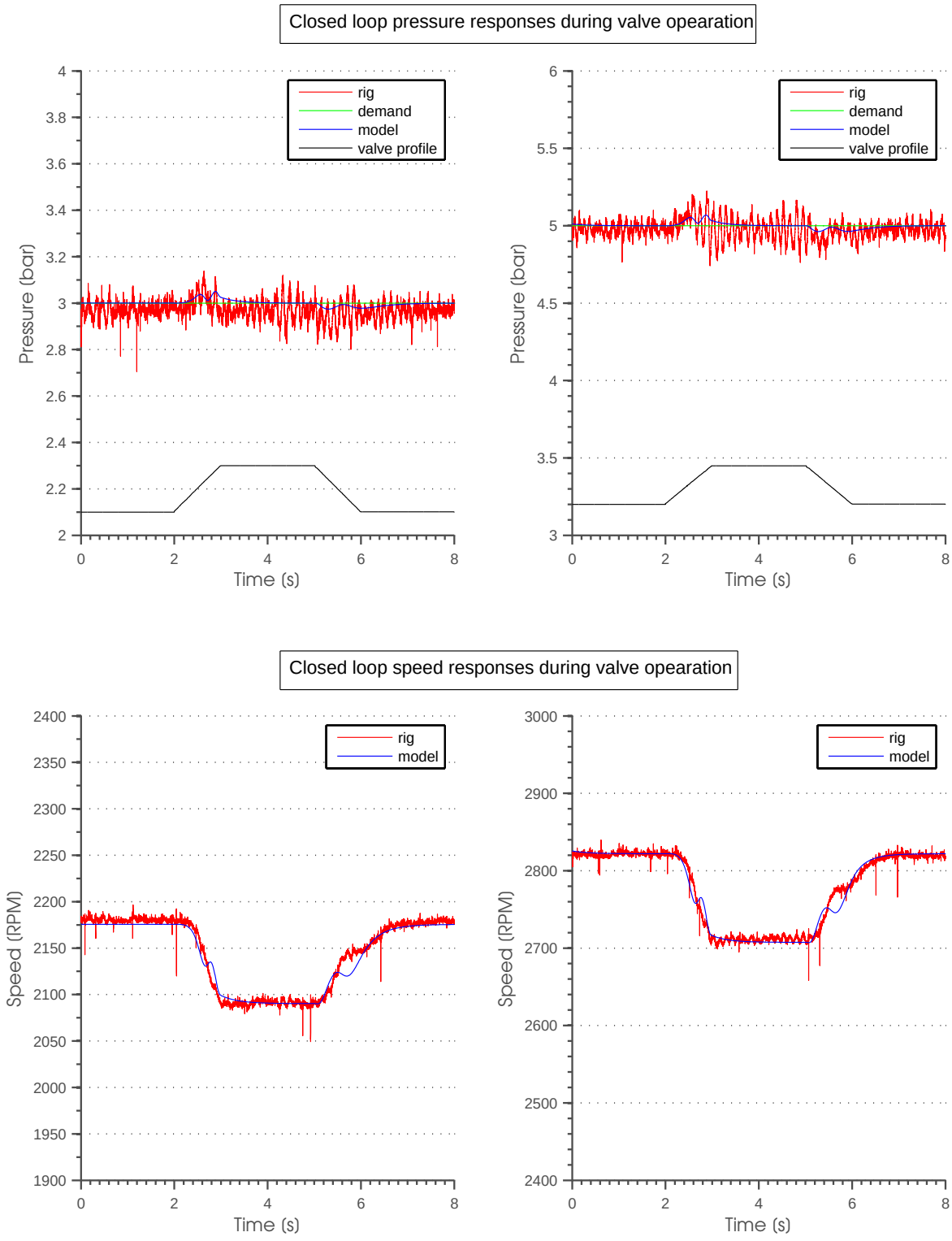

Figure 7.9. Closed loop responses during valve operation

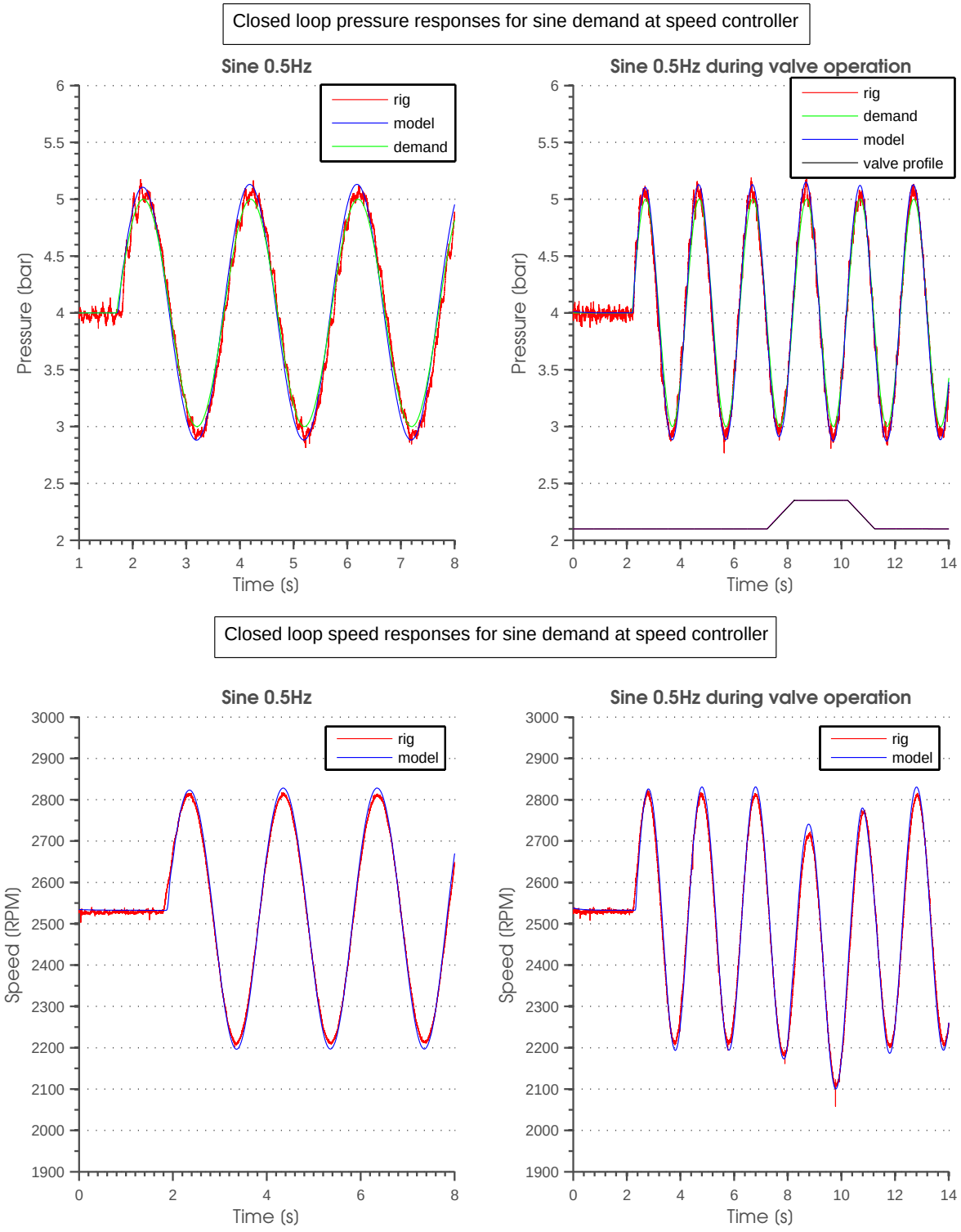

Figure 7.10. Closed loop responses for sine demand at speed controller and during valve operation

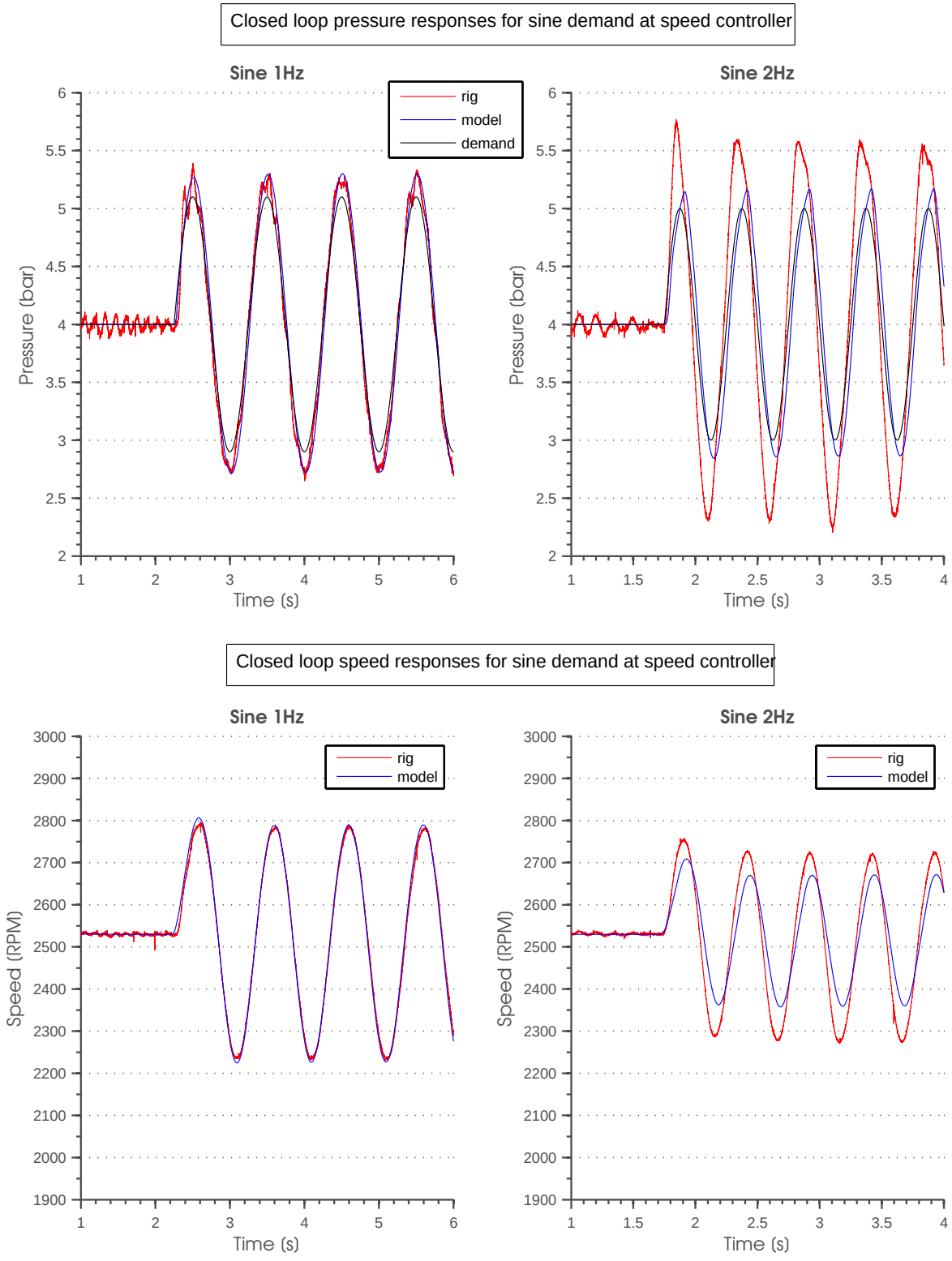

Figure 7.11. Closed loop responses for sine demand at speed controller when the valve is fully open

7.3 Open Loop Valve and Pump Simultaneous Control

During sudden valve closure, significant pressure transients can be generated in the system, especially in the case when the pipeline is long. A second important problem is the flow overshoot during valve closure. Flow overshoot is defined as the fluid volume passed by the ball valve during valve closure. Clearly, the overshoot will be small when the closure is rapid, but this will accompanied by a significant pressure surge.

In order to deal with the complex interaction between pressure surge and flow overshoot, a suitable control strategy was investigated as part of the Active Valve and Pump technology project. An optimised-time control strategy is presented in another thesis dealing with the valve control [30]. This approach is extended here to include the simultaneous control of the valve. The schematic layout of the pump and valve control is shown in figure 7.12.

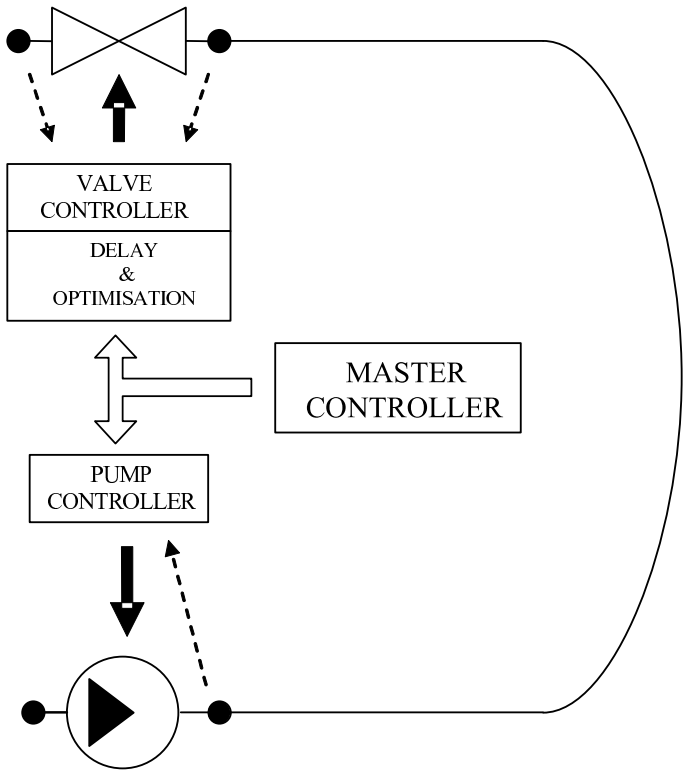

Figure 7.12. Open-loop instantaneous control of pump and valve strategy - diagram

The proposed control strategy uses a master controller which in turn generates control signals for both the pump and the valve controllers. The pump controller can operate in the motor operation mode which maintains the pressure at the set reference point thus eliminating the pressure disturbances in the system. The second mode is termed valve mode where the pump speed is reduced to decrease the flow in the system with a view to reducing the surge pressure during subsequent sudden valve operations.

In the valve mode the pump speed is maintained at the reference point until valve closure is about to begin. During the valve closure, the pump speed is reduced using a ramp profile where the start time and speed of pump operation depends on a chosen profile. Several different pump profiles were implemented as shown in figure 7.13. A ramp control signal was chosen as the demand control signal, due to the ease of implementation and potential system shock reduction present during step and exponential time-constant-based changes.

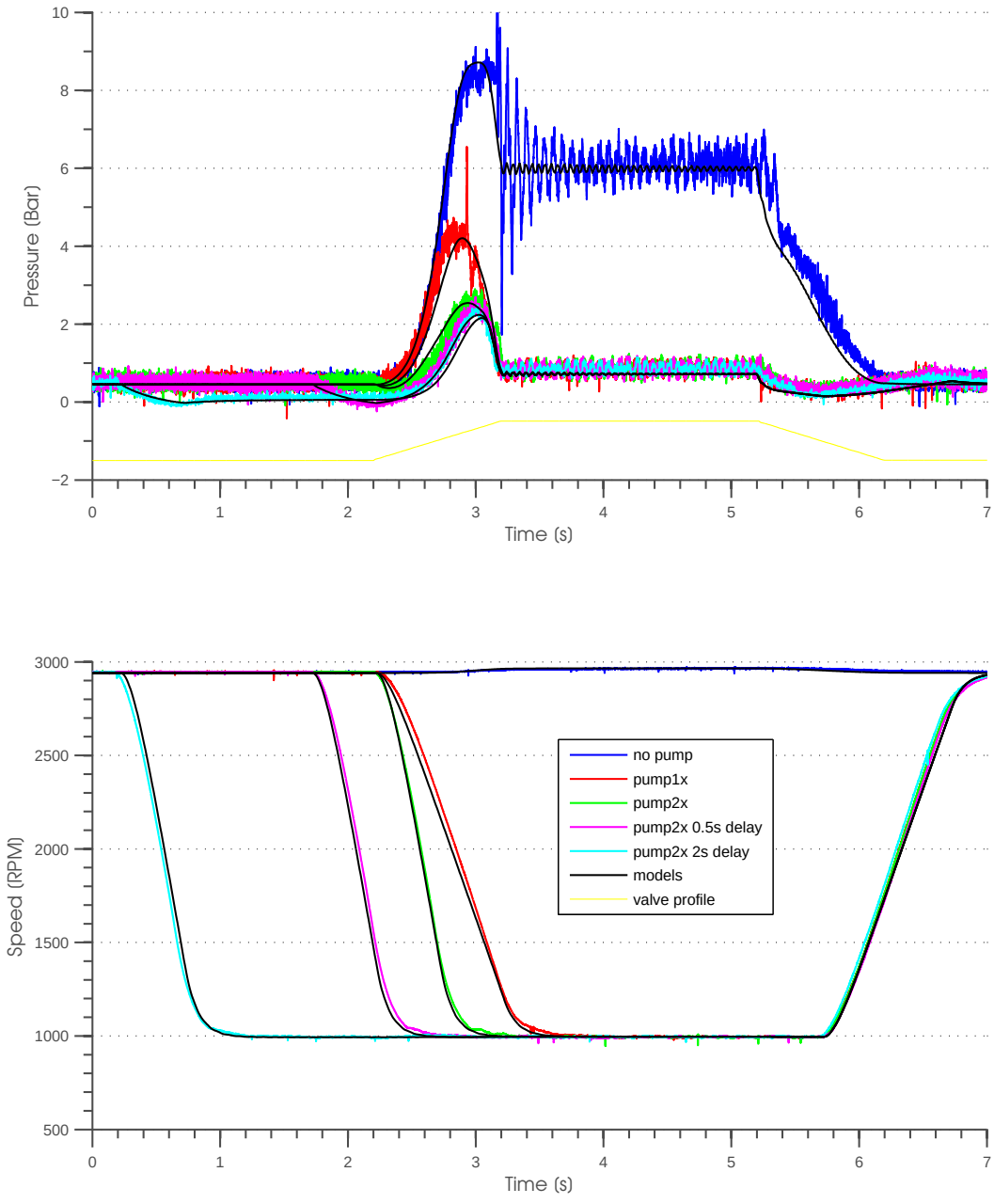

Figure 7.13. Open-loop instantaneous control of pump and valve strategy - results of pressure surge reduction

Figure 7.13 includes four different pump control profiles combined with valve closing and opening. In addition, sudden valve closure at a pump constant speed 'no-pump' is given to show the benefits of the proposed control strategy. The speed reduction level was chosen based on the pump operation time and the inverter safety requirements. A value of 0.5s was chosen as the fastest time for the reducing the pump speed, during which the speed could be reduced by a factor of two-thirds. Therefore, during the simultaneous pump and valve control tests, the speed was reduced from its maximum level of 3000rpm to 1000rpm. The closure/opening time of the ball valve was set to 1s.

The 'pump1x' profile is based on the same pump and valve operating and starting and finishing times. The profile 'pump2x' represents the operation where the pump and valve start at the same time but the pump speed reduction time is two times faster compared to the valve closing time. It is evident that the faster speed reduction gives a lower surge pressure falling(from 9bar to about 3bar) compared to 'pump1x' (from 9bar to about 5bar), due to the fact that for half of the valve closure profile the pump speed is at its minimum setting with the pump operating at a reduced flow rate. In order to further minimise the transient system conditions, delayed pump profiles were created. The pump double-speed profile, based on the system dominant time constant delay, is shown as 'pump2x 05s delay'. Here the pump speed reduction is introduced at about a half second before valve closure begins. In this case the valve starts to closed when the pump is operating at its minimum speed setting. Although the characteristic pressure surge bump is still visible its magnitude is now reduced to about 2.5bar. The two second delay profile 'pump2x 2s delay' has also been implemented to investigate the benefits to be gained from a longer delay. It is evident that the longer delay does not introduce a further reduction of the pressure surge. The speed behaviour using different pump operating profiles is shown in the lower part of figure 7.13. It is evident that the developed model predicts accurately the test rig behaviour using the proposed control strategy .

The predicted flow overshoot for all the investigated closure profiles is depicted in figure 7.14. Two graph are shown where the upper indicates the flow overshoot calculated with respect to the valve operation time, whereas the lower graph shows the flow overshoot related to the pump operation time. The valve flow overshoot is always referenced to the valve operation time (1s) while the pump operation time varies and depends upon the pump start time as can be seen from figure 7.14.

Looking at the flow overshoot with respect to the valve operating time, a minimum value is obtained for the profile using a 2s delay. This reduces the overshoot volume from 6.5L to 2.5L, with an overall operation time of 3s. Looking at the overshoot with respect to the start of the pump operation, the same profile generates a maximum flow overshoot of 12L, approximately two-times higher that the original value. The best results are obtained using a 0.5s delay profile. Although the pump volume overshoot is slightly higher than the original, the valve overshoot volume is reduced by 50% and the operating time is also

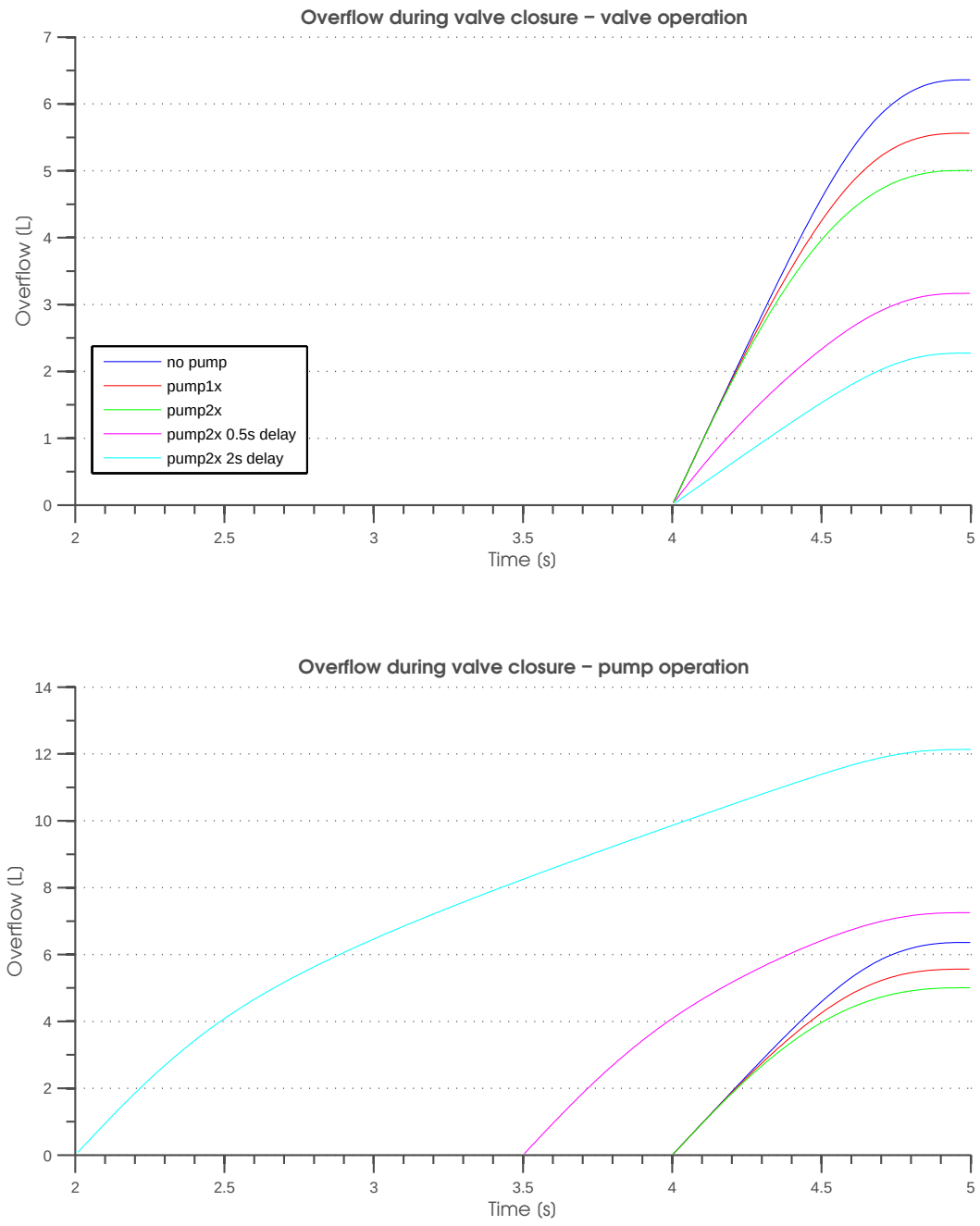

Figure 7.14. Open-loop instantaneous control of pump and valve strategy - results of flow volume overshoot reduction

reduced by a factor of 2 (1.5s). If no-delay is used, the 'pump2x' profile is recommended since in both cases the overshoot volume is reduced. In general, the longer the pump delay the higher the flow overshoot will be generated with respect to the pump operation and the lower the valve overshoot with respect to the valve operating time.

The summarised results of the proposed control technique are given is table 7.7. Considering both pressure reduction and flow volume overshoot, the best results are achieved when the pump speed is reduced two times faster than the valve closure time. The further pressure surge reduction is obtained when the profile with the system maximum time constant delay ('pump2x 05s delay') is applied but it requires extra time (maximum system time constant) which extends the complete operating time. As a result, the corresponding flow volume overshoot with respect to the complete operating time is increased. Additional tests with longer delays were undertaken (e.g 'pump2x 2s delay' profile) but the results obtained do not show the improvement of the pressure surge reduction.

Profile	unit	no-pump	pump1x	pump2x	pump2x 0.5s delay	pump2x 2s delay
Operation time	s	1	1	1	1.5	3
Pressure value	bar	8.7	4.4	2.6	2.4	2.3
Pressure reduction	%	-	49.4	70.1	72.4	73.5
Valve volume overshoot	L	6.35	5.55	5	3.15	2.27
Pump volume overshoot	L	6.3	5.56	5	7.25	12.1

Table 7.7. Pressure surge and flow volume overshoot reduction - summary

7.4 Closure

In order to identify the fuel system behaviour in terms of well-established linear analysis techniques, a linear model was developed for the fuel test rig. The linearised responses obtained were then compared with the full non-linear model behaviour and the results show good agreement when the pressure curves are compared. The system was described by transfer functions and the frequency responses obtained were presented on Bode diagrams. The system was linearised at different operating conditions and is characterised by a dominant time constant and DC gain for each considered case.

The open-loop responses of the system were investigated experimentally including unit-step, unit-ramp, valve disturbance and sinusoidal signals. The closed-loop control of the pump outlet pressure was implemented using an analogue PI controller. This study demonstrated that the PI control system can achieve acceptable tracking performance and anti-disturbance rejection for the pump outlet pressure control. Acceptable controller performance is achieved up to 1Hz. Moreover, the resulting pressure overshoots using the

PI control are small during sudden system changes as shown by the step responses. From the simulation results it was found that the model can predict the fuel rig behaviour during both open-loop and closed-loop control. Therefore, the model can be used to design a more efficient and robust controller for the pump outlet pressure. However, it is necessary to improve the model if control signals faster than 2Hz are to be applied since the model is limited to this bandwidth.

The simultaneous control of the ball valve and the pump strategy to minimise the pressure surge and reduce flow volume overshoot is presented. A number of valve-pump control profiles are proposed. It is evident that the proposed strategy can significantly reduce the pressure surge and minimise the flow overshoot in the fuel rig. It was concluded that if the pump speed reduction time is half of the valve operation time the best results are achieved.

Chapter 8

Digital Controller for the Induction Motor Drive System

8.1 Introduction

Recent developments in power electronics and microelectronics allow modern control techniques to be used in electric motor and motion control systems. The use of digital signal processors (DSP) has permitted the implementation of fast, efficient and accurate control techniques for induction motor drive systems in real time. In addition, these embedded systems can be readily reprogrammed for different configurations and applications, adding a degree of flexibility that cannot be achieved using analogue counterparts.

The behaviour of the analogue PI controller presented in chapter 7 can be affected by system changes. Furthermore, it is difficult to optimise the controller performance due to system parameter uncertainty and non-linearities. A real-time digital controller for controlling the fuel pump outlet pressure is presented in this chapter. Different control techniques are investigated and compared in a closed-loop configuration for the pump outlet pressure control, including a discrete PID controller with gain scheduling, an adaptive real-time PID controller and a fuzzy-logic-based digital controller.

The controller design and implementation presented in this chapter is limited to a simulation study only, since it was not possible to undertake the controller performance validation due to hardware problems encountered during the testing. It had been intended to use the DSP-based embedded controller (TMS320C6713 DSK) for the real-time control strategy development. However, due to a hardware failure, the real-time testing was stopped and the real-time control implementation was postponed and assigned to future work.

A major part of the software for the embedded controller had already been created in the C-programing language for the investigated controllers prior to the problem with the implementation and this is included in appendix D. The success obtained for the implementation of the analogue PI controller presented in chapter 7, where the simulation results were successfully validated using the experimental data, gives confidence that the findings obtained from the simulation study presented in this chapter could be successfully implemented on the fuel test rig.

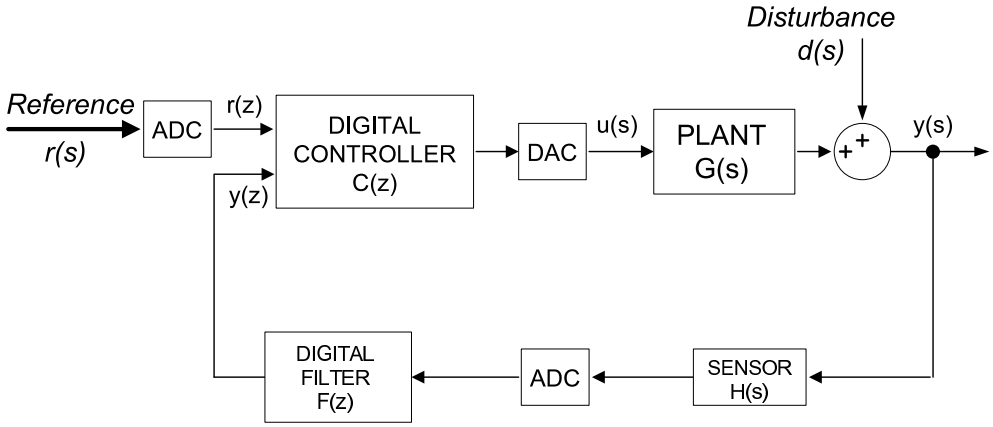

Figure 8.1. Digital controller

The block diagram of the overall digital control system is shown in figure 8.1. The system operates in continuous mode with a digital controller. The input signals to the controller are discretised using a 8kHz sampling frequency, resulting in 0.125ms time intervals between samples. As seen on the diagram, the input to the digital controller is the discrete reference signal r(z) and the digitally filtered system output y(z). The discrete controller C(z) determines the control signal for the inverter input to the fuel system test rig (plant G(s)). A disturbance to the system $d(s)$ can be applied using the ball valve. The pressure sensor, described as H(s), included in the feedback to the controller, has been modelled as a first order lag having unity gain and a sensor time constant of 5ms.

8.1.1 Digital filter

In order to eliminate electrical noise and any other undesired high frequency interferences, the pressure feedback signal is filtered. A finite response filter (FIR) has been designed and implemented to suppress the undesired components and noise. A 256 point kernel, h, having a 10Hz cutoff frequency was designed using the Matlab filter design toolbox (FDATool) and its transfer function described in the z-domain can be expressed as follows

$$F(z) = \sum_{i=1}^{256} h(i) z^{-i} \tag{8.1}$$

The filter was designed using the Windowed-Sinc method using a Hamming window. The resulting filter impulse response and its frequency response characteristics are presented in figure 8.2.

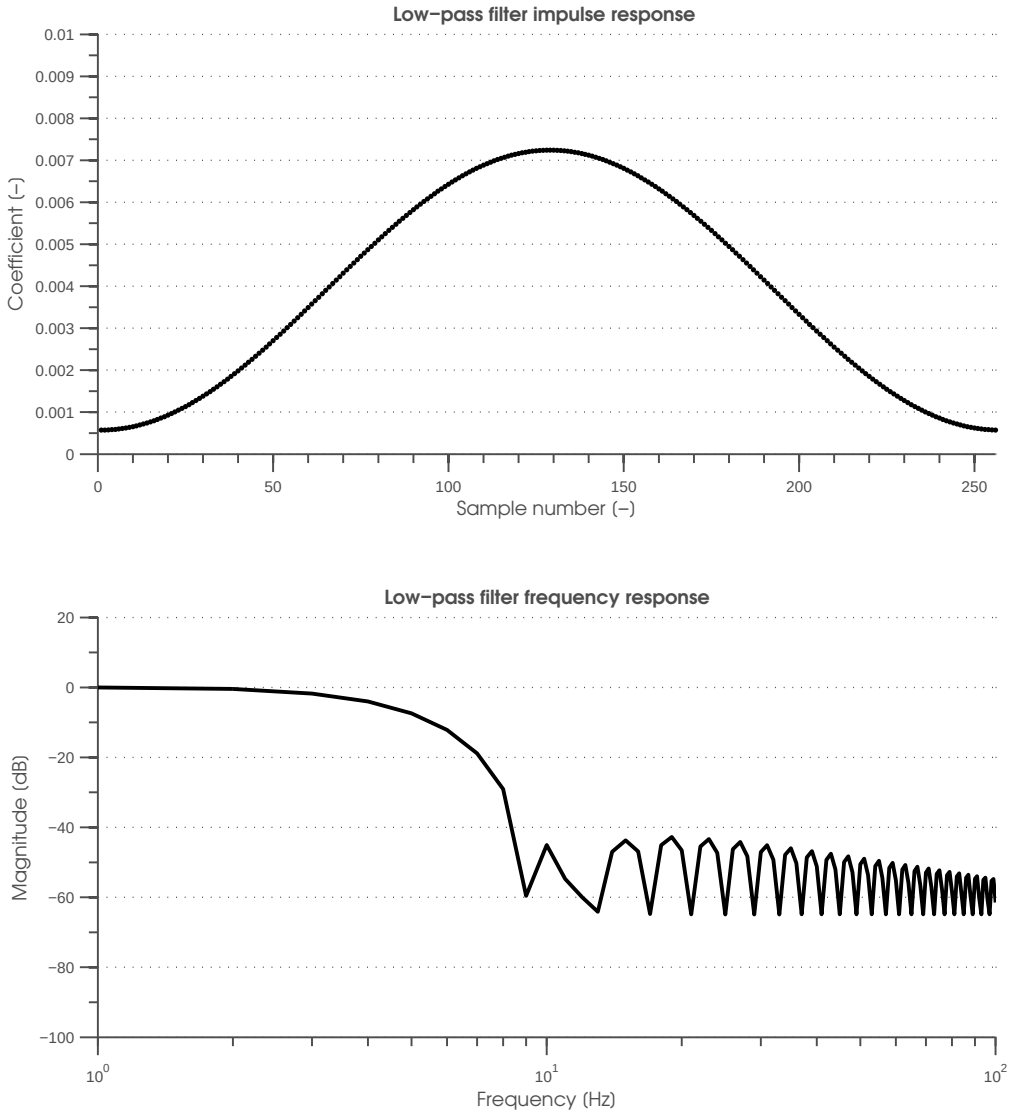

Figure 8.2. 10Hz low-pass digital filter characteristics

The filter has been implemented in the time domain using the following convolution equation

$$y(n) = \sum_{i=1}^{256} h(i)x(n-i) \tag{8.2}$$

where $x(n)$, $h(n)$ and $y(n)$ are the input signal, the filter impulse response and the output signal, respectively. This low-pass filter was used for filtering the feedback pressure signal.

8.2 Discrete PID controller

A conventional discrete Proportional-Integral-Derivative (PID) controller has been designed to control the pump outlet pressure. The classical parallel PID structure was chosen instead of the feed-forward control strategy used in the analogue PI controller presented in chapter 7. A discrete PID controller can be implemented in the z-domain using a transfer function in the following form [66]

$$C(z) = K_p + K_i \frac{T}{2} \frac{z+1}{z-1} + K_d \frac{z-1}{Tz} \tag{8.3}$$

where T is the sampling time and K_p, K_i and K_d are the proportional, integral and derivative gains, respectively.

To improve the controller performance and to limit the nonlinear effects of the inverter saturation present during sudden reference changes or system disturbances, an integral anti-windup strategy has been incorporated into the controller. The implemented anti-windup technique is based on back-calculation. During saturation, the integral term in the controller is re-computed, setting the controller output slightly over the saturation limit and as a consequence the inverter control signal can react rapidly to the control error changes [67]. The rate at which the controller output is reset is governed by the feedback gain coefficient K_b. The inverse of the back calculation coefficient K_b, which determines how quickly the integral is reset, called the tracking time constant T_t, has been calculated as a function of the integral and derivative gains as follows [67]

$$K_b = \frac{1}{T_t} = \sqrt{\frac{K_i}{K_d}} \tag{8.4}$$

The block diagram of the discrete PID controller with the anti-windup system is depicted in figure 8.3. The extra feedback path is created for the anti-windup to reset the integrator dynamically. During saturation limits the control error signal is generated and fed to the integrator input through the back calculation gain K_b, otherwise the PID controller works in the normal mode [68].

The controller was tuned using the Matlab PID tuning toolbox and the gains set to obtain a 5% overshoot. Due to the fuel rig system non-linearities, the system gains and the time response variations at different operating conditions, shown in section 7.1.7, were used to determine the PID gains at different operating points. The gains obtained are shown in figure 8.4.

The discrete PID controller was tuned for the system condition at a given operating point where the gains have adapted to the dynamic properties of the fuel test rig. If the fuel system conditions vary, the control system stability is reduced or the responses becomes more sluggish and the gains of the controller have to be re-set to obtain optimum performance.

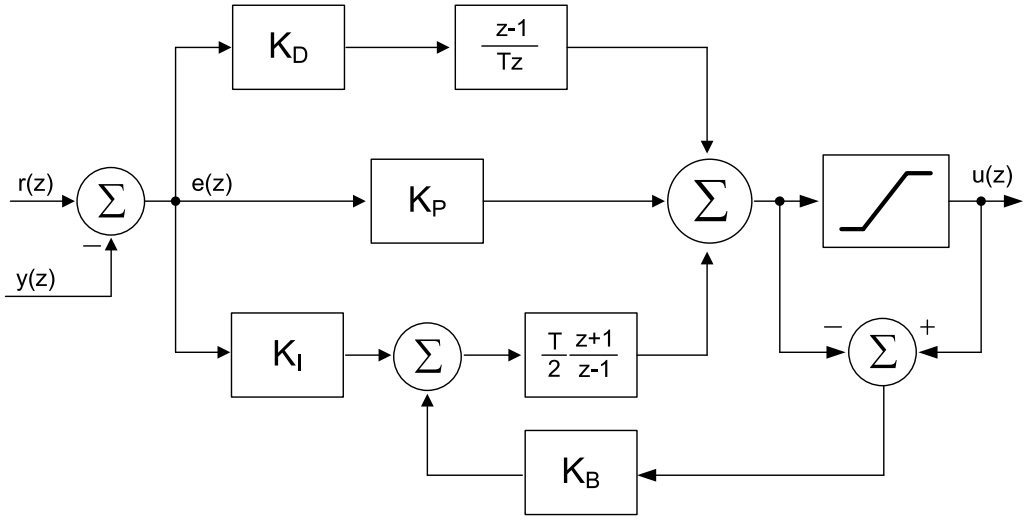

Figure 8.3. Discrete PID controller

The gains obtained at different operating conditions can be approximated/interpolated [69], thus allowing a systems's performance to be improved over a range of operating conditions. The use of a PID controller incorporating scheduled gains improves both the stability and the time responses of the system. The values of gains over a range of operating conditions were approximated by interpolating discrete data using a linear function and the results are shown in figure 8.4 along with the discrete tuned gain values.

8.2.1 IIR based PID controller

The discrete PID controller was implemented using the Infinite Impulse Response (IIR) filter. The controller equation given in (8.3) can be rewritten as the IIR filter transfer function expressed in the z-domain as [70]

$$C(z) = \frac{a_0 + a_1 z^{-1} + a_2 z^{-2}}{1 - z^{-1}} \tag{8.5}$$

where the numerator coefficients can be found from the following

$$a_0 = K_p + \frac{K_i T}{2} + \frac{K_d}{T} \tag{8.6}$$

$$a_1 = -K_p + \frac{K_i T}{2} - \frac{2K_d}{T} \tag{8.7}$$

$$a_2 = \frac{K_d}{T} \tag{8.8}$$

It is clear from equation (8.5) that the PID controller has one fixed pole and two flexible zeros. The IIR filter implementation of the discrete PID controller does not suffer from

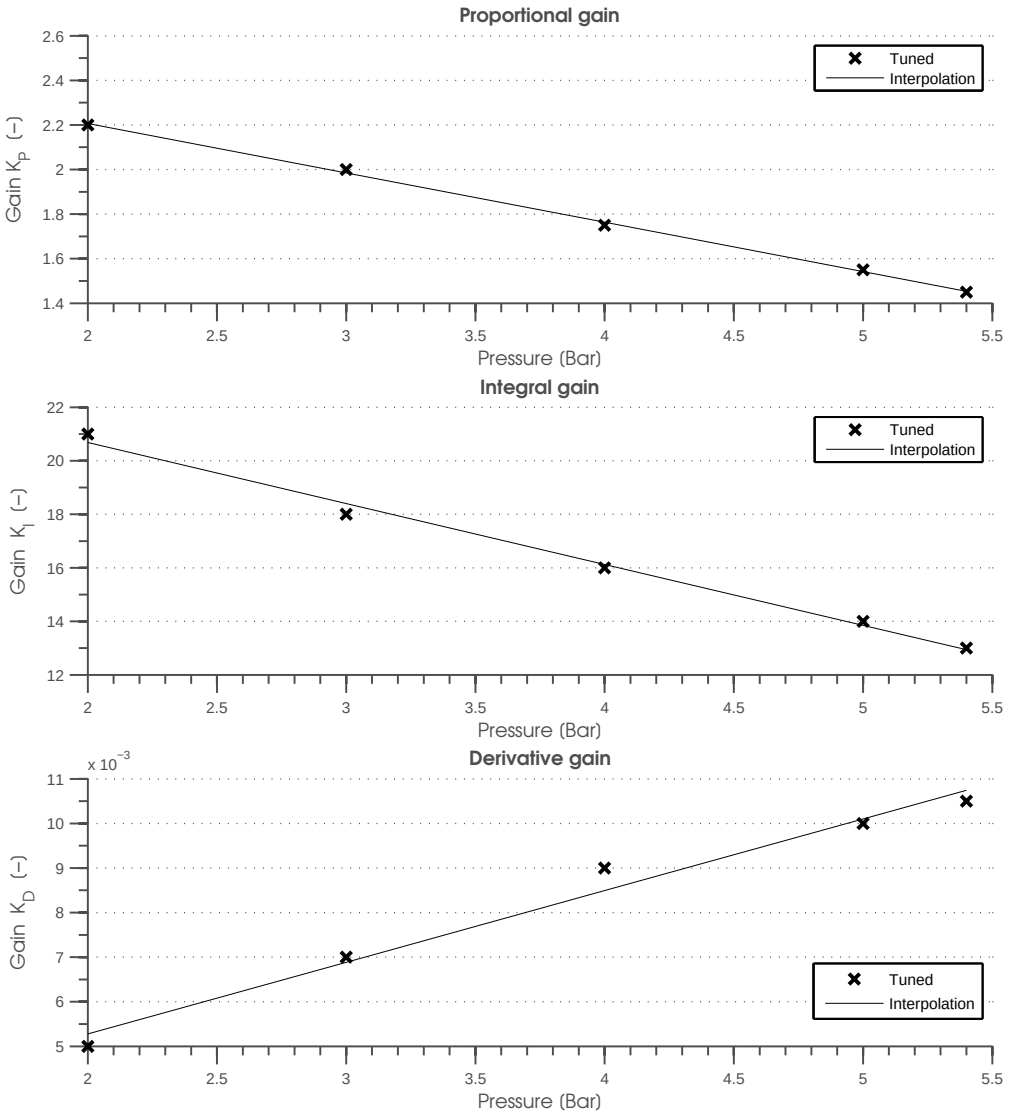

Figure 8.4. Discrete PID controller gains

integral windup, since it does not make use of a sum of the errors to generate the integral action. Even if the control signal is constrained, only the three last samples are taken for the controller output calculation.

By taking the inverse z-transformation of equation (8.5), the difference equation is obtained resulting in a real-time IIR algorithm [71] for the discrete PID controller, which is easy to implement in an embedded system. Equation (8.5) can be expressed as

$$D(z) = D(z)\,\frac{M(z)}{M(z)}\,\frac{Y(z)}{X(z)} \tag{8.9}$$

where $X(z)$ and $Y(z)$ are the input and output of the controller, respectively and $M(z)$ is a dummy transfer function.

Performing the inverse Z-transform on the following terms

$$Y(z) = \left(a_0 + a_1 z^{-1} + a_2 z^{-2}\right) M(z) \tag{8.10}$$

$$X(z) = \left(1 - z^{-1}\right) M(z) \tag{8.11}$$

the real time discrete PID controller difference equations can be obtained as follows

$$y(n) = a_0 m(n) + a_1 m(n-1) + a_2 m(n-2) \tag{8.12}$$

$$m(n) = x(n) + m(n-1) \tag{8.13}$$

8.3 Adaptive PID controller

Some parameters of the fuel test rig are expected to change with time, but the exact nature of the change is not predictable. Therefore, the standard PID controller with fixed gains does not consistently regulate the system's dynamic behaviour. A method of changing the PID gains is required such that the gains can adapt to meet the requirements of the test rig. The adaptive PID controller can be used for this purpose. Using this control strategy, the gains of an adaptive controller are adjusted to compensate for changes in input signal, output signal, or the system parameters. In this way, an adaptive system can learn the signal characteristics and track slow changes.

The adaptive PID controller was designed and implemented in Matlab/Simulink using the adaptive control strategy shown in figure 8.5. The adaptive control scheme can be considered as a two stage controller. The first part is a real time IIR PID controller, which calculates the controller output for given a control error e_1 using initial or updated PID parameters. The adaptation stage follows the PID operation and the controller gains are updated based on the control error and the performance error e_2. This process continues until the error e_2 approaches zero.

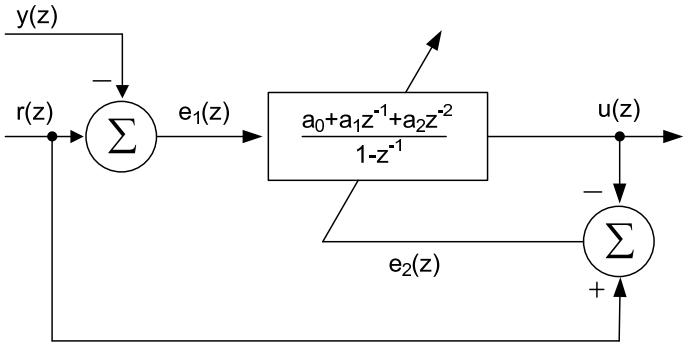

Figure 8.5. Adaptive PID controller

In order to optimise the controller behaviour the performance function $e_2(z)$ is determined as the difference between the reference signal $r(z)$ and the adaptive controller output $u(z)$ [72], ie

$$e_2(z) = r(z) - u(z) \tag{8.14}$$

The mean squared error function $E[e_2(z)]$ is used to minimise $e_2(z)$ with respect to the controller parameters and to adjust the controller coefficient, where E represents the expected value.

A quadratic objective function J_o was created based on the minimum value of the E function with respect to the controller parameters [72],

$$J_o\,(a_0, a_1, a_2) = \frac{1}{2}\,(E[e_2(z)])^2 = \frac{1}{2}\left[r(z) - \left(\frac{a_0 + a_1 z^{-1} + a_2 z^{-2}}{1 - z^{-1}}\right) e_1(z)\right]^2 \tag{8.15}$$

The first derivative (gradient) of the mean squared error function is used to find the minimum of the J_o function with respect to the controller coefficients [71],

$$\frac{\partial\, J_o}{\partial a_0} = -2r(z)\left(\frac{1}{1 - z^{-1}}\right) e_1(z) + 2\left(\frac{a_0 + a_1 z^{-1} + a_2 z^{-2}}{1 - z^{-1}}\right)\left(\frac{1}{1 - z^{-1}}\right) e_1^2(z) \tag{8.16}$$

$$\frac{\partial\, J_o}{\partial a_1} = -2r(z)\left(\frac{z^{-1}}{1 - z^{-1}}\right) e_1(z) + 2\left(\frac{a_0 + a_1 z^{-1} + a_2 z^{-2}}{1 - z^{-1}}\right)\left(\frac{z^{-1}}{1 - z^{-1}}\right) e_1^2(z) \tag{8.17}$$

$$\frac{\partial\, J_o}{\partial a_2} = -2r(z)\left(\frac{z^{-2}}{1 - z^{-1}}\right) e_1(z) + 2\left(\frac{a_0 + a_1 z^{-1} + a_2 z^{-2}}{1 - z^{-1}}\right)\left(\frac{z^{-2}}{1 - z^{-1}}\right) e_1^2(z) \tag{8.18}$$

The above first-order approximations indicate that the gradient is basically the product of the reference signal r and the control error signal e_1. Better convergence can be obtained when the performance error e_2 is used instead of the set-point signal with the control error [71].

The general adaptive mechanism is used to update the PID coefficients [73] as follows

$$a_n(k + 1) = a_n + \beta e_2(k) e_1(k - n) \tag{8.19}$$

where k is the current sample for a given sample period T, β is an adaptation rate and $n = 0, 1, 2$, respectively.

The adaptive controller was tested on the nonlinear fuel test rig model at different operating conditions. The adaptation rate β was chosen based on the stability and performance tests and a value of 5×10^{-8} was used. A large adaptation rate makes the system unstable whereas a small value makes the controller incapable of achieving the gain adaptations. The adaptation algorithm starts with the controller coefficients (a_0, a_1, a_2) based on a prior knowledge of the fuel system dynamics and an average value of the fixed PID gains.

8.4 Fuzzy logic controller

Despite their advantages, conventional PID controllers suffer from the fact that the controller must be re-tuned when the operating conditions change. When a process becomes too complex to be described by analytical models, it is unlikely to be efficiently controlled using conventional approaches.

An alternative method for controlling the fuel pump outlet pressure is an intelligent process control method such as fuzzy logic. The fuzzy controller (FLC) operates in a knowledge-based way, and its knowledge relies on a set of linguistic *if-then* rules, like a human operator. Fuzzy logic controllers are independent of plant modelling and can therefore deliver good output control despite the existence of severe non-linearity and parameter variation and uncertainty in a system [74].

The fuzzy logic controller has been designed to control the pump outlet pressure using the Matlab Fuzzy Logic Toolbox [75]. A schematic view of the controller is shown in figure 8.6. The reference signal is compared with the feedback signal and a control error is produced. The backward difference operation is used to approximate the derivative of the error control signal. These two signals constitute the input to the fuzzy logic block (FLC) where a voltage change/increment is produced. The output of the fuzzy logic engine represents the voltage increment to the inverter. The voltage increments are summed to produce the inverter control voltage [76]. In order to eliminate windup, the backward calculation anti-windup technique is used.

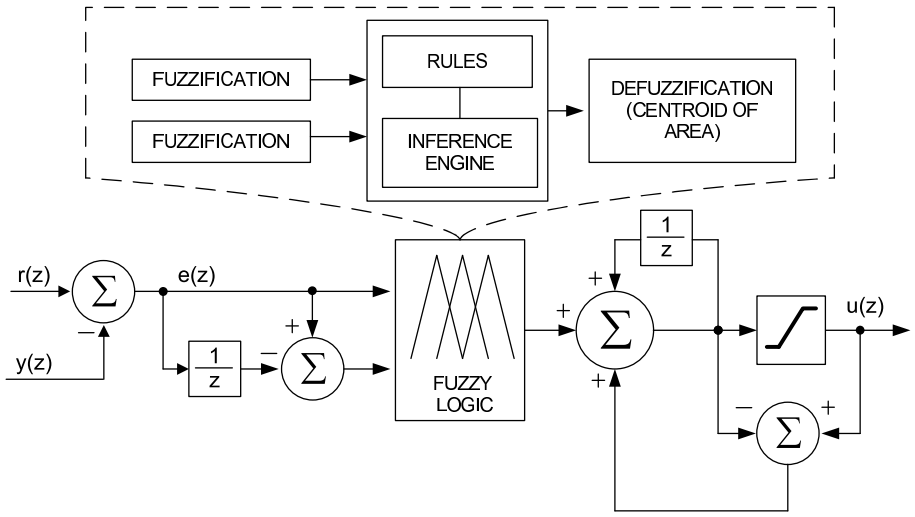

Figure 8.6. Fuzzy logic controller

The FLC includes three major blocks: fuzzification, an inference mechanism, and defuzzification. The FLC controller uses two crisp (clear value) inputs, control error and derivative of control error, to produce an output. The pressure control error is calculated

by comparing the reference and the feedback pressure signals,

$$e(n) = r(n) - y(n) \tag{8.20}$$

whereas the error rate of change is calculated as the difference for given sampling time T,

$$de(n) = \frac{e(n) - e(n-1)}{T} \tag{8.21}$$

The FLC input signals are converted to degrees of membership (fuzzification) by a lookup table in one or several membership functions. The grade of membership for all its members describes a fuzzy set. Every element x, in the universe of discourse (all the possible values) $\mu(x)$, is a member of a fuzzy set A with a grade of membership, including zero, that can be expressed as

$$A = \{(x, \mu(x))\} \tag{8.22}$$

The fuzzification block maps crisp variables to the fuzzy sets within a certain degree of membership. The membership functions for both the control error and change in the control error have been created. Fuzzy sets for each membership functions (MF) are described by linguistic variables. The linguistic variables with the corresponding fuzzy sets and describing shape functions of each membership function are given in tables 8.1 and 8.2 for the control error and rate of change of control error, respectively. The corresponding output member function is given in table 8.3.

Figure 8.7 shows all of the membership functions for the input and output variables created for the fuzzy logic controller for the fuel pump outlet pressure control. All the MFs are asymmetrical because near the origin, the signals require more precision. There are five MFs for the control error e and three for the error rate of change de, whereas there are seven for the output Δu. All the MFs are symmetrical for positive and negative values of the variables.

Fuzzy set	Linguistic variable	Shape	Values
ENL	negative large	trapezoidal	[-5 -5 -4 -1]
ENS	negative small	triangular	[-2 -1.5 0]
EZ	around zero	triangular	[-1 0 1]
EPS	positive small	triangular	[0 1.5 2]
EPL	positive large	trapezoidal	[1 4 5 5]

Table 8.1. Fuzzification of control error signal

Fuzzy set	Linguistic variable	Shape	Values
DN	negative	triangular	[-0.01 -0.01 -1e-5]
DZ	around zero	triangular	[-0.002 0 0.002]
DP	positive	triangular	[1e-5 0.01 0.01]

Table 8.2. Fuzzification of rate of change of control error

Fuzzy set	Linguistic variable	Shape	Values
VNL	negative large	trapezoidal	[-0.04 -0.035 -0.030 -0.025]
VNM	negative medium	triangular	[-0.02 -0.015 -0.01]
VNS	negative small	triangular	[-0.01 -0.005 -0.0]
VZ	around zero	triangular	[-0.003 0 0.003]
VPS	positive small	triangular	[0.0 0.005 0.01]
VPM	positive medium	triangular	[0.01 0.015 0.02]
VPL	positive large	trapezoidal	[0.025 0.030 0.035 0.04]

Table 8.3. Controller output fuzzy set

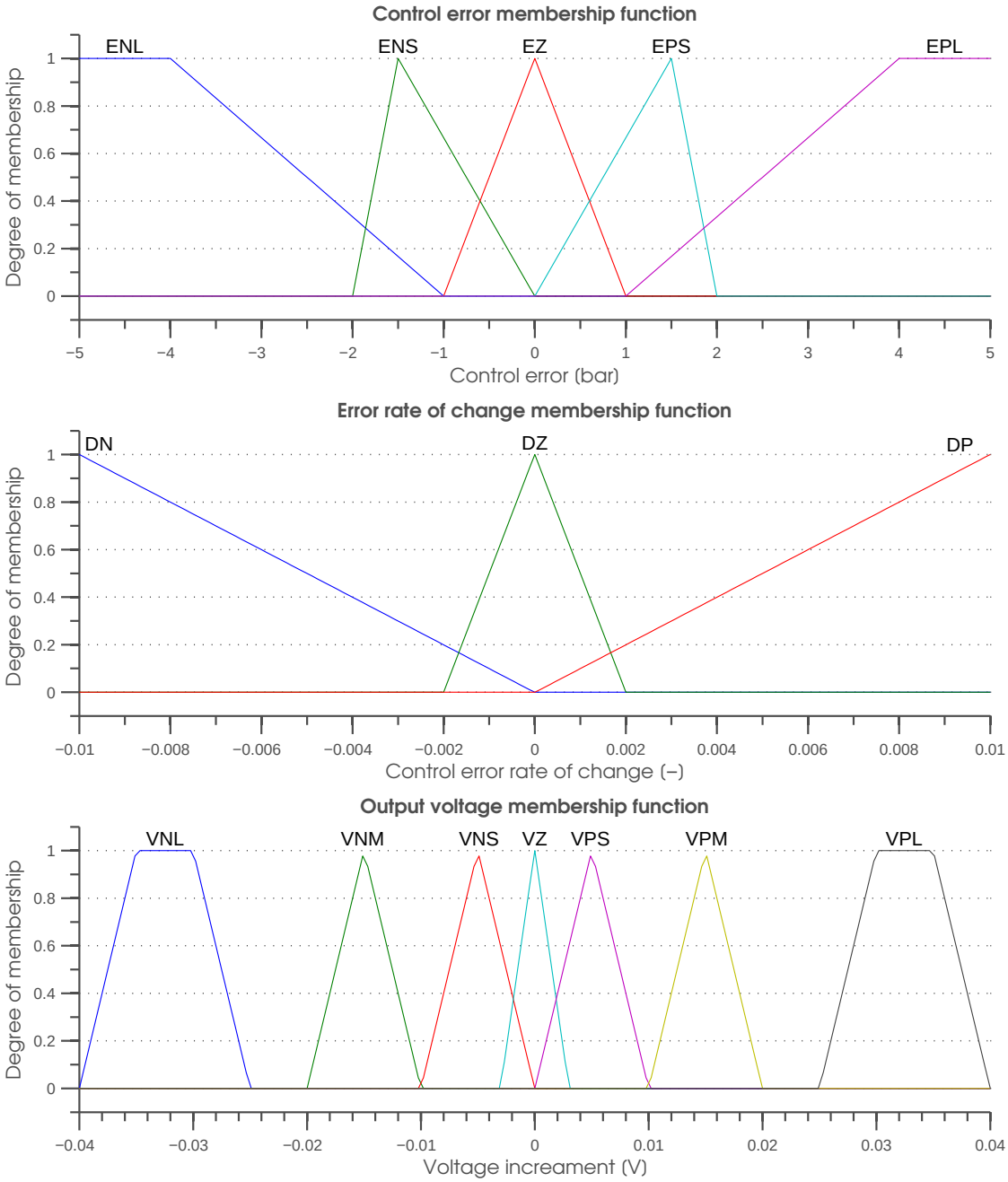

Figure 8.7. Fuzzy logic membership functions

A fuzzy logic operation is based on the rules formed for the controller. The basic function of the fuzzy inference engine is to compute the overall value of the control output variable based on the individual contribution of each rule in the rule-base. Once the inputs have been fuzzified, the degree of membership of each input variable is known and the rule evaluation takes place. The Mamdani fuzzy inference mechanism [74] has been used to evaluate the consequent (output) fuzzy sets based on the antecedent fuzzy sets (inputs).

A set of rules were obtained from observation of the operation of the fuel rig system. The developed rule-base has two inputs (the error and the error change) and one output (voltage increment) as a control action. A linguistic controller contains rules based on the *if - then* format. Examples of the rules formulated and used for the FLC controller are given below.

if *error* is *EZ* and *rate of error* is *DZ* then *output* is *VZ*

if *error* is *EPL* then *output* is *VPL*

As each input-output data pair, which consists of a crisp numerical value of the control error and the rate of change of control error, is processed, fuzzy rules are fired and a corresponding output is generated. Each rule defines the output value for the fuzzified input values. If two or more conditions are used the fuzzy logic operator *AND (min)* is used to find the output.

The fuzzy logic controller operation is based on rules for the control operation as shown in the two-dimensional table 8.4. The rules of the fuzzy system show how the two fuzzy inputs are related to the fuzzy output. The inputs and output results can be plotted as a surface for visual inspection as shown in figure 8.8.

control error	rate of change of error	voltage increment
ENL		VNL
EPS	DN	VNM
ENS		VNS
EZ	DZ	VZ
EPS		VPS
ENS	DP	VPM
EPL		VPL

Table 8.4. Fuzzy controller rules

There is an output fuzzy set value for each rule. To obtain the crisp output from the controller, all the rule outputs are summed. The aggregated output has to be defuzzified and the centre of gravity method has been used in the FLC controller design for this purpose.

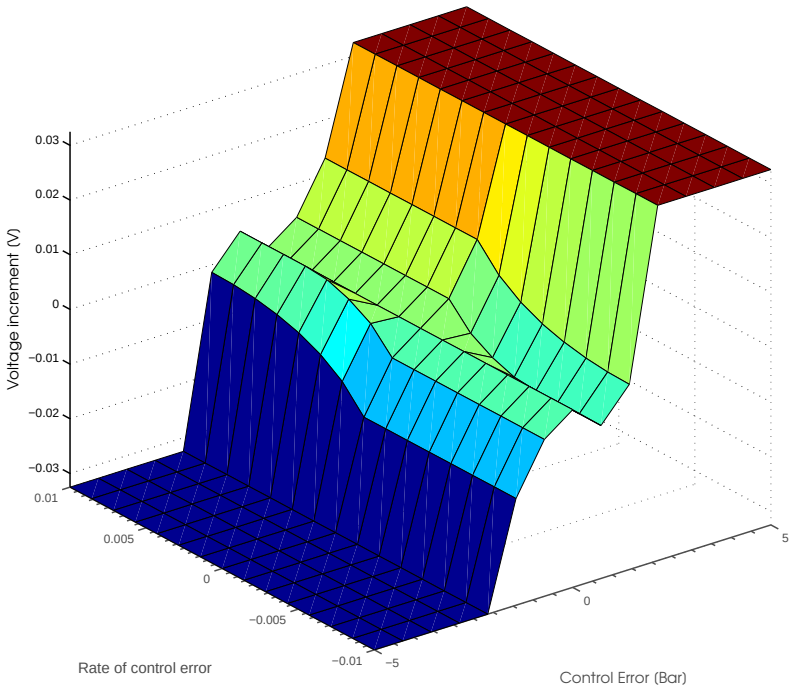

Figure 8.8. Surface view of fuzzy controller output

The centroid defuzzification used [74] is calculated as follows

$$\Delta u = \frac{\sum_i \mu(x_i)(x_i)}{\sum_i \mu(x_i)} \tag{8.23}$$

The output from the fuzzy logic controller is the voltage increment based on the controller input signals. To obtain the actual voltage to control the inverter, the voltage increments are summed. Since the output of the controller is a memory stage, during prolonged control periods large errors can be generated and a windup phenomenon can be created. The backward counting anti-windup technique has been applied to keep the inverter voltage in the required operating region. The backward counting coefficient has been set to unity to obtain the direct elimination of saturation error.

8.5 Closed loop digital control

The controllers have been implemented in Matlab/Simulink and incorporated into the fuel test rig non-linear model described and validated in chapter 6. The controller closed loop performance has been simulated for different reference signals when the the ball valve is operated. The closed-loop responses obtained for all the digital controllers are compared and discussed in the following section.

The simulation results obtained for all the controllers are shown in figures 8.9 - 8.12. These results were obtained following the introduction of a change in demand pressure and the disturbance condition caused by the operation of the ball valve. Each figure includes the pump outlet pressure responses at two different operating conditions for the applied control pattern. The open loop responses and pressure demand signals are included along with the controller responses to show the controller performance. In addition, the valve closure profile is given to indicate the valve operation. The valve is initially open and is ramped fully closed, held closed for a period of time before being ramped fully open again.

The controller's behaviour during sudden valve closure at two different constant-pressure reference levels of 3bar and 5bar is shown in figure 8.9. During valve closure, the pump outlet pressure was prevented from rising to its maximum level as shown on the open loop response due to the controllers reducing the pump speed. In this way the pump outlet pressure is maintained at the required reference level. The simulation results obtained from all the control techniques show good pressure regulation. However, the fuzzy logic pressure response is slightly faster due to the non-linear 'bang-bang' control strategy scheme used, although very small (less than 50 mBar) oscillations exist. Both fixed and adaptive PID controllers exhibit good pressure regulation (with error less than 2.5% in relation to the reference signal) with slightly superiority of the adaptive PID.

The closed loop responses for a step demand in pressure are presented in figure 8.10. The step-up and step-down control signals were implemented to show the system behaviour during positive and negative step changes. Two different pressure demand signals have been tested, 5-4-5 and 3-4-3 bar steps, and the valve closure was applied to introduce some pressure disruption. It can be seen from the figure, that the pump output pressure follows the control signal with good accuracy, although very small pressure overshoots are present in all the investigated cases. It is evident that the predicted controller responses are well-damped. All the controller responses are in close agreement and compensate for the pressure variations caused by the ball valve closure. Although the fuzzy controller exhibits small steady state oscillations, the pump outlet pressure response is stable. The adaptive PID controller performs slightly better than the fixed gain schedule PID controller.

The closed loop responses when a 1s unit ramp signals (5-4-5 and 3-4-3) are applied as the reference pressure are given in figure 8.11. From the figure it is evident that the pump pressure follows the reference signal with good accuracy for all the investigated control techniques and, due to the fact that the system is well damped, the dynamic response is very good. The simulated results obtained for all the controllers show that all the investigated controllers successfully keep the pump outlet pressure on the reference level, although the fuzzy logic controller compensates for pressure changes at a faster speed and a smaller steady error during the ramping periods. The fixed scheduled gains has the highest steady-state error and the slowest time response.

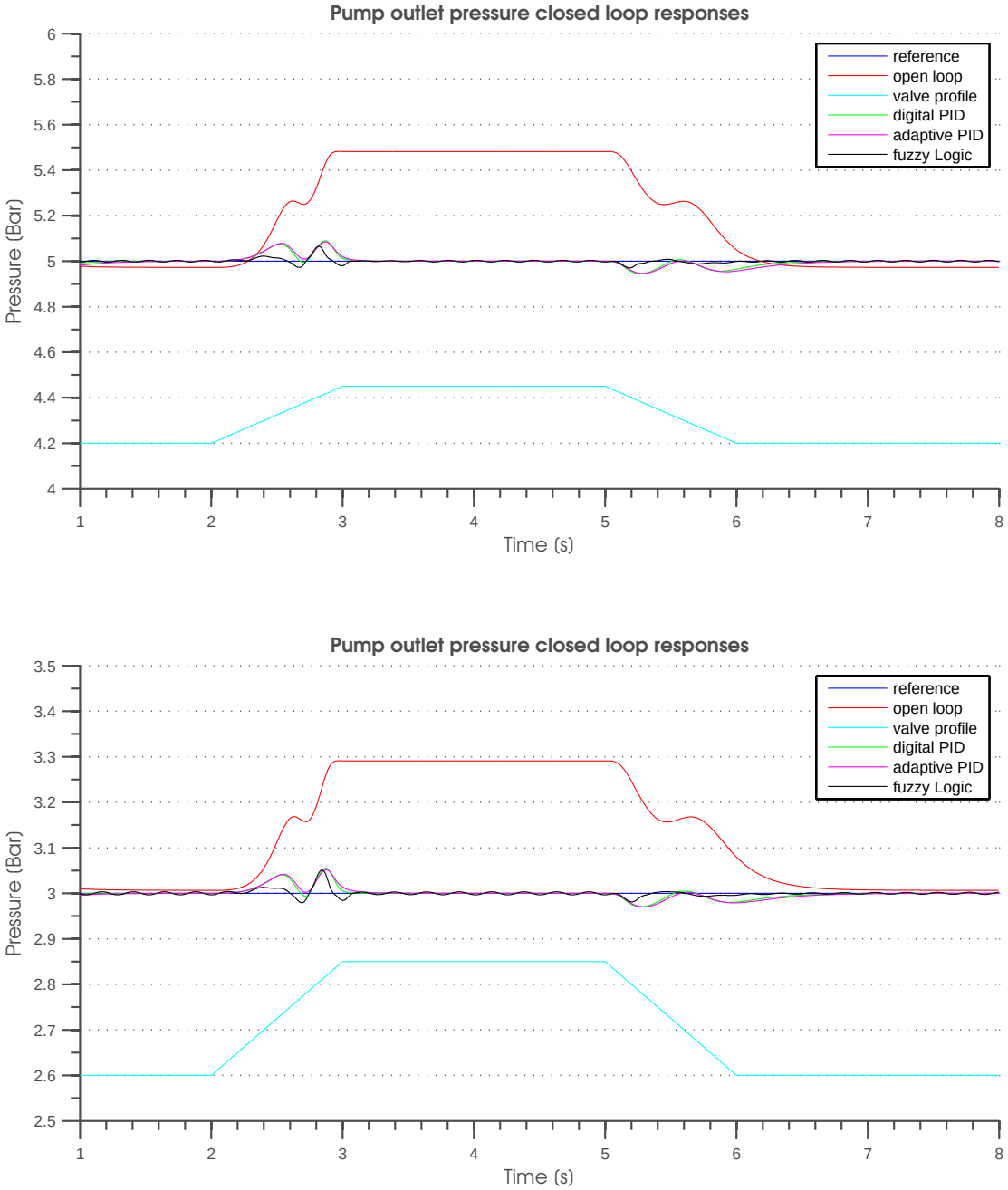

Figure 8.9. Pump outlet pressure responses during valve closure

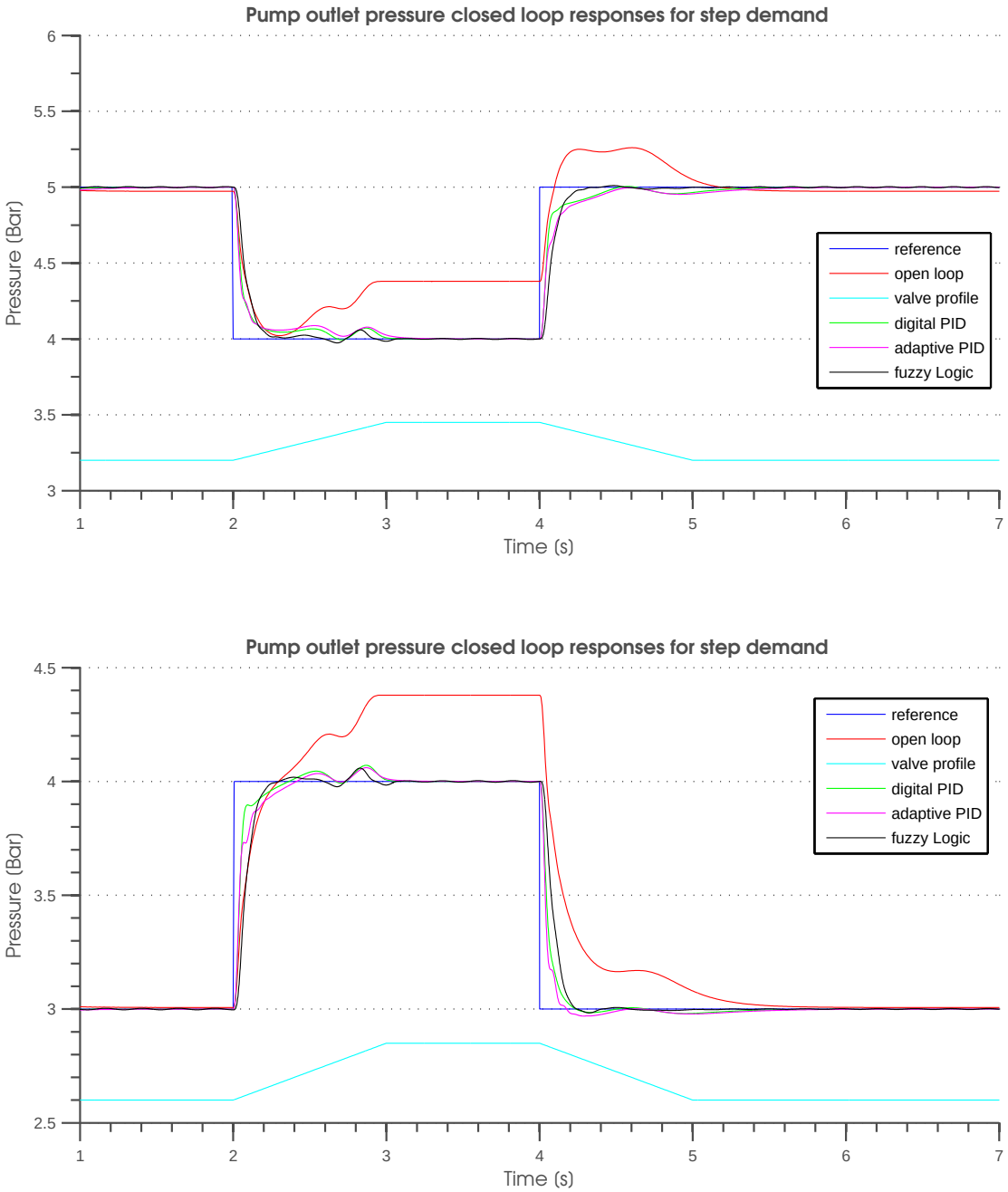

Figure 8.10. Pump outlet pressure responses for step demand during valve closure

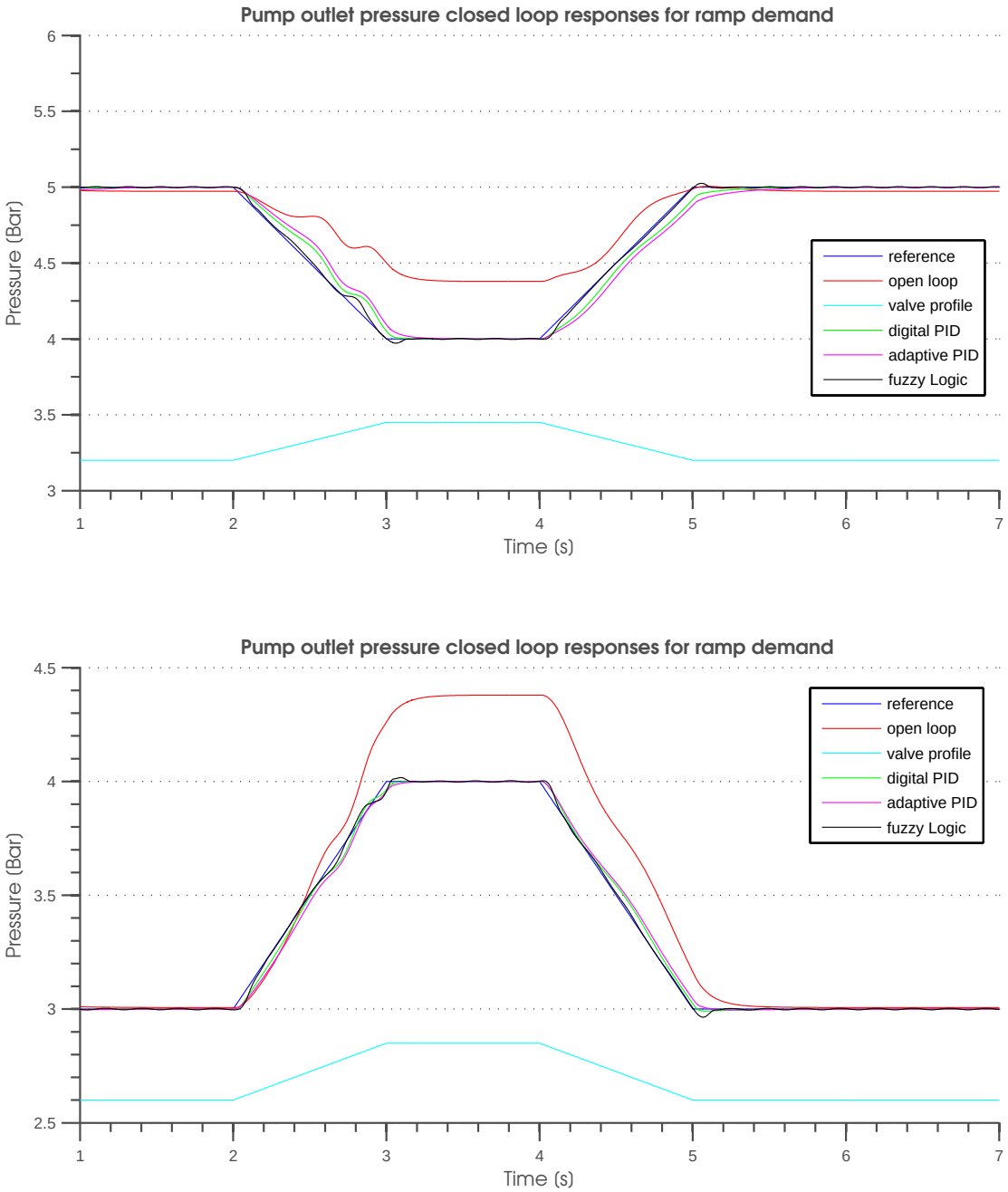

Figure 8.11. Pump outlet pressure responses for ramp demand during valve closure

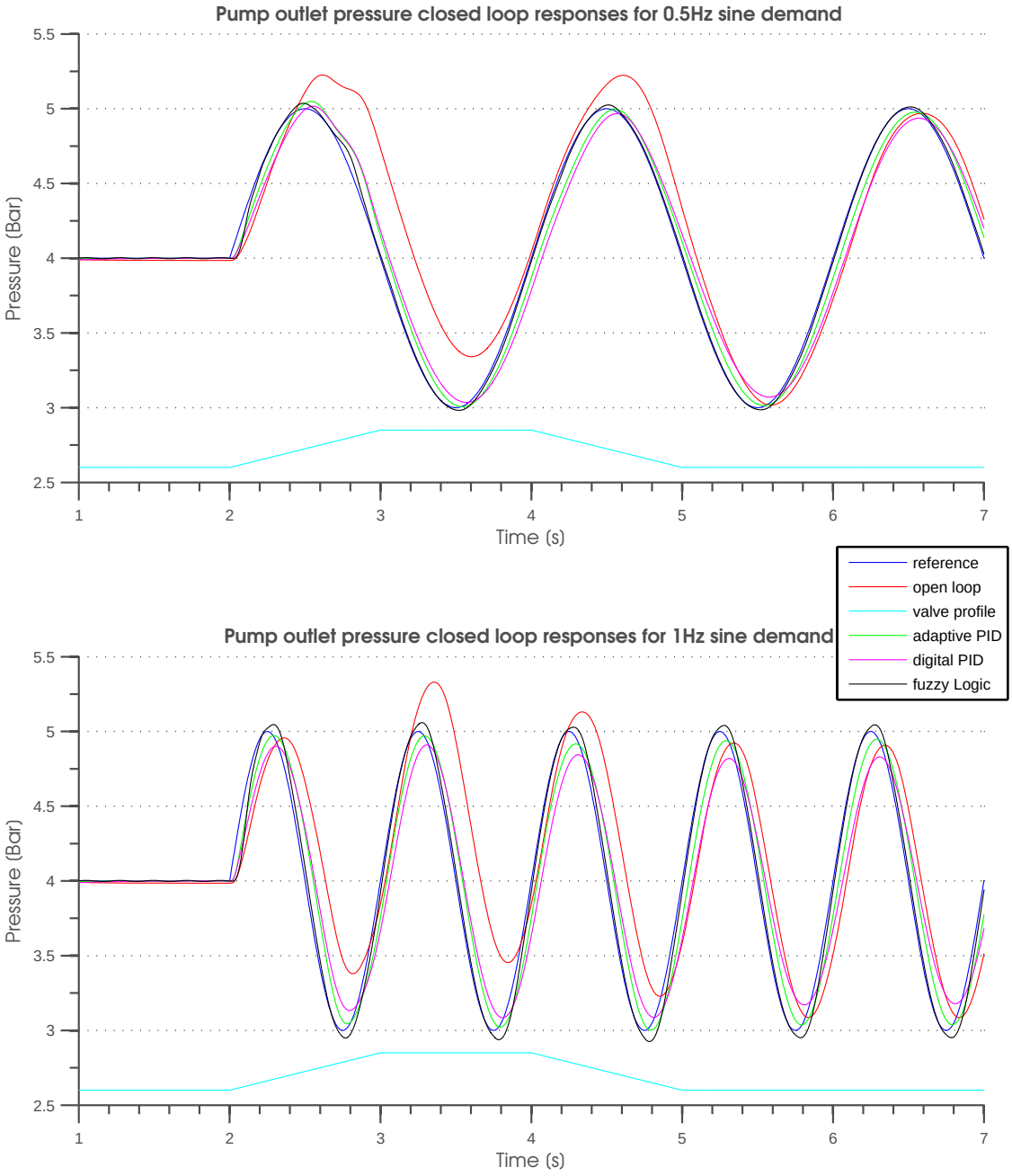

Figure 8.12. Pump outlet pressure responses for sine demand during valve closure

The pump outlet pressure responses to a sine reference signal in closed loop control are shown in figure 8.12. The upper graph shows how the pressure follows a 0.5Hz sine control signal and the lower graph shows the responses obtained at 1Hz. In both cases the ball valve was operated in accordance with the profile shown on the figures. It is evident that the controllers are capable of controlling the pump outlet pressure to closely follow a reference signal even though a disturbance is present in the system. During valve closure, when a disturbance is entered into the system, the controllers reduce the motor speed to compensate for pressure changes. The simulation results obtained for all the controllers show good performance, although the fixed gain PID control tends to lag most behind the demand signal and exhibits the largest steady state error. The fuzzy logic control strategy exhibits the best time responses with the smallest steady state error. The adaptive PID controller performance is better than its fixed gain counterpart due to the ongoing gain optimisation involved. However, the gain adaptation is not sufficient to eliminate the steady state error, due to the small adaptation rate used. Including a higher adaptation rate, however, makes the system response oscillatory when sudden reference changes are applied to the controller input.

8.6 Closure

Different digital control strategies were investigated for controlling the pump outlet pressure. A discrete PID controller with scheduled gains is described and successfully implemented in the fuel test rig nonlinear simulation model. Two different implementations of this controller are presented including the classical parallel structure with integrator anti-windup and a real time algorithm based on a IIR filter. The gain scheduling method was added to the classical PID to improve the pump pressure responses at different operating conditions.

The adaptive PID control scheme was implemented using a IIR filter based PID algorithm. The adaptation algorithm is based on the general adaptation scheme, where two error signals are the inputs to the controller. The controller performance error has been determined and based on this the adaptation rate chosen. A fuzzy logic type controller was also designed to control the pump outlet pressure. The fuzzy logic operation is explained and the control surface for the developed controller presented. This control scheme does not require any knowledge of the plant and nonlinear control characteristics and was shown to work very well.

The controllers' performance is compared using the nonlinear model of the fuel test rig. The test results indicate that all the controllers perform satisfactorily, although some differences exist. An overshoot is not present on any of the investigated controllers and the settling times are also satisfactory. It was found that the fixed gain PID with scheduled gains is the worst option for the pump pressure control due to its design assuming fixed,

linear system dynamics. The adaptive PID controller was shown to control and regulate the pump outlet pressure with good accuracy. However, the performance of this controller is largely dependent on the chosen adaptation rate since this factor influences the controller stability and time responses. For sudden control error changes the controller's gains adapt quickly, however during small changes the adaptation is less good. Although the adaptation rate could be increased, this may increase the pressure overshoot during sudden changes in control error. The adaptive controller parameters converged to optimal values and the pump outlet pressure followed the demand signals.

The fuzzy logic control strategy give the fastest response due to the nonlinear technique used for the fuzzy set implementation. Some oscillations exist in steady state, due to the bang-bang type of operations involved in the fuzzy set evaluation. However, the controller performance is stable and the oscillation peaks are less that 50mBar. The peaks are independent of the level of reference control signal applied to the controller. It was shown that this type of control strategy works very well for different pressure demand signals and can also compensate for sudden system pressure changes, despite the lack of knowledge of the investigated system dynamics.

As was mentioned at the beginning of the chapter, the controller design and implementation is limited to a simulation study, due to problems with the hardware. Therefore, it was not possible to validate the simulated data using the experimental test results. However, based on the successful design of the analogue PI controller presented in chapter 7, where the simulation data is validated using the test rig experimental results, it is assumed that the simulated results provide an accurate assessment of the controller performance. Based on the simulation study, the fuzzy logic control technique is recommended for future fuel test rig pump pressure regulation and development, because it offers the best accuracy and the fastest responses despite not using precise knowledge of the plant behaviour.

Chapter 9

Conclusions

The fuel systems fitted to the current generation of civil transport aircraft are rather complicated, due to the presence of multiple tanks, pumps, valves and consequently a complex pipeline structure. During fuel transfer between tanks for the centre of gravity control or for engine feed, and re-fuel operations, a number of pumps and valves are involved resulting in complex pressure and flow interactions. When transfer of fuel between tanks is employed, high pressure surges can occur when the valves are closed very rapidly. This leads to serious pressure surge problems which could damage the fuel system. In re-fuel operations the quantity of the fuel transfer to the tanks has to be controlled in order to avoid a volume overflow and, as a consequence, pressure surges are produced. Electric motor drive system control techniques have been investigated in this thesis to minimise the pressure surges during sudden system changes and the flow overshoot during fuel transfers and re-fuel operations. It is proposed that the current control method of electrically driven centrifugal-type pumps could be replaced by improved open and closed loop strategies, where the flow overshoot can be minimised and the pressure surges reduced.

A research overview into new technology in aerospace has been conducted and new trends are presented. This indicates that it is likely that existing non-electric power systems, and drives and actuators will be replaced by electrical equivalents. To make this transition possible a number of new or improved motor drive systems will be required, such as more sophisticated induction- motor-based drive systems to drive centrifugal pumps in the fuel system. The control operation and performance of an improved control system for an induction-motor fuel-pump drive system has been investigated in this thesis by developing simulation and experimental models of the drive systems and aircraft fuel line.

The simulation results obtained have been validated by comparison with experimental

data acquired from the fuel-line test rig. The test rig was originally designed and built to determine the operating characteristics of an AC induction motor and the fuel test rig developed for the Active Valve and Pump Technology Project has been modified to include appropriate control and data acquisition software. Analytical and numerical methods have been applied to determine the test rig parameters and working fluid properties.

The steady-state and dynamic modelling methods for a typical fuel-pump drive AC induction motor are discussed and presented. The methods were applied to a Lowara induction motor used to drive the centrifugal pump fitted in the fuel test rig. A second identical Lowara induction motor was purchased and tested, and the experimental data obtained from the induction motor test rig was used for model validation.

A method for measuring the parameters of an induction motor is described and applied to the Lowara induction motor and three sets of tests have been performed. The measured data are compared to the values obtained from the manufacturer and two sets were shown to give good agreement.

A steady-state AC induction motor model has been developed using the equivalent circuit lumped-parameter approach. The model can predict torque, current, power components, power factor and efficiency and has been applied to the motor in the test rig. Based on the parameter values obtained from the manufacturer and those data measured on the test rig, the motor steady-state characteristics have been evaluated. Results from motor simulation have been validated using the experimental data from the induction motor test rig. It is shown that the model and the test rig data are in close agreement (error less than 10%). However, the model predictions are limited to the linear region due to the assumptions made including lack of magnetic saturation and skin effect. The simple torque approximation equation, called the Kloss formula, has been presented and validated using the developed steady-state torque model.

Methods of simulating the dynamic behaviour of an induction motor have been investigated. Generalised machine theory has been applied to analyse transient behaviour. A transient model developed using an arbitrary rotating reference frame is described and validated using published data. The transient torque-speed characteristics of the Lowara motor have been determined using measured parameters. It has been shown that both the steady-state and transient models predict the behaviour of the Lowara induction motor consistently well by comparing simulation model results with practical measurements.

A Finite Element model of the induction motor has been developed using the in-house MEGA simulation software package. The dimensions of the Lowara induction motor were measured and separate meshes for the stator and the rotor were created independently before being joined together to form the complete model. The complete motor cross-section was configured and the physical material properties of the motor assigned to the model, forming a two-dimensional model of the Lowara motor. A separate FEM model

of the end of the motor was created in order to determine the stator end-turn and the rotor end-ring external parameters required for the complete FEM analysis. The data obtained were compared to the end-ring resistance determined using analytical methods and good agreement was obtained. The two dimensional analysis of the FEM model was performed and it was found that the 2D model is insufficient to simulate the complete motor behaviour due to torque variations with angular displacement. Therefore, a two dimensional multi-slice $2\,^1/_2\,\mathrm{D}$ version was created, where four slices were joined together and configured to obtain an approximation to a full 3D model.

The steady-state motor characteristics were predicted using the $2\,^1/_2\,\mathrm{D}$ model and the results compared with the results obtained from a Simulink model and experimental data. The locked rotor characteristics of the starting torque and current were determined from measurements at the rated conditions. The data obtained from the MEGA simulations show generally good trend with the Simulink predictions and the test-rig results. The steady-state torque and current versus operating speed characteristics were also determined. Although the results obtained from MEGA are slightly different from the Simulink data, acceptable data correlation (in the normal low-slip operating linear region) is obtained when compared to the experimental results. The transient characteristics of the motor were investigated. A practical free-running motor test was performed and the obtained torque-speed characteristics have been compared with the Simulink predictions. These show a similar pattern of variation, but different peak values. A practical motor acceleration test with a load connected to the shaft was also performed. The torque results obtained generally compared well with the Simulink counterpart, but, as found for the free-run test, the peak values differ slightly. However, both transient models reach the same steady state operating points, resulting in good agreement (error less than 10%) in the linear region.

The MEGA and Simulink models were compared for both steady state and transient behaviour. However, a transient experimental validation has not been undertaken because of current safety constraints. The model performance differences are thought to be caused by model inaccuracies, since the MEGA model is only a $2\,^1/_2\,\mathrm{D}$ approximation to the real motor geometry and the precise material properties were not known, whereas the Simulink model is based on the lumped parameter approach, where the skin effect, magnetic saturation and thermal effects are not taken into account. The 3D model of the Lowara induction motor has not been studied since the computation time needed to obtain the motor characteristics was extremely long. Due to difficulties related to the FEM model incorporation into the complete fuel test rig the MEGA results have been used as the alternative way to validate the Simulink model.

The mathematical methods of modelling the hydraulic components used in the fuel test rig are described and the component models developed. The centrifugal pump model developed by Boyd [31] has been modified to represent the actual centrifugal pump used

in the fuel test rig. The pump model is based on the measured and then normalised dimensionless pressure-flow and hydraulic power-torque characteristics of the pump. This approach allows the pump behaviour to be predicted at different operating conditions including variable speeds when connected to motor drive system. The mathematical modelling approach developed by Roberts [30] for the ball valve simulation, has been used to create the valve model in Simulink. This model is based on experimental measurement. These allow the valve relationships, such as the flow coefficient and the valve area, to be determined and expressed as a function of valve angle.

The flow in a long pipeline has been characterised and appropriate pipe models have been created based on *Darcy's* equation. At low-values of Reynolds number, laminar flow is employed. Turbulent flow ($Re > 2300$) is modelled using a nonlinear friction factor relationship known as *Halland's* equation or using a dimensionless head relationship. Both approaches have been used in the pipe modelling with the former approach used to represent the main pipeline and the latter for return line back to tank.

The steady-state pressure losses associated with the various rig components have been included in the analysis. The couplings, bends and the return line measured losses have been expressed as K factors and have been represented as equivalent length of straight pipe in the pipe model. The compressibility of the fluid has been taken into account and presented as a function of the fluid volume and the effective bulk modulus. An inertia model has been developed, where the fluid inertance is expressed in terms of the fluid properties and the pipeline dimensions. In addition, cavitation and air release in the fluid has been modelled using a reduced bulk modulus.

In order to simulate the behaviour of the fuel test rig a nonlinear model has been created, based on the mathematical models developed for the individual components. These components have been modelled as individual blocks and linked together to create the complete system model. The complete model includes sub-models for the electric drive system, the centrifugal pump, the long section of pipeline with included minor losses, the tank, the motor driven ball valve used to the control flow, and a return line.

The system model has been developed using two different model/simulation packages and the results obtained have been compared with measured data. Bath*fp* (fluid power simulation package) and Simulink have been used to simulate the performance of the test rig during both steady-state and dynamic operations. The differences between the simulation packages have been discussed and the results obtained from both packages compare well in general and show good trend with the rig data. The Simulink model has been chosen for further test rig simulations as the main simulation tool due to the convenience of model implementation and modifications as well as due to the faster time of the solution.

The performance of two different inverters connected to the motor have been investigated

showing their impact on the pump behaviour. It is clear that the Moeller inverter can deliver better quality three-phase power to the motor, compared to the Hydrovar inverter used by Lowara for controlling the speed of their pump.

Simulations of the fuel test rig have been performed using both simulation packages and the results obtained compared to practical results. The pump pressure-flow characteristics have been validated using the complete test rig model for different supply conditions. It is shown that the pump model is capable of predicting the actual pump behaviour. The experimental responses of the induction motor for torque and current are compared with sets of simulation model results. The torque model predictions match the measured data well, however, the current results differ by a few percent most likely due to error in the estimation of the motor parameters.

The steady-state and transient simulations versus time have been performed for the complete model and validated against experimental data. The models have been tested for a number of different supply conditions and under two developed valve operation profiles. It is shown that the system and component models are capable of predicting the rig performance over a range of operating conditions, despite the modelling assumptions made. Acceptable fits between practical rig results and simulation results are obtained for the pump outlet pressure, the system flow rate and the valve upstream and downstream pressures responses. The shaft speed and torque models have also been validated and small differences of up to a few percent were found between model and rig results, most likely due to imperfect motor parameter estimation, especially for the Bath*fp* model where a less accurate model was used for the torque prediction. Nevertheless, by comparing the measured and simulated data it is clear that the Simulink nonlinear model is able to predict the fuel rig behaviour and could therefore be used to investigate different control strategies for the pump outlet pressure regulation.

In order to evaluate the fuel system behaviour predictions using linear control techniques, linear models of the test rig components were developed and inter-connected to constitute the complete fuel test rig. The obtained linearised-system responses were then compared with the full non-linear model behaviour and acceptable pressure curve fit was obtained. The system was described by transfer functions and the obtained frequency responses presented on Bode diagrams. The model was linearised at different operating points and characterised by a dominant time constant and DC gain for each case. The system performance was analysed at three different valve angles and four different operating speeds, showing that the inverter-disturbed pump outlet pressure responses are fairly constant regardless of the pump speed. The valve-disturbed pump pressure responses, however, depend on the valve angle position and the responses obtained become slower with increasing valve angle.

The open-loop responses of the system have been investigated experimentally using dif-

ferent input references including unit-step, unit-ramp, valve disturbance and sinusoidal signals. The system simulation-model results match the measured behaviour well, although the best results were obtained with low frequency control signals. The closed-loop control of the pump outlet pressure was implemented using an analogue PI controller, where the controller gains were determined using the transfer function approach. However, in the actual fuel test rig a hidden gain was found to be present in the controller and as a consequence, the PI controller gains were adjusted to achieve acceptable performance level. The simulation responses have been compared with experimental data and agree well. By applying a simple proportional plus integral (P+I) controller to the pump drives, the pump outlet pressure was controlled to match the required set-point/reference value. This study has demonstrated that the PI control system can achieve acceptable tracking performance and anti-disturbance rejection for the pump outlet pressure control. Acceptable controller performance is achieved up to 1Hz. Moreover, the resulting pressure overshoots using the PI control are small during sudden system changes as shown by the step responses. From the simulation results it was found that the model can predict the fuel rig behaviour during both open-loop and closed-loop control. Therefore, the model can be used to design a more efficient and robust controller for the pump outlet pressure. However, it is necessary to improve the model/system if control signals with frequency content above than 2Hz are to be applied since the model output ceases to accurately follow higher frequency inputs.

The simultaneous use of the ball valve and the pump control strategy is proposed to minimise the pressure surge and reduce flow volume overshoot. Simulations were developed to investigate the impact of the shaft speed reduction on the valve upstream pressure and the flow overshoot during a sudden valve closure. A number of valve-pump control profiles were developed and compared with measured data, showing good plot fit. It is evident that the proposed strategy can significantly reduce the pressure surge and minimise the flow overshoot in the fuel rig. It was concluded that the best results are achieved when the pump speed reduction time is two times faster than the valve operation time. The results of the simulations have shown that, in this case, such a control technique had a very significant impact on the system pressure. In addition a reduction in the flow overshoot is achieved, although better results have been obtained when the pump starts operation prior to valve operation. Other benefits of the proposed control technique over the current on-off system include a minimisation of cavitation at the downstream side of the valve and a reduction of the stresses acting on the valve and the fuel system.

Different digital control strategies have been investigated for controlling the pump outlet pressure. A discrete PID controller with scheduled gains is described and successfully implemented in the fuel test rig nonlinear simulation model. Two different implementations of this controller are presented including the classical parallel structure with integrator anti-windup and a real time algorithm based on an IIR filter. The gain scheduling method

was added to the classical PID to improve the pump pressure responses at different operating conditions. The adaptive PID control scheme was implemented using a IIR filter based PID algorithm. The adaptation algorithm is based on the general adaptation scheme, where two error signals form the inputs to the controller. The controller performance error has been determined and based on this the adaptation rate chosen. A fuzzy logic type controller was also designed to control the pump outlet pressure. The fuzzy logic operation is explained and the control surface for the developed controller presented. This control scheme does not require any knowledge about the plant and nonlinear control characteristics and was shown to work very well.

The controllers' performances are compared using the nonlinear model of the fuel test rig. The test results indicate that all the controllers perform satisfactorily, although some differences exist. An overshoot is not present on any of the investigated controllers and the settling times are also satisfactory. It was found that the fixed gain PID with scheduled gains is the worst option for robust pump pressure control. The adaptive PID controller was shown to control and regulate the pump outlet pressure with good accuracy. However, the performance of this controller is largely dependent on the chosen adaptation rate since this factor influences the controller stability and time responses. For sudden control error changes the controller's gains adapt quickly, however during small changes the adaptation is less good. Although the adaptation rate could be increased, this may increase the pressure overshoot during sudden changes in control error. The adaptive controller parameters converged to optimal values and the pump outlet pressure followed the demand signals.

The fuzzy logic control strategy gives the fastest responses due to the nonlinear technique used for the fuzzy set implementation. Some oscillations exist in steady state, due to the bang-bang type of operations involved in the fuzzy set evaluation. However, the general controller performance is fast and stable, and the low-level hunting oscillation peaks are less that 50mBar. The peaks are independent from the reference control signal applied to the controller. It was shown that this type of control strategy works very well for different pressure demand signals and can also compensate for sudden system pressure changes. It has the great advantage of requiring relatively little knowledge of the system transfer function.

9.1 Recommendations for Future Work

The developed simulation models reported in this thesis provide a useful tool for evaluating both system components and system control design for fuel systems. Such simulations could be extended to form the basis of a fault detection/prediction tool or be a tool for system stability/reliability improvement. Additional work is required to improve the specific controller developed for the fuel test rig. It is shown that the control system response is limited to about 2Hz bandwidth. Hence, further work is required to allow

control the system to be extended to higher frequencies. The induction motor model needs to be developed further to include skin effects, magnetic saturation and thermal effects. There is scope to improve the predicted dynamic behaviour of the centrifugal pump by extending the model to include more than one lumped stage. The pipelines are modelled using the lumped parameter approach where the cavitation is expressed as a Bulk modulus reduction. The implementation of a more detailed representation of cavitation hammer effect is required to improve the pipe model accuracy. A distributed-parameter pipe model could also improve accuracy and transient response of the pipeline.

Experimental validation of the digital controllers' simulated performance should be conducted using the fuel test rig experiments. The proposed fixed gain, adaptive PID and fuzzy logic control algorithms for the pump outlet pressure control should be implemented on a digital controller. It is recommended that this be undertaken using a DSP-based control card. An integrated algorithm for the simultaneous valve and pump control should be considered as an alternative to the master and slave control approach currently used. This could be implemented on the single DSP control board along with the pump outlet pressure controller.

A further extension to the proposed control techniques is suggested where the faster valve closures could result in large pressure peaks. An additional technique is required to compensate for the time delay caused by the transport lag of the pipeline. The valve closure profiles should be optimised for the shaft speed reduction in order to minimise the fuel transfer quantity overshoot.

References

[1] R. Schroer. Electric power. A century of powered flight: 1903-2003. *Aerospace And Electronic Systems Magazine*, 18(7):55–60, 2003.

[2] R.I. Jones. The More Electric Aircraft: The past and the future? *IEE Colloquium On Electrical Machines And Systems For The More Electric Aircraft*, November 1999.

[3] L. Faleiro. Beyond the More Electric Aircraft. *Aerospace America*, 2005.

[4] R.E.J. Quigley. More Electric Aircraft. *Applied Power Electronics Conference And Exposition*, pages 906–911a, March 1993.

[5] S.J. Cutts. Collaborative approach to the More Electric Aircraft. *International Conference On Power Electronics, Machines And Drives*, pages 223–228, June 2002.

[6] M.E. Elbuluk and M.D. Kankam. Motor drive technologies for the Power-By-Wire (PBW) program: Options, trends and tradeoffs - Part I: Motors and controllers. *Aerospace And Electronic Systems Magazine*, 10(11):37–42, November 1995.

[7] I. Moir. More Electric Aircraft - system considerations. *IEE Colloquium On Electrical Machines And Systems For The More Electric Aircraft*, pages 10/1–10/9, November 1999.

[8] J.A. Weimer. Electrical power technology for the More Electric Aircraft. *12th Digital Avionics Systems Conference*, pages 445–450, October 1993.

[9] R.T. Rubertus. Application of high temperature magnetic materials. *IEEE Transactions On Magnetics*, 36(5):3373–3375, September 2000.

[10] J.A. Weimer. The role of electric machines and drives in the More Electric Aircraft. *IEEE International Electric Machines And Drives Conference*, 1:11–15, June 2003.

[11] W. Pearson. The more electric/all electric aircraft-a military fast jet perspective. *IEE Colloquium on All Electric Aircraft*, 1998.

[12] K. Emadi and M. Ehsani. Aircraft power systems: technology, state of the art, and future trends. *Aerospace and Electronic Systems Magazine, IEEE*, 15:28–32, 2000.

[13] M.E. Elbuluk and M.D. Kankam. Potential starter/generator technology for future aerospace application. *Aerospace And Electronic Systems Magazine IEEE*, 11(10):17–24, Ovtober 1996.

[14] G.M. Raimondi, T. Sawata, M. Holme, A. Barton, G. White, J. Coles, P.H. Mellor, and N. Sidell. Aircraft embedded generation systems. *International Conference On Power Electronics, Machines And Drives*, pages 217–222, June 2002.

[15] M.J. Provost. The more electric aero-engine: a general overview from an engine manufacturer. In *International Conference on Power Electronics, Machines and Drives*, pages 246–251, 2002. Bath,UK, (Conf. Publ. No. 487).

[16] M. Bailey, N. Hale, G. Ucerpi, J.A. Hunt, S. Mollov, and A Forsyth. Distributed electrical power management architecture. *IEE Colloquium on Electrical Machines and Systems for the More Electric Aircraft*, 1999.

[17] M.A. Maldonado and G.J. Korba. Power management and distribution system for a More-Electric Aircraft (MADMEL). *IEEE Aerospace and Electronic Systems Magazine*, 14(12):3–8, December 1999.

[18] K.C. Reinhardt and M.A. Marciniak. Wide-bandgap power electronics for the More Electric Aircraft. *Energy Conversion Engineering Conference,IECEC 96, Proceedings of the 31st Intersociety*, 1996.

[19] K.W.E. Cheng. Comparative study of AC/DC converters for More Electric Aircraft. *Seventh International Conference On Power Electronics And Variable Speed Drives*, pages 299–304, September 1998.

[20] A. Uan-Zo-Li, R. Burgos, F. Wang, D. Boroyevich, F. Lacaux, and A. Tardy. Comparison of prospective topologies for aircraft autotransformer-rectifier units. *Industrial Electronics Society, IECON '03. The 29th Annual Conference of the IEEE*, 2003.

[21] B. Thomas. The influence of nickel on the magnetic and mechanical properties of Co-Fe-V alloy. *IEEE Transactions On Magnetics*, 16(2):444–454, March 1980.

[22] W.G. Homeyer, E.E. Bowles, S.P. Lupan, P.S. Walia, and M.A. Maldonado. Advanced power converters for More Electric Aircraft applications. *Proceedings Of The 32nd Intersociety Energy Conversion Engineering Conference*, 1:591–596, July 1997.

[23] D. Kankam and M. Elbuluk. A survey of power electronics applications in aerospace technologies. *36th Intersociety Energy Conversion Engineering Conference*, 2001.

[24] P.W. Wheeler, J.C. Clare, L. de Lillo, K.J. Bradley, M. Aten, C. Whitley, and G. Towers. A comparison of the reliability of a matrix converter and a controlled rectifier-inverter. *2005 European Conference on Power Electronics and Applications*, 2005.

[25] V. Bondarenko, M.S. Mazzola, R. Kelley, Cai Wang, Yi Liu, and W. Johnson. SiC devices for converter and motor drive applications at extreme temperatures. *Aerospace Conference, IEEE*, 2006.

[26] M.K. Kazimierczuk and R.C. Cravens. Application of super capacitors for voltage regulation in aircraft distributed power systems. *27th Annual IEEE Power Electronics Specialists Conference*, 1:835–841, June 1996.

[27] A.G. Jack, B.C. Mecrow, and J.A. Haylock. A comparative study of permanent magnet and switched reluctance motors for high - performance fault - tolerant applications. *IEEE Transactions On Industry Applications*, 32(4):889–895, July/August 1996.

[28] R. Krishnan and A.S. Bharadwaj. A comparative study of various motor drive systems for aircraft applications. *Industry Applications Society Annual Meeting IEEE*, September/October 1991.

[29] R.M. Crowder. Electrically powered actuation for civil aircraft, actuator technology:, current practice and new developments. *IEE Colloquium On Actuator Technology*, pages 5/1–5/3, May 1996.

[30] A. Roberts. *Active Valve and Pump Technology - Modelling and Experimental Investigation into the Performance of an Aircraft Fuel System Ball Valve*. PhD thesis, University of Bath, 2010.

[31] L. Boyd. *Active Valve and Pump Technology - Modelling and Control of Variable-Speed Trim Transfer Pumps in Aircraft Fuel Systems*. PhD thesis, University of Bath, 2008.

[32] M.I. Soumelidis. *Active Valve and Pump Technology, Project Update*. University of Bath, Centre for Power Transmission and Motion Control, Department of Mechanical Engineering Faculty of Engineering and Design, May 2006.

[33] IEEE. *IEEE Standard Test Procedure for Polyphase Induction Motors and Generators, ANSI/IEEE Std 112-1984*. IEEE, 1985.

[34] S. Ayasun and C.O. Nwankpa. Induction motor test using Matlab/Simulink and their integration into undergraduate electric machinery courses. *IEEE Transactions on Education*, 48(1):37–46, 2005.

[35] G. McPherson. *An introduction to electrical machines and transformers*. John Wiley and Sons, 1990.

[36] J. Hindmarsh. *Electrical Machines*. Pergamon Press, 1st edition, 1965.

[37] H.K. Messerle. *Dynamic Circuit Theory*. Pergamon Press, 1st edition, 1965.

[38] T.L. Skvarenina and DeWitt W.E. *Electrical Power and Controls*. Pearson Education, Inc., 2nd edition, 2004.

[39] C. Ong. *Dynamic Simulation of Electric Machinery Using Matlab/Simulink*. NJ Prentice Hall, New Jersey, 1998.

[40] D. Relji, D.B. Ostoji, and V.V. Vasi. Simple speed sensorless control of induction motor drive. *Sixth International Symposium Nikola Tesla*, October 18 20 2006.

[41] Z. Halamka and J. Pavelka. The speed control of the induction motor by the change of supply voltage. *Silnoprouda Electrotechnika a Elektroenergetika*, 2001.

[42] A. Hughes. *Electric motors and drives : fundamentals, types and applications*. Oxford Newnes/Elsevier, 3rd edition, 2006.

[43] P. Krause and O. Wasynczuk. *Electromechanical Motion devices*. McGraw-Hill, 1989.

[44] P. Krause. *Analysis of Electric Machinery*. McGraw Hill Book Company, New York, 1986.

[45] H. Akagi, E.H. Watanabe, and M Aredes. *Instantaneous power theory and applications to power conditioning*. John Wiley and Sons, 2007.

[46] R.J. Hill-Cottingham, P.C. Coles, D. Rodger, and H.C. Lai. Numerical models of an induction machine. *Magnetics, IEEE Transactions on*, 39(3):1551–1553, 2003.

[47] Applied Electromagnetic Research Centre. *MEGA V6.30, User Manual*. University of Bath.

[48] D. Rodger, H. C. Lai, and P.J. Leonard. Coupled elements for problems involving movement. *IEEE Transactions on Magnetics*, 26:548550, 1990.

[49] H.C. Lai, D. Rodger, and P.J. Leonard. A finite element method for problems with moving parts. *International Conference on Computation in Electromagnetics*, pages 211–213, 1991.

[50] P.J. Leonard, H.C. Lai, and D. Rodger. Finite elements and circuits. *IEE Colloquium on Power Electronic Systems Simulation*, pages 6/1–6/4, 1998. (Ref. No. 1998/486).

[51] N. Allen, H.C. Lai, P.J. Leonard, and D. Rodger. External circuit, movement, and periodicity considerations in the design of electrical machines using finite elements. In *Seventh International Conference on Electrical Machines and Drives*, pages 126–130, 1995. (Conf. Publ. No. 412).

[52] H.C. Lai and D. Rodger. Comparison of 2D and 3D finite element modelling results of a skewed induction machine. In *International Conference on Power Electronics, Machines and Drives*, pages 365–368, 2002. (Conf. Publ. No. 487).

[53] H.C. Lai and D. Rodger. Modelling rotor skew in induction machines using 2D and 3D finite element schemes. In *Electric Machines and Drives Conference Record, 1997. IEEE International*, pages WB3/5.1–WB3/5.3, 1997.

[54] F. Kreith. *Fluid mechanics*. CRC Press LLC, 2000.

[55] J.F. Douglas. *Fluid mechanics*. Pearson Prentice Hall, 2005.

[56] B.S. Massey and J. Ward-Smith. *Mechanics of Fluids*. Taylor and Francis, 8th edition, 2006.

[57] C.W. Richards, D.G. Tilley, and C. Brain. *The Bathfp Model Reference Guide*, 1999.

[58] Metzger & Willard, Inc. http://www.metzgerwillard.com.

[59] F. M. White. *Fluid Mechanics*. McGraw-Hill International Edition, 4th edition, 1999.

[60] D. McCloy and H.R Martin. *Control of Fluid Power, Analysis and Design*. Ellis Horwood Limited, 2nd edition, 1980.

[61] R. Gupta. *Introduction to Systems*. New Age International, 2005.

[62] The MathWorks Inc. *MATLAB user's guide*, version 7.4 edition, 2007.

[63] The MathWorks Inc. *Simulink user's guide*, version 6.6 edition, 2007.

[64] M.N. Sahinkaya. *Control Systems, Lecture Notes*. University of Bath, 2008.

[65] K. Ogata. *Modern control engineering*. Prentice Hall, 4th edition, 2002.

[66] C. L. Phillips and H. Nagle. *Digital control system analysis and design*. Prentice-Hall, 1995.

[67] K. J. Astrom. *Control System Design*. Lecture notes, chapter 6, PID control notes, http://www.cds.caltech.edu/~murray/courses/cds101/fa02/caltech/astrom.html, 2002.

[68] K. J. Astrom and R. M. Murray. *Feedback Systems: An Introduction for Scientists and Engineers*. Princeton University Press, 2008.

[69] F. Haugen. *PID Control*. Tapir Academic Press, 2004.

[70] S. Kamalasadan and A. Hande. A PID controller for real-time DC motor speed control using the C505C microcontroller. In *Proceedings of the 17th International Conference on Computer Applications in Industry and Engineering*, page 3439, 2004.

[71] J. Tang and R. Chassaing. PID controller using the TMS320C31 DSK for real-time DC motor control. In *Proceedings of the 1999 Texas Instruments DSPS Fest Conference*, 1999.

[72] R. Chassaing. *Digital Signal Processing and Applications with the C6713 and C6416 DSK*. Wiley-Interscience, 2005.

[73] J. Tang, R. Chassaing, and W. J. Gomes III. Real-time adaptive PID controller using the TMS320C31 DSK. In *Proceedings of the 2000 Texas Instruments DSPS Fest Conference*, 2000.

[74] S. N. Sivanandam, S. Sumathi, and S. N. Deepa. *Introduction to Fuzzy Logic using Matlab*. Springer, 2006.

[75] The MathWorks Inc. *Fuzzy Logic Toolbox user's guide*, 1999.

[76] V. Chitra and R. S. Prabhakar. Induction motor speed control using fuzzy logic controller. *World Academy of Science, Engineering and Technology*, 2006.

Appendix A

Parameters and Properties of the Fuel Test Rig Nonlinear Model

(a) Pressure - flow

Name	value
β_1	1.0835×10^7
β_2	1.1643×10^6
β_3	3.436×10^4
β_4	17.8113
β_5	−10.4845
β_6	2.1193

(b) Torque-hydraulic power

Name	value
γ_1	9711
γ_2	−3018
γ_3	253.09
γ_4	0.3901
γ_5	0.1263
γ_6	0.1153

Table A.1. Pump - fitting polynomial coefficients

(a) Flow coefficient

Name	value
v_{c1}	-2.192×10^7
v_{c2}	5.395×10^{-8}
v_{c3}	-5.326×10^{-6}
v_{c4}	2.648×10^{-4}
v_{c5}	-6.452×10^{-3}
v_{c6}	4.0456×10^{-2}
v_{c7}	1.398

(b) Orifice area

Name	value
v_{a1}	1.564×10^{-9}
v_{a2}	-5.328×10^{-7}
v_{a3}	7.206×10^{-5}
v_{a4}	-5.512×10^{-3}
v_{a5}	2.969×10^{-1}
v_{a6}	1.085
v_{a7}	0

Table A.2. Valve - fitting polynomial coefficients

Parameter	Symbol	Value	Unit
Stator resistance	R_s	0.776	Ω
Stator leakage reactance	X_s	1.780	Ω
Rotor resistance	R_r	0.908	Ω
Rotor leakage reactance	X_r	2.667	Ω
Magnetizing reactance	X_m	93.94	Ω
Inverter gain	K_i	31.41	-
Inverter time constant	t_i	0.1	s
Inverter V/f constant	k_Ψ	8	V/Hz
Motor Inertia	J_m	0.019	kgm^2
Load Inertia	J_l	0.020	kgm^2

Table A.3. Motor drive system

Name	symbol	value	unit
fluid bulk modulus	B_f	8.17×10^9	Pa
pipe Young modulus	E	69×10^9	Pa
fluid density	ρ	998	kg/m^3
gravity acceleration	g	9.81	m/s^2
fluid kinematic viscosity	ν	1.004×10^{-6}	$\text{m}^2\text{/s}$
fluid dynamic viscosity	μ	1.002×10^{-3}	kg/ms

Table A.4. Fuel system fluid properties

Name	symbol	value	unit
pipe length	l	16.6	m
pipe relative roughness	ϵ/d	5.5×10^{-5}	-
return line length	l_{rl}	4	m
return pipe diameter	d_{rl}	0.05	m
pipe diameter	d	0.0344	m
valve internal diameter	d_v	0.036	m
pipe wall thickness	t_w	0.0025	m
pump impeller radius	r	0.0735	m
pump positive displacement	υ	6.0686×10^{-4}	m^3
minor losses K factor	K	1.7	-

Table A.5. Fuel test rig dimensions

Appendix B

Test Rig Sensors and Acquisition Data

Data Translation - DT9834-1604-16 series		
analogue inputs	-	16
analogue outputs	-	4
sampling rate	kS/s	500
accuracy	% full scale	0.05

Table B.1. Data acquisition module -ADC and DAC

Lem/Fluke Norma - 5000 series		
inputs	-	6
bandwidth	Hz	DC to 10M
sampling rate	S/s	1M
accuracy	% full scale	0.05

Table B.2. Power analyser

Gems Sensors - 2200AGB series		
pressure range	bar	0-10
bandwidth	kHz	unspecified
accuracy	% full scale	0.25
Druck Ltd. - PDCR 10/35L series		
pressure range	bar	0-20
bandwidth	kHz	unspecified
accuracy	% full scale	0.1

Table B.3. Static pressure transducers - SGPTs

Entran - EPX N03 series		
pressure range	bar	0-35
bandwidth	kHz	< 35
accuracy	% full scale	0.25

Table B.4. Dynamic pressure transducer - PRPTs

Bestobell Meterflow Ltd - M9/2000/250B series		
flow rate range	L/min	50 to 1100
response time	ms	50
accuracy	% full scale	0.22

Table B.5. Turbine flow meter

Westland Aircraft Ltd - S2 series		
load range	Nm	0 to 160
speed range	rev/min	0 to 6000
bandwidth	Hz	unspecified
accuracy	% full scale	0.11
TorqueSense - E300 RWT1 series		
load range	Nm	0 to 100
speed range	rev/min	0 to 15000
bandwidth	Hz	1600
accuracy	% full scale	0.15

Table B.6. Torque transducers

Toothwheel Hall transducer		
teeth number	-	60
speed range	rev/min	0 to 6000
bandwidth	Hz	unspecified
accuracy	% full scale	0.15

Table B.7. Speed transducer

Thermocouple		
temperature range	℃	-40 to +125
bandwidth	Hz	unspecified
accuracy	% full scale	0.5

Table B.8. Thermocouple

Appendix C

Fuel Test Rig - Nonlinear Model

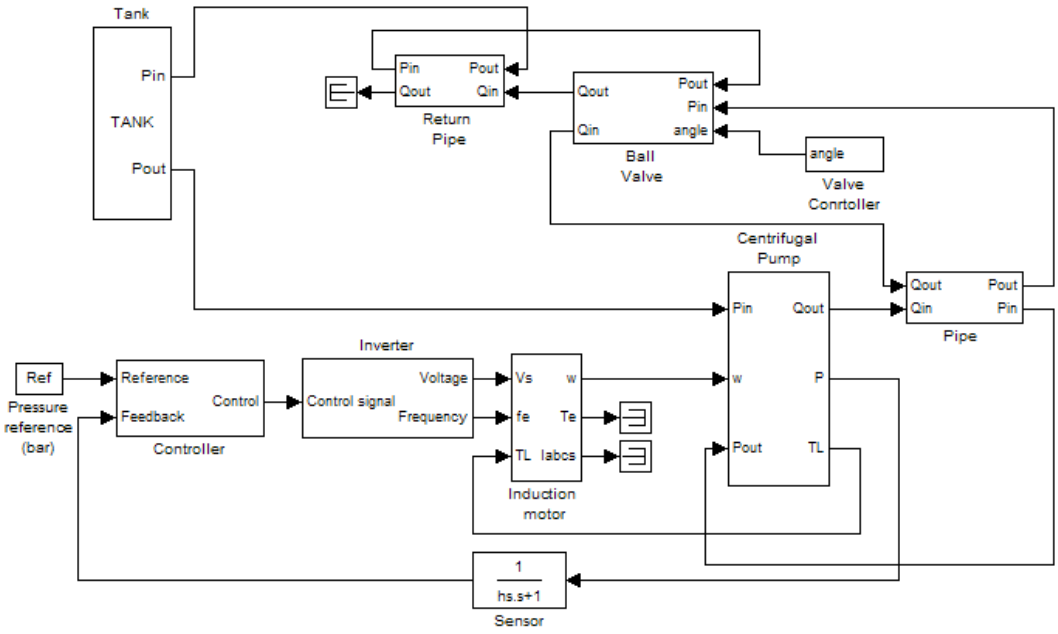

Figure C.1. Nonlinear model of the fuel test rig

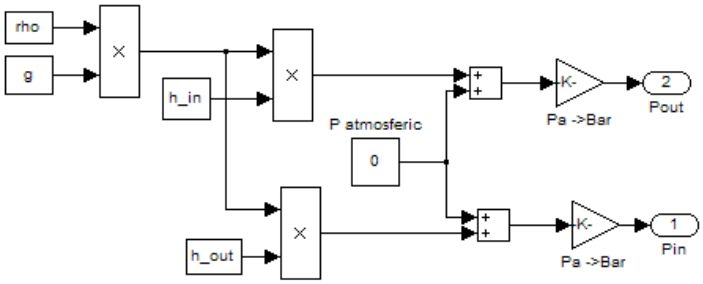

Figure C.2. Tank

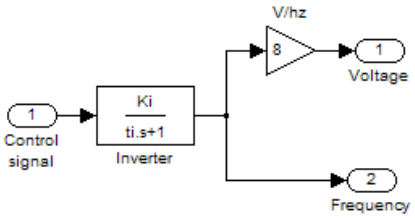

Figure C.3. Inverter

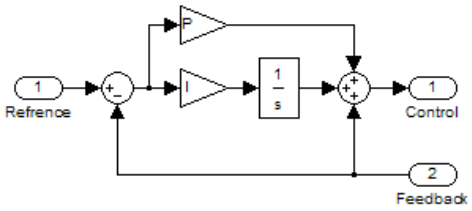

Figure C.4. Analogue PI controller

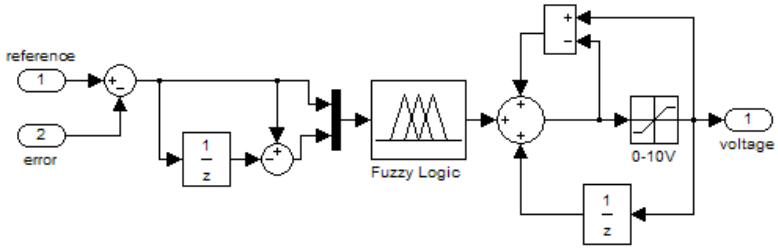

Figure C.5. Fuzzy logic controller

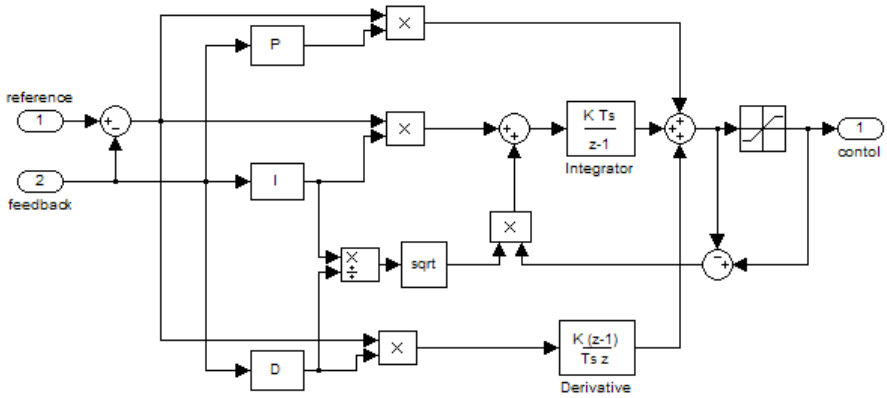

Figure C.6. Fixed gain PID controller

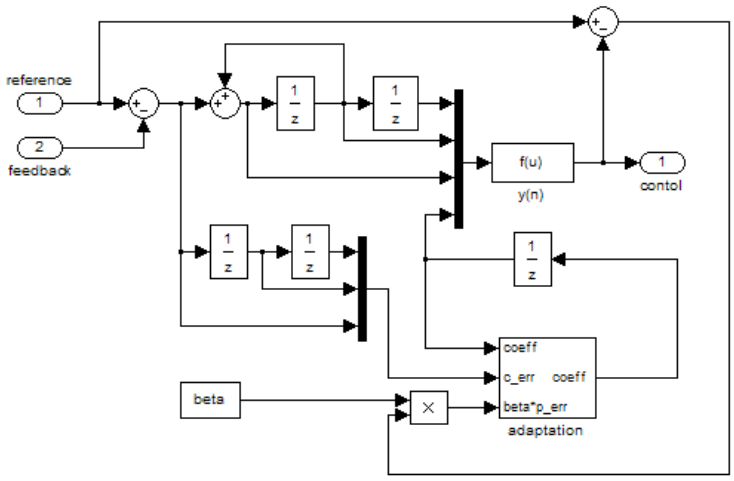

Figure C.7. Adaptive gain PID controller

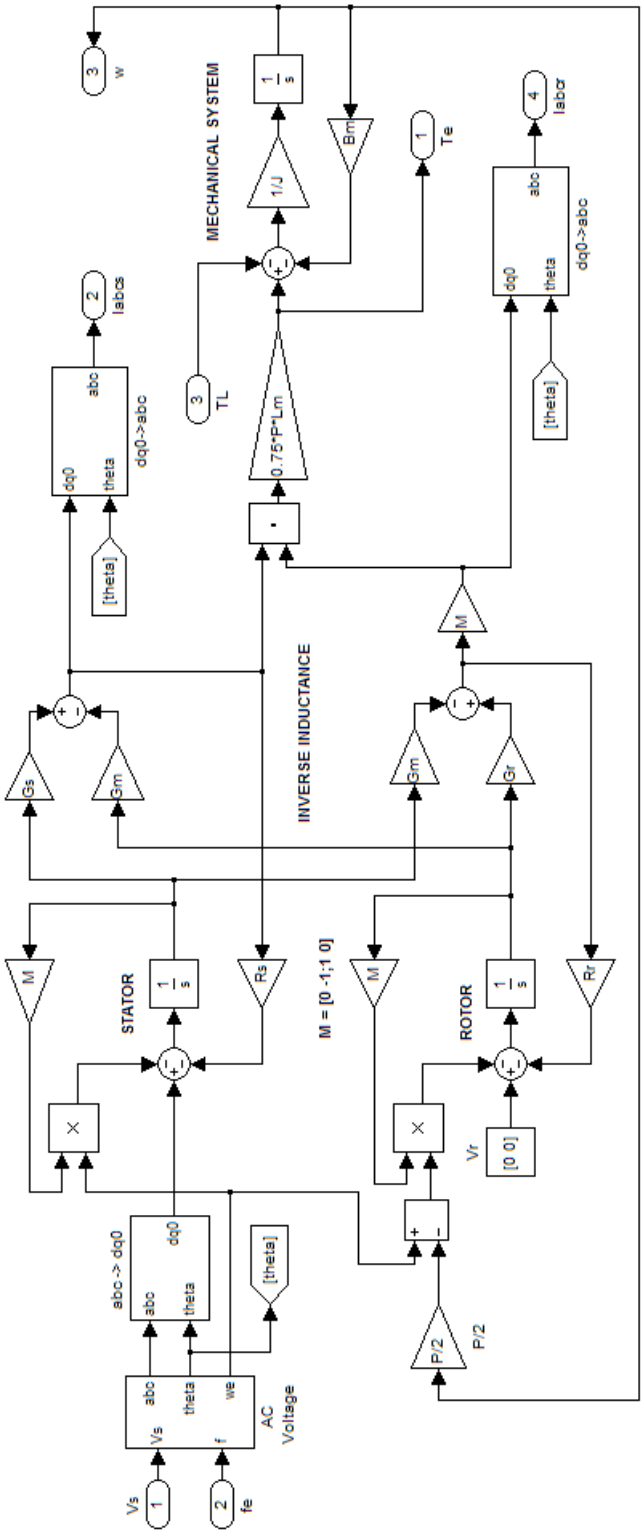

Figure C.8. Induction Motor

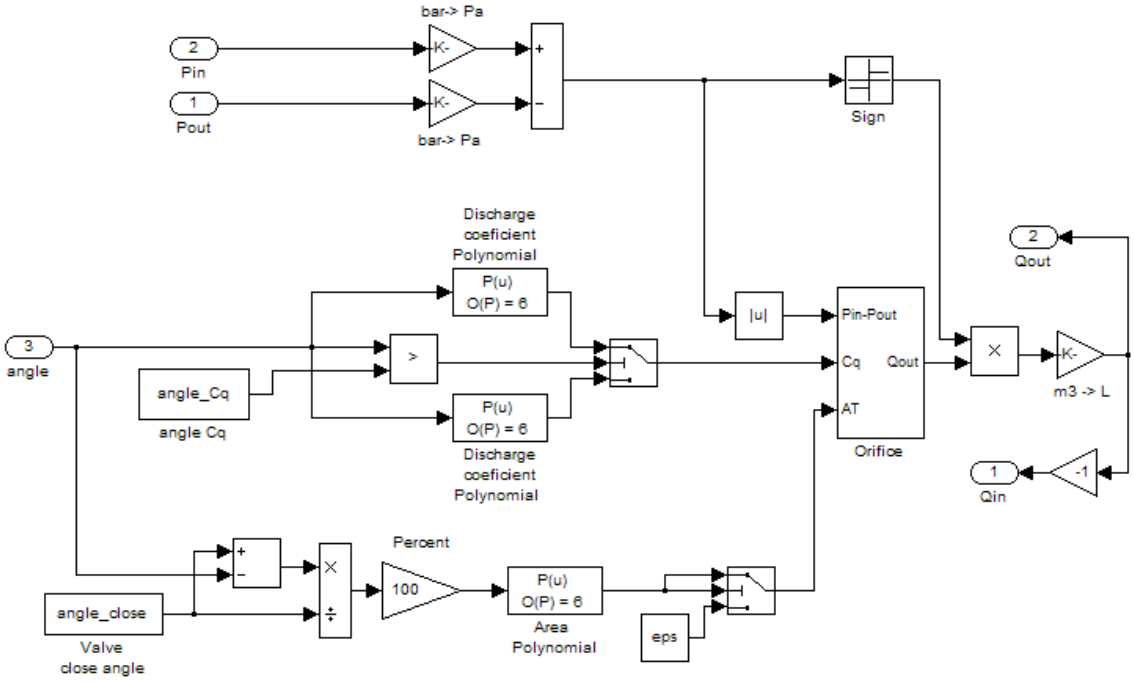

Figure C.9. Ball valve

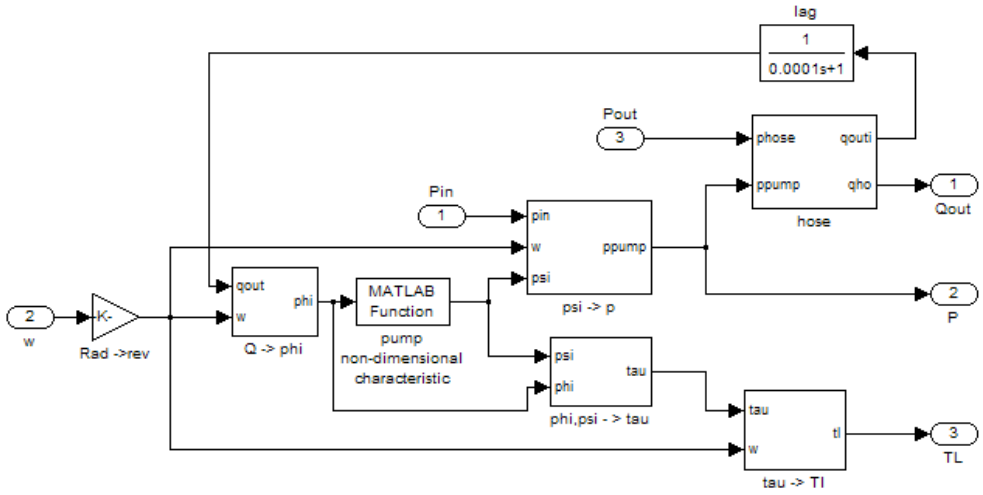

Figure C.10. Centrifugal pump

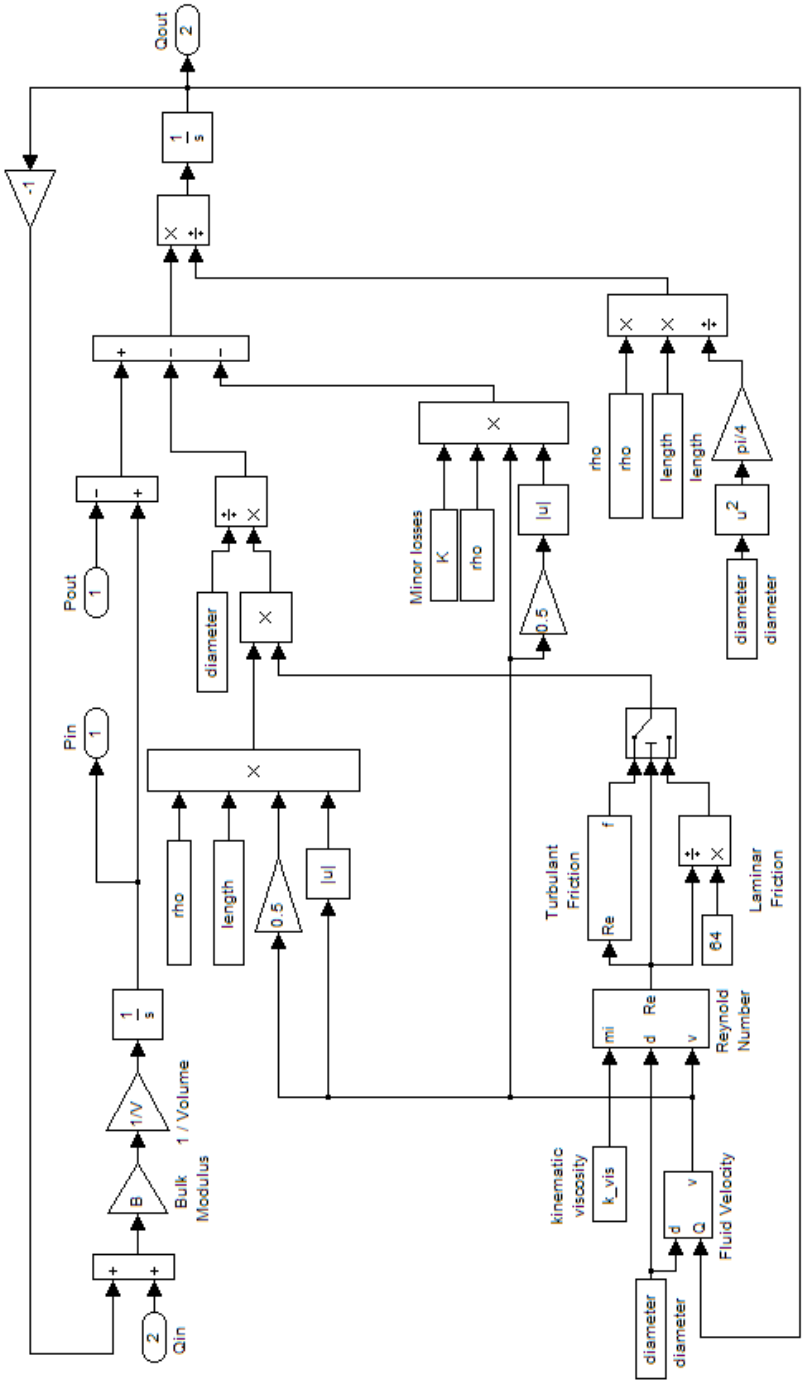

Figure C.11. Pipeline - one lumped segment

Appendix D

C/C++ Controller Implementation

```
/* FIR LOWPASS FILTER  */
float filter(float input,float *dly)
{
  short i;
  float yn;

  dly[N-1] = input;                    //newest sample to buffer
  yn = dly[0] * h[N-1];                //y(0)=x(n-(N-1))*h(N-1)
  for (i = 1; i < N; i++)              //loop for the rest
  {
    // convolution - y(n)=x[n-(N-1-i)]*h[N-1-i]
    yn += dly[i] * h[N-(i+1)];
    // update delays
    dly[i-1] = dly[i];
  }
    // return sample from filter
    return yn;
}
```

Listing D.1. FIR filter C-based code listing

```
/* CONTROLLER MAIN ROUTINE */
#define N 256
//filter coefficient file - h[N] kernel
#include "filter.cof"
// filter delay samples for refrence and feedback
static float array_ref[N]={0},array_fed[N]={0};
// control errors and PID coefficients arrays
static float error[3]={0}, a[3]={0}, adapt_error[3]={0};
// set sampling rate
Uint32 fs=DSK_AIC23_FREQ_8KHZ;
// convergance factor
#define beta 5e-8
// function declaration
float filter(float input, float *dly);              // Filter
float pid_controller(float ref, float feed);        // PID
void  pid_adaptation(float ref, float feed);        // Adaptation
// main routine for adaptive PID
void main()
{
  // variables declaration
  float reference, feedback, output;
  short i;
  // init DSK, codec for polling operation
  init_DSK_poll();

  while(TRUE)
  {
    // get input data from the ADC
    reference = ReadDataADCL();
    feedback = ReadDataADCR();
    // filter data
    reference = filter(reference,array_ref);
    feedback  = filter(feedback,array_fed);
    // IIR PID controlller
    output=pid_controller(reference,feedback);
    // update PID gains
    pid_adaptation(reference,feedback);
    // send data to ADC
    WriteDataDAC(output);
   }
}
```

Listing D.2. Controller C-based code listing

```
/* PID ROUTINE BASED ON REAL-TIME IIR ALGHORITM */
float pid_controller(float ref, float feed)
{
  float e,y;
  // Control error
  e = ref-feed;
  // Calculate PID output
  error[0] = e + error[1];
  y = a[0]*error[0] + a[1]*error[1] + a[2]*error[2];
  // Update error delay samples
  error[2] = error[1];
  error[1] = error[0];
  return y;
}
```

Listing D.3. Real time PID C-based code listing

```
/* PID COEFFICIENT ADAPTATION */
void pid_adaptation(float ref, float feed)
{
  float perf_error;
  // Find the adaptor delay
  adapt_error[0] = ref - feed ;
  perf_error = beta * adapt_error[0];
  // Update PID numerator coefficients
  a[0] = a[0] + (perf_error * adapt_error[0]);
  a[1] = a[1] + (perf_error * adapt_error[1]);
  a[2] = a[2] + (perf_error * adapt_error[2]);
  // Update the adaptors delays
  adapt_error[2]=adapt_error[1];
  adapt_error[1]=adapt_error[0];
}
```

Listing D.4. PID gains adaptation C-based code listing